



**HAL**  
open science

# Magnetic shielding topology applied to low power Hall thrusters

Lou Grimaud

► **To cite this version:**

Lou Grimaud. Magnetic shielding topology applied to low power Hall thrusters. Other. Université d'Orléans, 2018. English. NNT : 2018ORLE2046 . tel-02165921

**HAL Id: tel-02165921**

**<https://theses.hal.science/tel-02165921v1>**

Submitted on 26 Jun 2019

**HAL** is a multi-disciplinary open access archive for the deposit and dissemination of scientific research documents, whether they are published or not. The documents may come from teaching and research institutions in France or abroad, or from public or private research centers.

L'archive ouverte pluridisciplinaire **HAL**, est destinée au dépôt et à la diffusion de documents scientifiques de niveau recherche, publiés ou non, émanant des établissements d'enseignement et de recherche français ou étrangers, des laboratoires publics ou privés.

**ÉCOLE DOCTORALE ÉNERGIE, MATÉRIAUX, SCIENCES  
DE LA TERRE ET DE L'UNIVERS**

**LABORATOIRE : INSTITUT DE COMBUSTION  
AÉROTHERMIQUE RÉACTIVITÉ ET ENVIRONNEMENT**

**Thèse** présentée par :

**Lou GRIMAUD**

soutenue le : **25 Octobre 2018**

pour obtenir le grade de : **Docteur de l'Université d'Orléans**

Discipline : **Physique**

**Magnetic shielding topology applied to low power Hall  
thrusters**

**Thèse dirigée par :**

**Stéphane MAZOUFFRE**

Directeur de recherche, ICARE, CNRS Orléans

**RAPPORTEURS :**

**Stéphane BÉCHU**

Directeur de Recherche, LPSC, Université Grenoble Alpes

**Georg HERDRICH**

Priv. Doz. Dr.-Ing, IRS, University of Stuttgart

**JURY :**

**Laïfa BOUFENDI**

Professeur des Universités, GREMI, Université d'Orléans

**Laurent GARRIGUES**

Directeur de Recherche, LAPLACE, Université de Toulouse

**Georg HERDRICH**

Docteur Privatdozent, IRS, University of Stuttgart

**Stéphane BÉCHU**

Directeur de Recherche, LPSC, Université de Grenoble

**Stéphane MAZOUFFRE**

Directeur de Recherche, ICARE, CNRS Orléans

**Claude BONIFACE**

Docteur Ingénieur en Propulsion Électrique, CNES



---

## Acknowledgements

All you are going to read would not have been possible without a the help of numerous others.

First and foremost all my thanks go to Stéphane. Without him and the thrust he put in me I wouldn't have been able get into this amazing field that is the world of electric propulsion. His continuous support and mentorship during the duration of my PhD have been the key that has opened so many door for me.

All the electric propulsion team at ICARE has also been an integral part of making this adventure so enjoyable. I would like to start by thanking Sedina who has always been available for her advice and knowledge, sharing cooking tips, getting excited over rocket new and finding obscure Russian papers. Julien and Denis have been amazing at welcoming me in the lab and showing me the ropes. Moreover a lot of the work presented here is built on the foundations laid down by Julien. I can't count the number of conversations over coffee with Romain and the times his bottomless toolbox has saved me. I hope that George, who sadly didn't stay nearly long enough in the team, had as much of a good time in Orléans as I had getting to work with him. And the last but by no mean the least is Benjamin with whom I have shared a lot of hours in the lab setting up our respective experiments but also outside the lab over beers. His has always been available to help without any hesitations. Finally a tour of the electric propulsion team wouldn't be complete without mentioning all the interns who have worked here over the years, thank you for bringing your amazing attitude and passion to the team. As for Thibault who is just starting his own PhD adventure I hope you find it as interesting and fulfilling as I did.

ICARE is not of course only the electric propulsion team. I have extra thanks to give to Guillaume who was always there to help but also make fun of stupid mistakes. His expertise and patience during the sometime long and tedious test campaign was invaluable. My thanks also go to Eric and Laurent who assisted me numerous times when I was stuck on some mechanical problems. Finally the administrative team at ICARE has a special place in this thesis in making sure everything went as smoothly as possible.

Outside the lab I have had the chance to meet and work with some of the most interesting people in the electric propulsion field. Laurent Garrigues has been a huge contributor to this thesis and has been amazing at welcoming me into the electric propulsion community, especially during conferences. Claude Boniface has been an essential part of this work. His guidance, trust and willingness to fight for funding has made a lot of the work presented here possible.

Collaborations and conferences have been the opportunity to meet a lot of interesting and friendly people. Among them I would specially mention Marcel and Sarah who have been particularly friendly and ready to discuss their work.

I also own big thanks to the AskScience team for the different perspectives, and the necessary distractions.

Finally I can't conclude this acknowledgments without thanking my family. While they do not know much about space propulsion or plasma physics but they understand very well what following a passion project is. I have always enjoyed your full support on all those projects and I am infinitely grateful for this.

---

# Contents

<b>Contents</b>	<b>iii</b>
<b>List of Symbols</b>	<b>vii</b>
<b>List of Abbreviations</b>	<b>ix</b>
<b>List of Figures</b>	<b>xi</b>
<b>List of Tables</b>	<b>xv</b>
<b>1 Electric propulsion: basic principle, applications and new challenges</b>	<b>1</b>
1.1 Basics of space propulsion . . . . .	1
1.2 Electric propulsion . . . . .	2
1.2.1 Fundamental principles . . . . .	2
1.2.2 Different types of of electric thrusters . . . . .	3
1.2.3 Applications of electric propulsion . . . . .	4
Attitude control . . . . .	4
Stationkeeping . . . . .	5
Use case for orbit transfer . . . . .	5
Drag compensation . . . . .	6
End of life managment . . . . .	6
1.2.4 Industrial development of electric propulsion . . . . .	7
1.3 Hall thruster . . . . .	7
1.3.1 Working principle . . . . .	7
1.3.2 History . . . . .	8
1.4 Motivations . . . . .	10
1.4.1 Limitations of small Hall thrusters . . . . .	10
1.4.2 Lifespan of Hall thrusters and magnetic shielding concept . . . . .	10
1.4.3 Content of the thesis . . . . .	11
<b>2 Plasma diagnostics and performance measurement applied to Hall thrusters</b>	<b>13</b>
2.1 Test chambers . . . . .	13
2.1.1 NExET . . . . .	13
2.1.2 PIVOINE-2g . . . . .	14
2.2 Plume probing . . . . .	15
2.2.1 Measurement setup . . . . .	15
NExET . . . . .	15
Pivoine-2g . . . . .	16
2.2.2 Data processing . . . . .	16
2.3 Thrust measurement . . . . .	17
2.3.1 Trust stand design . . . . .	17
Mechanical design . . . . .	17
Measurement setup . . . . .	18
2.3.2 Issues with the low thrust stand configuration . . . . .	18
2.3.3 Processing the thrust stand data . . . . .	19

	Computing the thrust . . . . .	19
	Anode efficiency and specific impulse . . . . .	19
	Uncertainty estimations . . . . .	20
2.4	Laser Induced Fluorescence . . . . .	21
2.4.1	Basic principle . . . . .	21
2.4.2	Implementation . . . . .	21
2.4.3	Limitations and sources of error . . . . .	22
2.4.4	Data interpretation . . . . .	23
	Computing the electric field from IVDF . . . . .	23
2.5	Probes versus Laser Induced fluorescence for acceleration region probing . . . . .	23
2.5.1	Limitations of probe diagnostics . . . . .	23
2.5.2	Presentation of thrusters and probes used . . . . .	23
	Thrusters . . . . .	23
	Probe designs . . . . .	24
2.5.3	Macroscopic effects . . . . .	26
	ISCT200-GEO - Low-power discharge . . . . .	26
	SPT-100-ML - High-power discharge . . . . .	30
2.5.4	Local effects on the ion velocity distribution . . . . .	30
	Emissive probe . . . . .	30
	Langmuir Probe . . . . .	32
2.6	Conclusion . . . . .	33
<b>3</b>	<b>Low power Hall thrusters: scaling and performances</b>	<b>35</b>
3.1	Thruster scaling . . . . .	35
3.1.1	Existing thruster power range . . . . .	35
3.1.2	Scaling laws . . . . .	37
	Channel diameter and width . . . . .	37
	Channel length . . . . .	37
	Magnetic field . . . . .	38
3.2	The ISCT200-GEO and ISCT100 Hall thrusters . . . . .	38
3.2.1	Channel geometry . . . . .	38
3.2.2	Permanent magnets and field generation . . . . .	39
3.3	Results on the ISCT100 scaling . . . . .	39
3.3.1	Discharge envelope . . . . .	39
3.3.2	Plume divergence and characteristics . . . . .	41
	Plume current density profiles . . . . .	41
	Plume characteristics . . . . .	41
3.3.3	Performances . . . . .	42
3.3.4	ISCT100-V2 performance with BN-SiO <sub>2</sub> . . . . .	44
3.4	Results on the ISCT200-GEO scaling . . . . .	45
3.4.1	Discharge current and electron mobility . . . . .	45
3.4.2	Propellant utilization . . . . .	47
3.4.3	Divergence . . . . .	47
3.5	Conclusion . . . . .	48
3.5.1	Effects of channel geometry . . . . .	48
3.5.2	Effects of magnetic field intensity . . . . .	48
<b>4</b>	<b>Physics of a small magnetically shielded Hall thruster</b>	<b>49</b>
4.1	Erosion phenomenon in Hall thrusters . . . . .	49
4.1.1	The mechanism of ion sputtering . . . . .	50
	Classical semi-empirical model . . . . .	50
	Synergistic erosion . . . . .	50
4.1.2	Ion acceleration in Hall thruster . . . . .	51
	Main axial flow . . . . .	51
	Sheath behavior . . . . .	51
	Other secondary effects . . . . .	53

---

4.1.3	Anomalous erosion . . . . .	53
4.2	Overview of the magnetic shielding concept . . . . .	56
4.2.1	Equipotentiality of the magnetic field lines . . . . .	56
4.2.2	Magnetic field topology . . . . .	56
	General shape . . . . .	56
	Magnetic circuit design . . . . .	56
4.2.3	Existing MS thrusters . . . . .	57
4.2.4	Summary of existing results . . . . .	58
4.3	The ISCT200-MS magnetically shielded thruster . . . . .	58
4.3.1	The ISCT200-US baseline thruster . . . . .	58
4.3.2	Geometry . . . . .	59
4.3.3	Magnetic field . . . . .	59
4.4	Discharge characteristics . . . . .	60
4.4.1	Discharge current . . . . .	60
4.4.2	Thermal behavior . . . . .	60
4.5	Ion behavior . . . . .	62
4.5.1	Main acceleration region . . . . .	62
	Ion velocity distribution shape . . . . .	62
	Axial electric field . . . . .	63
	Ion density . . . . .	64
	Consequences on erosion . . . . .	65
4.5.2	Near wall behavior . . . . .	65
	Visual evidences of magnetic shielding . . . . .	65
	Ion velocity distributions . . . . .	67
	Ion flux at the walls . . . . .	71
4.5.3	Pole behavior . . . . .	71
	Visual evidences of pole erosion . . . . .	71
	Ion and neutral velocity distribution near the poles . . . . .	72
4.6	Conclusion . . . . .	75
<b>5</b>	<b>Performance of a magnetically shielded Hall thruster with graphite and ceramic walls</b>	<b>77</b>
5.1	Alternative wall material for Hall thrusters . . . . .	77
5.1.1	Previous work on alternative material for Hall thrusters . . . . .	77
5.1.2	Implementation on the ISCT200-MS and ISCT200-US . . . . .	78
5.2	Performance . . . . .	79
5.2.1	Discharge current . . . . .	79
	Envelope and discharge current . . . . .	79
	Discharge stability . . . . .	80
5.2.2	Electric field distribution . . . . .	83
5.2.3	Plume . . . . .	83
	Measurements in the NExET chamber . . . . .	83
	Measurements in the PIVOINE-2G chamber . . . . .	85
5.2.4	Thrust, specific impulse and efficiency . . . . .	85
	Unshielded thruster . . . . .	85
	Magnetically shielded thruster . . . . .	86
	Comparison between both thrusters . . . . .	87
5.3	Discussion on the performance of the magnetically shielded thruster . . . . .	89
5.3.1	Multiple ionization . . . . .	89
5.3.2	Effective ionization surface . . . . .	90
5.3.3	Magnetic topology . . . . .	91
5.3.4	Wall materials and Hall thruster physics . . . . .	92
5.3.5	Ground testing of magnetically shielded thrusters . . . . .	92
5.4	Conclusion . . . . .	93

---

<b>6</b>	<b>Improving performances of low power magnetically shielded Hall thruster</b>	<b>95</b>
6.1	PIC hybrid simulation results of the ISCT200-MS . . . . .	95
6.1.1	Overview of the code . . . . .	96
	Ions and neutrals . . . . .	96
	Electrons . . . . .	96
	Anomalous transport . . . . .	96
6.1.2	Results . . . . .	97
	Plasma properties . . . . .	97
	Performances . . . . .	100
	Erosion . . . . .	101
6.1.3	Conclusions from the simulations . . . . .	102
6.2	Design of the ISCT200-MS V2 . . . . .	102
6.2.1	Objectives . . . . .	102
6.2.2	Magnetic topology . . . . .	102
6.2.3	Magnetic circuit . . . . .	103
6.2.4	Discharge channel . . . . .	103
6.2.5	Insulation . . . . .	104
6.2.6	Thermal design . . . . .	104
6.2.7	Additively manufactured anode . . . . .	104
6.3	Conclusion . . . . .	105
	<b>Conclusion</b>	<b>107</b>
	Summary of results . . . . .	107
	Perspectives . . . . .	108
	<b>A Overview of low power thrusters</b>	<b>111</b>
	<b>B List of publications</b>	<b>115</b>
	<b>C Version française</b>	<b>117</b>
C.1	Propulsion électrique: principes de base, applications et nouveaux défis . . . . .	117
C.2	Diagnostiques plasmas et mesures de performances pour les propulseurs de Hall . . . . .	117
C.3	Propulseurs de Hall basse puissance: lois d'échelle et performances . . . . .	118
C.4	La physique d'un petit propulseur de Hall à écrantage magnétique . . . . .	118
C.5	Performances d'un propulseur de Hall à écrantage magnétique avec des parois en graphite et céramique . . . . .	119
C.6	Améliorations des performances de propulseurs de Hall à écrantage magnétique de faible puissance . . . . .	120
C.7	Conclusion . . . . .	120
	<b>Bibliography</b>	<b>121</b>

# List of Symbols

$m_{tot}$	Total initial mass of the spacecraft
$\Delta m$	Mass of propellant expended
$m_{pay}$	Payload mass
$m_{power}$	Mass of the power system
$\Delta V$	Change in velocity
$g$	Acceleration of gravity at sea level
$I_{sp}$	Specific Impulse
$V_e$	Exhaust velocity
$T$	Thrust
$\dot{m}$	Total propellant mass flow
$\dot{m}_a$	Propellant mass flow through the anode
$\eta$	Thruster efficiency
$P$	Power
$C$	Mass efficiency of the power system
$\Delta t$	Transit time
$I_{ion}$	Total ion current in the plume
$j$	Ion current density
$\alpha_{d,j}$	Divergence angle
$\eta_{prop}$	Propellant utilization efficiency
$\eta_I$	Ion beam current fraction
$m_{Xe}$	Xenon atom mass
$q_{mean}$	Ion mean charge
$V_d$	Discharge voltage
$I_d$	Discharge current
$P_a$	Anode discharge power
$\eta_a$	Anode efficiency
$v_{mp}$	Most probable velocity
$e$	Electron charge
$h$	Channel width
$L$	Channel length
$d$	Mean channel diameter
$Y$	Erosion susceptibility
$\phi_s$	Sheath potential
$k$	Boltzmann constant
$T_e$	Electron temperature
$\gamma$	Secondary electron emission coefficient
$n_e$	Electron density
$E$	Electric field
$B$	Magnetic field
$\Omega_e$	Hall parameter
$\eta_{Xe^+}, \eta_{Xe^{2+}}, \eta_{Xe^{3+}}$	Fraction of ion $Xe^+, Xe^{2+}, Xe^{3+}$



# List of Abbreviations

HT	Hall Thruster
SPT	Stationary plasma thruster
TAL	Thruster with Anode Layer
CHT	Cylindrical Hall Thruster
RF	Radio Frequency
FEEP	Field Emission Electric Propulsion
MPD	Magnetoplasmadynamics (thruster)
PPT	Pulsed Plasma Thruster
VAT	Vacuum Arc Thruster
ECR	Electron Cyclotron Resonance
VASIMR	Variable Specific Impulse Magnetoplasma Rocket
GEO	Geosynchronous Equatorial Orbit or Geostationary Orbit
GTO	Geosynchronous Transfer Orbit
MEO	Medium Earth Orbit
LEO	Low Earth Orbit
VLEO	Very Low Earth Orbit
NSSK	North-South Station Keeping
SERT-1	Space Electric Rocket Test 1
GOCE	Gravity field and steady-state Ocean Circulation Explorer
STEX	Space Technology Experiment
ISCT	ICARE Small customizable Thruster
NExET	New Experiments in Electric Thrusters
PIVIONE	Propulsion Ionique pour les Voies Orbitaux, Interprétations et Nouvelles Expériences
LIF	Laser Induced Fluorescence
IVDF	Ion Velocity Distribution Function
NVDF	Neutral Velocity Distribution Function
RPA	Retarding Potential analyzer
EP	Emissive Probe
LP	Langmuire Probe
MS	Magnetic Shielding
US	Unshielded
MS-HT	Magnetically Shielded Hall Thruster
US-HT	Unshielded Hall Thruster
JPL	Jet Propulsion Laboratory
MaSMi	Magnetically Shielded Miniature Hall thruster
HERMeS	Hall Effect Rocket with Magnetic Shielding
ARRM	Asteroid Redirect Robotic Mission
LOP-G	Lunar Orbital Platform-Gateway
FEMM	Lunar Orbital Platform-Gateway



# List of Figures

1.1	Thrust to power ratio for a range of specific impulse and efficiencies. . . . .	2
1.2	SERT-1 spacecraft with the two gridded ion thruster mounted on each side. . . . .	4
1.3	Mass fraction as a function of Isp and transit time for a 2500 m/s maneuver with electric propulsion. . . . .	6
1.4	Working principle of a Hall thruster . . . . .	8
1.5	Components of a SPT type Hall thruster . . . . .	9
2.1	The NExET test bench . . . . .	14
2.2	The PIVOINE-2g chamber . . . . .	15
2.3	Planar probes with their guard ring as used in the NExET vacuum chamber . . . . .	15
2.4	Faraday cup and its mounting system used for plume measurements in PIVOINE-2g. . . . .	16
2.5	Definition of the spherical coordinate system used for integration. The Z axis represent the thrust firing axis. . . . .	17
2.6	Schematics of the thrust balance used in the PIVOINE-2g test chamber. . . . .	18
2.7	Oscillations of the light thrust stand as seen by PIVOINE's acquisition chain . . . . .	19
2.8	Example of the raw data obtained during a thrust measurement with a 200 W thruster . . . . .	20
2.9	Layout of the LIF spectroscopy system. . . . .	21
2.10	Layout of the LIF spectroscopy system inside the vacuum tank with the thruster mounted on a 2 axis translation stage. . . . .	22
2.11	Electrostatic probe geometry . . . . .	24
2.12	Probe potential measured along the ISCT200-GEO channel axis with emissive probes. The influence of the heating current on the measured profiles is shown. (The position X=0 mm refers to the channel exit plane.) . . . . .	25
2.13	Representation of the Hall thruster and probe mounted on the fast translation stage. . . . .	26
2.14	Plasma potential and electric field along the channel axis of the ISCT200-GEO as measured by emissive probe (EP), Langmuir probe (LP) and LIF spectroscopy. The discharge was set at 200 V for 1 mg/s of xenon. . . . .	27
2.15	Floating potential along the channel axis in the ISCT200-GEO as measured by Langmuir probe (LP) and cold emissive probe (EP). The discharge was set at 200 V for 1 mg/s of xenon. . . . .	28
2.16	Discharge current as a function of the Emissive probe position in the ISCT200-GEO. The red line represents a moving average for readability. The current was acquired as the heated probe is translating at 250 mm/s toward the truster. . . . .	29
2.17	Spectrogram of the discharge current as a function of the postion of the probe in the ISCT200-GEO. The current was acquired as the heated emissive probe is translating at 250 mm/s toward the truster. . . . .	29
2.18	Plasma potential and electric field along the channel axis in the SPT-100-ML as measured by emissive probe (EP) and LIF spectroscopy. The discharge was set at 3 mg/s of Xenon. . . . .	30
2.19	IVDFs in the vicinity of the emissive probes inside (-5 mm), at the exit plane (0 mm) and outside (+5 mm) of the ISCT200-GEO. . . . .	31
2.20	IVDFs in the vicinity of the simple alumina tube inside (-5 mm), at the exit plane (0 mm) and outside (+5 mm) of the ISCT200-GEO. . . . .	31
2.21	IVDFs in the vicinity of the Langmuir probes inside (-5 mm), at the exit plane (0 mm) and outside (+5 mm) of the ISCT200-GEO. . . . .	32

3.1	Characteristics dimensions of a Hall thruster . . . . .	37
3.2	The ISCT200-GEO Hall thruster in the $2S_0$ configuration . . . . .	38
3.3	The ISCT100 Hall thruster in the $2S_0 B_0$ configuration. . . . .	39
3.4	Discharge current for different configurations as a function of anode mass flow and discharge voltage. . . . .	40
3.5	Current density profiles across the plume of each configurations at 200 V 0.5 mg/s, 300 V 0.5mg/s and 200 V 0.6 mg/s operating conditions. The dashed lines represent the divergence angle $\alpha_d$ . . . . .	41
3.6	Thrust versus discharge power for different mass flow rates . . . . .	43
3.7	Specific impulse versus discharge voltage for different mass flow rates . . . . .	43
3.8	Anode efficiency versus discharge power for different mass flow rates . . . . .	43
3.9	Comparison of performances between the ISCT100-V1 in $2S_0, 2B_0$ configuration with $Al_2O_3$ walls and the ISCT100-V2 in $2S_0, 2B_0$ configuration with $BN-SiO_2$ walls: discharge current (a), thrust (b), anode specific impulse (c) and anode efficiency (d). . . . .	44
3.10	Discharge current for the different configurations and operating points of the ISCT200-GEO. . . . .	45
3.11	Ion beam current for the different configurations and operating points of the ISCT200-GEO. . . . .	46
3.12	Ion beam current fraction for the different configurations and operating points of the ISCT200-GEO. . . . .	46
3.13	Propellant utilization fraction for the different configurations and operating points of the ISCT200-GEO. . . . .	47
3.14	Divergence angle for the different configurations and operating points of the ISCT200-GEO. . . . .	48
4.1	Normal energy dependence and total erosion as a function of energy and angle for $BN-SiO_2$ . . . . .	51
4.2	Sheath potential versus electron temperature at equilibrium on a $BN-SiO_2$ surface when secondary electron emissions are limited by the space-charge potential. . . . .	52
4.3	Azimuthal drift velocity of ions in a 200 W wall less thruster at 200 V discharge voltage [1]. . . . .	53
4.4	Anomalous erosion as seen on the PPS-1350 thruster after 3500 hours of operation [2] . . . . .	54
4.5	Apparition of the anomalous erosion on a surface with 0.01 amplitude periodic sinusoidal rugosity under an ion flow at 60 degrees incidence angle. The color correspond to deviation from mean height. The final feature has the same wavelegnth but amplitudes of 0.8. . . . .	55
4.6	Average erosion rate calculated from simulation presented in figure 4.5 . . . . .	55
4.7	Schematic comparison between classical and magnetic shielding configurations. The black lines (top) represent the magnetic field lines and the blue lines (bottom) are the electric potential lines, colors illustrates the electron temperature. . . . .	57
4.8	Normalized magnetic field profile at the center of the discharge channel and near the walls for the ISCT200-US and ISCT200-MS. The distances are normalized by the length of the discharge channel. . . . .	59
4.9	Discharge current for various mass flow for the ISCT200-MS and ISCT200-US. The filled in band contains 90% of the current trace. . . . .	60
4.10	Comparison of the temperature measured by IR imaging at 200 V and 1 mg/s. The regions of interest are highlighted . . . . .	61
4.11	Temperature versus discharge power for the ISCT200-MS and ISCT200-US as measured by IR camera. Temperatures are averaged over the whole surface visible for each region of interest. . . . .	62
4.12	a) Magnetic field lines in an unshielded (top) and magnetic shielded thruster (bottom). Laser beam orientation for measurements b) along the center of the discharge channel, c) perpendicular to the inner and outer walls as well as parallel to the outer wall, d) perpendicular to the magnetic poles. The arrow represents the positive velocity direction . . . . .	62
4.13	Normalized axial IVDFs along the center of the discharge channel . . . . .	63
4.14	Electric field along the center of the discharge channel . . . . .	64
4.15	Comparison of relative metastable ion density profiles in US and MS Hall thrusters along the center of the discharge channel at 200 V discharge voltage. The profiles are normalized by their respective maximum value. . . . .	65
4.16	Ceramic walls of the ISCT200-US (left) and ISCT200-MS (right) highlighting, for the MS case, the absence of the characteristic erosion patern in the black deposit formed on the walls. . . . .	66

4.17	Picture highlighting the gap between the plasma and the walls in the magnetically shielded thruster. . . . .	66
4.18	IVDF perpendicular to the internal wall. Negative velocities indicate ions moving toward the wall. . . . .	68
4.19	IVDF perpendicular to the external wall. Negative velocities indicate ions moving toward the wall. . . . .	69
4.20	IVDF parallel to the external wall. Negative velocities indicate ions moving toward the anode. . . . .	70
4.21	Evidence of erosion above the ceramic caps (left). On the right is a front view of the ISCT200-MS without the caps. The top of the magnetic circuit is highlighted in red [3]. . . . .	72
4.22	Worst signal to noise ratio for normalized IVDFs above the internal and external magnetic poles . . . . .	72
4.23	IVDF perpendicular to the inner magnetic pole . . . . .	73
4.24	IVDF 2 mm above the internal pole of the ISCT200-MS with the laser firing along the thruster axis ( $0^\circ$ ) and off-axis ( $20^\circ$ ) . . . . .	74
4.25	NVDF 1 mm above the internal pole of the ISCT200-MS . . . . .	74
5.1	Discharge channel with the graphite inserts. The graphite inserts cover two thirds of the discharge channel length. . . . .	78
5.2	Discharge current for the US thruster with ceramic walls and graphite walls. The filled in areas delimit the top 10% and bottom 10% of the current oscillations are at this operating point. . . . .	79
5.3	Discharge current for the MS thruster with ceramic walls and graphite walls. The filled in areas delimit the top 10% and bottom 10% of the current oscillations are at this operating point. . . . .	80
5.4	Spectra of the discharge current for the US-HT with BN-SiO <sub>2</sub> (top) and graphite (bottom) walls for a range of discharge voltages at 1 mg/s. . . . .	81
5.5	Spectra of the discharge current for the MS-HT with BN-SiO <sub>2</sub> (top) and graphite (bottom) walls for a range of discharge voltages at 1 mg/s. . . . .	82
5.6	Most probable ion velocity (a) and electric field intensity (b) as a function of the distance from the exit plane. The vertical lines represent the position of the maximum of the magnetic field for the US-HT (continuous line) and MS-HT (dashed line). . . . .	83
5.7	Current density profiles measured across the plume with planar probes with guard rings at 200 V and 1 mg/s of xenon for the US-HT (top) and MS-HT (bottom). The dashed lines represent the divergence angle for the BN-SiO <sub>2</sub> (red) and graphite cases (black). . . . .	84
5.8	Discharge current (a), thrust (b), anode specific impulse (c) and anode efficiency (d) of the ISCT200-US. . . . .	86
5.9	Discharge current (a), thrust (b), anode specific impulse (c) and anode efficiency (d) of the ISCT200-MS. . . . .	87
5.10	Comparison between the thrust of the US and MS thrusters with ceramic wall . . . . .	88
5.11	Comparison between the anode efficiency of the US and MS thrusters with ceramic wall . . . . .	88
5.12	Comparison of the shape of the plasma between the unshielded and shielded thrusters. . . . .	90
5.13	Magnetic field topology and US (left) and MS (right) thrusters. The red line represents the maximum magnetic field intensity as well as the area of maximum electric field. The blue arrows show the direction of the electric field. . . . .	91
6.1	Simulation results for the ISCT200-US. <b>(a)</b> Electric potential (continuous lines) with respect to the magnetic field topology (dashed lines). <b>(b)</b> Electron temperature. <b>(c)</b> Ionization rate and mean ion velocity vectors . . . . .	98
6.2	Simulation results for the ISCT200-MS. <b>(a)</b> Electric potential (continuous lines) with respect to the magnetic field topology (dashed lines). <b>(b)</b> Electron temperature. <b>(c)</b> Ionization rate and mean ion velocity vectors . . . . .	99
6.3	Ion energy at the wall surface (left) and erosion rate prediction (right). . . . .	101
6.4	The ISCT200-MS-V2 magnetically shielded, low power, permanent magnet Hall thruster . . . . .	103
A.1	Anode efficiency for low power thrusters . . . . .	112

A.2 Anode efficiency for low power thrusters, with ICARE's thruster highlighted . . . . . 113

# List of Tables

1.1	Overview of the main actors of electric propulsion (ignoring arcjets and resistojets) . . . .	7
3.1	Overview of the data derived from plume measurements for the 200 V 0.6 mg/s and 300 V 0.5 mg/s cases in all the configurations. . . . .	42
4.1	Ion density and flux at the walls . . . . .	71
5.1	Overview of the data derived from plume measurements in the NExET vacuum chamber. All the cases presented were obtained at a mass flow of 1 mg/s of xenon. . . . .	84
5.2	Overview of the data derived from plume measurements in the PIVOINE vacuum chamber. All the cases presented correspond to a 200 V discharge voltage and are not corrected for multiply charged ions. . . . .	85
6.1	Comparison of simulated and experimental results for the shielded and unshielded thrusters. <sup>1</sup> from NExET test chamber, <sup>2</sup> from PIVOINE-2g test chamber. . . . .	101
A.1	Source of the data presented in figure A.2 . . . . .	111



# Chapter 1

## Electric propulsion: basic principle, applications and new challenges

### Contents

---

<b>1.1</b>	<b>Basics of space propulsion</b>	<b>1</b>
<b>1.2</b>	<b>Electric propulsion</b>	<b>2</b>
1.2.1	Fundamental principles	2
1.2.2	Different types of electric thrusters	3
1.2.3	Applications of electric propulsion	4
1.2.4	Industrial development of electric propulsion	7
<b>1.3</b>	<b>Hall thruster</b>	<b>7</b>
1.3.1	Working principle	7
1.3.2	History	8
<b>1.4</b>	<b>Motivations</b>	<b>10</b>
1.4.1	Limitations of small Hall thrusters	10
1.4.2	Lifespan of Hall thrusters and magnetic shielding concept	10
1.4.3	Content of the thesis	11

---

### 1.1 Basics of space propulsion

One of the fundamental equation of rocket propulsion is the so called “Tsiolkovsky rocket equation”. It describes what fraction of the total spacecraft mass needs to consists of propellant in order to increase the its velocity by a certain amount. The equation can be written as follow:

$$\frac{m_{tot} - \Delta m}{m_{tot}} = e^{\frac{-\Delta V \cdot g}{Isp}} \quad (1.1)$$

With  $m_{tot}$  the total initial mass of the spacecraft,  $\Delta m$  the mass of propellant expended in the maneuver,  $\Delta V$  the change in velocity or velocity increment,  $g$  the acceleration of gravity on Earth surface ( $\sim 9.81 \text{ m/s}$ ) and  $Isp$  the specific impulse. The specific impulse is the time in second a quantity of propellant can exert a thrust equal to its own starting weight at sea level. It is often more convenient to use instead a fictitious “exhaust velocity” defined by  $V_e = Isp \cdot g$ . This exhaust velocity is described as fictitious since it would be equal to the actual exhaust velocity only if all of the propellant was used for propulsion, exited at the same velocity and if all the propellant particles velocity vectors were aligned with the thrust vector. The rocket equation shows that the highest  $V_e$  is the less propellant is needed for the same change in velocity.

This exhaust velocity is also useful to express the thrust of the system ( $T$ ) as function of the propellant mass flow ( $\dot{m}$ )

$$T = \dot{m} \cdot V_e \quad (1.2)$$

From there we can also compute the efficiency of the thruster ( $\eta$ ) as the ratio of useful kinetic power in the plume over the input power ( $P$ ).

$$\eta = \frac{\frac{dE_k}{dt}}{P} = \frac{T \cdot V_e}{2 \cdot P} \quad (1.3)$$

This equation shows that, at fixed efficiency and input power, the thrust is inversely proportional to the specific impulse. Figure 1.1 illustrates the thrust to power ratios achievable over a range of specific impulses at various efficiencies. This equation is valid for all self contained reaction propulsion device. It shows that a high specific impulse can only be achieved at the cost of a lower thrust to power ratio.

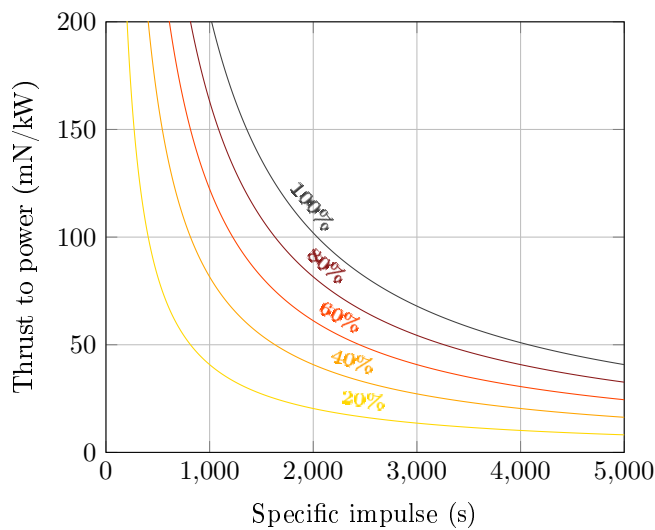


Figure 1.1: Thrust to power ratio for a range of specific impulse and efficiencies.

## 1.2 Electric propulsion

### 1.2.1 Fundamental principles

In chemical thruster the energy used to accelerate the propellant is contained within the propellant itself. This means that the exhaust velocity is controlled by the specific energy density of the propellant. Neglecting all losses from the conversion of the chemical to kinetic energy we can write

$$V_e = \sqrt{2 \cdot \frac{E}{m}} \quad (1.4)$$

with  $E$  the energy released by the reaction and  $m$  the reaction products mass.

The efficiency of a chemical thruster is thus fundamentally limited by the  $E/m$  ratio of the chemical reaction. The best commonly available propellant mix is the ubiquitous hydrogen/oxygen reaction. Thanks to its very light reaction product the theoretical maximum specific impulse is 529 s (the maximum reached is closer to 450 s in practice). Even higher energy densities are achievable with more exotic combinations (hydrogen/beryllium/oxygen or lithium/fluorine/hydrogen) but practical considerations with propellant storage, handling, stability and toxicity effectively makes them too complex to use.

Chemical thruster are thus limited to specific impulse under 500 s. Higher values can only be achieved if the energy source is decoupled from the reaction mass. Three main possibilities exist for in space applications. The first one is to use nuclear reactions (fission or fusion) as a heat source for the propellant.

The second solution is to heat the propellant with photons. Those could be either beamed as a laser from an external device or collected from solar radiation. The last, and most mature solution, is to use electromagnetic forces to provide energy to the propellant. This is what we refer to as “electric propulsion”<sup>1</sup>.

The issue with electric thrusters is that the electrical power available on board a spacecraft is currently very limited. Energy storage density in batteries is too poor to be useful and nuclear sources are not mature enough and have low power-to-weight ratio. The best practical source of electricity is photovoltaic panels. This restricts the power available on a spacecraft sized to fit in modern launcher fairings to a few tens of kilowatts. The thrust is thus at best a few newtons when the thruster takes advantage of the specific impulse achievable with electric propulsion ( $\geq 1000$  s).

### 1.2.2 Different types of electric thrusters

A wide variety of electric propulsion devices exist [5–9]. They can usually be divided into three categories: thermal, electrostatic, and electromagnetic systems.

The thermal thrusters are the most straightforward. Electrical energy is used to heat a working fluid which is then accelerated through a nozzle. The heating element can be as simple as a resistor. These **resistojets** are limited by the maximum working temperature of the heating material. One of the solutions to this problem is the **arcjet** which induces an electrical arc in the fluid itself in order to heat it. Gas or liquids can also be heated up by microwaves. This technique has the advantage of having no electrodes which can prolong the lifespan of the thruster. Electrothermal thrusters are often limited to under 1000 s of specific impulse but present the advantage of being fairly propellant agnostic.

The second solution is to use an electric field to accelerate ions. The simplest solution is the **gridded ion thruster**. A gaseous propellant is first ionized with a RF, microwave stage or DC discharge and the ions are then accelerated through an electric field generated by a gridded electrode. The beam of ions is then neutralized by an external cathode. In practice multiple grids are used to better control the potential drop, ion optics and electron backstreaming. The issue with this system is that the plasma is not kept quasi-neutral and thus is confronted with the Child-Langmuir limit for ion current extraction. That means that only moderate current (or thrust) density can be achieved. However since ionization and acceleration are separated, and sheath behavior around the electrode can be finely controlled, high specific impulses can be achieved (up to 10,000 s) with minimal divergence and erosion.

Another type of electrostatic thrusters are the field emission electric propulsion (**FEED**) systems as well as the **colloid thrusters**. Both rely on field effect to form Taylor cones in some fluids (liquid metals in FEED, ionic liquids in colloid thrusters) and extract ions. Due to limitations on the Taylor cone stability these thrusters are often confined to very low thrust applications ( $\sim \mu\text{N}$ ) and relatively high Isp ( $\geq 4000$  s). They need a large number of emission sites to be able to reach higher thrust.

Another way to exploit electrostatic acceleration is based around a **magnetic nozzle**. An initial plasma discharge is created and its electrons are heated up. They then diffuse along magnetic field lines shaped similarly to a classical rocket nozzle. This diffusion and expansion of the electron pulls along the ions in an ambipolar electric field. At some point the electrons leave the magnetic field lines and are ejected. Those thrusters are principally differentiated by their ionization and electron heating method. Popular variants include ECR heating and helicon discharges. Some of the operating mods in the VASIMR concept also rely on this principle.

Lastly in the electrostatic family is the **Hall thruster** (HT). In Hall thrusters an electric field is generated across a magnetic barrier where the plasma is kept quasi-neutral. This results in high thrust densities. More details on the principle behind Hall thrusters are available in section 1.3.1. Those thrusters benefit from a high propellant utilization ( $\geq 90\%$ ) and moderate specific impulse compared to other electric propulsion systems (between 1000 and 3000 s) which grants them one of the highest thrust to power ratio of all the plasma thrusters ( $\sim 50$  mN/kW).

The last type of thrusters are the electromagnetic thrusters. One of the most well known example is the magnetoplasmadynamic (**MPD**) thruster. A strong radial current is induced through a gas and generates an azimuthal magnetic field. This accelerates plasma axially through the Lorentz force. Since the current needs to be in the order of the kiloampere to produce a strong enough magnetic field that

---

<sup>1</sup>More exotic solutions have been proposed blurring the lines between those categories. Alternative energy storage and other means of energizing reaction mass are possible. For overviews of such concepts see reference [4] and [www.projectrho.com](http://www.projectrho.com)

technology is often associated with high power devices. However operating the MPD thruster in pulsed mode, or with an external applied magnetic field can make lower power utilization possible. The advantage of using the Lorentz force is that the thrust density can extremely high.

Other thrusters based on the use of Lorentz's force also exist. Some of the more most well known are the pulsed plasma thruster (**PPT**) and vacuum arc thruster (**VAT**). Both rely on striking a plasma arc between two electrodes. In the PPT the arc ablates a dielectric (traditionally Teflon) while in the VAT the cathode metal is ablated.

A great number of variants of the thrusters presented above have been proposed over the years. An exhaustive list would be beyond the scope of this introduction. More details can be found in the reviews [5–9].

### 1.2.3 Applications of electric propulsion

#### Attitude control

Since electric propulsion system are limited to low thrust by the energy available on board the spacecraft, they have often been confined to secondary propulsion applications. One of the most obvious one, and one of the first historical application of electric propulsion was for attitude control. After an unsuccessful launch in November of 1963, Zond-2 was launched on a Mars fly-by trajectory on November 30, 1964. It was fitted with an array of PPT for attitude control which was test fired on December 14. This was the first operational use of a plasma propulsion system in deep space [10] and their first practical use.

The Soviet efforts to be the first to test electric propulsion in space were beaten by the SERT-1 sub-orbital spacecraft (see figure 1.2) launched only a few months before on July 20, 1964. SERT-1 was a technology demonstration mission fitted with two gridded ion thrusters fed with cesium and mercury.

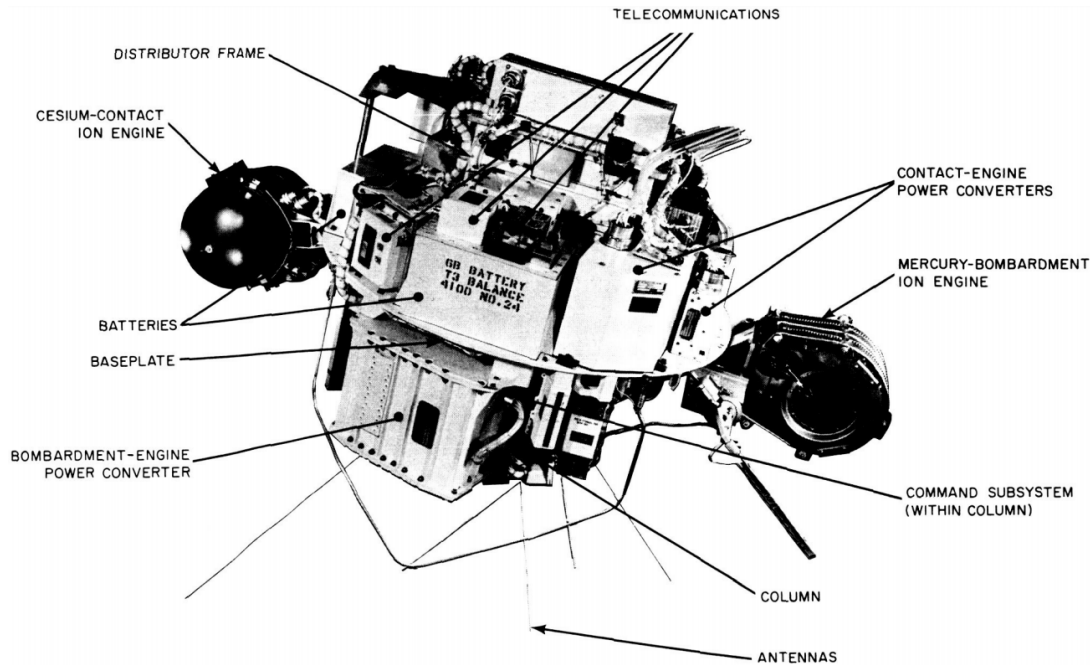


Figure 1.2: SERT-1 spacecraft with the two gridded ion thruster mounted on each side.

On top of the potential mass saving due to lower propellant utilization, electric propulsion offers the advantage of enabling very small impulse bits for attitude control. This has made electric propulsion system an attractive solution for missions requiring very precise pointing and positioning like the LISA mission.

### Stationkeeping

Another application where the low thrust is not a handicap is stationkeeping. Kilowatt class Hall thrusters like the SPT-100 have been used for several decades to handle north-south stationkeeping (NSSK) for geostationary satellites. This maneuver is required because of the lunar and solar gravitational perturbations on geostationary orbits. NSSK cost is in the order of 10 to 50 m/s per years. Cumulating this over the 10 to 15 years lifespan of a commercial GEO satellites the total impulse required makes high specific impulse systems valuable.

### Use case for orbit transfer

For larger orbit change the low thrust of electric propulsion systems can be a drawback. Looking at the rocket equation one would assume that since an increase in Isp results in a better mass fraction thrusters should be designed with the highest Isp possible. However we should remember that the rocket equation only accounts for the wet and dry mass and does not consider the whole system mass. For electric propulsion the mass of the electrical system required to power the thruster can be significant. Going back to the rocket equation we can write.

$$\frac{m_{pay} + m_{power}}{m_{tot}} = e^{-\frac{\Delta V}{V_e}} \quad (1.5)$$

With  $m_{pay}$  being the payload mass (or more precisely the mass of the spacecraft without propellant and power systems),  $m_{power}$  the power system mass (solar panels and power processing unit) and  $m_{tot}$  the total mass of the spacecraft at launch with propellant.

$$\frac{m_{pay}}{m_{tot}} = e^{-\frac{\Delta V}{V_e}} - \frac{m_{power}}{m_{tot}} \quad (1.6)$$

The power system mass can be simply expressed as

$$m_{power} = C \cdot P \quad (1.7)$$

with  $C$  the mass efficiency of the power system in kg/W and  $P$  the power needed by the thruster. The power can be express as a function of thrust ( $T$ ), exhaust velocity ( $V_e$ ) and thruster efficiency ( $\eta$ ) so the mass fraction of payload over total mass is

$$\frac{m_{pay}}{m_{tot}} = e^{-\frac{\Delta V}{V_e}} - \frac{C \cdot T \cdot V_e}{2 \cdot \eta \cdot m_{tot}} \quad (1.8)$$

and since the thrust is a function of propellant mass flow ( $\dot{m}$ ) and exhaust velocity with  $T = V_e \cdot \dot{m}$  we get

$$\frac{m_{pay}}{m_{tot}} = e^{-\frac{\Delta V}{V_e}} - \frac{C \cdot \dot{m} \cdot V_e^2}{2 \cdot \eta \cdot m_{tot}} \quad (1.9)$$

For a system that operates at a constant mass flow over the whole firing time ( $\Delta t$ )

$$\dot{m} = \frac{m_{prop}}{\Delta t} = m_{tot} \cdot \frac{1 - e^{-\frac{\Delta V}{V_e}}}{\Delta t} \quad (1.10)$$

Which means that

$$\frac{m_{pay}}{m_{tot}} = e^{-\frac{\Delta V}{V_e}} - \frac{2 \cdot C \cdot V_e^2}{\eta \cdot \Delta t} \cdot \left(1 - e^{-\frac{\Delta V}{V_e}}\right) \quad (1.11)$$

One of the main application of in space propulsion is the transfer of orbit from geostationary transfer orbit (GTO) to geostationary orbit (GEO) for commercial communication and TV satellites. This maneuver has been typically done by apogee thrusters on board the spacecraft and cost between 1500 and 1800 m/s of delta-v.

For a typical thruster energy efficiency  $\eta$  is 55%. The power system mass efficiency is assumed to be 0.0173 kg/W (0.0033 kg/W for the PPU [11] and 0.014 kg/W for the solar array [12]). We can calculate the optimal Isp for this transfer with an electric thruster so that the payload mass is maximized. The spiraling low thrust trajectory required by electric propulsion means that a standard GTO1500 insertion

orbit requires an additional 2500 m/s to reach GEO [13]. We can plot the payload mass fraction with respect to the Isp for different transit time (see figure 1.3). Assuming a 4 months long trip (as with the all electric EUTELSAT 172B GEO satellite) the optimal Isp is calculated at 1200s for a payload mass fraction of 0.64. Longer trips increase the mass fraction and the optimal specific impulse.

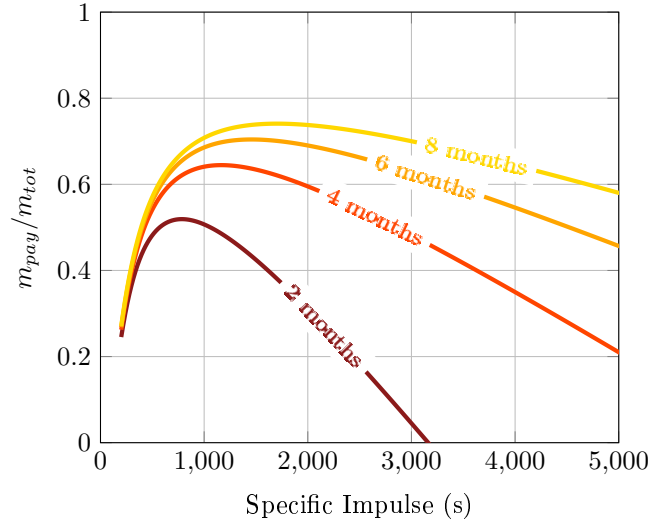


Figure 1.3: Mass fraction as a function of Isp and transit time for a 2500 m/s maneuver with electric propulsion.

Of course that calculation assumes that the power system is only required for propulsion and is useless for the payload, which is obviously not realistic and underestimates the optimal Isp. It also optimizes the mass ratio rather than the mass of payload to cost ratio, which is arguably more important for a commercial spacecraft. Figure 1.3 is nonetheless interesting in showing that specific impulses above 3000s are not very attractive for GEO bound satellites. It is more efficient for electric thrusters to operate in a high thrust to power mode than a high Isp one. This is why Hall thrusters are particularly interesting for the “all electric” GEO platforms. The typical specific impulse of commercial models (between 1500 and 1800s) is very well suited to that type of orbit transfer.

Development of dual modes Hall thrusters with low Isp/high thrust and high Isp/low thrust operating points is underway in order to be able to be efficient at both orbit transfer and stationkeeping.

This trade-off also applies for deep space missions. However those missions usually require larger delta-V changes and are less time sensitive. This favors the higher specific impulse gridded ion thrusters.

### Drag compensation

Another application where the low thrust and precise impulse control of electric propulsion is drag compensation for low and very low earth orbits (LEO and VLEO). This kind of orbits can be desirable for earth observation, low latency communication and some science applications (the European GOCE gravimeter for example). Depending on the altitude the residual atmospheric drag can be in the same order of magnitude as the thrust of a electric propulsion system. Continuous thrust can help prolong the spacecraft lifespan and reduce orbital perturbations due to drag.

### End of life management

The very good stability of most electric thruster propellant as well as the small mass and volume of some systems can make them ideal candidates to ensure proper disposal of the spacecraft at the end of it’s useful life. With the growing concern over orbital debris and new regulations being considered spacecraft orbiting above 500 to 600 km will probably need some form of propulsion to ensure that they reenter the Earth’s atmosphere in a timely fashion.

### 1.2.4 Industrial development of electric propulsion

The industrial landscape for electric propulsion is relatively varied and is undergoing rapid change. After being dominated by a few major actors the “newspace” revolution is bringing cheaper launch prices and smaller spacecraft which has spurred a number of new companies. Table 1.1 presents an overview of some of the companies producing or developing electric propulsion systems for the commercial market. Arcjets and resistojets have been omitted from that list as they are limited to low specific impulses.

Table 1.1: Overview of the main actors of electric propulsion (ignoring arcjets and resistojets)

Company	Products	Location
ArianeGroup	Gridded ion thrusters	Germany
Thales	HEMP	Germany
QuinetiQ	Gridded ion thrusters	United Kingdom
Fakel	Hall thrusters	Russia
SAFRAN	Hall thrusters	France
Sitael	Hall thrusters	Italy
Rafael	Hall thrusters	Israel
Aerojet Rocketdyne	Hall thrusters, PPT, Gridded ion thruster	Washington, USA
Busek	Hall thrusters, FEPP, Gridded ion thrusters, PPT	Massachusetts, USA
ENPULSION	FEPP	Austria
Accion systems	Colloid thrusters	Massachusetts, USA
Exotrail	Hall thrusters	France
Apollo Fusion	Hall thrusters	California, USA
Orbion Space Technology	Hall thrusters	Michigan, USA
COMAT	VAT	France
Phase4	Electrodless magnetic nozzle	California, USA
ThrustMe	Gridded ion thrusters	France
T4i	RF thruster with magnetic nozzle	Italy
Momentum	Microwave electrothermal thruster	California, USA
Mars Space	PPT	United Kingdom
Neumann Space	VAT	Australia
Ad Astra Rocket Co.	Electrodless magnetic nozzle	Texas, USA
Exo Terra Corp.	Hall thrusters	Colorado, USA
SETS	TAL/Hall thrusters	Ukraine

## 1.3 Hall thruster

### 1.3.1 Working principle

Hall thrusters are, on paper, fairly simple devices [14–17]. They consists in an annular discharge chamber traversed by a radial magnetic field. An external cathode provides electrons that are attracted to the positively charged anode inside the discharge channel. The orthogonal magnetic field (radial) and electric field (axial) make the electrons drift in the azimuthal direction. This is the Hall current which gives its name to the thrusters. The Hall current is responsible for ionizing the neutral gas injected in the anode area. The electrons confined in the magnetic barrier localize the potential drop near the maximum magnetic field area. The resulting electric field accelerates the ions to high speed. Part of the electrons generated by the cathode are used to neutralize the ion beam. The principle is illustrated on figure 1.4. The acceleration in Hall thrusters happens in an area where the plasma is quasi-neutral. That means that high current densities can be reached as there are no space charge effects. Ionization is also very efficient with more than 90% of the propellant being ionized in large thrusters ( $\geq 1$  kW). This efficient ionization at even modest voltages (around 300 V) means that Hall thrusters can achieve some of the highest thrust to power ratio in all the plasma thrusters.

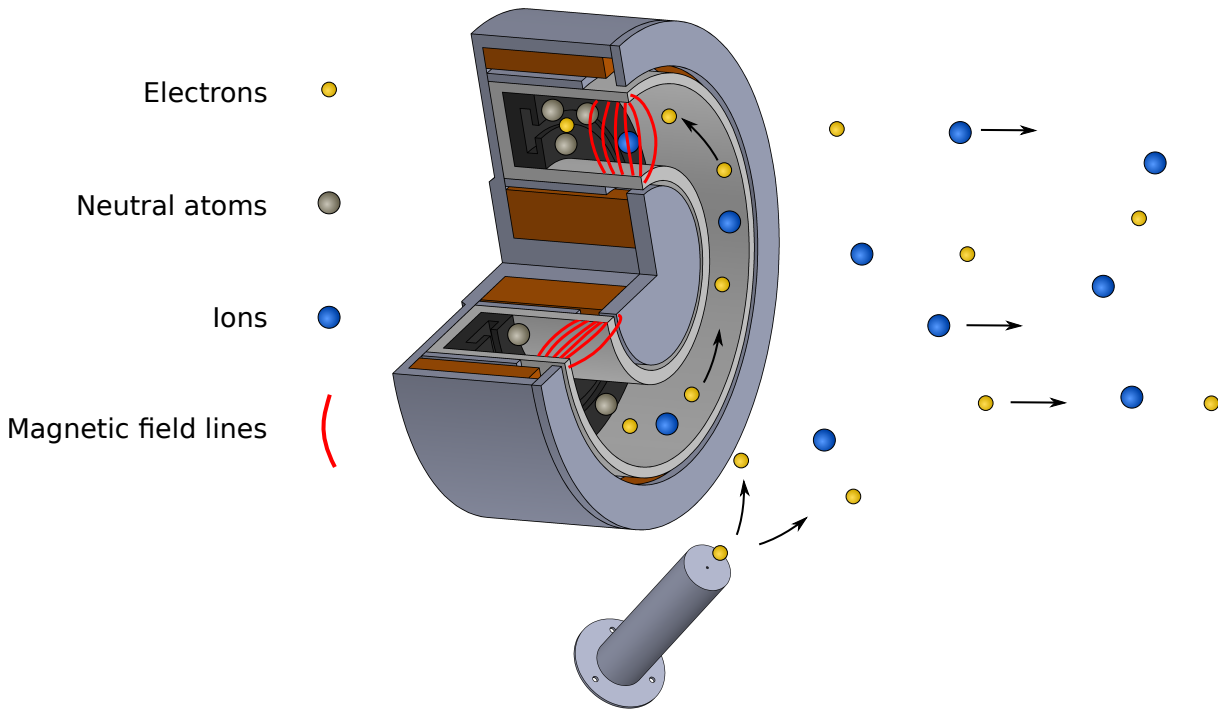


Figure 1.4: Working principle of a Hall thruster

Two main types of Hall thrusters have been studied [18]. The most common is the so called “stationary plasma thruster” (SPT) or sometime referred to as the “magnetic layer” thruster. The schematic of such a thruster can be found in figure 1.5. The anode is inside the discharge channel and the walls of the discharge channel are covered with dielectric material (typically boron nitride compounds). The ionization and acceleration regions are relatively wide and their position is not controlled by the electrodes but by the magnetic field intensity and topology.

The second type of Hall thruster is called “thruster with anode layer” (TAL). The main difference with the SPT type is that instead of dielectric walls, the discharge channel is conductive and maintained at the anode potential. In most TAL thrusters ring electrodes are placed at the exit of the discharge channel and are maintained at the cathode potential. This forces the location of the acceleration region between those two electrodes. The acceleration region in TAL is usually narrower than in SPT.

Traditionally the magnetic field is generated by electromagnets. A single internal coil is used but the several coils wound around individual magnetic cores, or one big coil wound around the whole thruster can be used for the external part. The magnetic flux is directed by a magnetic circuit made of magnetic steel, iron or iron-cobalt alloys. Near the exit of the discharge channel magnetic pole pieces shape the magnetic field in this critical area. Magnetic screen parallel to the discharge channel walls can also be used to shape the field. Lastly “trim coils” can provide another degree of freedom to adjust the magnetic field shape. Another way of generating the magnetic field is to use permanent magnets and will be discussed further in this thesis.

Hall thrusters have a total efficiency ranging from 30 to 70% depending on their size. They achieve thrust to power ratio of around 50 to 60 mN/kW and specific impulses between 1000 and 3000 seconds. They are also relatively compact with a thrust density greater than 30 N/m<sup>2</sup>. This makes them particularly well suited to operations on geostationary satellites or other spacecraft where transit time cannot be too long.

### 1.3.2 History

While the potential of electric propulsion had been widely recognized by the early 50’s, its suspected applications were far from what is seen nowadays. Plasma propulsion systems were first imagined as powerful thrusters capable of reducing transit times for heavy cargo or manned missions in deep space.

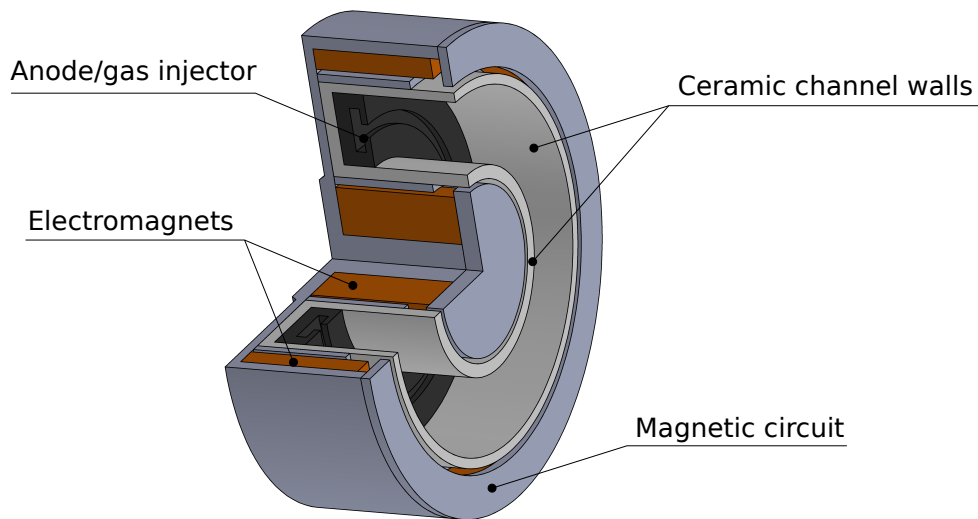


Figure 1.5: Components of a SPT type Hall thruster

When it was realized that the advent of powerful light electrical sources would not be as fast as the progress in the propulsion system themselves focus was shifted to lower specific impulse and more energy efficient systems.

The history of the Hall thruster development is mostly dominated by the work performed in the Soviet Union during the cold war. As such few of the primary sources and original publications are available to non-Russian speaking audience. Luckily a few of the inventors wrote an overview of the development activities in English after the end of the cold war [19]. The original concept for a Hall current accelerator came out of the Institute of Atomic Energy (IAE, also sometime referred to as the Kurchatov institute or KIAE) as plasma sources for fusion applications but soon spread out to other laboratories and design bureaus such as the famous OKB-1 headed by Korolev himself, the TsNIIMASH and the future design bureau (FDB) Fakel. The two main designs of TAL and SPT thrusters seemed to have been developed fairly independently. The first flight of a Hall thruster was the SPT based Eo-1 launched on the Meteor 1-10 satellite in December 1971. It demonstrated successful operation in space for more than 200 hours at a discharge power of 1 kW. After this first successful flight the development efforts expended considerably and came to include laboratories such as the Moscow Institute of Electronics and Automatics (MIREA), the Kharkiv Aviation Institute (KhAI, now in Ukraine), the Moscow State University (MSU) and the Moscow Aviation Institute (MAI). A lot of those laboratories are still active in Hall thruster and cathode development today.

This considerable work on Hall thrusters led to the use of Hall thrusters for a variety of applications. Conventional stationkeeping of geostationary communication satellite (Cosmos-1540 and Cosmos-2054 for example) was performed as well as more exotic missions in MEO and LEO. Notable examples include propulsion for the Cosmos-1818 and Cosmos-1867 reconnaissance satellites powered by TOPAZ-1 nuclear reactors. By the year 1990 the SPT-70 built by Fakel had been flown at least 50 times [20]. TAL development for moderate power applications (ie around 1 kW) lagged behind during this time and does not appear to have been operated in space before the end of the cold war.

Outside the Soviet block, while the concept was known since the early 60's [21–23], the technology was not pursued as actively even tho their potential niche of moderate Isp and high thrust to power were identified [24].

In the early 90's the Hall thruster emerged from Russia having already undergone decades of research and optimization. As soon as 1991 the American Ballistic Missile Defense Organization (BMDO) put in place a technology transfer program to evaluate the performances of the various Russian Hall thrusters and in particular the SPT-100 and the D-55 TAL [20]. This led to the first flight of a TAL HT and the first flight of a HT on an American mission with the TAL-WSF on the STEX spacecraft.

The HT technology has now spread to numerous laboratories all over the world with the main places of production being Russia, the United states, France, Japan, Italy, Israel and China. The power ranges of existing thrusters have also expanded from a few tens of watts to the hundred kilowatt range. More details on the range of existing thruster is available in section 3.1.1.

## 1.4 Motivations

### 1.4.1 Limitations of small Hall thrusters

For the past few years progress in electronic component miniaturization have driven a revolution in satellite design. A new range of capabilities are now available in small form factors with lower power requirements. This means that smaller satellites can achieve more complex missions and can benefit from lower launch cost with rideshare opportunities on big launchers. Such small satellites have been used for everything from Earth observation, telecommunication, technology demonstration and astronomical studies.

In order to benefit from the best launch price, those spacecraft are often launched as secondary payload and thus are not always delivered on the most optimal orbit. The missions have to be either designed for that non-optimal orbit or a longer waiting period is needed to find the right launch opportunity. Once in orbit if the satellite does not have an on board propulsion system it is nearly impossible to change orbital parameters easily. Some limited control can be achieved by using the residual atmospheric drag in low earth orbit but this is done at the cost of satellite lifespan.

In LEO, spacecraft lifespan is limited by this residual drag. Missions with no propulsion are limited to a few years before reentering. However for higher orbit the drag is not significant enough to ensure passive deorbitation in a reasonable timeframe. New directives are coming online on orbital debris management and want to ensure proper disposal of spacecraft at the end of their useful life. To answer those issues small satellites needs to be equipped with propulsion systems. Since those satellites are often heavily constrained by mass and volume limitations, plasma propulsion comes in as an obvious answer. Hall thruster being one of the most mature of these systems it has received a lot of interest for small satellite application.

One of the biggest challenge for Hall thrusters for smallsats is their scaling. The reduced satellite size mean that not a lot of power is available for propulsion. Depending on the spacecraft the power available can range from a few watts (cubesats) to a few hundred watts. Historically Hall thruster have been designed to operate between 500 (SPT-70) and 1500 W (SPT-100). While significant commercial efforts have been done on the high power side with 5 kW class thrusters the lower power side has not seen as much use in space so far.

However low power thrusters have been relatively popular in laboratory setting. Their lower cost of construction and operation is attractive for research purposes. An overview of low power Hall thrusters is available in appendix A. It is readily apparent that there is quite an important dispersion in the performance figures. This is caused in part by the lack of good scaling principles. This plot also highlights the decrease in performance as the discharge power is lowered. The main issue seems to stem from higher losses to the walls as the discharge channel surface to volume increase in smaller thrusters.

### 1.4.2 Lifespan of Hall thrusters and magnetic shielding concept

One of the important metric of a propulsion system, especially a high specific impulse one is that total impulse. This total impulse ( $I$ ) is defined in terms of thrust ( $T$ ) and firing time ( $\Delta T$ )

$$I = T \times \Delta t \tag{1.12}$$

With the relatively high specific impulse reached by Hall thrusters one would expect high total impulse. The low thrust inherent to the power limitations of electric propulsion means that high total impulse can only be reached if the thruster is fired for thousands of hours.

However the issue in Hall thrusters is that the fast stream of ions accelerated inside the discharge channel causes sputtering of the discharge channel walls. This erosion eventually reaches the magnetic circuit and destroy the thruster. This is the main failure mechanism in Hall thrusters today. Kilowatt and above Hall thrusters can reach 10,000 hours of operation but the issue is more pronounced in small

thrusters where the ceramic walls of the discharge channel are not as thick. For small thruster the lifespan is often limited to 3000 hours or lower [25]. This is an issue in applications where high total impulse is needed, like for deep space exploration or orbital tugs missions. The erosion also changes the shape of the discharge channel which can influence the discharge characteristics of the thruster as well as the performances.

While more sputter resistant material than boron nitride compounds exist they tend to result in lower performances in terms of thrust to power ratio and anode efficiency [26]. The solution is to make sure that no fast ions collide with the walls. The first way to achieve this is to only accelerate the ions once they have left the discharge channel. This was investigated by Kapulkin [27–30]. The concept was initially based on having an ionization stage inside the channel followed by a magnetic barrier placed outside the thruster where the ions would be accelerated. This was followed by single stage concepts where the ions are created at the exit of the thruster. This has been further investigated at ICARE with the “wall-less” concept where the discharge channel is completely removed [31–33]. Sadly performances and stability of such thruster have so far proved to be well below that of standard configurations.

In this work we focus on the other method called **magnetic shielding** to control the ions. This relies on a specific magnetic field topology that protects the walls from both the fast ions and the energetic plasma sheath at the walls. With effective shielding five fold increase in thruster lifespan can easily be achieved [34]. This topology also reduces the interactions between the walls and the plasma which could, in principle, reduce the wall losses that plague small Hall thrusters.

### 1.4.3 Content of the thesis

An overview of the facilities, diagnostics and processing methods used in this thesis is presented in chapter 2. This chapter also discusses the influence of the measurement techniques on the discharge and in particular the disturbance associated with probing the inside of the discharge channel of a thruster.

The performances of small Hall thrusters are the topic of chapter 3. Tests with different channel geometries and magnetic field strengths have been realized for a 100 W and 200 W Hall thrusters in order to assess the effect of electron confinement and surface to volume ratio.

The erosion phenomenon in Hall thrusters as well as the principle behind magnetic shielding and its application to a small low power Hall Thruster is the topic of chapter 4. Chapter 5 deals with the performance of small magnetically shielded thrusters. These performances are compared to an equivalent standard unshielded thruster of same size and construction. Lower performances are achieved in this new configuration and the reasons behind this are investigated using the experimental data gathered. Chapter 6 focuses on how those performances can be improved while still increasing the lifespan of small Hall thrusters. Simulation results obtained from a collaboration with the LAPLACE laboratory are used for this analysis.



## Chapter 2

# Plasma diagnostics and performance measurement applied to Hall thrusters

### Contents

---

<b>2.1</b>	<b>Test chambers</b>	<b>13</b>
2.1.1	NExET	13
2.1.2	PIVOINE-2g	14
<b>2.2</b>	<b>Plume probing</b>	<b>15</b>
2.2.1	Measurement setup	15
2.2.2	Data processing	16
<b>2.3</b>	<b>Thrust measurement</b>	<b>17</b>
2.3.1	Trust stand design	17
2.3.2	Issues with the low thrust stand configuration	18
2.3.3	Processing the thrust stand data	19
<b>2.4</b>	<b>Laser Induced Fluorescence</b>	<b>21</b>
2.4.1	Basic principle	21
2.4.2	Implementation	21
2.4.3	Limitations and sources of error	22
2.4.4	Data interpretation	23
<b>2.5</b>	<b>Probes versus Laser Induced fluorescence for acceleration region probing</b>	<b>23</b>
2.5.1	Limitations of probe diagnostics	23
2.5.2	Presentation of thrusters and probes used	23
2.5.3	Macroscopic effects	26
2.5.4	Local effects on the ion velocity distribution	30
<b>2.6</b>	<b>Conclusion</b>	<b>33</b>

---

## 2.1 Test chambers

### 2.1.1 NExET

NExET (New Experiments in Electric Thrusters) is the low power test bench at ICARE. The vacuum chamber is a 0.7  $\varnothing$  by 1.8 m stainless steel cylinder (see figure 2.1). The pumping stack consists of a large dry pump, a 350 l/s turbo-molecular pump and cryogenic pump cooled to approximately 30 K. The xenon pumping speed is calculated to be 8000 l/s. When operating with thrusters between 100 and 300 W a background pressure between 1 and  $5 \times 10^{-5}$  mBar is achieved.



Figure 2.1: The NExET test bench

This test bench is highly modular and can be fitted with a 35 cm radius rotating arm for divergence and plume measurements (see section 2.2.1). It can also be equipped with fast translation stages for electrostatic probing (see section 2.5.2). This is the test chamber where all the LIF spectroscopy measurements were conducted (see section 2.4). Additionally the view ports can be changed to IR transparent materials such as  $\text{CaF}_2$  or  $\text{ZnSe}$  for thermal imagery.

Multiple mounting points for windows and electrical feedthroughs allow for easy installation of equipment and diagnostics over a wide range of electrical power and optical wavelengths.

A graphite backstop is affixed to the end of the cylinder to limit ion sputtering by the thruster beam.

### 2.1.2 PIVOINE-2g

The PIVOINE-2g test facility is ICARE's high power electric propulsion test bench. The chamber is dimensioned to accept thrusters up to 20 kW in discharge power. The vacuum tank is a 2.2  $\varnothing$  by 4 m stainless steel cylinder (see figure 2.2). It is fitted with a main airlock for easy access to the thruster without breaking vacuum. The thruster itself is mounted on the thrust stand at the end of a translating arm. More details on the thrust stand are available in section 2.3.1. Two side airlocks are also present. They share a single translating arm and can be used for probing the plasma plume. Finally a motorized semi-circular rotating arm with a 70 cm radius is centered on the thruster to be able to sweep its plume. This arm can be fitted with various probes [35].

A rough vacuum is obtained through a primary pumping system. The chamber is fitted with 10 two stage cryoheads regulated at 43 K to evacuate xenon. An additional cryopump is maintained at 16 K to deal with lighter gases such as air. The cryopumps are thermally protected by baffles cooled with liquid nitrogen. The maximum pumping speed with all of the pumping systems active is 220,000 l/s of xenon.

The cryogenic system is mounted at the opposite end from the thruster and is protected from ion bombardment by graphite tiles.

Even with only 40% of the cryoheads working the pressure is excellent when operating the low power thrusters ( $\leq 300$  W). The measured xenon partial pressure is around  $5 \times 10^{-6}$  mBar. This makes background pressure effects negligible and results in lower discharge currents at similar voltage and xenon mass flow compared to the NExET chamber. This lower discharge current is explained by a less ingestion of ambient neutrals [36, 37].

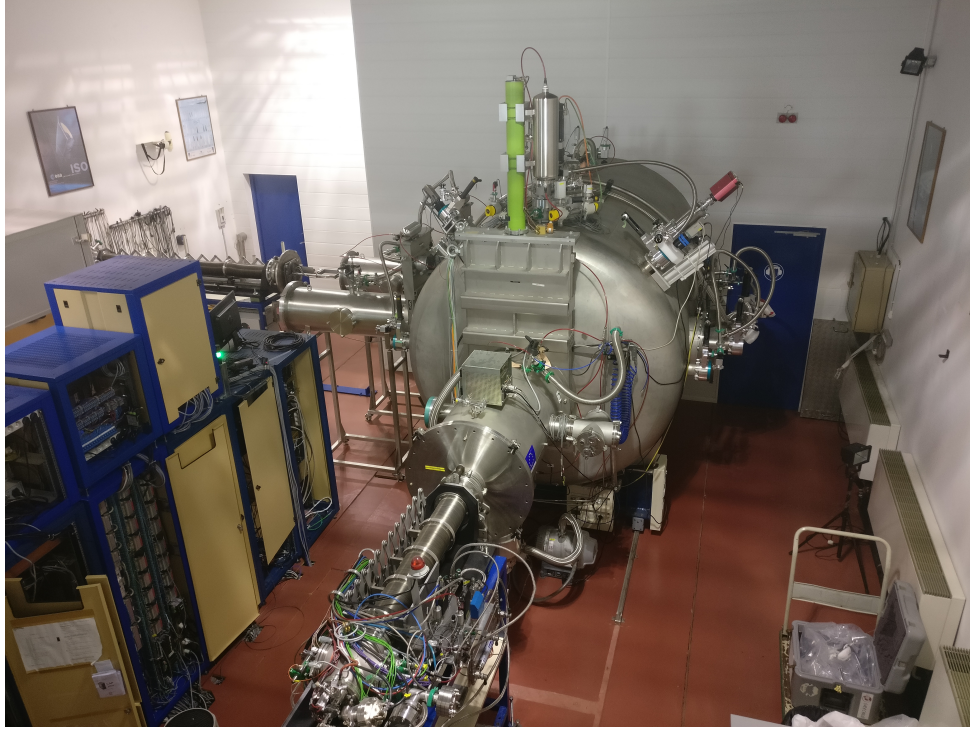


Figure 2.2: The PIVOINE-2g chamber

## 2.2 Plume probing

### 2.2.1 Measurement setup

#### NExET

Stainless steel planar probes with guard rings are used to measure the ion current in the NExET vacuum chamber. A picture of the probes is available on figure 2.3. The collector diameter is 5.6 mm and the guard ring width is 1 mm. Those dimensions were chosen to obtain a fine enough spatial resolution while maintaining a sufficient size compared to the expected sheath thickness near the center axis of the thruster. At large angles the plasma density decrease and the sheath size increase. The guard ring becomes undersized and thus the precision of the measurement decreases. The probes are mounted on a rotating arm at a distance of 34 cm from the thruster exit plane.



Figure 2.3: Planar probes with their guard ring as used in the NExET vacuum chamber

The acquisition chain consists in a Keithley 2410 sourcemeter that is used to both polarize the probe and measure the collected current. An external power supply takes care of the guard ring polarization. Guard ring and collector are kept at the same potential. The current is collected at 80 points between

-90 and +90 °. Each point consists of 10 samples. More details on the probe setup in the NExET vacuum chamber can be found in references [13] and [3].

**Pivoine-2g**



Figure 2.4: Faraday cup and its mounting system used for plume measurements in PIVOINE-2g.

Plumes measurements in the PIVOINE-2g chamber were performed with 25 mm diameter Faraday cup probe (see figure 2.4). The collimator electrode has a 15 mm hold for collection. The collection electrode is made out molybdenum.

This probe is mounted on a rotating arm 70 cm from the thruster exit plane (approximately 20 thruster diameters). The probe surface is polarized by a Keithley 2410 source meter that also measured the collected ion current. More details on the probe design and utilization can be found in reference [35].

The arm is rotating on a 180 degree arc in front of the thruster and the ion current is measured over 70 individual points. The acquisition electronics is the same as for the NExET test bench.

**2.2.2 Data processing**

The data collected is not corrected for charge exchanges or any other effects. It is carefully integrated over the whole hemisphere facing the thruster to get the total ion current. Figure 2.5 shows the coordinate system used for the integration. The 180 degree arc is defined by a constant  $\phi$  angle and a sweep from  $-\pi/2$  to  $\pi/2$  of  $\theta$ .

Since measurements are taken on only one axis we need to assume that the ion current is at least symmetric with respect to one plane containing the main axis x of the thruster. The profile can then be integrated over the hemisphere with equation (5.1).

$$I_{ion} = \int_{\phi=0}^{\pi} \int_{\theta=-\frac{\pi}{2}}^{\frac{\pi}{2}} j(\theta) \cdot (\sin \theta \cdot r) d\phi \cdot r d\theta \tag{2.1}$$

$$I_{ion} = \int_{\theta=-\frac{\pi}{2}}^{\frac{\pi}{2}} \pi \cdot r^2 \cdot \sin \theta \cdot j(\theta) d\theta \tag{2.2}$$

However the data collected is not a continuous function and the discreet integration is necessary:

$$I_{ion} = \sum_i \pi \cdot r^2 \cdot \sin \theta_i \cdot j(\theta_i) \Delta\theta \text{ for } \theta_i \in [-\pi/2, \pi/2] \tag{2.3}$$

The advantage of this method is that it only assumes axial symmetry and does not need a Gaussian functions to be fitted to the profile. The divergence angle is calculated by finding the half angle of the cone containing 90% of the total current.

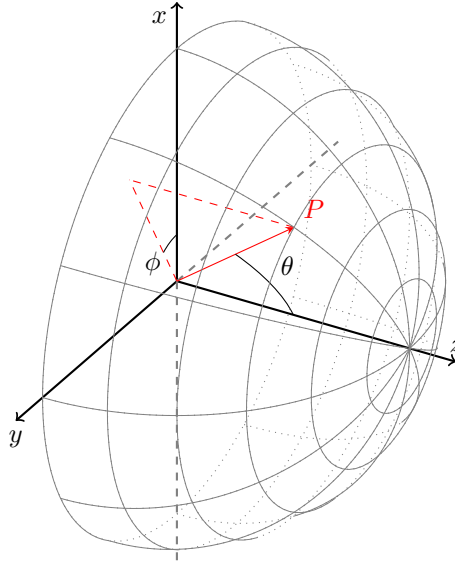


Figure 2.5: Definition of the spherical coordinate system used for integration. The Z axis represent the thrust firing axis.

We define the beam efficiency  $\eta_I$  as the ratio of collected ion current over the total discharge current. The propellant utilization  $\eta_{prop}$  is the ratio of collected ions (assuming those are simply charged) over the number of neutral atoms injected at the anode. It is computed using the equation (2.4). The mean charge of the ion  $q_{mean}$  is assumed to be  $1e$  for the results presented here. This is a strong assumption, especially on a magnetically shielded thruster. It will be discussed with the results in section 5.3.1.

$$\eta_{prop} = \frac{I_{ion} \cdot m_{Xe}}{q_{mean} \cdot \dot{m}_a} \quad (2.4)$$

## 2.3 Thrust measurement

### 2.3.1 Thrust stand design

#### Mechanical design

All of the thrust measurements presented in this thesis were carried out at the PIVOINE-2g test facility.

The PIVOINE-2g vacuum chamber is equipped with an airlock that allows quick access to the thruster without re-pressurizing the whole chamber. The thruster is mounted at the end of a hollow steel boom that translates it from the outside of the chamber into the airlock and in the main chamber. To accommodate this system the thrust stand had to be designed to fit through the airlock. The stand is a pendulum design. A basic schematics of the thrust balance is illustrated in figure . The titanium frame onto which the thruster is affixed is suspended by three braided steel wires (two at the front, one at the back). The electric connections to the thruster and the cathode are made through a flexible Kapton PCB to minimize their spring constant. The gas connections are done with 1/16th inch flexible tubing.

The tension over each of the suspension wire is equalized with a set of balance weights. No active or passive damping system is used.

A set of weights attached to the mobile part of the thrust stand by a thread are used for calibration. The weights pull on the thrust axis thanks to a pulley mounted on ball bearing. The friction caused by that pulley system is taken into account by a preload weight so that it is present in all configurations (thrust, no thrust and calibration).

The fixed part of the balance is made out of titanium which limits thermal deformation effects. Two moving structures have been tested on this setup. For a given sensor a light pendulum provides a better thrust sensitivity. Anticipating the low thrust of our 200 W thrusters a new light aluminium chassis was

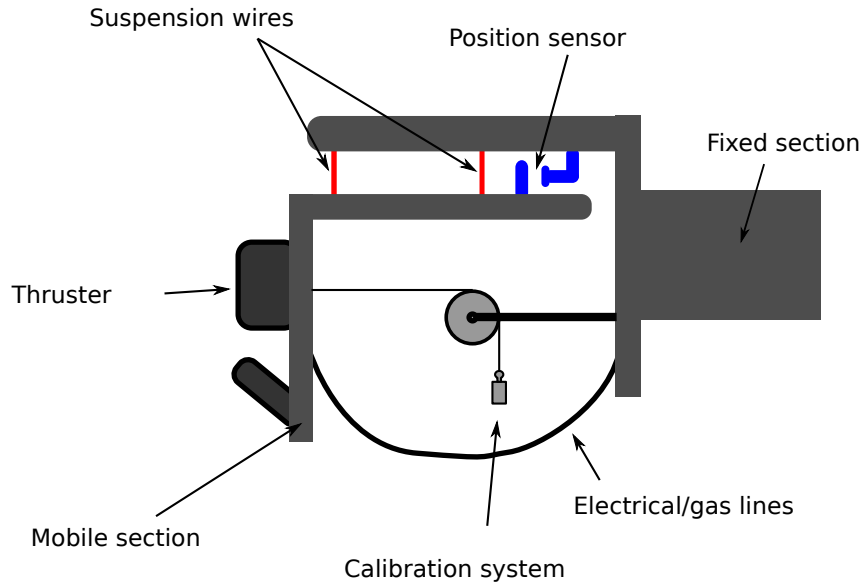


Figure 2.6: Schematics of the thrust balance used in the PIVOINE-2g test chamber.

built to replace the older heavier titanium one. The new mobile structure weighted only 3.6 kg which put the total suspended mass at around 6 kg.

### Measurement setup

To measure the displacement a capacitive sensor is used. It is placed on a translation stage on the fixed part of the stand and measures the displacement of plate on top of the mobile part. The sensor only has a measurement range of  $500 \mu\text{m}$ , the translation stage allows to position the sensor in the middle of its range during measurements to have the best sensitivity possible.

The sensor and acquisition chain has a sensitivity around  $\pm 0.15 \mu\text{m}$ . The sensor position is recorded every second.

The procedure used for measuring the thrust is as follow:

- The thruster is switched on and allowed to stabilize. The position of the balance with the thruster ON is recorded.
- The thruster is switched off and after the few minutes the position of the balance at rest is recorded.
- One of the two reference masses is suspended, which gives us one reference point for a known thrust force. This position is recorded.
- The second of the two masses is also released. The position with the combined weight of the two mass is also recorded.

### 2.3.2 Issues with the low thrust stand configuration

The lighter aluminium structure was tested first in order to get the best possible sensitivity for our low power thrusters. With a 6 kg suspended mass and 84 mm long suspension wire the displacement was expected to be around  $1.4 \mu\text{m}$  per millinewtons. The would have resulted in 3.5 time increase in sensitivity.

However once the translating arm was extended the thrust balance was found to be widely oscillating (see figure 2.7).

Recording those oscillations at a higher sampling frequency reveals that they correspond to the natural resonant frequency of a simple pendulum with a length corresponding to the one of the suspension wires. This frequency is measured at 1.74 Hz for a theoretical calculated of 1.72 Hz confirming that the this triple wire suspension system acts like a simple pendulum. This frequency is probably excited by the cryo-pumps cycling at 1.9 Hz which is why they do not get dampened over time.

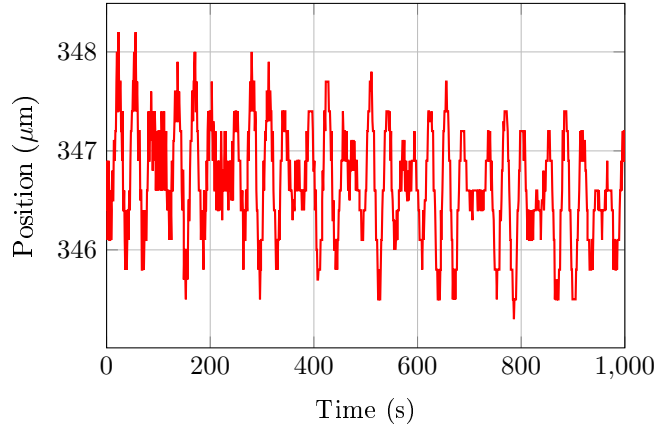


Figure 2.7: Oscillations of the light thrust stand as seen by PIVOINE’s acquisition chain

To counteract those kind of oscillations most low thrust measurement systems have some sort of dampening system, usually electromagnetic based. Calculations show that a few square centimeter of strong permanent magnets (neodymium) a few millimeters over a copper plate should be enough to dampen the oscillations. However this setup could not be implemented in time for the test campaign.

After that setback we took the decision to use the heavier titanium thrust stand for all measurements.

### 2.3.3 Processing the thrust stand data

#### Computing the thrust

The automatic processing system built into PIVOINE’s controller only uses one single sample point for the 4 recorded conditions described in section 2.3.1. This makes the computed thrust value very noise sensitive and does not account for thermal drift very well. This is not an issue for thrusters in the 50 mN range or above but it induces significant errors for the 5 to 15 mN we are measuring.

Looking at the raw sensor data displayed in figure 2.8 a few things are readily apparent. First the noise is significant compared to the amplitude of the signal we are trying to measure. The noise is also aliased which shows that we are partly limited by the resolution of the 8 bits ADC system. Secondly there is a slow but steady drift in the order of 0.1  $\mu\text{m}/\text{min}$  likely due to the thermal load on the thrust stand.

To minimize uncertainties and error bars in order to obtain a precise value of the thrust the following processing pipeline is setup. First the thermal drift is removed by fitting a linear function to the measurements with the thruster on and subtracting it to the whole interval of interest. Once detrended the transfer function of the balance is computed by performing a linear regression over the three calibration points. Those calibration points are the average of the signal for each case. From there the thrust is obtained and is used to compute the specific impulse and the anode efficiency. The transfer function is checked for consistency across all the acquisitions to make sure that no unexpected disturbance was recorded. The dispersion in the measured positions is included into the uncertainty computations.

#### Anode efficiency and specific impulse

Alongside the thrust stand position all the other parameters of the thruster are measured and recorded every second. This includes discharge voltage ( $V_d$ ) and current ( $I_d$ ) as well as anode mass flow ( $\dot{m}_a$ ).

From those figure the anode discharge power ( $P_a$ ), anode efficiency ( $\eta_a$ ) and Isp are computed with the thrust ( $T$ ) obtained earlier.

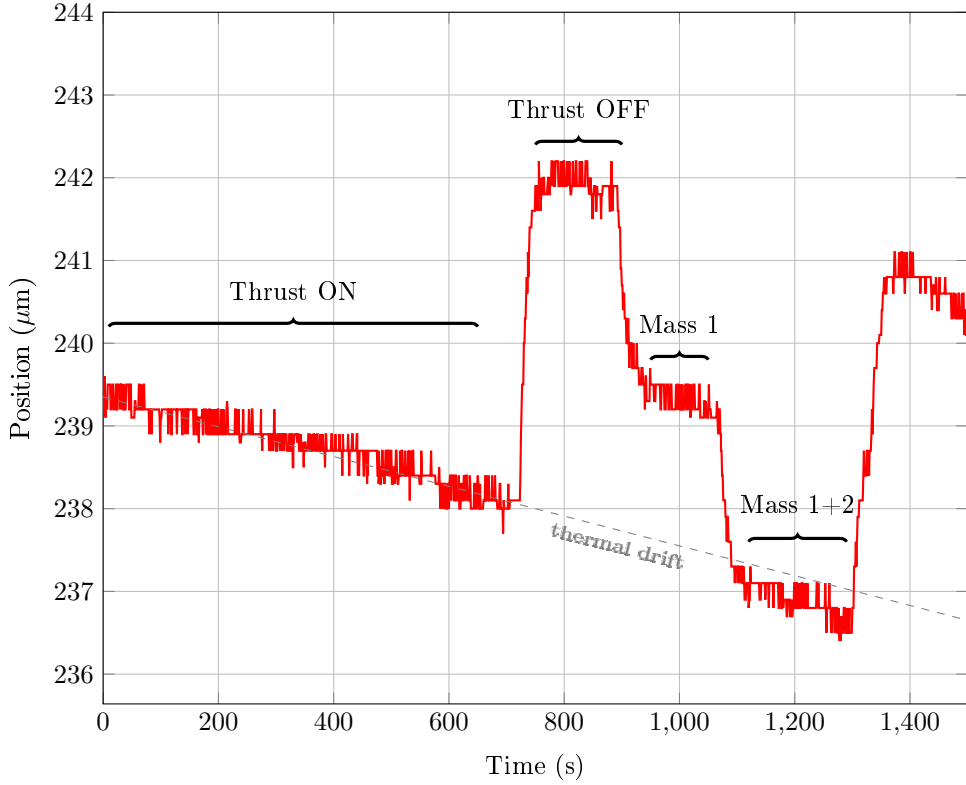


Figure 2.8: Example of the raw data obtained during a thrust measurement with a 200 W thruster

$$P_a = I_d \times V_d \tag{2.5}$$

$$\eta_a = \frac{T^2}{2 \cdot \dot{m}_a P_a} \tag{2.6}$$

$$Isp = \frac{T}{g \cdot \dot{m}_a} \tag{2.7}$$

**Uncertainty estimations**

The initial data is fairly noisy and limited in resolution. A careful error propagation analysis is performed. The uncertainty due to oscillations of the thrust stand is fairly small as each reference position is recorded for at least 30 seconds. The main limit of the precision of the setup is the absolute resolution of the sensor chain ( $\pm 0.15 \mu m$ ) which gives a one standard deviation error bar of around  $0.08 \mu m$  for each of the 4 positions of interest. As a result the uncertainty for the transfer balance coefficient is around 3%.

The uncertainty calculation are performed for each pair of measurements and calibration. For the case presented in figure 2.8 (ISCT200-US with BN-SiO<sub>2</sub> at 200 V, 1 mg/s) we get a thrust of  $10.13 \pm 0.42$  mN (k=1).

Even tho they are in the order of 0.1%, the uncertainties on the voltage and current measurement are also taken into account for efficiency and specific impulse calculation. The uncertainty on the mass flow rate is even smaller and is neglected.

For the example presented here, it results in an anode efficiency of  $31 \pm 3 \%$  (k=1) and an Isp of  $1030 \pm 42$  s (k=1). Most of the uncertainties come from the resolution of the thrust stand.

## 2.4 Laser Induced Fluorescence

### 2.4.1 Basic principle

Laser induced fluorescence (LIF) spectroscopy is an optical diagnostic providing access to the neutral and ion velocity distribution functions (NVDF and IVDF respectively). The technique itself as well as the setup used at ICARE is presented in more details in reference [38, 39]. A brief overview is presented here as well as some important details, limitations and side effects relevant to this study.

A narrow-bandwidth tunable diode laser is used to excite the  $5d^4F_{7/2} \rightarrow 6p^2D_{5/2}^0$  transition at 835.95 nm (in vacuum) of metastable  $Xe^+$  ions. The fluorescence light is collected through a fiber and sent to a photomultiplier via a monochromator to isolate the 541.9 nm fluorescence line. The laser wavelength and fluorescence signal intensity allow us to obtain the velocity by computing the Doppler shift as well as the relative ion density.

We chose to probe the neutral population starting from the  $6s[1/2]_2^0(1s5)$  resonant state, exciting in the near infrared at 834.91 nm and observing the fluorescence at 473.4 nm. The 823.16 nm transition from a metastable state can also be used. However since the excited state emits back at 823.16 nm it can be hard to distinguish between LIF photons, spontaneous emissions, and reflected or stray light when probing close to a surface.

### 2.4.2 Implementation

The optical setup for the air side is shown on figure 2.9. A single mode tunable laser diode with an external amplifier is used to create the near infrared laser beam. A fraction of the main beam is split off to a Fabry-Pero interferometer to check for mode hops. The wavelength is measured by a HighFinesse wave-meter with a worst case absolute precision of 70 mHz (corresponding to 60 m/s). Power output of the laser is monitored by a photo-diode or a power meter. The main beam is modulated by a mechanical chopper and then injected into a 5  $\mu\text{m}$  core diameter single-mode optical fiber. This fiber is used to feed the laser inside the vacuum chamber. Figure 2.10 illustrates the vacuum side of the setup.

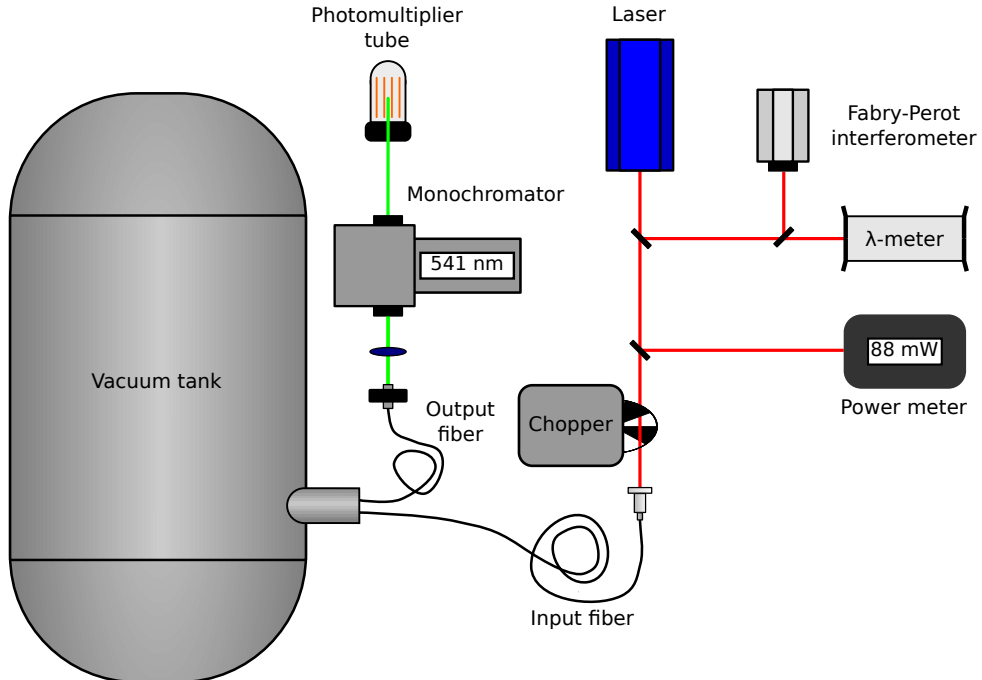


Figure 2.9: Layout of the LIF spectroscopy system.

The fluorescence signal is collected by a bi-convex, uncoated, fused silica lens that focuses it into a 200  $\mu\text{m}$  diameter multi-mode optical fiber. Two different lenses were used in this research, for the measurements at the walls and at the center of the discharge channel we used a lens 25 mm diameter

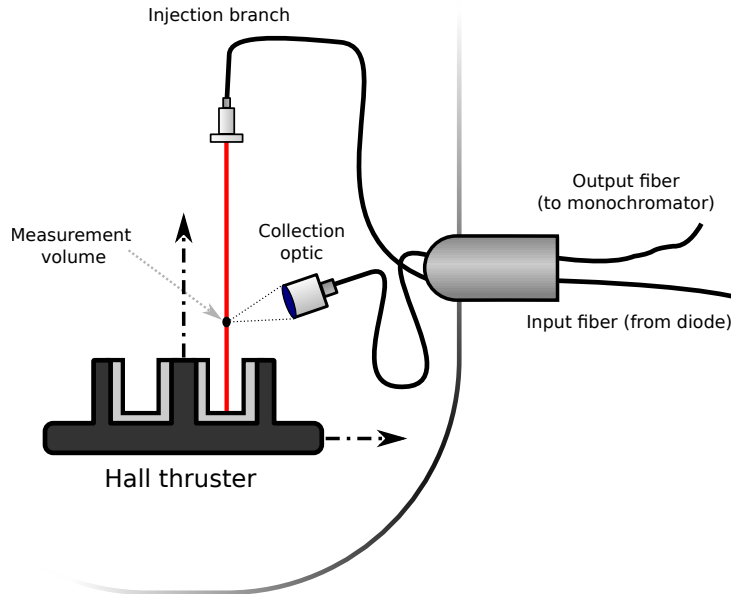


Figure 2.10: Layout of the LIF spectroscopy system inside the vacuum tank with the thruster mounted on a 2 axis translation stage.

with a 40 mm focal. Near the magnetic poles, since the fluorescence signal was a lot fainter a 50.8 mm diameter and 38.1 mm focal length lens was used.

The collected signal is then fed into a 40 cm Czerny-Torner monochromator tuned to the fluorescence wavelength and finally a photo-multiplier. The background noise from spontaneous fluorescence is removed with a lock-in amplifier extracting the signal modulated at the chopper frequency.

This measurement technique is considered non-disturbing to the thruster discharge as the power density of the laser ( $\sim 15 \text{ mW/mm}^2$ ) is at least an order of magnitude lower than the power density of the plasma. At this power density, optical transitions of interest are weakly saturated with no apparent impact on the velocity distribution functions measured. No macroscopic effects are seen on the thruster in term of mean discharge current or discharge stability.

### 2.4.3 Limitations and sources of error

The position of the points probed during this study can induce sources of error usually neglected when doing simple axial LIF spectroscopy along the center of the discharge channel.

The laser is fired toward the thruster and eventually bounce on either the discharge channel or the magnetic pole surface. Those surfaces have not undergone any special treatment. When measuring velocities normal to the thruster surfaces, the measurement volume is directly in the path of possible laser reflection. The impact surface, consisting of clean or dirty ceramic or roughed up metal were not prepared in any special way to prevent reflections. Specular reflection on those surfaces would produce a “ghost” mirror image of the VDF centered on  $v=0 \text{ m/s}$  line. The exact effects of diffuse reflection are less obvious. It should however manifest itself as general broadening of the obtained VDF with a less defined symmetry centered on the 0 velocity axis.

Some of the areas of interest when probing MS-HT (magnetic poles and channel walls) are regions of high magnetic fields intensity where the Zeeman effect can become significant. Moreover the orientation of the magnetic field lines can be very different in the probed area between the field lines and the laser axis. Exact estimation of this effect is complex due to the numerous isotopes of Xenon and the uncertainties in the exact magnetic field topology. During his IVDF measurements over the magnetic pole of the shielded H6 thruster, Jorns estimated that Zeeman effect would result in a 15% overestimation of the ion temperature [40]. Since this thesis presents a mostly qualitative, rather than quantitative, analysis of the IVDFs, we have not attempted to correct for the Zeeman effect.

### 2.4.4 Data interpretation

#### Computing the electric field from IVDF

From the IVDFs at different positions it is possible to compute the electric field experienced by those ions. Different techniques exist which offer different levels of accuracy [41]. We chose to compute the potential drop ( $V$ ) experienced by the ions by looking at their kinetic energy corresponding to their most probable velocity ( $v_{mp}$ ) as explained in equation 2.8.

$$V = \frac{m_{Xe} \cdot v_{mp}^2}{2e}, \quad (2.8)$$

with  $e$  being the ion charge in Coulombs and  $m_{Xe}$  the xenon ion mass.

The electric field was then computed by taking the derivative of this potential with respect to the position. This is done using a second order centered difference scheme. Since only the most probable velocity (ie the position of the maximum of the IVDF) is required, this method is fast and is less sensitive to noisy data.

## 2.5 Probes versus Laser Induced fluorescence for acceleration region probing<sup>1</sup>

### 2.5.1 Limitations of probe diagnostics

Some of the prime areas of interest in a Hall thruster are the ionization and acceleration regions. The exact plasma conditions in these regions are relatively unknown and as such are complicated to simulate. They are the regions where most of the anomalous conductivity occur and where most of the energetic processes are taking place.

The classical way to measure plasma parameters is to use electrostatic probes. Retarding potential analyzers (RPA), Langmuir probes (simple, double or triple) and emissive probes have all been used with success in the plume of all thrusters to measure ion and electron density, electron temperature and ion velocity distribution functions (IVDF) [42–46]. Comparisons between probing methods can easily be found in the literature [47, 48]. Probing of the plume does not appear to significantly disturb the plasma discharge. However measurements inside the thruster are less straightforward [49–53]. High particle flux and density warrant special precautions. Ablation of the ceramic insulators being one of the main identified perturbation causes, several investigators have chosen to use small probes with low residence time inside the thruster [51]. Nevertheless, even with those techniques, it is currently unreasonable to consider probe-induced disturbances in the channel of Hall thruster as negligible. The following section highlights the differences between plasma potential measured by emissive probes (EP), Langmuir probes (LP) and laser induced fluorescence (LIF) spectroscopy. EP and LP effect on the macroscopic thruster parameters as well as the local perturbations are measured by the non-intrusive (and thus non-disturbing) LIF.

### 2.5.2 Presentation of thrusters and probes used

#### Thrusters

In this study two different thrusters have been used.

The ISCT200-GEO is a 200 W laboratory Hall thruster that has been extensively studied at ICARE [54]. It delivers around 10 mN of thrust at a 250 V operating voltage and an anode mass flow rate of 1 mg/s of Xenon. The thruster can be fitted with a set of interchangeable ceramic channel walls allowing to change both materials and channel width. This study is done at fixed width but with both  $\text{Al}_2\text{O}_3$  and  $\text{BN-SiO}_2$  walls. The geometry chosen is our so called  $2S_0$  configuration corresponding to twice the usual channel width to diameter ratio. This thruster was fired inside the NExET vacuum chamber (see 2.1.1). More information about this  $2S_0$  configuration can be found in chapter 3 section 3.2.1.

---

<sup>1</sup>Adapted from:

Lou Grimaud, Aude Pétin, Julien Vaudolon, and Stéphane Mazouffre. Perturbations induced by electrostatic probe in the discharge of Hall thrusters. *Review of Scientific Instruments*, 87(4):043506,

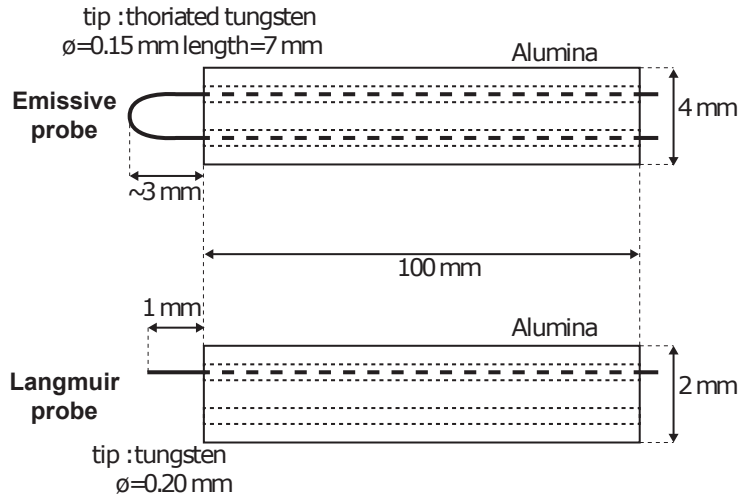


Figure 2.11: Electrostatic probe geometry

The SPT-100-ML [55] is a 1.5 kW thruster derived from the Russian SPT100 [56]. This medium size thruster can produce about 80mN of thrust at an operating voltage of 300 V and an anode mass flow rate of 5 mg/s of Xenon. On this thruster the discharge channel is made out of BN-SiO<sub>2</sub>. Moreover a slot has been machined in the external wall and a hole was drilled at the back of the channel to allow optical probing of the inside of the thruster [57]. The SPT-100-ML was mounted in the much larger PIVOINE-2g test facility (see 2.1.2)

Both those thrusters are operated with a heated LaB<sub>6</sub> MIREA hollow cathode. The cathode mass flow rate was 0.2 mg/s of Xenon for the ISCT200-GEO and 0.4 mg/s for the SPT-100-ML.

### Probe designs

The emissive probes used are made in house and consists in a loop of thoriated tungsten wire crimped at both ends into fine copper tubes [58, 59]. These copper tubes are insulated from the plasma by an alumina tube. The size of each element can be seen in figure 2.11. The heating current going through the filament is controlled by a E3633A Agilent power supply. To keep the probe potential floating with respect to the ground the power supply is isolated with an isolator-transformer [59]. The probe voltage is recorded by an oscilloscope. Since emissive probes work by canceling the plasma sheath by thermionic emission, the temperature of the tip, and thus the heating current is a crucial parameter. When a sufficient flux of electrons is emitted, the sheath surrounding the thoriated tungsten wire is neutralized and the probe potential approaches the plasma potential [60–64]. Figure 2.12 shows the effect of the heating current on the measured potential inside the ISCT200-GEO operated at 200 V and 0.86 A discharge parameters for an anode mass flow rate of 1 mg/s. This figure highlights the fact that the appropriate heating current depends on the plasma characteristics. A rather sharp behavior change is visible around 4 A in the regions of higher electron temperature inside the discharge channel. At 4 amperes and above the probe floating potential is close to the plasma potential.

In accordance to this results a heating current of 4.4 A was used throughout this work.

Langmuir probes are also made by our team using the same alumina tubes as for the emissive probes. The collecting surface consists of a 1 mm long and 0.2 mm diameter tungsten wire. The size was chosen to keep a reasonable probe length compared to the gradient expected as a sturdy enough filament. The voltage sweep and current acquisition are done with an ALP Impedans control system. To extend the +/-150 V sweep range of the ALP system an additional DC power supply can be added in series between the probe and the acquisition system. This power supply is isolated via transformer and allows us to add up to 150 V of offset to the prob tip. Plasma potential was calculated from the current voltage (I-V) curve by finding the maximum of its first derivative. Light filtering was done on this first derivative to isolate the maximum more easily.

Both probe being of similar size, they have been mounted on the same fast translation stage [43, 58]. This piezoelectric stage has a maximum acceleration of 2000 m/s<sup>2</sup> and a maximum speed of 350 mm/s over

## 2.5. PROBES VERSUS LASER INDUCED FLUORESCENCE FOR ACCELERATION REGION PROBING

---

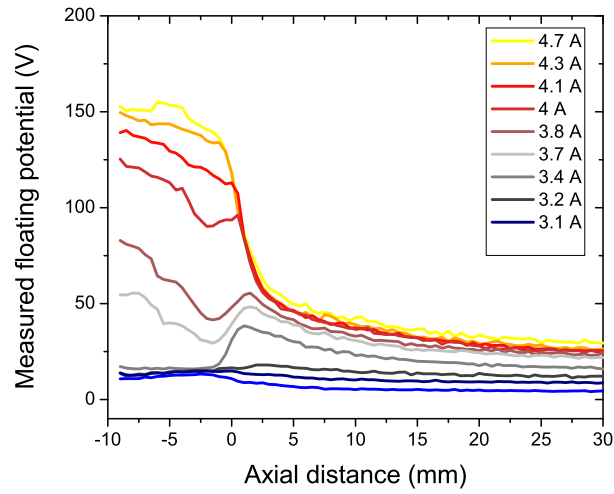


Figure 2.12: Probe potential measured along the ISCT200-GEO channel axis with emissive probes. The influence of the heating current on the measured profiles is shown. (The position X=0 mm refers to the channel exit plane.)

a 90 mm course. As seen on figure 2.13, we used it to move the probes in and out of the discharge channel, parallel to the main axis of the thruster. The low power thruster was also mounted on a perpendicular translation stage for fine position adjustments. All the data presented in this section has been acquired along the centerline of the channel.

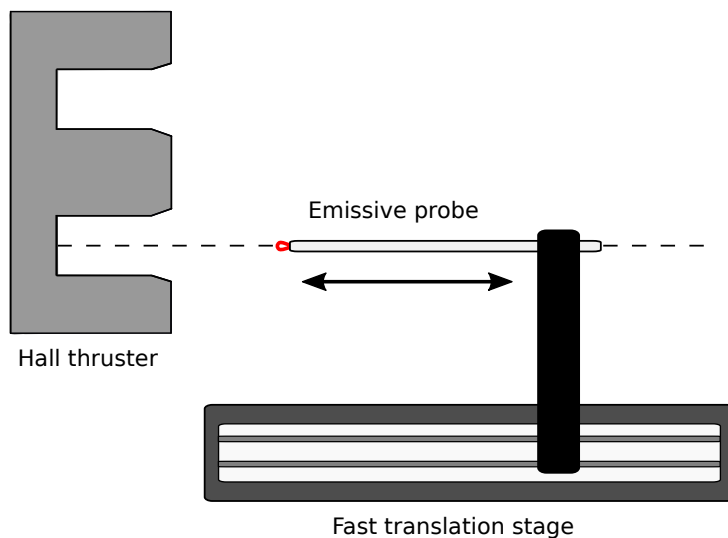


Figure 2.13: Representation of the Hall thruster and probe mounted on the fast translation stage.

### 2.5.3 Macroscopic effects

#### ISCT200-GEO - Low-power discharge

Measurements of the plasma potential with the three types of diagnostics have been performed on the ISCT200-GEO. Results with both alumina and BN-SiO<sub>2</sub> wall are presented in figures 2.14. No consistent measurement bias between optical and probe techniques is observed. Amplitude-wise the maximum of the electric field measured by LIF is either in the middle or below the probe results. Comparison between the position of the maximum is complicated since the LIF results in the Al<sub>2</sub>O<sub>3</sub> case are very different from the ones given by the probe. This could be an indication of a change of the discharge mode. However both LIF and probes detect the “double peaks” structure seen in this case. This double peak structure has already been observed by Vaudolon [65] and is currently unexplained.

Looking only at the probe results, we see in both cases that the emissive probes measure a higher maximum for the electric field that is located further upstream. The difference is mostly seen inside the channel. The shift in position for the electric field is explained by the shift in position of the plasma potential measured by the emissive probe. A proposed explanation is that the emissive probe underestimates the plasma potential due to the fact that the emitted electron are colder than the plasma electron. The plasma potential being directly proportional to the electron temperature, a systematic error is expected inside the channel, where the electron temperature is high. The probe is also subjected to plasma heating that will increase the filament electron emissivity, effectively increasing the measured floating potential as if the heating current was increased.

Additionally the shear size of the tungsten loop make measurement in the high potential gradient region imprecise. The design of the electrical circuit should provide us with the potential value of the middle of the loop. However inside the thruster the plasma potential can change by as much as 100 V in less than 5 mm. Comparing this to the size of the probe (3 mm) explains the smoother curve obtained with the emissive probe. Moreover, as Haas [66] observed, the length of conducting tungsten placed in these low electron mobility region appears to short-circuit the discharge.

The floating potential was also measured with both probes. Since in this case the emissive probe is left cold and effectively act as Langmuir probes, both should give the same result. However the results in figure 2.15 show completely different profiles once the probes are in the thruster. The main difference between the probes being the shape of the conducting tip, we assume that the discrepancy in the profiles is due to the length of the tungsten loop of the emissive probe (3 mm versus the 1 mm for the Langmuir probe). Moreover the alumina tube for the emissive probe has a diameter of 4 mm (vs 2 mm for the Langmuir probe) which is a significant increase in size compared to the channel width of 10 mm of the ISCT200-GEO. Once again this highlights the size issue emissive probes have in high gradient environments such as the interior of a Hall thruster.

Our emissive probe measurements with respect to the position along the channel axis are carried

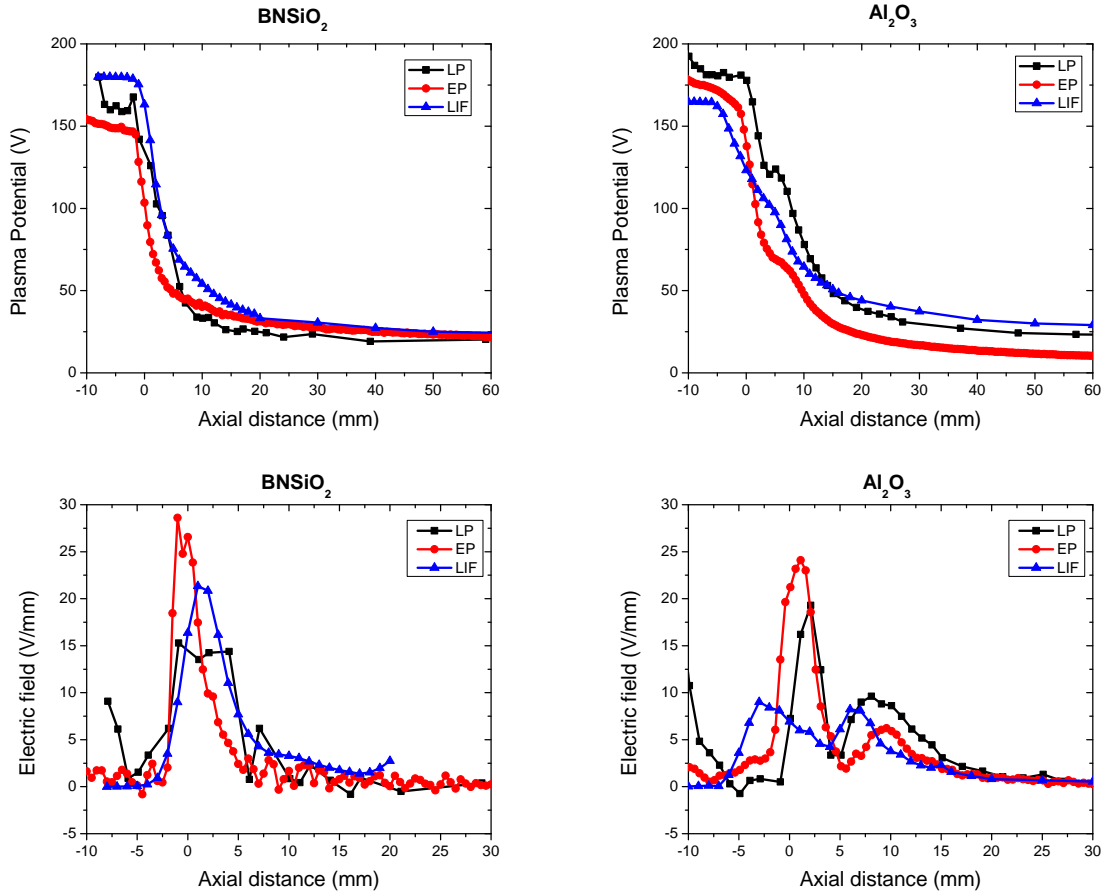


Figure 2.14: Plasma potential and electric field along the channel axis of the ISCT200-GEO as measured by emissive probe (EP), Langmuir probe (LP) and LIF spectroscopy. The discharge was set at 200 V for 1 mg/s of xenon.

out during a back and forth “sweeping” motion of the translation stage. Figure 2.16 records the current during such a sweep. It is immediately apparent that the dynamics of the discharge current is very heavily influenced by the position of the probe. More precisely, the probe has no effect on the discharge while its tip is at more than 5 mm (half the channel width) from the exit plane of the thruster. Once it passes this threshold the dynamics of the current are dramatically altered. While far from the thruster the current exhibits large asymmetric oscillations between +1.2 and -0.8 A of the mean value, the discharge suddenly changes to a more stable behavior with oscillations only 0.2 A in amplitude. This is also the position where the mean value of the current start to increase. 5 mm upstream of the exit plane another more violent oscillating regime appears. These oscillations mean value and amplitude are higher than in the undisturbed case. These transition regions appear about half a channel width upstream and downstream of the exit plane.

Figure 2.17 highlights the changes in discharge current dynamics as the probe is inserted. The figure is a spectrogram of the discharge current done by performing a fast Fourier transform over a short sliding window of sample points. Once again we find the same 3 discharge modes for  $x > 5$  mm,  $5 \text{ mm} > x > -5$  mm and  $x < -5$  mm. The principal mode of oscillations seen around 12 kHz in the undisturbed case completely disappear in the exit plane area before reappearing at a slightly lower frequency once the probe is inside the thruster. Note that the discharge current reacts very fast to the probe insertion. The probe goes through the “exit plane area” (5 mm to -5 mm) in only 50 ms but there is still a distinct discharge current behavior associated with this area. This is not surprising as the various characteristic frequencies of the plasma are well above the 100 kHz.

This is slightly different from the behavior noticed with fast emissive probes by Staack [67] and Langmuir probes by Jorns [68]. In these studies the perturbations only appeared once the probe was

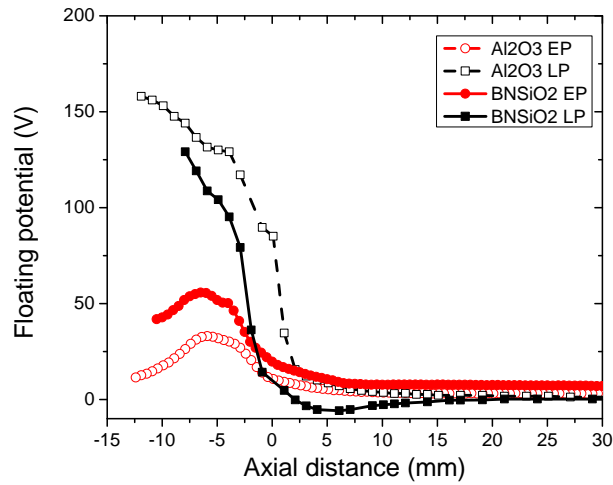


Figure 2.15: Floating potential along the channel axis in the ISCT200-GEO as measured by Langmuir probe (LP) and cold emissive probe (EP). The discharge was set at 200 V for 1 mg/s of xenon.

inside the thruster. Moreover, in Jorns' case the average discharge current decreased as the probe was inserted. However the behavior change seen at -5 mm is around the same position (relative to the thruster channel size) as what Jorns observed. The difference in magnetic field topology (and thus electric field position) between the thrusters could explain the difference in behavior. Jorns also used a significantly larger thruster.

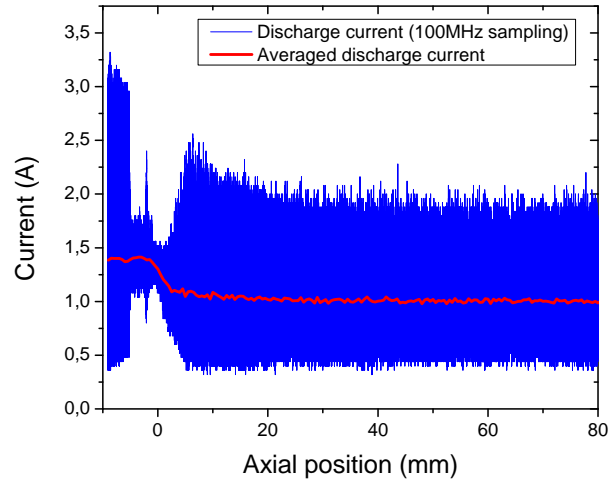


Figure 2.16: Discharge current as a function of the Emissive probe position in the ISCT200-GEO. The red line represents a moving average for readability. The current was acquired as the heated probe is translating at 250 mm/s toward the truster.

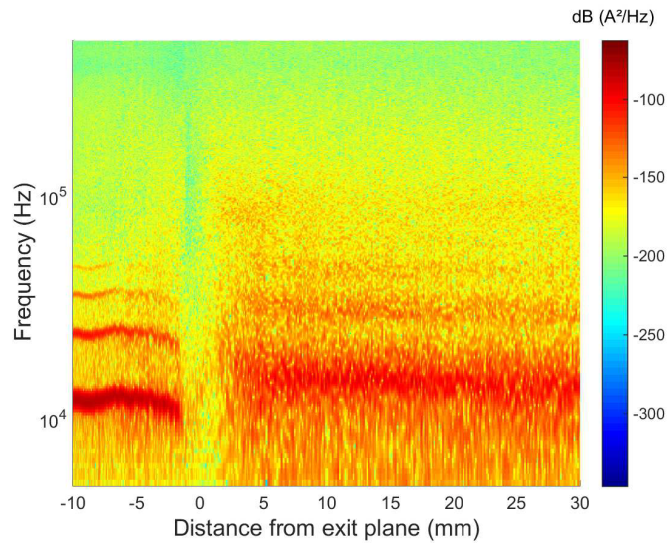


Figure 2.17: Spectrogram of the discharge current as a function of the position of the probe in the ISCT200-GEO. The current was acquired as the heated emissive probe is translating at 250 mm/s toward the truster.

**SPT-100-ML - High-power discharge**

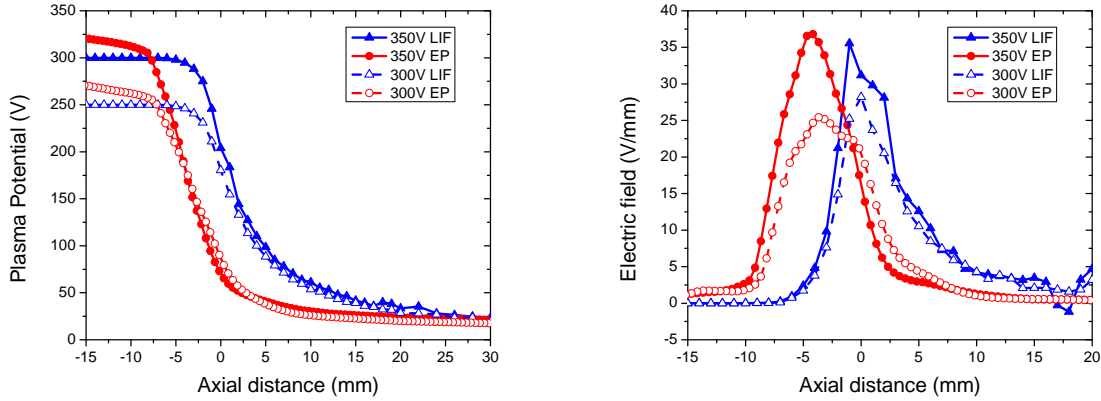


Figure 2.18: Plasma potential and electric field along the channel axis in the SPT-100-ML as measured by emissive probe (EP) and LIF spectroscopy. The discharge was set at 3 mg/s of Xenon.

Emissive probe and LIF spectroscopy measurements in the channel of the SPT100-ML are shown in figure 2.18. The electric field found with the probe is shifted roughly 5 mm upstream of the one found by LIF. This behavior has already been observed by Hargus [49]. A possible explanation raised to explain this results at the time was that the ion velocity was used in the LIF potential calculation. This choice gives less weight to the low velocity ion population and can thus be subject to errors in the ionization region. However our electric field, computed with the most probable ion velocity, shows a similar behavior. The choice of the most probable ion velocity is motivated by the results presented by Vaudolon [65] which point to this method giving the closest results to a true Boltzmann equation derivation.

This is further evidence that the difference between LIF and probe measurements are physical in nature, and not an artifact of the processing method.

**2.5.4 Local effects on the ion velocity distribution**

**Emissive probe**

In order to see the local effect of the probe on the discharge we have also measured the full IVDFs by LIF at -5, 0 and 5 mm relative to the exit plane, with and without probes. Due to mechanical constraints the LIF measurement point was positioned about 2 mm millimeter below and 1 mm upstream of the probe tip, but still at the center of the discharge channel. All the distances used in this experiment are relative to the probe tip (or where it would be when the probe was not used). Figure 2.19 presents the results we obtained. LIF acquisitions are relatively slow as the system needs a couple of minutes to cover the whole range of ion velocities. The longer residence time inside the thruster leads to heating of the alumina tube that can induce more side effects due to ablation of the tip of the probe as well as a change in the alumina dielectric properties. To account for this effects, acquisitions were also done with a non-heated intact emissive probe, a probe with a broken filament, as well as a simple alumina tube without any filament (fig 2.19 and 2.20). The probe with a broken filament was used to see if the residues left by a “burnt up” filament on the alumina tube had any effects.

The main perturbing effects are apparent when the probe is at the exit plane and is heated. The principal velocity group of ion is shifted to higher energy. Perturbations associated with the presence of a cold probe or a single alumina tube are also observed but are significantly weaker in comparison. The tungsten filament doesn’t have an discernible effect by itself.

At 5 mm downstream of the exit plane no significant perturbations are seen. This position correspond to where the transition on the current behavior happens in the ISCT200-GEO. Furthermore the electric field at this point has already tapered off (see fig 2.14).

At -5 mm the alumina tube gets “white hot” after about a minute inside the plasma. We also observe an increase of the discharge current as the probe gets hotter. To preserve the thruster and the probe, LIF

2.5. PROBES VERSUS LASER INDUCED FLUORESCENCE FOR ACCELERATION REGION PROBING

---

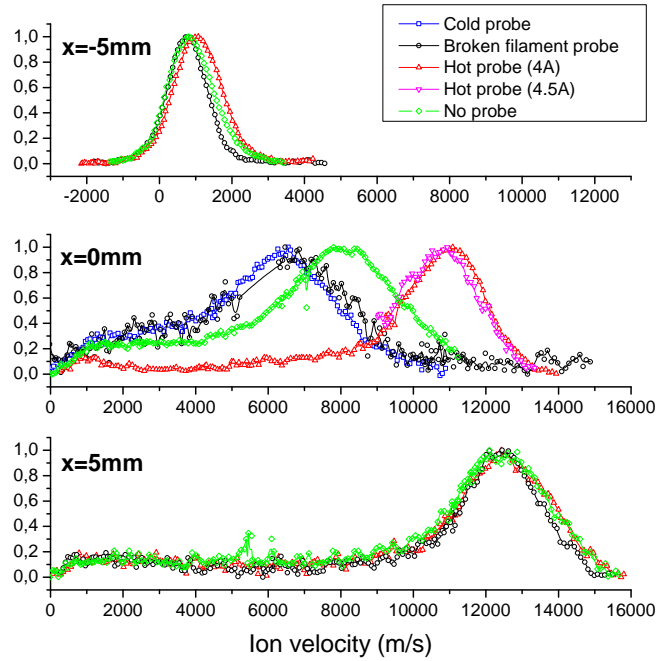


Figure 2.19: IVDFs in the vicinity of the emissive probes inside (-5 mm), at the exit plane (0 mm) and outside (+5 mm) of the ISCT200-GEO.

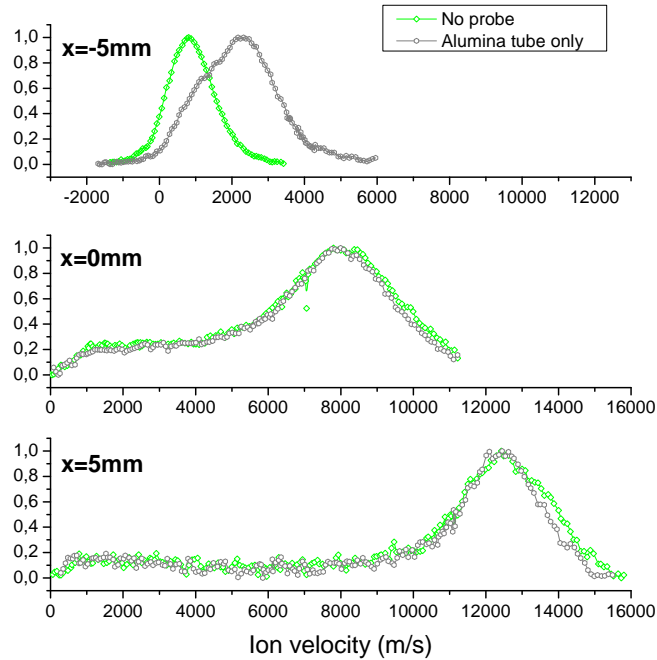


Figure 2.20: IVDFs in the vicinity of the simple alumina tube inside (-5 mm), at the exit plane (0 mm) and outside (+5 mm) of the ISCT200-GEO.

data acquisition was done during the transient regime. Due to this time sensitive effect, the replicability of the IVDF at this position was poor. However our data suggest that plasma heating of the alumina has a bigger effect than the probe heating. This is further supported in section 2.5.4 when similar results are obtained using non-heated Langmuir probes.

The increase in both mean and most probable ion velocity is a good indication that the acceleration region, and thus the electric field, are displaced toward the anode by the probe.

### Langmuir Probe

Similar LIF spectroscopy acquisitions have been performed with Langmuir probes. Since the main difference between them and emissive probes is the fact that they are polarized, we particularly looked at the influence of negative (ion collecting) and positive (electron collecting) polarizations relative to the plasma potential. We also did some sweeping probe measurements to simulate the situation when multiple I-V curves are recorded for averaging purposes.

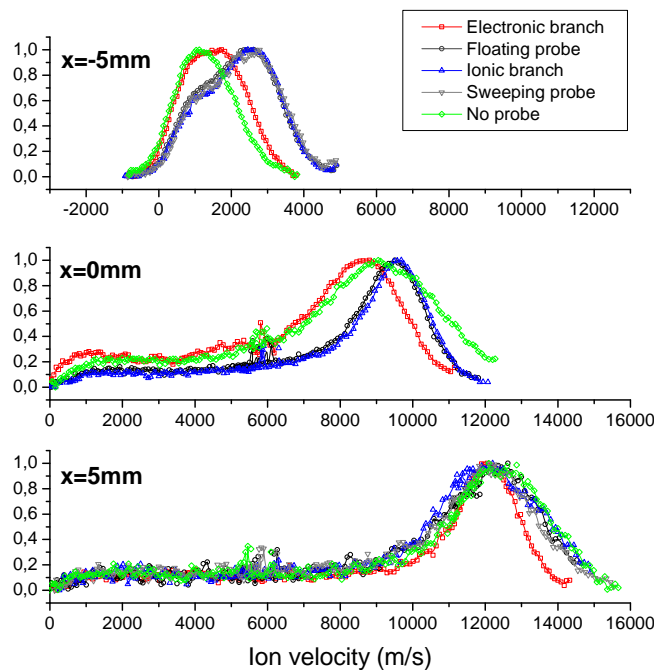


Figure 2.21: IVDFs in the vicinity of the Langmuir probes inside (-5 mm), at the exit plane (0 mm) and outside (+5 mm) of the ISCT200-GEO.

As seen in figure 2.21 at -5 mm relative to the exit plane the behavior is comparable to the one of the emissive probe. However when the probe tip is polarized positively the most probable ion velocity is lower than in the other cases when the probe is present.

At the exit plane we have a similar situation with three different types of IVDF. The one with a floating probe and a negatively polarized probe are once again shifted toward higher velocities compared to the undisturbed case. The positively polarized one has a most probable velocity close to the control case but the mean velocity is lower as there is less high energy ions.

At 5 mm downstream the positively polarized probe shows a similar phenomenon while the floating and negatively polarized probes do not seem to induce any perturbations.

Probes with sweeping potential induce the same perturbations as negatively or floating probes for all positions.

## 2.6 Conclusion

While inserting electrostatic probes in HT has been known to cause perturbations, we have presented here a direct comparison of the electric field measured with emissive probe, Langmuir probe and non-intrusive LIF spectroscopy. A significant difference, mainly in position, is observed in both a small and medium sized HT.

By considering both discharge current and IVDF measurements at different probe position we can identify two important factors in the perturbations. First the probes only start to have effect on the discharge when they get close to the exit plane of the thruster. This is seen both on the discharge current, with a threshold around 5 mm downstream of the exit plane, and on the IVDF where the probe effect start to show up between 0 and +5 mm. This effect is present even when fast probing methods are used. The discharge reaction times seen in section 2.5.4 shows that mechanical translation systems are unlikely to be ever fast enough to outrun these probe induced perturbations.

The second major factor seems to be the temperature of the alumina tube of the probe body. IVDFs of cold and hot probe tip show a distinct profile difference. This could explain the position factor as probes gets hotter and hotter as they progress upstream.

This second phenomenon supports the concept of fast translating probe as a less invasive diagnostic method. A shorter residence time inside the hot part of the discharge would not only preserve the lifespan of the probe tip but would not let the alumina tube get as hot. Several properties such as conductivity [69] and secondary electron emission are temperature dependent. The alumina at high temperature could be the source of the perturbations observed. Staack's [70] investigations show that these two properties have a major influence on the probe induced perturbations. He proposed and tested with good results several alternative materials (namely segmented graphite and tungsten) for the probe body. Boron Nitride is also a good candidate as demonstrated by Reid [71].

In that respect Langmuir probes should have less influence on the discharge as they are not heated apart from when they collect high electron currents. Their slightly longer measuring time compared to emissive probes (when a full voltage sweep is done) should be negligible as this electronic sweep can be made short enough (in the order of a millisecond) to fit within the minimum time it takes to mechanically retract the probe.

As a consequence probe measurement inside and right at the exit plane of Hall thruster should be considered very carefully. On top of the already high errors on plasma properties associated with the important temperature gradient and magnetic field present, the behavior of the discharge itself is significantly perturbed by the presence of the probe. Simulation validation and performance assessment should be done with data collected with non-intrusive methods such as LIF or Thomson scattering.

Lastly it is worth remembering that the perturbations observed on the IVDF are for the metastable ions. The probes inserted inside the thruster modify electron properties ( $n_e, T_e$ ) as well as the plasma dynamics. This is certain to change the density of excited states relative to the ground state. Although unlikely the ground state could remain undisturbed by the probe insertion as the excited states do not always accurately reflect the ground state [72].

## 2.6. CONCLUSION

---

# Chapter 3

## Low power Hall thrusters: scaling and performances <sup>1</sup>

### Contents

---

<b>3.1 Thruster scaling</b>	<b>35</b>
3.1.1 Existing thruster power range	35
3.1.2 Scaling laws	37
<b>3.2 The ISCT200-GEO and ISCT100 Hall thrusters</b>	<b>38</b>
3.2.1 Channel geometry	38
3.2.2 Permanent magnets and field generation	39
<b>3.3 Results on the ISCT100 scaling</b>	<b>39</b>
3.3.1 Discharge envelope	39
3.3.2 Plume divergence and characteristics	41
3.3.3 Performances	42
3.3.4 ISCT100-V2 performance with BN-SiO <sub>2</sub>	44
<b>3.4 Results on the ISCT200-GEO scaling</b>	<b>45</b>
3.4.1 Discharge current and electron mobility	45
3.4.2 Propellant utilization	47
3.4.3 Divergence	47
<b>3.5 Conclusion</b>	<b>48</b>
3.5.1 Effects of channel geometry	48
3.5.2 Effects of magnetic field intensity	48

---

## 3.1 Thruster scaling

### 3.1.1 Existing thruster power range

The most successful and used Hall thruster in the recent time has been the SPT-100 from Fakel. This Hall thruster operates at 1350 W and has been launched on more than 70 spacecrafts as of the summer of 2017 [73]. Similarly the 600 W SPT-70 was launched at least 26 times. Those two thrusters represent the majority of the Hall thrusters used in space. This power range is particularly adapted to station-keeping of satellites in geostationary orbit (GEO). A number of alternatives exist to the SPT-100. Among them

---

<sup>1</sup>Adapted from:  
S. Mazouffre and L. Grimaud, "Characteristics and Performances of a 100-W Hall Thruster for Microspacecraft," *IEEE Trans. Plasma Sci.*, vol. 46, no. 2, pp. 330–337, Feb. 2018.

are the PPS-1350 family from SAFRAN or the BHT-1500 made by Busek. Typical anode efficiency for this size of thruster is around 55%.

The more recent trend of all electric geostationary satellites has pushed toward the design of more powerful thrusters. The different actors in the industry seems to have converged toward 5 kW thruster with the SPT-140 from Fakel, the PPS-5000 from SAFRAN and the XR-5 produced by Aerojet Rocketdyne and derived from the BPT-4000. Those thrusters, when operated two at a time, can ensure GTO to GEO transfer in only a few months (typically 4 months for a dry mass of 2 tons). They are characterized by an anode efficiency of around 60%.

While the two categories described above represent most of the current commercial market for Hall thrusters, developments in other power ranges has been underway since the very beginning of electric propulsion. For exploration missions in interplanetary space with heavier spacecraft, higher power thruster are desirable in order to obtain reasonable transit times. National space agencies have supported the development of thrusters in the 10 to 100 kW range for such missions. On the Soviet and Russian side the SPT-230 (15 kW) and SPT-290 (35 kW) are the most notable examples. However earlier thrusters with more exotic dual stage TAL architectures were tested up to 50 kW (TM-50) and the TsNIIMASH reported reaching 150 kW with bismuth propellant in the 60's [19, 74]. American efforts on the high power side began with the creation of the 10 kW T-220 (in collaboration with the Keldysh Research Center in Moscow) followed by the indigenous 20 kW NASA-300, 40 kW NASA-400 and the 50 kW NASA-457 (tested up to 72 kW) [75, 76]. Another novel architecture investigated for high power Hall thruster is the "nested channel" concept with the X2 (20 kW) and X3 (100 kW) thrusters [77, 78]. The Busek company also developed the 20 kW BHT-20k [79]. European development in this domain has been less ambitious. The two high power Hall thrusters of note are the PSS-20k ML jointly developed by CNRS and Safran under the European research grant HiPER [80] and the 20 kW HT20k currently in development by Sitael [81]. Lastly Chinese research institute have started developing a 50 kW class nested channel thruster [82]. For those larger Hall thrusters the anode efficiency can reach up to 75%.

Our area of interest for this study is the lower power thrusters. We define low power Hall thrusters as thrusters operating at less than 500 W. This lower power range has received a lot of attention recently with the proliferation of smaller satellites. Lower launch cost and improved electronics have dramatically increased the attractiveness of small, micro and nano-satellites. Their applications range from Earth observation to communication (internet of things), scientific experiments and more. Electric propulsion is particularly attractive for such applications because of its higher specific impulse. Propulsion systems on smallsat have been proposed for constellation deployment, end of life management and better agility to deal with space debris and mission requirements. Constellations of hundreds of such satellites are currently planned with individual satellites mass ranging from a few kilograms to 500 kg. This means that the power available is limited (from 10 W to 1 kW). Hall thruster are one of the prime candidate for this kind of applications.

While few commercial thrusters with flight heritage exist in this power range, a number of low power thrusters have been developed by laboratories all over the world. The lower cost of construction, and more importantly testing, have made them quite attractive for academic research. Surveying the literature, more than 20 thrusters in this power range are reported to exist and the performance of about 3 quarter of them are publicly available. Appendix A presents an overview of the thrusters with relatively standard architectures and with publicly available performance figures for the anode efficiency.

As seen in figure-A.2, anode efficiency numbers vary greatly between thrusters in this power range. Two thrusters can be considered outliers with efficiencies significantly higher than their competitor. The commercial BHT-200 from Busek reaches the 50% mark at 230 W and the CAMILLA-HT-55 developed at Technion is at 47% for the same discharge power. However between 200 and 250 W the efficiency of most of the thrusters referenced here is between 30 and 40%. Most of the work has been done above 150 W.

It is worth noting that even lower power Hall thrusters type have been built and tested. Among other the ISCT100 presented in this chapter, but also the SPT-20 [83] and SPT-30 [84, 85] as well as the BHT-100 [86]. At this size magnetic field generation, thermal management and mechanical tolerances start to become more challenging. For that reason low power Hall type thruster often use configurations different from classical SPT cases. One example are the cylindrical Hall thrusters (CHT). In CHTs the inner magnetic pole is pushed to the back of the discharge channel. This reduces the total area of the surfaces in contact with the plasma and should in theory reduce the energy losses at the walls [87]. Notable examples include the TCHT-4 from the Osaka institute of technology [88] and the 2.6 cm cylindrical

Hall thruster built at Princeton [89]. One of the smallest Hall type thruster built for propulsion and where efficiency measurement were attempted is a nominally 50 W TAL built by Khayms in 2000 [90]. Efficiency was estimated to be around 6%. At lower discharge power we find the Micro Hall Thruster from Stanford with a designed discharge power of 15 W [91] as well as the BHT-20 operating between 5 and 25 W [92,93]. However no thrust measurements exist for those thrusters.

### 3.1.2 Scaling laws

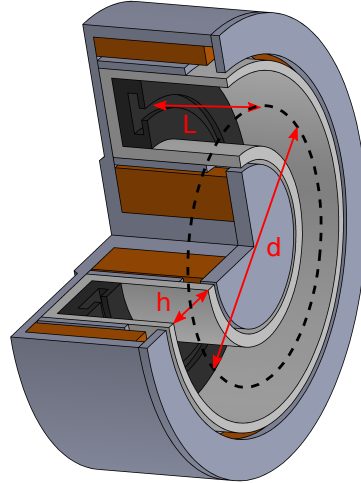


Figure 3.1: Characteristics dimensions of a Hall thruster

#### Channel diameter and width

In order to maintain sufficient plasma and neutral density for efficient ionization, the area of the thruster must be scaled with the discharge power. An overview of the different scaling methods can be found in reference [94]. The critical thruster dimensions  $h$ ,  $d$  and  $L$  are defined on figure 3.1.

One of the most important energy loss mechanism in Hall thrusters is the collision of electrons with the walls. The power deposited at the walls is in the order of  $10 \text{ kW/m}^2$  [95,96]. To have an appropriate channel volume while minimizing wall losses the surface to volume ratio must be as small as possible. This means that the ratio of the width of the channel ( $h$ ) to the mean diameter ( $d$ ) needs to be as big as possible. We define  $S_0$  the surface area of the channel:

$$S_0 = \pi \cdot h \cdot d \quad (3.1)$$

In our thrusters  $S_0$  is defined such that the ration  $h/d$  is equal to the one of the well known SPT-100. The channel width can then be changed to increase this reference surface area. By increasing  $S_0$  while keeping the mean diameter  $d$  constant we effectively change the surface to volume ratio.

This design principle of decreasing the surface over volume ratio is of course what lead to the invention of cylindrical Hall thrusters (CHTs) for low power applications.

#### Channel length

No strong agreement exist on the scaling of the discharge channel length ( $L$ ) [94]. The channel length should be long enough that the neutral density becomes homogeneous across the thruster and must also be large compared to the typical ionization length. This is the so called ‘‘Melikov-Morozov criterion’’. In this study the discharge channel length was kept fixed.

### Magnetic field

Several different methods exist for scaling the magnetic field intensity. The main constraint is that the field must be strong enough so that the electrons are efficiently confined by the magnetic barrier. In practice that means that the electron Larmor radius must be small relative to the thruster dimensions and that their gyration frequency needs to be large compared to their collision frequency.

Those requirements suggest that a small thruster should have a very large magnetic field (and inversely for larger ones). However by experience most thrusters (whatever their size) have a nominal magnetic field strength of a few hundred gaussses [83]. The kilogauss field calculated by some scaling methods render the thruster unstable and impossible to ignite. It is nonetheless interesting to compare performances with different magnetic field strength.

Downscaling thrusters can also presents challenges to the realization of good magnetic topologies. Magnetic lines need to be kept mostly perpendicular to the walls and it is preferable to keep the anode area free of magnetic field. Difference in topologies can greatly affect the performances and have even more effect than dimensions or magnetic field intensity [13]. This is something to keep in mind when comparing different thrusters scaled with different methods.

## 3.2 The ISCT200-GEO and ISCT100 Hall thrusters

### 3.2.1 Channel geometry

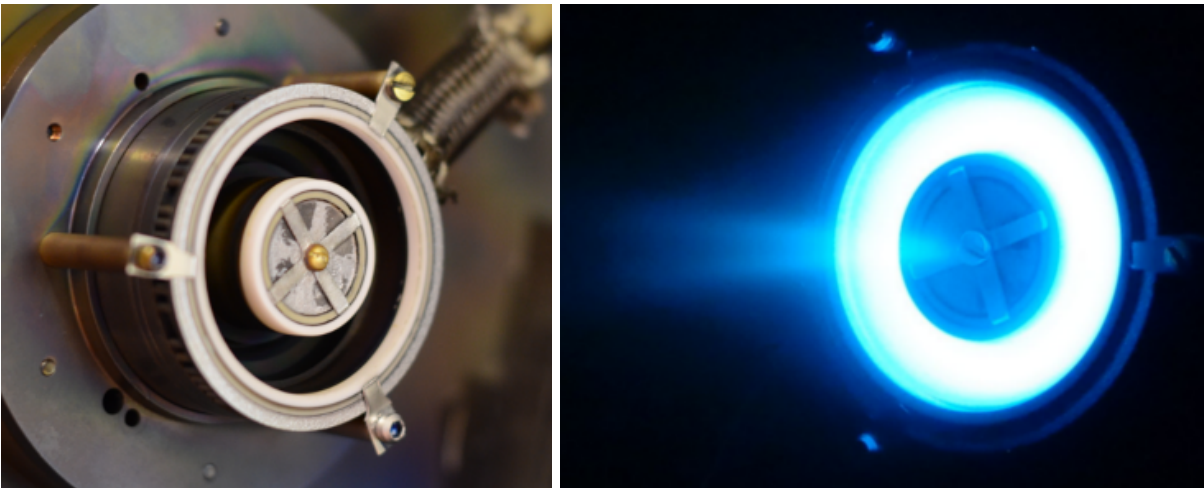


Figure 3.2: The ISCT200-GEO Hall thruster in the  $2S_0$  configuration

The ISCT200-GEO was designed to test different channel widths and magnetic field strengths for a 200 W Hall thruster. The default channel width is  $3S_0$  but it can be reduced to  $2S_0$  and  $S_0$  thanks to ring inserts. These inserts do not change the mean diameter. Wall materials can also easily be changed between  $\text{Al}_2\text{O}_3$  and  $\text{BN-SiO}_2$ . The results presented below are done with  $\text{BN-SiO}_2$ . Pictures of the ISCT200-GEO in the  $2S_0$  configuration can be seen figure 3.2.

The ISCT100 is a 100 W Hall thruster with similar design as the ISCT200-GEO. The largest channel diameter in the ISCT100 is the  $2S_0$  configuration but it can also be adapted to a  $S_0$  channel. The ISCT100 can be seen figure 3.3. On these pictures the thruster is featured with its oversized radiator. Since the ISCT100 is a laboratory thruster the thermal design is not optimized for mass or size. The discharge channel for the  $2S_0$  configuration was initially designed for  $\text{Al}_2\text{O}_3$  due to its thinness. The inserts used to switch to the  $S_0$  configuration are however  $\text{BN-SiO}_2$ . The data presented in section 3.3.1, 3.3.2 and 3.3.2 are with those inserts. A second version of  $2S_0$  ceramics were then manufactured out of  $\text{BN-SiO}_2$  to test their robustness and see if the performances were improved by the change in material. This new variant of the thruster is name the ISCT100-V2 in this document. Results on the  $2S_0$   $\text{BN-SiO}_2$  ISCT100-V2 are presented in section 3.3.4.

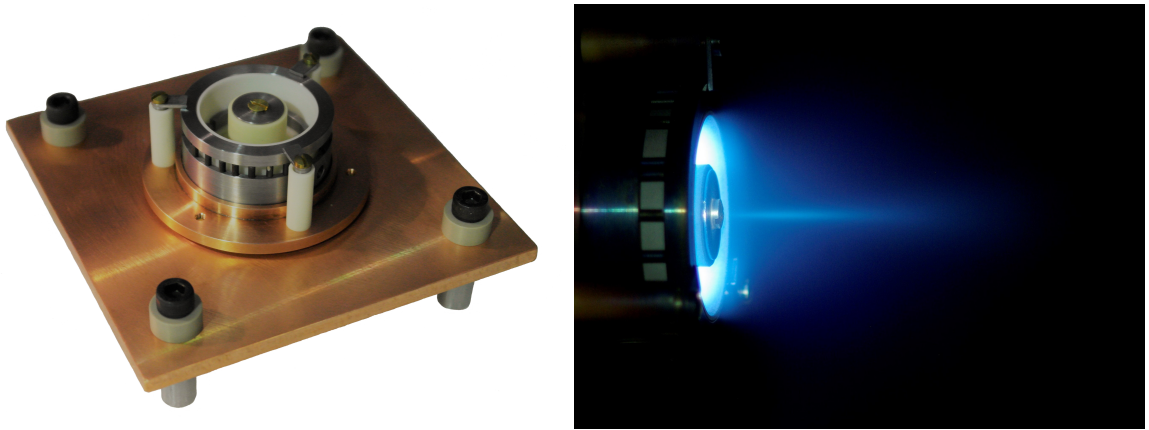


Figure 3.3: The ISCT100 Hall thruster in the  $2S_0 B_0$  configuration.

### 3.2.2 Permanent magnets and field generation

Both thrusters use permanent magnets as their magnetic flux source. The magnets are small millimeter size cylinders placed just inside and outside the discharge channel. Ring segments can also be used to increase the packing factor and obtain more magnetic flux. Samarium Cobalt is used for its high coercivity, high Curie point and good thermal stability.

The use of permanent magnets does not allow for continuous variation of the magnetic field once under vacuum. However the magnetic field strength can be varied by changing the number of magnets. The pure iron (ARMCO) magnetic circuit for both thrusters is designed to be in a linear regime for the points tested. That means that the shape of the magnetic field is not significantly changed when magnets are removed or added. Of course this is true assuming equilibrium is maintained between the inner and outer poles.

In this study the field strength is only changed in the ISCT100, previous work was done on this aspect the ISCT200-GEO in reference [97]. The field has a classical topology with a maximum close to the exit plane of the thruster but slightly inside the discharge channel. A modern topology with a focusing magnetic lens is used. Two field intensity are tested:  $B_0$  and  $2B_0$ . The  $2B_0$  field is chosen to have twice the maximum intensity at the center of the discharge channel as  $B_0$ .

The ISCT200-GEO can also change magnetic field strength. The field is usually set to either a reference  $B_0$  value or  $1.7B_0$ . It can also be increased all the way to  $2.3B_0$ . In the results presented in section 3.4 the field is set to  $1.7B_0$ .

## 3.3 Results on the ISCT100 scaling

### 3.3.1 Discharge envelope

The four different configurations of channel width ( $S_0, 2S_0$ ) and field strength ( $B_0, 2B_0$ ) were tested first in the NExET vacuum chamber to assess their operating envelope and stability. Operating pressure was between 1 and  $4 \times 10^{-5}$  mBar depending on mass flow.

Figure 3.4 shows the map of tested operating points. The shaded areas cover 90% of the discharge current oscillations. This was done to make sure no isolated discharge anomaly would distort the results.

All the configurations were tested from extinction voltage up to either 200 W discharge power, the apparition of hot spots in the discharge channel or spontaneous shutdown (whichever came first). Spontaneous shutdown seemed to be mainly caused by very high oscillations. The thruster was left operating for at least 5 minutes at each points. We ensured that the thruster was not transitioning between two discharge modes by watching the dynamics of the discharge current on the oscilloscope. While this waiting time is not enough completely thermalize the thruster, it at least ensures that the discharge channel wall temperature is close to the steady state.

Before even looking at current profile it is interesting to note that thruster start up was made considerably harder as the magnetic field was increased and the channel width narrowed. The  $S_0 2B_0$  case

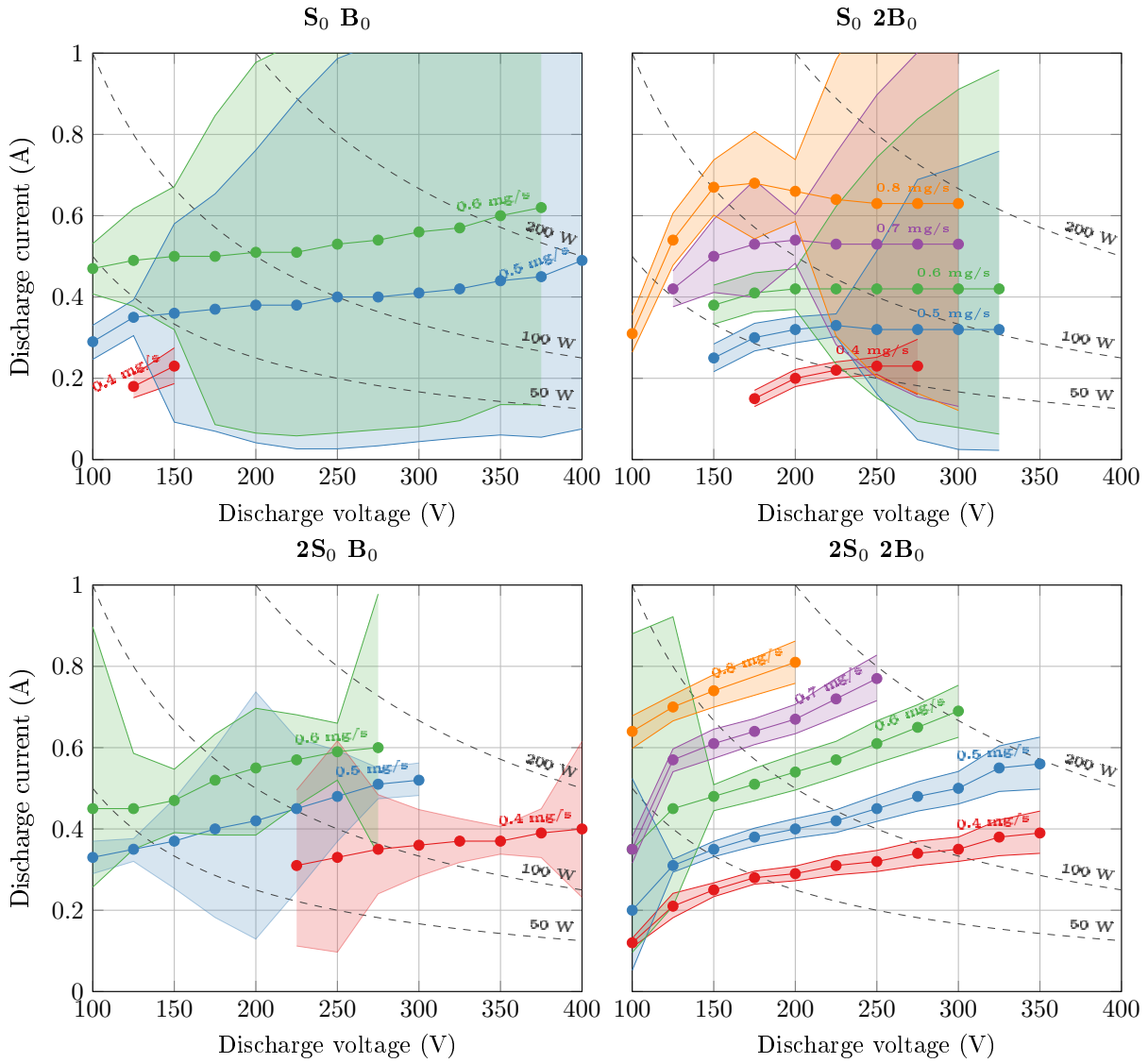


Figure 3.4: Discharge current for different configurations as a function of anode mass flow and discharge voltage.

required high voltage ( $\sim 400$  V) and high mass flow ( $\sim 1$  mg/s) in order to ignite.

Out of all those configurations only the  $2S_0 2B_0$  one is stable over a large number of operating points. Both  $2B_0$  configurations have a discharge envelope resembling a classical Hall thruster such as the SPT-100 [26].

In the  $2S_0 2B_0$  case the oscillations are limited to around 10% of the mean discharge current for most points. Above 150 V there is a steady moderate increase of discharge current as the voltage increase for a fixed mass flow. The oscillations also slightly increase with voltage but the strong oscillation regime sometime seen at higher voltage is not observed.

The  $S_0 2B_0$  case displays a local maximum of the discharge current between 150 and 200 V before settling into a nearly constant mean discharge current. As the voltage is increased a high oscillation “breathing mode”-like regime appears. This regime was only seen above 350 V for the SPT100 [26]. In the ISCT100 with the  $S_0 2B_0$  configuration it appears as low as 225 V.

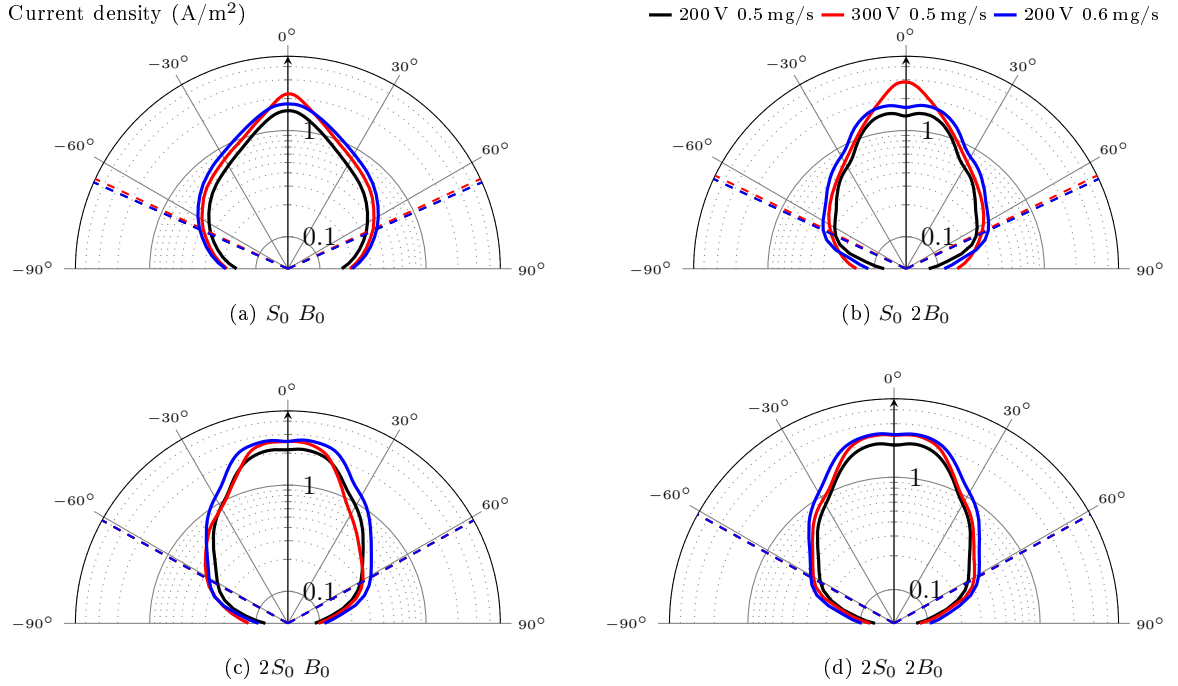


Figure 3.5: Current density profiles across the plume of each configurations at 200 V 0.5 mg/s, 300 V 0.5mg/s and 200 V 0.6 mg/s operating conditions. The dashed lines represent the divergence angle  $\alpha_d$ .

### 3.3.2 Plume divergence and characteristics

#### Plume current density profiles

For all configurations an ion current density profile was acquired across the plume. The profiles at three different operating points can be seen on figure 3.5.

The  $S_0 B_0$  case clearly shows an unfocused beam with a significant portion of the ion current present at high angles. The  $S_0 2B_0$  only has this unfocused current density distribution at 300 V and 0.5 mg/s. For both cases it is correlated with very high current oscillation regimes.

On the profiles corresponding to more stable operating points, the two peaks, coming from the two sides of the discharge channel, are visible. The resolution of those two peaks is associated with a stable and well focused beam.

#### Plume characteristics

From the angular distribution of the ion current density the total ion current, the ion current fraction ( $\eta_I$ ), the divergence angle ( $\alpha_d$ ) and the propellant utilization fraction ( $\eta_{prop}$ ) are calculated. Equations detailing the process can be found in section 2.2.2.

Some test chamber effects can modify the ion current profiles. Most notably residual plasma and charge exchange with neutral residual gas in the chamber can artificially increase the collected ions current. This effect is particularly strong at high angles where the background plasma density can be in the same order as the plasma coming from the thruster. Moreover those high angles contribute more to the total integrated current as they represent a bigger slices of the integration hemisphere.

Correction factors can vary from very complex fitting of the experimental profiles to a pre-existing plume shape model to very simple background subtraction. Since all the plume data presented in the study is taken in the same chamber and under identical conditions for both geometrical configuration and probe, they should be comparable with no additional post processing. We however chose to remove the background plasma by subtracting a fixed offset corresponding to the average flux measured at  $+90^\circ$  and  $-90^\circ$ . This ensure that the data is at least somewhat comparable to other publications. However such comparisons should be made with great care as chamber effects, probe design and data processing

### 3.3. RESULTS ON THE ISCT100 SCALING

procedures can greatly influence the numerical results [35].

Table 3.1: Overview of the data derived from plume measurements for the 200 V 0.6 mg/s and 300 V 0.5 mg/s cases in all the configurations.

	$V_d$ (V)	$\dot{m}_a$ (mg/s)	$S_0$			$2S_0$		
			$\alpha_d$ ( $^\circ$ )	$\eta_I$	$\eta_{prop}$	$\alpha_d$ ( $^\circ$ )	$\eta_I$	$\eta_{prop}$
$B_0$	300	0.5	65	57%	62%	63	63%	77%
	200	0.6	66	53%	59%	61	71%	82%
$2B_0$	300	0.5	64	69%	60%	62	69%	81%
	200	0.6	65	64%	62%	61	72%	76%

Table 5.2 shows an example of the plume data obtained in all four configurations for the 200 V 0.6 mg/s and the 300 V 0.5 mg/s points. Those respectively represent a discharge power close to 100 W and 140 W for all configurations.

From this table it is apparent that the main influence on the divergence angle is the channel width. The  $S_0$  configurations all have higher divergence than the  $2S_0$  ones. Widening the discharge channel also seems to considerably increase the propellant ionization. This agrees with previous observations on the ISCT200-GEO [54]. The ion current fraction ( $\eta_I$ ) is also increased by the wider channel but mainly for the higher mass flow and lower voltage operating point.

The magnetic field intensity does not have as much influence on the plume. The loss of one degree of divergence at higher field strength is not conclusive. While the error bars of such measurement are complicated to estimate, they are almost certainly higher than one degree [35]. The ion beam current fraction shows an increase particularly significant at the higher voltage. This is consistent with the fact that HT fitted with coils generally increase their magnetic field at higher voltage. Finally the propellant utilization does not have any clear behavior tied to the magnetic field intensity.

#### 3.3.3 Performances

Thrust measurements were performed at the Pivoine-2g test facility. Since the ISCT100 operates at much lower power (and thus lower mass flow) than what the chamber is designed for, excellent background pressure were achieved. During testing all the measurement points were taken between 4 and  $6 \times 10^{-6}$  mBar xenon corrected pressure.

Due to the limited time available on the Pivoine-2g chamber only the  $S_0 2B_0$  and  $2S_0 2B_0$  configurations were measured. The  $S_0 2B_0$  proved to be even harder to start than in the NExET chamber. This was probably due to the lower background pressure. As a result only two operating points were measured in this configuration.

In the two configurations tested the discharge current were slightly lower in the Pivoine-2g chamber than in the NExET one. This is once again probably pressure related. It is well known that the discharge current tends to decrease when the pressure is lower [35].

A thrust between 4 and 9 mN was measured across the operating envelop tested (figure 3.6). At equivalent mass flow and discharge voltage the  $S_0 2B_0$  configuration both had a lower thrust, a lower specific impulse and a lower anode efficiency. The  $2S_0 2B_0$  configuration achieves an Isp between 850 and 1300 s (figure 3.7) and an efficiency between 25 and 32% on most of the design operating range (figure 3.8). Thrust, Isp and efficiency increased with mass flow. A significant uncertainty ( $\pm 3\%$ ) is present on the anode efficiency due to the limits in thrust stand sensitivity.

The best operating point was reached at 300 V 0.7 mg/s with a discharge power of 180 W, a thrust of 9 mN, an anode specific impulse of 1300 s and an anode efficiency of 32%.

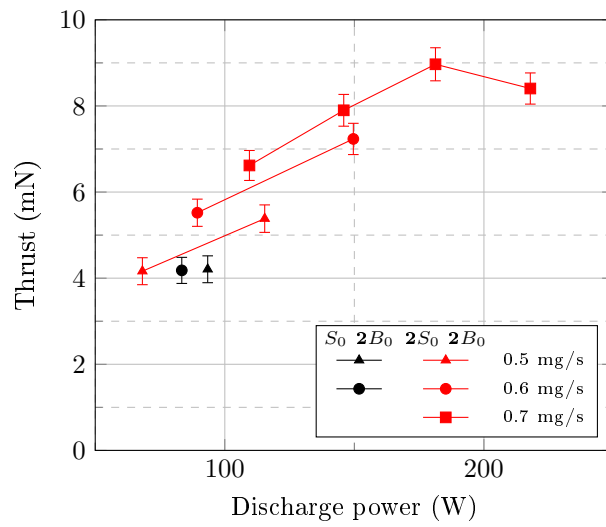


Figure 3.6: Thrust versus discharge power for different mass flow rates

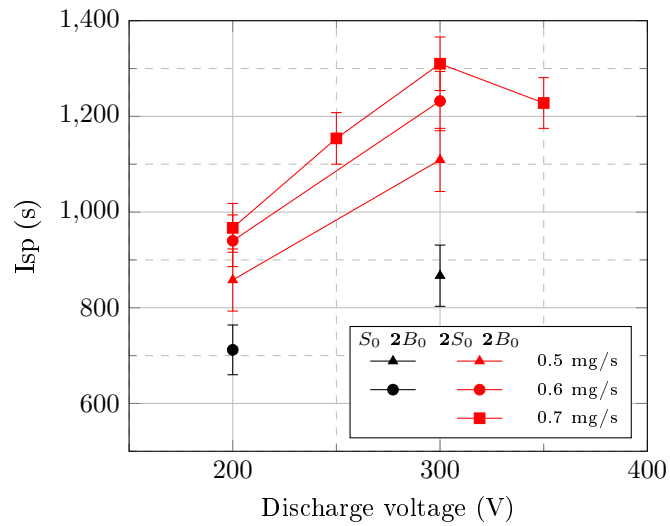


Figure 3.7: Specific impulse versus discharge voltage for different mass flow rates

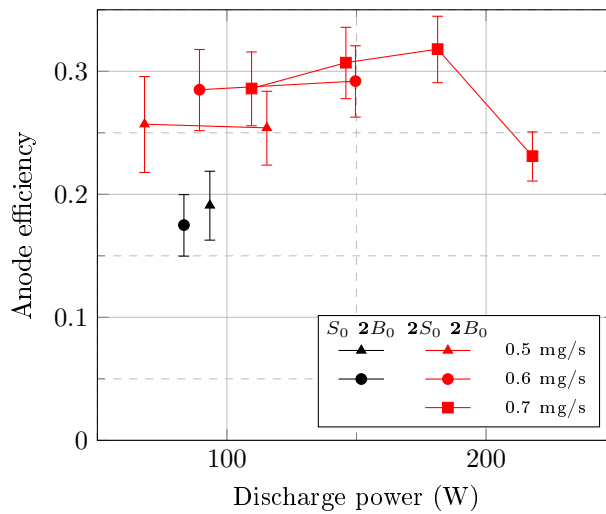


Figure 3.8: Anode efficiency versus discharge power for different mass flow rates

3.3.4 ISCT100-V2 performance with BN-SiO<sub>2</sub>

After this test campaign it was decided to take the risk to change the very thin  $2S_0$  ceramic discharge channel from Al<sub>2</sub>O<sub>3</sub> to BN-SiO<sub>2</sub>. Figure 3.9 presents the difference between the two thruster as measured in the PIVOINE-2g test chamber.

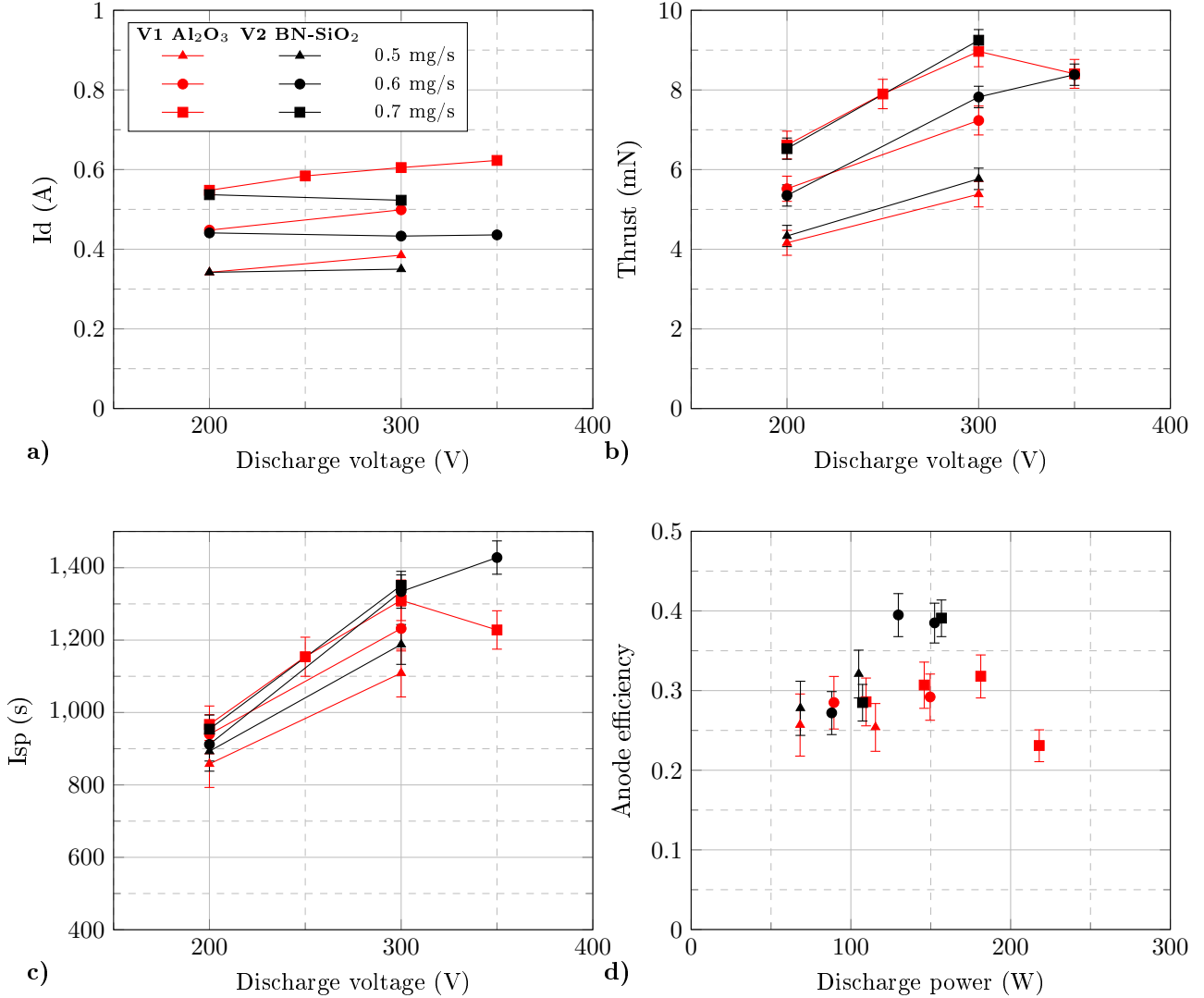


Figure 3.9: Comparison of performances between the ISCT100-V1 in  $2S_0$ ,  $2B_0$  configuration with Al<sub>2</sub>O<sub>3</sub> walls and the ISCT100-V2 in  $2S_0$ ,  $2B_0$  configuration with BN-SiO<sub>2</sub> walls: discharge current (a), thrust (b), anode specific impulse (c) and anode efficiency (d).

As expected the differences in thrust and specific impulse are minimal at equivalent discharge voltage and xenon mass flow. This is similar to results obtained on the SPT-100 with Al<sub>2</sub>O<sub>3</sub> and BN-SiO<sub>2</sub> walls [26, 98, 99] and will be discussed in more details in chapter 5. The main difference in the discharge current above 200 V. The BN-SiO<sub>2</sub> version has a significantly lower discharge current which results in a much better anode efficiency.

These results show that an efficiency of 40% between 125 and 160 W is achievable. This is on par with the best results found in the literature at this power range, rivaling the BHT-100 [86] in anode efficiency without the additional burden of powering the electromagnet coils.

### 3.4 Results on the ISCT200-GEO scaling

The study on the ISCT200-GEO was less exhaustive as previous study have been performed at ICARE on the scaling of this thruster [94,100]. However the previous studies were conducted with  $\text{Al}_2\text{O}_3$  channel walls instead of the  $\text{BN-SiO}_2$  used here.

The measurements were performed in the NExET test bench. The data acquired was limited and only consisted in the mean discharge values and a sweep with the flat probes described in section 2.2.1.

The thrusters was operated in the  $1S_0$ ,  $2S_0$  and  $3S_0$  geometries. The test matrix sweeps discharge voltage or 150, 200 and 300 V for a xenon mass flow of 1 mg/s and mass flows of 0.8, 1.0 and 1.2 mg/s for a fixed discharge voltage of 200 V. The 250 V at 1.0 mg/s for the  $3S_0$  geometry could not be sustained is absent from this data set.

#### 3.4.1 Discharge current and electron mobility

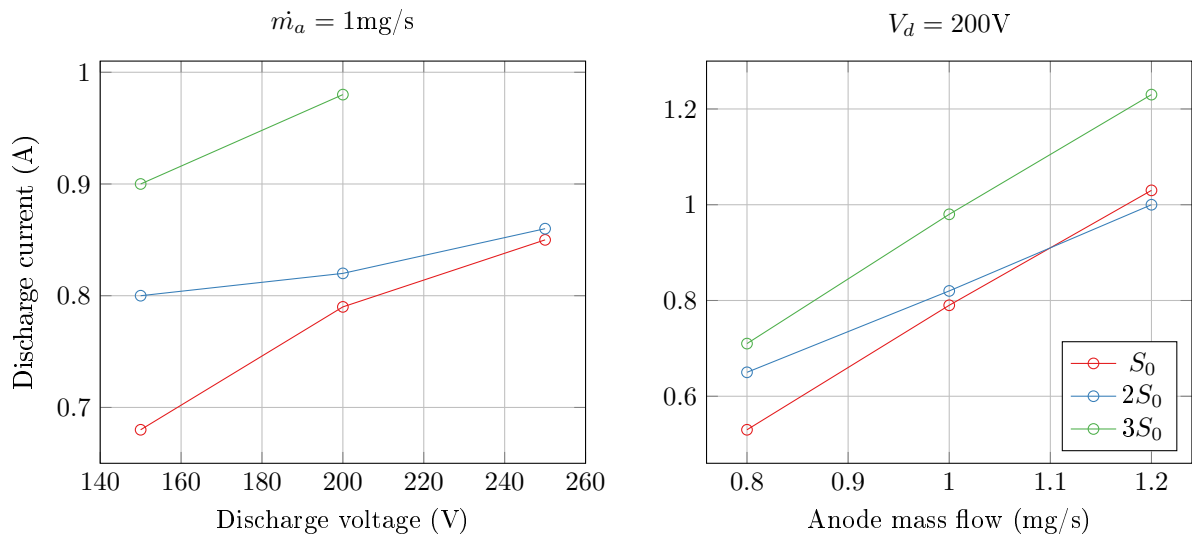


Figure 3.10: Discharge current for the different configurations and operating points of the ISCT200-GEO.

Figure 3.10 shows the discharge current for the three geometries. The  $3S_0$  case has a much higher discharge current than the other test cases. However as seen in figure 3.11 the ion beam current collected by the probes is not very different between the  $2S_0$  and the  $3S_0$  configuration. This high discharge current can be explained by the ion beam current fraction (see figure 3.12). A large electron current is present in the  $3S_0$  configuration. This is probably due to a poor electron confinement. Since the magnetic field is constant this high mobility could be caused by the low density in the larger channel. The  $3S_0$  geometry has 3 times the front section area of the  $1S_0$  case and 1.5 times the one of the  $2S_0$  case. This means neutral density should proportionally be lower which lower electron/neutral collision frequency.

This is interesting since to keep a constant electron diffusion rate (from electron/neutral collisions) the magnetic field should be proportional to the neutral density [94]. We see here that in a situation where the magnetic field is fixed and the neutral density is decreased the electron mobility seems to increase! This could mean that the high electron current seen in the  $3S_0$  configuration could be due to anomalous transport phenomena. While no thrust measurement is available we expect that this high electron current would considerably lower the anode efficiency of the thruster.

For the  $1S_0$  case the ion beam current fraction is also low. This is less surprising as the higher neutral density (with the same magnetic field intensity) means a higher classical electron mobility. The larger surface to volume ratio also means that a larger portion of the ions are expected to be lost due to wall collisions.

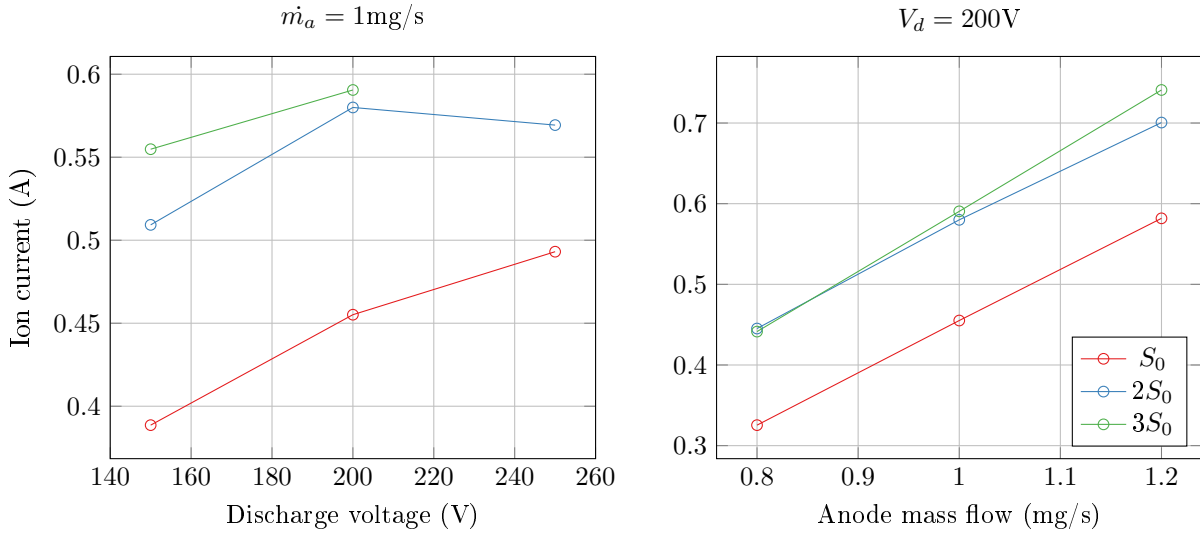


Figure 3.11: Ion beam current for the different configurations and operating points of the ISCT200-GEO.

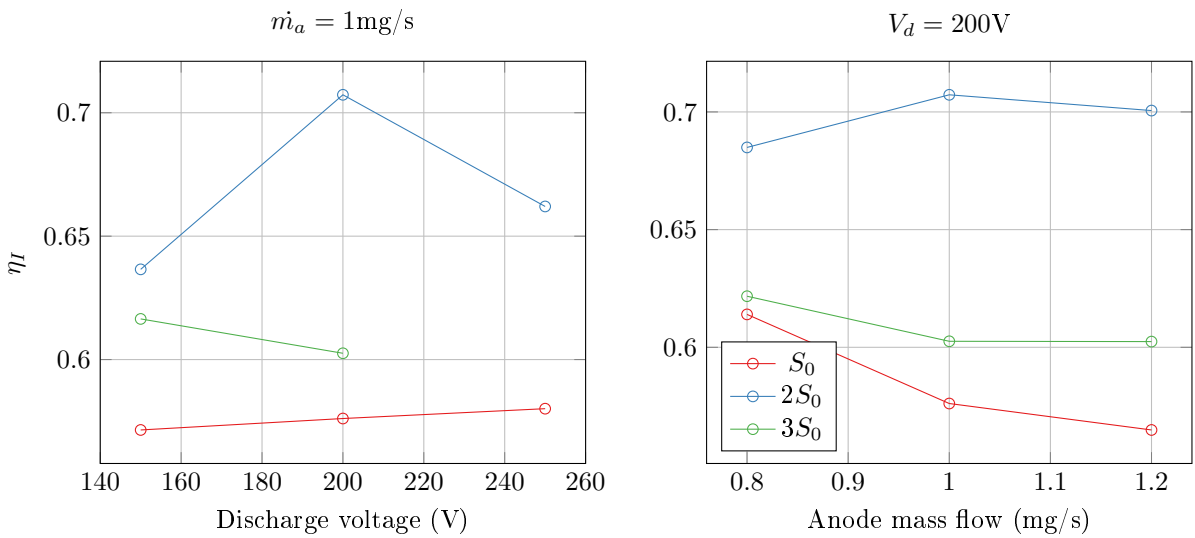


Figure 3.12: Ion beam current fraction for the different configurations and operating points of the ISCT200-GEO.

### 3.4.2 Propellant utilization

The propellant utilization for the different configurations can be seen on figure 3.13. Unsurprisingly propellant utilization increases with discharge voltage as more efficient ionization takes place. Propellant utilization for the  $2S_0$  and  $3S_0$  cases are roughly comparable (with a slight edge for the  $3S_0$  configuration) while the  $1S_0$  geometry is 15 to 20 percentage points lower. This is consistent with wall losses and in agreement with previous results obtained with  $Al_2O_3$  [54].

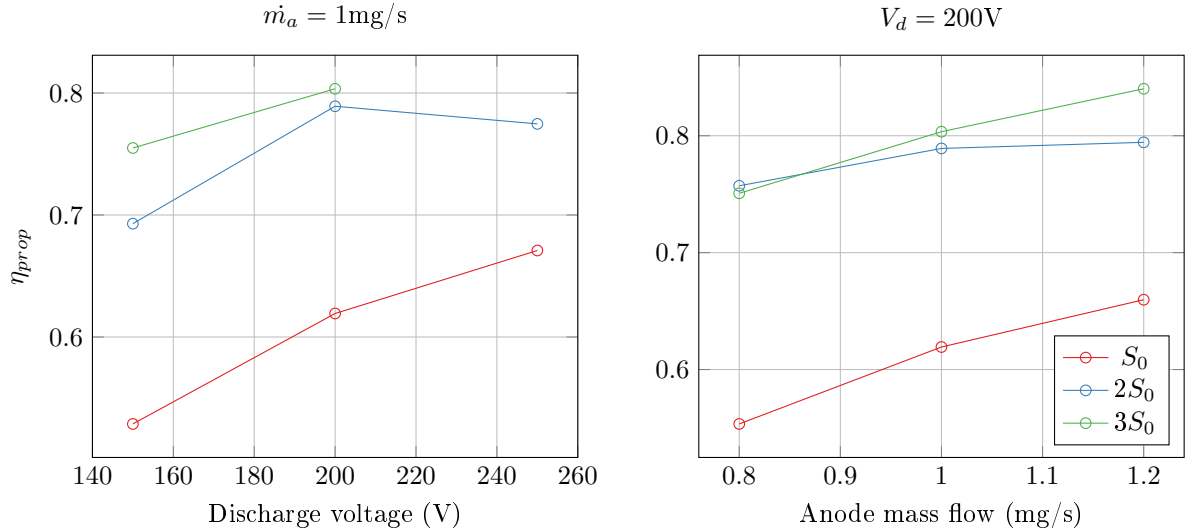


Figure 3.13: Propellant utilization fraction for the different configurations and operating points of the ISCT200-GEO.

### 3.4.3 Divergence

Finally we can consider the divergence (figure 3.14). The  $2S_0$  case has the lowest measured divergence. Since the magnetic topology is fixed only two main phenomena can influence the plume divergence. The first one is the collisions with the walls. This can have a focusing effect on the ion plume. However in our case we see that the narrower channel has a higher divergence.

The second phenomenon controlling the divergence angle is the position of the acceleration region. Using electrodes inside the discharge channel Raitse showed the plume divergence could be reduced by positioning the acceleration region further upstream [101]. He also saw that reducing the channel width can push the acceleration downstream and thus increase the plume divergence [102]. He attributes the shift in position to the higher proportion of secondary electron (emitted from the walls) to primary increasing the mobility inside the channel. This seems to be what is causing the higher divergence of the  $1S_0$  configuration.

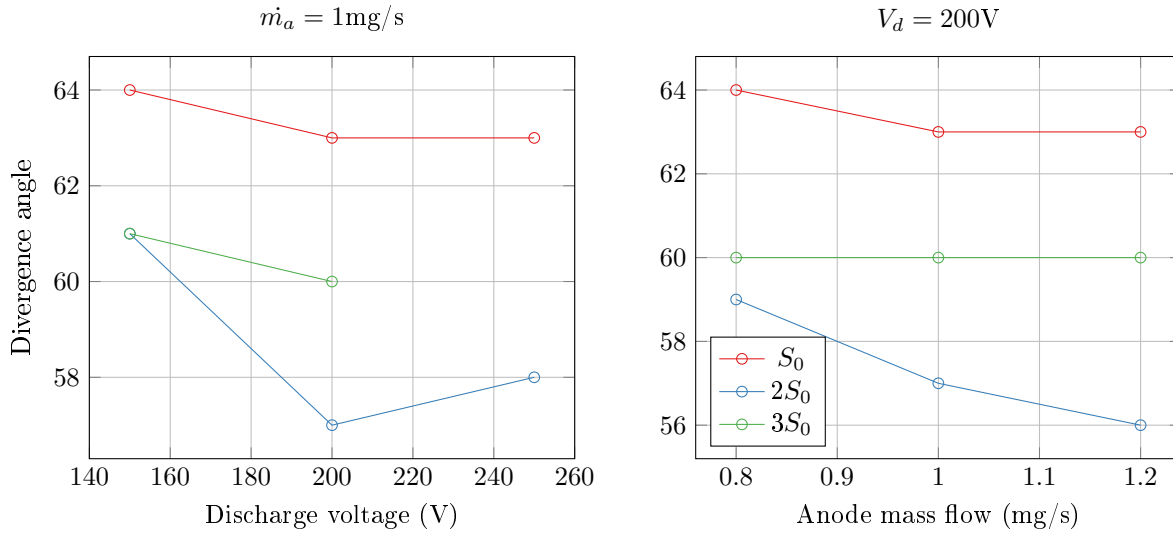


Figure 3.14: Divergence angle for the different configurations and operating points of the ISCT200-GEO.

## 3.5 Conclusion

### 3.5.1 Effects of channel geometry

The channel width has several effects on the discharge. Narrow channel thruster configurations seem to be in general less stable and harder to start. According to our plume measurements the propellant utilization is the main factor affected by channel width, with the narrower channel leading to worst ionization. This could be due to the fact that the larger surface to volume ratio results in more ions being lost to collisions with the walls. It is thus preferable to increase the width to diameter ratio in small thrusters compared to bigger ones. However in the ISCT200-GEO the ion beam current fraction decreases at the largest channel width. This could be indicative of an optimal width.

The divergence is also affected by the change in channel width. Contrary to what could be expected a wider channel reduces the divergence. This effect was explained by Raitses [103] as a change in the position of the acceleration region. In a narrower thruster the acceleration region can be pushed downstream and thus the jet of ion is less collimated by the walls.

This lower propellant utilization translates to a lower thrust, Isp and efficiency.

### 3.5.2 Effects of magnetic field intensity

The stronger magnetic field has a stabilizing effect on the discharge and considerably broaden the operating envelope of the thruster. It also slightly reduces the mean discharge current. This effect seems to be due to lowering the electron transport and can be seen in table 5.2 where the ion current fraction is higher in the  $2B_0$  configuration. With that lowered discharge current we expect the  $2B_0$  to have a higher efficiency.

# Chapter 4

## Physics of a small magnetically shielded Hall thruster <sup>1</sup>

### Contents

---

<b>4.1 Erosion phenomenon in Hall thrusters</b> . . . . .	<b>49</b>
4.1.1 The mechanism of ion sputtering . . . . .	50
4.1.2 Ion acceleration in Hall thruster . . . . .	51
4.1.3 Anomalous erosion . . . . .	53
<b>4.2 Overview of the magnetic shielding concept</b> . . . . .	<b>56</b>
4.2.1 Equipotentiality of the magnetic field lines . . . . .	56
4.2.2 Magnetic field topology . . . . .	56
4.2.3 Existing MS thrusters . . . . .	57
4.2.4 Summary of existing results . . . . .	58
<b>4.3 The ISCT200-MS magnetically shielded thruster</b> . . . . .	<b>58</b>
4.3.1 The ISCT200-US baseline thruster . . . . .	58
4.3.2 Geometry . . . . .	59
4.3.3 Magnetic field . . . . .	59
<b>4.4 Discharge characteristics</b> . . . . .	<b>60</b>
4.4.1 Discharge current . . . . .	60
4.4.2 Thermal behavior . . . . .	60
<b>4.5 Ion behavior</b> . . . . .	<b>62</b>
4.5.1 Main acceleration region . . . . .	62
4.5.2 Near wall behavior . . . . .	65
4.5.3 Pole behavior . . . . .	71
<b>4.6 Conclusion</b> . . . . .	<b>75</b>

---

### 4.1 Erosion phenomenon in Hall thrusters

The goal of implementing the magnetic shielding topology is to reduce the erosion of the discharge channel. Before discussing the specifics of the magnetically shielded Hall thruster it is important to better understand what the erosion mechanisms are and how they are related to the rest of the thruster physics.

---

<sup>1</sup>Adapted from:

L. Grimaud and S. Mazouffre, "Ion behavior in low-power magnetically shielded and unshielded Hall thrusters," *Plasma Sources Sci. Technol.*, vol. 26, no. 5, p. 55020, Apr. 2017.

### 4.1.1 The mechanism of ion sputtering

#### Classical semi-empirical model

Surface erosion in plasma thrusters is due to energetic ions impacting and sputtering the wall material. Several processes are responsible for driving the ions toward to wall. These processes are detailed in section 4.1.2.

The sputtering process itself is poorly characterized for the materials and energy level of interest in Hall thrusters. Few data set exist for sputtering of BN-SiO<sub>2</sub> by particles with energy lower than the 200 to 300 eV range seen in HT. Data presented by Garnier et Al. and Kim et Al. are often used but offer low resolution in the critical 20 to 50 eV ion energy area [104,105]. They require extensive curve fitting to be exploitable. Yamamura and Tawara have developed a semi-empirical model popular for numerical simulations which introduces an erosion threshold [106]. This model is then often fitted to match thruster erosion rate measurement.

Yamamura and Tawara's model (see equations (4.1) (4.2) (4.3) and figure 4.1) depends both on the ion energy and incidence angle.

$$Y = Y_n \cdot Y_\theta \quad (4.1)$$

Where  $Y$  is the erosion rate in mm<sup>3</sup>/C and can be split into two factors:

$$Y_n(E) = \frac{AE^{0.474}}{1 + BE^{0.3}} \left(1 - \sqrt{\frac{E_{th}}{E}}\right)^{2.5} \quad (4.2)$$

and

$$Y_\theta = \cos(\theta)^{-F} \cdot e^G \quad (4.3)$$

$$F = -f \cdot \left(1 + 2.5 \frac{aE^{-0.5}}{1 + BE^{-0.5}}\right) \quad G = -\Sigma \cdot \left(\frac{1}{\cos \theta} - 1\right) \quad (4.4)$$

With  $Y_n$  the normal component of the erosion only depending on the ion energy and  $Y_\theta$  the angular correction factor depending on both ion energy and incidence angle.

The erosion rate at low energy is determined by the ill defined  $E_{th}$  erosion threshold. For  $E_{th} = 30$  eV in BN-SiO<sub>2</sub> we have  $A = 0.000320828$  mm<sup>3</sup>·C<sup>-1</sup>·eV<sup>-1</sup>,  $B = -0.139106$ . Finally  $f = 5.97563$ ,  $a = -3.63786$  and  $\Sigma = 1.41355$ . The angular ( $Y_\theta$ ) and energy ( $Y_n$ ) dependence function are shaped as seen in figure 4.1. Two phenomena are worth noting :

- The energy threshold, defined by  $E_{th}$  in equation (4.2), fixes the value under which erosion is negligible. The exact value of this threshold is not very well known but is usually taken between 20 and 50 eV [107,108].
- There is a strong angular dependence on the erosion rate with a maximum erosion rate for incidence angles close to 70 degrees for BN-SiO<sub>2</sub>.

#### Synergistic erosion

While the main contribution to the erosion is the ion bombardment, most of the energy deposited at the wall comes from the electron flux. Estimations of the total energy flux to the walls range from 5 kW/m<sup>2</sup> (measured by IR imagery [95]) to 20 kW/m<sup>2</sup> (PIC-hybrid simulation [96]) with more than 90% coming from the electrons. Sarrailh et al [109] argue that the electron flux is a non-negligible factor in the erosion of the ceramic walls. This is particularly acute in BN-SiO<sub>2</sub> were electrons at 10 to 25 eV can have enough energy to disturb the oxygen bonds. Measurements on the Saint Gobain's BN M26 (a type of BN-SiO<sub>2</sub> ceramic) show that the presence of an electron beam in addition to the ion beam can greatly increase the erosion rate.

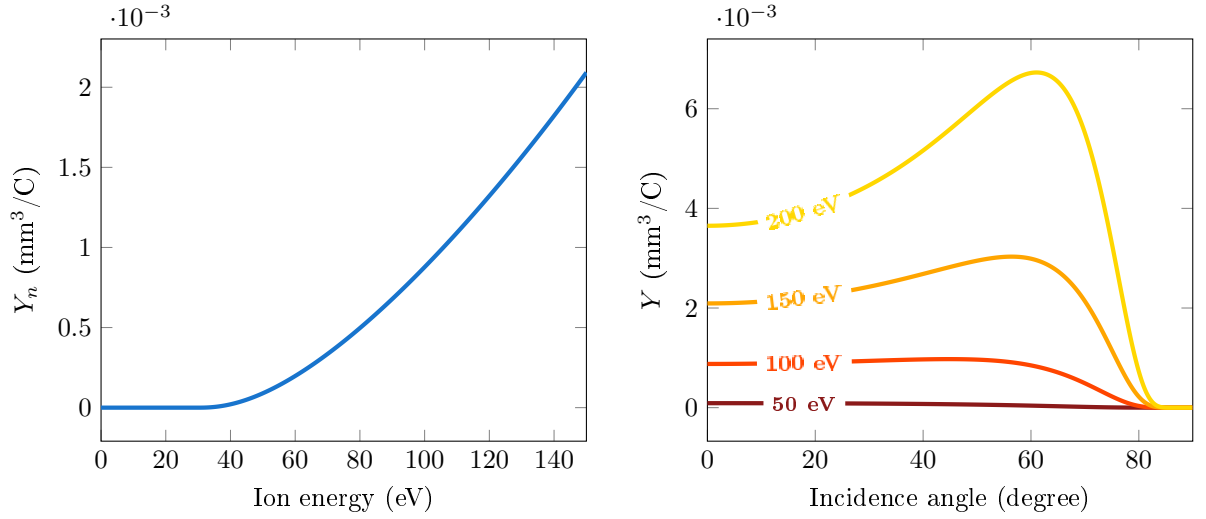


Figure 4.1: Normal energy dependence and total erosion as a function of energy and angle for BN-SiO<sub>2</sub>

### 4.1.2 Ion acceleration in Hall thruster

#### Main axial flow

The main acceleration mechanism for ions inside a Hall thruster is the (mostly) axial electric field. This electric field is located near the maximum magnetic field intensity and has an amplitude of several hundred volts per centimeters in typical operating conditions (see section 2.5.3 for examples). The acceleration region width is usually in the order of 10 mm and accelerates the ions up to an energy corresponding to about 90% of the discharge voltage.

This means that for a typical discharge voltage of 300 V the ions quickly reach a velocity corresponding to an energy of 270 eV which is well above the erosion threshold discussed in section 4.1.1. This electric field can be considered perpendicular to the magnetic field lines [110] and as such is mostly axial in a traditional Hall thruster.

#### Sheath behavior

The other principal acceleration mechanism for the ions is the plasma sheath near the dielectric walls of the discharge channel. For a simple sheath where all the electrons are captured by the surface the potential drop in the sheath is simply proportional to the electron temperature. Assuming a Maxwellian electron distribution function and ions with a Bohm velocity at the sheath edge we can write:

$$\phi_s = \frac{kT_e}{e} \ln \sqrt{\frac{M}{2 \cdot \pi m}} \quad (4.5)$$

With  $\phi_s$  the sheath potential drop,  $M$  the ion mass and  $m$  the electron mass. For xenon ions we get  $\phi_s = 5.27 \times \frac{kT_e}{e}$ , which means that for electron temperatures of 30 eV, as measured in standard Hall thrusters, the sheath could produce ions with a kinetic energy of 180 eV normal to the walls!

The reality is that the electrons are not just absorbed by the walls. Part of them are re-emitted and thus change the potential drop in the sheath. At equilibrium this secondary emission (SEE) can be space-charge limited. The full derivation done by Hobbs and Wesson [64] shows that the space-charge limits the ratio of re-emitted electron over incident electrons ( $\gamma$ ):

$$\gamma_{max} = 1 - 8.3 \left( \frac{m}{M} \right)^{\frac{1}{2}} \approx 0.983 \quad (4.6)$$

We can add the secondary emission effect to the sheath potential calculation [15, 64]:

$$\phi_s = \frac{kT_e}{e} \ln \left( \sqrt{\frac{M}{2 \cdot \pi m}} \cdot (1 - \gamma) \right) \quad (4.7)$$

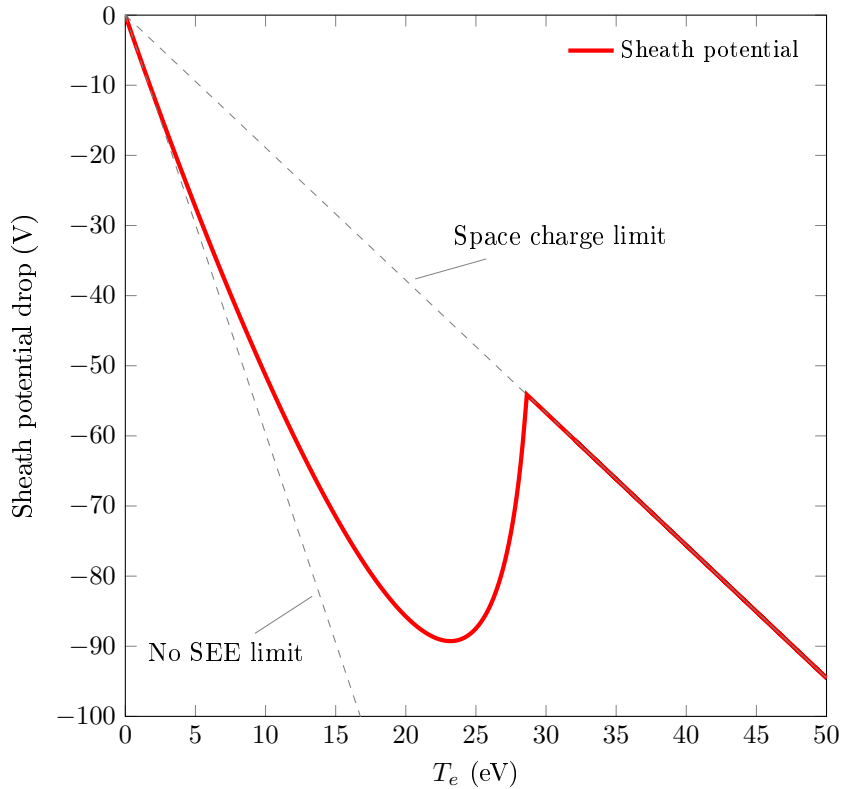


Figure 4.2: Sheath potential versus electron temperature at equilibrium on a BN-SiO<sub>2</sub> surface when secondary electron emissions are limited by the space-charge potential.

And thus the sheath potential drop (at equilibrium) should be at minimum:

$$\phi_s = -1.02 \frac{kT_e}{e} \quad (4.8)$$

Using a simple secondary emission model as in reference [15] we can calculate a more realistic sheath potential over the range of electron temperatures encountered in a typical Hall thruster. Figure 4.2 shows how the sheath potential is bounded between the case of no secondary electron emissions and the space charge limited regime. This considerably limits the energy of the sheath compared to a purely non-emissive sheath. However the potential difference observed can still reach more than the 50 V threshold required for boron nitride erosion. This sheath acceleration also compounds with the main axial electric field to produce fast gazing ions that have a higher chance to be in the 60 to 80 degrees incidence angle range, where the erosion is maximum.

In reality complex phenomena occur at the walls. These are generally grouped together under the term secondary electron emissions (SEE) but their dynamic is far more complex than a simple  $\gamma$  coefficient dependent on the electron temperature. In reality electrons colliding with the walls can have three types of behaviors:

- They can be simply reflected with the same energy.
- They can be backscattered after losing some of their energy into the material.
- They can be absorbed by the material and produce “true” secondary electrons. These electrons are expelled with low energy from the material and represent most of the electron population.

Since these 3 categories of emitted electrons are very different it is better to consider the total electron emission yield (TEEY) [111]. The relative importance of each population is strongly dependent on material, incident electron energy and incidence angle. The experimental data available for the relevant energy levels and materials is scarce.

Moreover the electron velocity distribution function in the thrusters is neither isotropic nor Maxwellian. The sheath is not at equilibrium and PIC simulations seems to suggest that reverse sheaths can form when the electron energy is high and drive the TEEY above one [112–114].

### Other secondary effects

The ions also have a small azimuthal drift velocity. The exact mechanism of acceleration is not totally known. Part of the velocity is due their large, but not totally negligible, Larmor radius [97]. Another factor is the low and high frequency azimuthal plasma oscillations in the discharge channel [1, 115]. As seen in figure 4.3 the most probable ion velocity can reach 1200 m/s which correspond to only 1 eV of energy. This drift velocity can thus be neglected when considering erosion mechanisms.

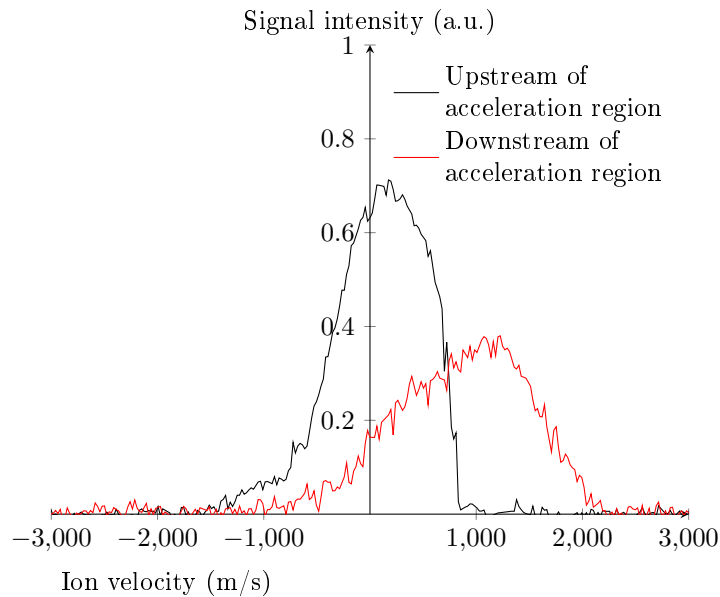


Figure 4.3: Azimuthal drift velocity of ions in a 200 W wall less thruster at 200 V discharge voltage [1].

### 4.1.3 Anomalous erosion

Erosion is not a straightforward linear process. The erosion rate changes with time. As a rule of thumb the average thickness change  $\delta$  follows the law [19]:

$$\delta = A \cdot (t)^{\frac{2}{3}} \quad (4.9)$$

With  $A$  the proportionality coefficient and  $t$  the total firing time.

Moreover most HT display “anomalous erosion”. This term refers to patterns appearing in the ceramic after several hundred hours of firing time. Figure 4.4 shows the characteristic striation pattern appearing on most thruster.

The exact origin of this pattern remains unknown. The spacing between each crests is close to the electron Larmor radius which tends to suggest that the phenomenon is related to electron behavior.

However as Morozov showed in reference [110], thanks to the angular dependency of the erosion rate, tiny regular patterns can be amplified by the erosion process. Figure 4.5 shows a simulation of the erosion process. This demonstration is done with an arbitrary fixed ion current and as such can be considered non dimensional. The initial conditions are set to be a surface with sinusoidal imperfections of 0.01 amplitude and a period of 2. The ion flux is set to come with a 60 degree incidence angle and 150 eV energy and the erosion rate angle dependency is calculated for BN-SiO<sub>2</sub> with equation (4.3). This small initial pattern is unstable under the ion bombardment and the peak to peak size of the features is amplified by more than 80 times.



Figure 4.4: Anomalous erosion as seen on the PPS-1350 thruster after 3500 hours of operation [2]

This demonstration shows that even if the electrons have a very small effect (perhaps due to the synergistic erosion effect discussed in section 4.1.1) the strong angular dependency of the erosion rate can amplify small periodic patterns.

Interestingly the apparition of the pattern slows down the erosion as the exposed surfaces face the ion flux at more favorable angles. This is illustrated in figure 4.6.

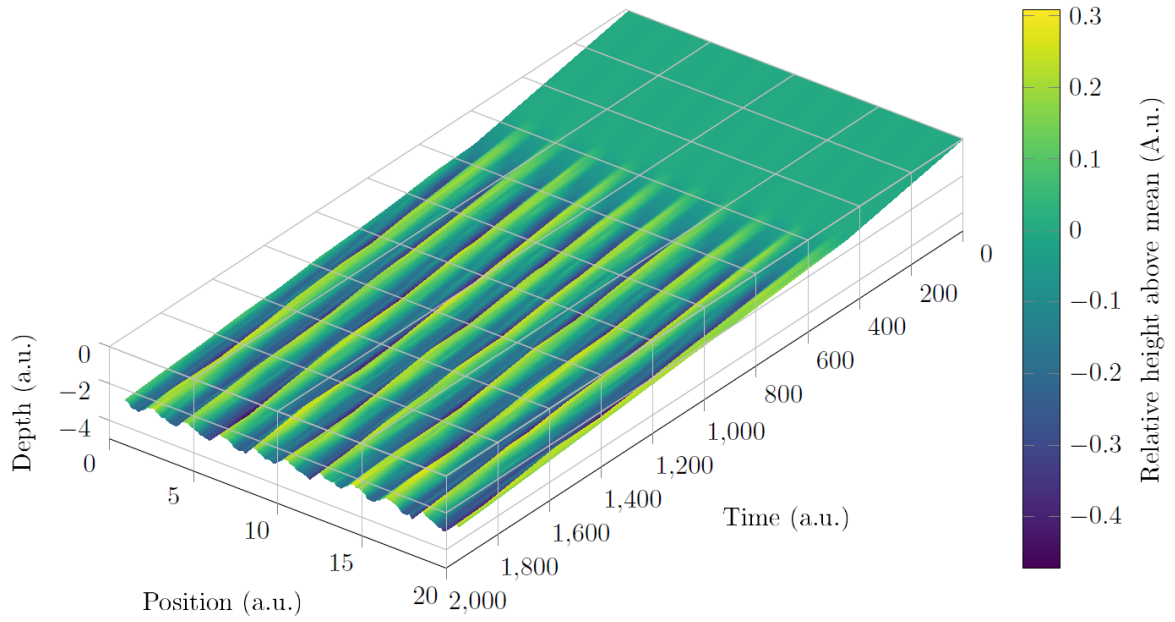


Figure 4.5: Apparition of the anomalous erosion on a surface with 0.01 amplitude periodic sinusoidal rugosity under an ion flow at 60 degrees incidence angle. The color correspond to deviation from mean height. The final feature has the same wavelegnth but amplitudes of 0.8.

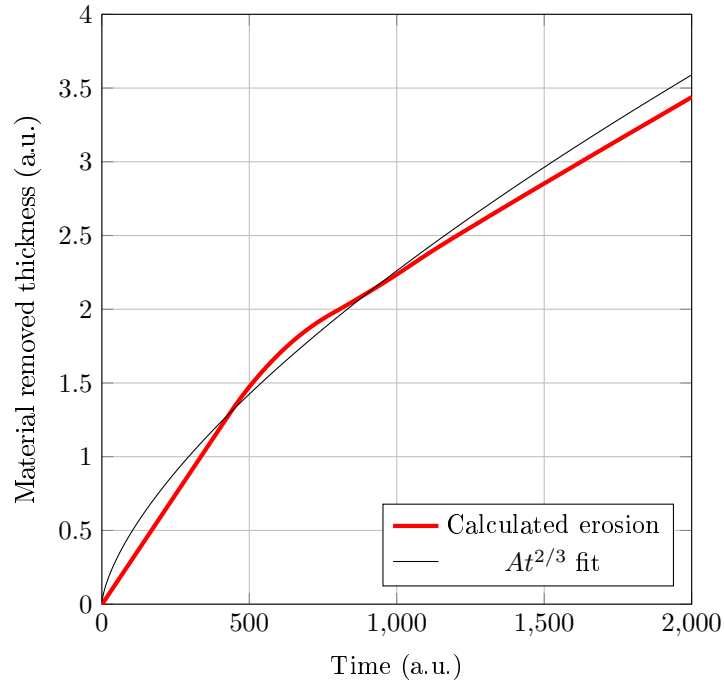


Figure 4.6: Average erosion rate calculated from simulation presented in figure 4.5

## 4.2 Overview of the magnetic shielding concept

### 4.2.1 Equipotentiality of the magnetic field lines

Electrons diffusivity through a magnetic field is much lower perpendicular to the magnetic field lines than along them. Disregarding the anomalous conductivity their ratio is in the order of the square of the electron Hall parameter (typical  $\Omega_e \geq 100$ ) [15]. The result is twofold. First the electron temperature does not varies much along the magnetic field lines and those lines can be considered isothermal. Second, the potential along those lines can be written as:

$$\Phi_{\parallel} = \Phi_T + \frac{kT_e}{e} \ln \frac{n_e}{n_0} \quad (4.10)$$

With  $\Phi_{\parallel}$  the plasma potential along the field line.  $\Phi_T$  is called the thermalized potential by Morozov [110] and is constant. As a result the electric field along the field lines is:

$$E_{\parallel} = \frac{kT_e}{e} \nabla_{\parallel} \ln n_e \quad (4.11)$$

This means that for moderate electron density changes and electron temperatures the electric field along the magnetic field lines is small. It is however not null and isopotential electric field lines do not perfectly align with the magnetic field lines. This difference is illustrated in figure 4.7.

### 4.2.2 Magnetic field topology

#### General shape

The general shape of the magnetic field in a magnetically shielded Hall thruster is shown in figure 4.7. In a classical thruster the field lines are mostly perpendicular to the walls. This means that the main axial electric field is tangent to the walls. There is also a region of hot (generally estimated at 30 eV and more) electrons in direct contact with the walls that creates a strong sheath. In a MS-HT one of the magnetic field lines is directed to be tangent to the walls and go from the magnetic pole area on the downstream face of the thruster to the anode area. This line is called the “grazing line”. This has several effects:

- The electric field is directed mostly away from the wall instead of being tangent to it. That reduces the flux of ions with high energy and high incidence angle impacting the surface.
- The cold electrons from the anode area can form a colder “protection” layer along the surface of the thruster and thus reduce the sheath potential. They also minimize the effects of the gradients of electron density and thus the magnitude of  $E_{\parallel}$  (see equation (4.11)).
- The hot electrons in the ionization and acceleration region are better confined to the center of the discharge channel.

The result is a topology that is designed to reduce the energy of the ions colliding with the walls and thus the erosion rate.

#### Magnetic circuit design

The creation of this grazing line is not a simple matter. While details on the method used in the ISCT200-MS cannot be shared publicly, the challenges of curving a magnetic field line in such a manner are readily apparent. Very high initial magnetic flux must be generated and a precise knowledge of both the magnetic flux source (coils or magnets) and the magnetic material properties is needed. This includes characteristics over the whole operating temperature range.

One way to achieve this kind of topology is to extend the “magnetic screens” often found between the coils and the discharge channel toward the exit plane of the thruster. This method was used by Conversano in the 300 W MaSMi-40 and the 500 W MaSMi-60 magnetically shielded Hall thrusters and his detailed in his patent [116].

The consequence of making this grazing line (at least in a small thruster) is that the maximum of the magnetic field is pushed downstream. In simulations no configuration combining both a true grazing

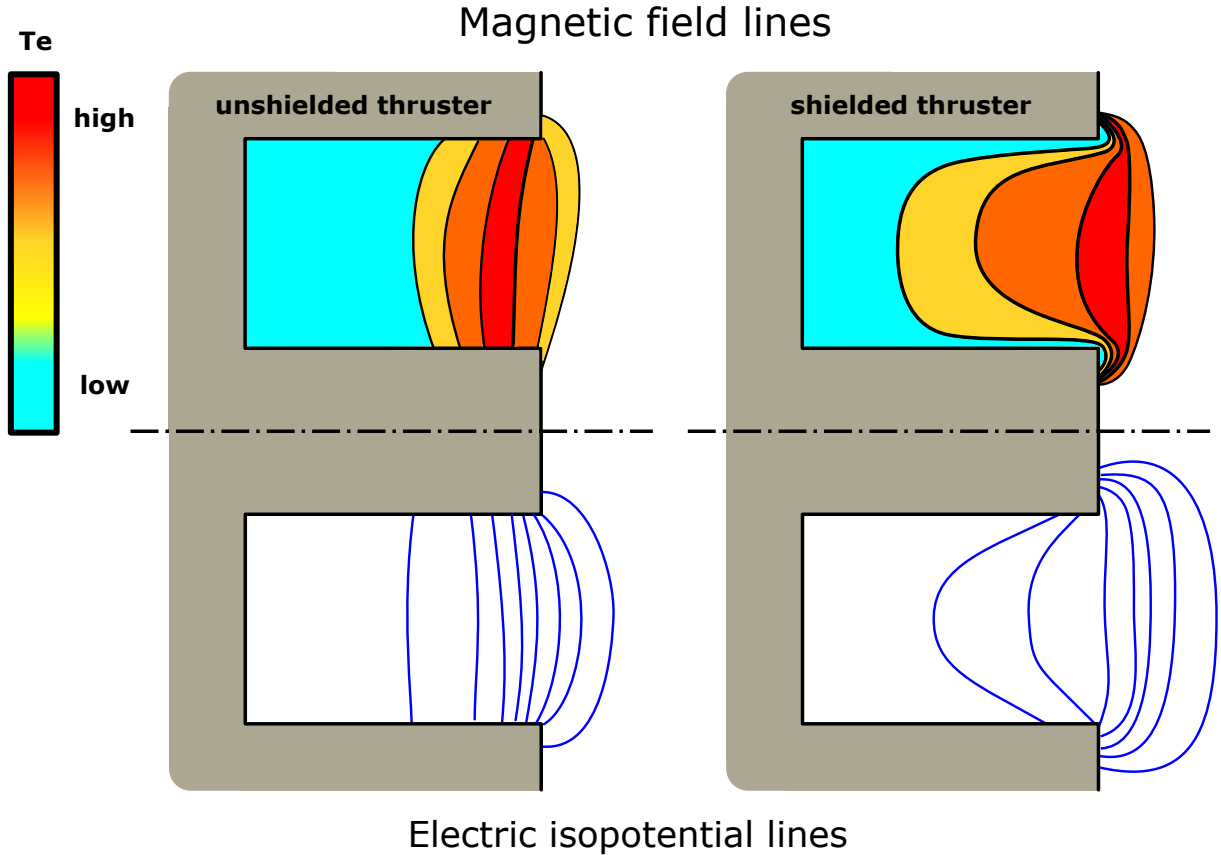


Figure 4.7: Schematic comparison between classical and magnetic shielding configurations. The black lines (top) represent the magnetic field lines and the blue lines (bottom) are the electric potential lines, colors illustrates the electron temperature.

line reaching all the way to the anode area and a maximum of the magnetic field inside the thruster were found. While data on the exact magnetic field topology is usually not available in the literature, it appear that the point of maximum radial magnetic field along the centerline of the discharge channel was also pushed downstream in the NASA-300MS compared to the NASA-300M [117]. We suspect that a configuration with a grazing line and an internal maximum is physically impossible without a magnetic flux source inside the discharge channel.

Finally the chamfering of the exit corner of the discharge channel wall can help the magnetic field lines conform to the wall shape. It is however not strictly required for magnetic shielding nor is it indicative of a magnetically shielded thruster.

### 4.2.3 Existing MS thrusters

The first documented evidence of magnetic shielding were found during lifetime testing of the BPT-4000 thruster [118]. After 6000 h of firing time erosion effectively stopped. This phenomenon was investigated by the Jet Propulsion Laboratory (JPL) and given the name “magnetic shielding” [119]. This was quickly followed by an extensive numerical and experimental work to modify the existing H6 laboratory thruster into a magnetically shielded one called the H6-MS [120–122]. This thruster was then subsequently tested with graphite conducting walls in 2013 [123].

Similarly NASA’s 20 kW NASA-300M thruster was modified into the NASA-300MS [117]. The experience gained on the H6-MS and the NASA-300MS was used to start development of a 12.5 kW magnetically shielded thruster named HERMeS [124, 125]. This thruster was originally designed for applications such as the now canceled Asteroid Redirect Robotic Mission (ARRM) [125]. It is being repurposed for the

solar electric propulsion module of the Lunar Orbital Platform-Gateway (LOP-G)

Around that time work was also started at JPL on lower power MS-HT. An initial 4 cm diameter thruster called the MaSMi-40 was built and tested [126]. Due to relatively poor performances and thermal issues [127] a 6 cm diameter HT called the MaSMi-60 was built [25,128]. Following more promising results on this slightly larger HT, development on the MaSMi-60 continued with the MaSMi-60-LM2 [129] and MaSMi-60-EM [130].

Another low power MS-HT is under development by the Busek corporation under the name BHT-100 [86]. It showed impressive performance for this discharge power but it is unclear if complete and efficient shielding was achieved. Collaboration between the Colorado State University and the Exoterra company seems to point toward the development of a small magnetically shielded thruster. Apart from a patent no information on this project is available [131].

Since the H6-MS was based around a modified unshielded H6 thruster. JPL, the Air Force Research Laboratory (AFRL) and the University of Michigan have decided to develop a dedicated 6 kW MS-HT called the H9 [132]. This new version solves some issues of saturation in the magnetic circuit of the H6-MS.

Development outside the United States have been limited. Some preliminary results were obtained by ICARE in 2014 by using the highly versatile PPS-Flex research Hall thruster [133]. Results on dedicated thrusters at ICARE are detailed in this document.

The SITAEL corporation and the university of Pisa also started studies on a prototype 5 kW flexible thruster capable of magnetic shielding. This new thruster is named the HT5k-M and is based on SITAEL's HT5k platform [134,135]. Moreover they have started to modify the 200 W classe HT100 thruster and have achieved partial shielding of the discharge channel [136].

Several Chinese research institutions report having built a 5 kW MS-HT but little information is available in English [82].

#### 4.2.4 Summary of existing results

While magnetic shielding is a relatively new development in plasma propulsion, over 60 articles and conference proceedings about magnetically shielded thrusters have been published since 2010. A detailed summary of each one of them will not be presented here. Additional details will be brought up in the relevant sections.

The first prime area of interest is of course the performance of MS-HTs. For the H6-MS and the NASA-300MS direct comparisons exist between a shielded and unshielded version [117,121,137,138]. In both cases the performances are strikingly similar. Thrust, specific impulse, power efficiency and divergence angle are within a couple percents between the US and MS thrusters. In general the MS-HT has slightly higher ISP and divergence for a given mass flow and discharge voltage.

The biggest difference is the content of the plume. While in a US thruster the singly charged ions represent more than 80% of the ion population, this proportion can be as low as 60% in a MS-HT. The result is a average charge per ion increasing from 1.1 to as much as 1.3 e. This increase is thought to come from a higher electron temperature more favorable to multiple ionization. This is probably caused by the smaller contact area between the hot electrons and the walls [121].

The thermal load on the thruster also seems to be reduced with as much as 100 °C lower temperature for the ceramic walls [117,121,139].

### 4.3 The ISCT200-MS magnetically shielded thruster

#### 4.3.1 The ISCT200-US baseline thruster

The ISCT200-US is a 200 W class, unshielded Hall thruster roughly 40 mm in diameter. The magnetic field is generated with permanent magnets and shaped through a pure iron magnetic circuit. The permanent magnet design allows us to place copper heat drains at strategic locations around the ceramic discharge channel.

The nominal discharge channel is in the 2S0 configuration (see section 3.2.1) and is made out of BN-SiO<sub>2</sub> M26. A slight chamfer is present at the exit of the thruster. The anode consist in a ring on the last few millimeter of the external wall. Gas is injected from the bottom of the discharge channel and is independent from the anode.

This thruster was built to test different magnetic topologies in order to increase ionization efficiency with xenon and krypton discharges [13]. However there has been no optimization done to increase performances once those have been measured. It was built on more than a 10 years of cumulative experience on low power Hall thruster with permanent magnets at Orleans [140].

This thruster is reliable and simple which makes it the ideal reference point for a comparative study between unshielded and shielded thrusters. The ISCT200-MS thruster is designed to copy this reference.

### 4.3.2 Geometry

The ISCT200-MS shares the exact same channel geometry as the ISCT200-US. In fact the ceramic channel parts are interchangeable between the two thrusters. The chamfered exit plane, while not strictly necessary helps accommodate the grazing lines. The gas injector and anode are also identical. The overall external dimensions are similar with a total thickness of about 4 cm and an external diameter of roughly 7 cm.

### 4.3.3 Magnetic field

Like the ISCT200-US the ISCT200-MS's magnetic field is created by permanent magnets. We use approximately one hundred identical small magnets in order to reduce manufacturing cost. Permanent magnets reduce the heat load created by joule heating of traditional coils. They are however sensitive to temperature change. The magnetic field in the thruster was simulated using the open source software FEMM [141] and great care was taken to take into account the effect of temperature on both the magnets and the magnetic circuit parts.

The use of magnets dispenses us from installing real magnetic screens as in the American thrusters [116]. This simplifies the thermal design of thruster. Curving the magnetic field lines to achieve the MS configuration requires about 30% more magnetic material than in the ISCT200-US to obtain the same field intensity.

In order to have the best comparison possible we chose to keep the same magnetic field amplitude and profile. As it can be seen in figure 4.8 this means having the same value of maximum magnetic field intensity at the center of the discharge channel as well as the same field intensity gradients. In order to achieve the grazing line the position of the maximum of the magnetic field must be pushed outside the thruster, downstream of the exit plane. Figure 4.8 also shows the magnetic flux intensity at the walls of the thruster.

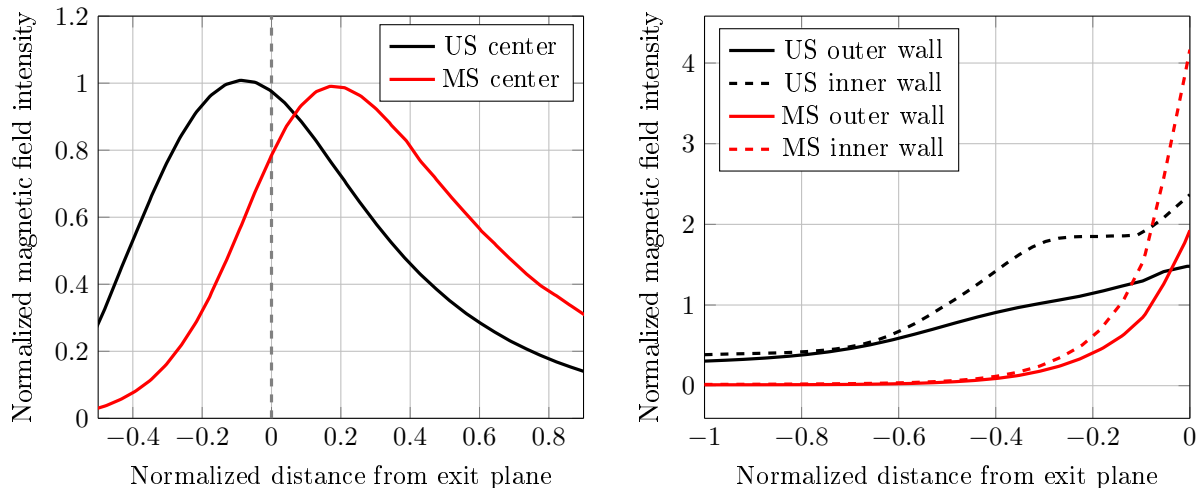


Figure 4.8: Normalized magnetic field profile at the center of the discharge channel and near the walls for the ISCT200-US and ISCT200-MS. The distances are normalized by the length of the discharge channel.

The magnetic field were measured for both thrusters at ambient temperature with a Hall effect probe. Despite the challenges associated with measuring in such a small volume measurements agree well with simulations.

## 4.4 Discharge characteristics

### 4.4.1 Discharge current

The average discharge current and its oscillations were first measured in the NExET test chamber for both thrusters. Figure 4.9 shows the characteristics for both thrusters.

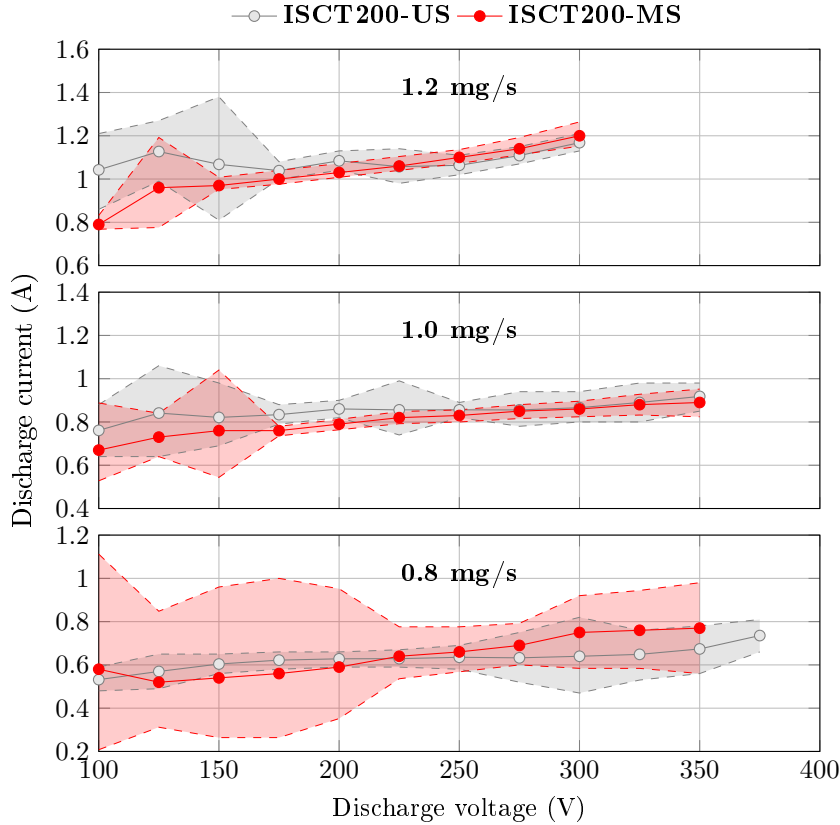


Figure 4.9: Discharge current for various mass flow for the ISCT200-MS and ISCT200-US. The filled in band contains 90% of the current trace.

At 1 and 1.2 mg/s and above 200 V there is little difference between the average discharge current of both case. The amplitude of the oscillations are also similar with only a very slightly more stable discharge in the MS case. Below 200 V the ISCT200-US exhibits a maximum of the discharge current around 125 to 150 V which is characteristic of thrusters operating with boron nitride [14]. This bump in current is mostly absent in the MS-HT. At 0.8 mg/s the MS-HT has a steeper I-V characteristic and is less stable than the standard thruster.

The frequency content for each operating point can be found in section 5.2.1.

### 4.4.2 Thermal behavior

The thermal behavior of the thrusters was investigated in a power band ranging from 110 to 220 W. To measure the temperature we used an Optris PI400 IR camera, observing from 7.5 to 13 microns with a resolution of 382x288 pixels, through a ZnSe viewing port. Figure 4.10 shows a comparison of the two thrusters general thermal behavior at the nominal 200 V 1 mg/s point. Those images are not corrected for local emissivity.

The issue with infrared imaging is that the computed temperature is highly dependent on the material emissivity. Through previous infrared studies of Hall thrusters [95] we have a good estimate of the emissivity of the BN-SiO<sub>2</sub> ceramic which allowed us to correct for it in figure 4.11. Metal surfaces such as the anode can have very different emissivity depending on the surface finish, oxidation level and view

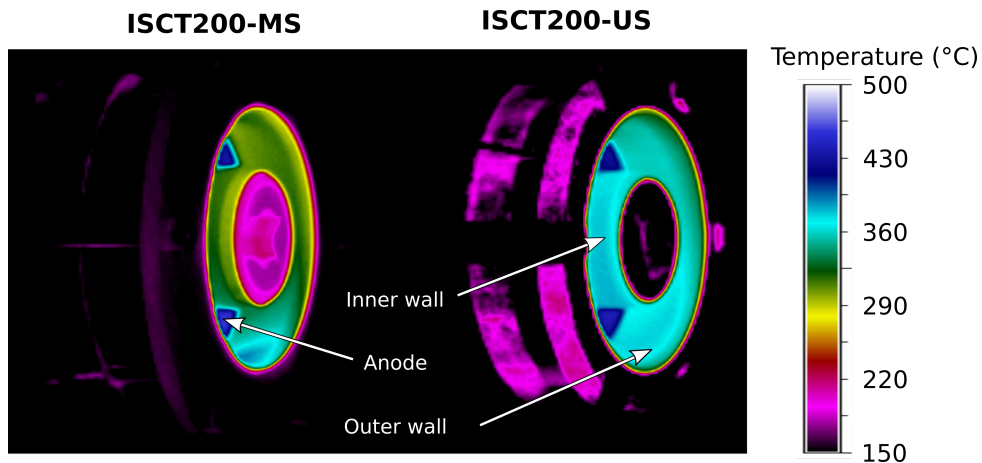


Figure 4.10: Comparison of the temperature measured by IR imaging at 200 V and 1 mg/s. The regions of interest are highlighted

angle. Absolute values of the anode temperature are thus not very precise but provide a good idea of the relative temperature difference between the two thrusters.

The wall temperature is measurably lower in the MS-HT with an internal wall temperature around  $60^{\circ}\text{C}$  colder and external wall temperature  $30^{\circ}\text{C}$  colder on average than on the /US. These surface measurements seem to show that there is less heat flux at the wall on the MS thruster. Anode temperature of the MS-HT is higher than for the US-HT (by about  $40^{\circ}\text{C}$  on average). Those results are in accordance with measurements on the H6 Hall thruster from JPL where lower temperature were seen on the walls near the exit of the discharge channel while the anode was hotter in the magnetically shielded version [142]. This could be explained by the presence of the grazing field lines collecting electrons near the walls and funneling them toward the anode. This would reduce the electron collisions with the wall (and thus the heating) while increasing the effective collection area of the anode.

It is unlikely that temperature has any effect on the erosion rate and can be used to explain the longer lifespan of MS-HT. While data on erosion yield dependence with temperature is scarce, the Moscow Aviation Institute (MIA) measured no major increase in the sputter yield of  $\text{BN-SiO}_2$  when the temperature stays below  $400^{\circ}\text{C}$  [143].

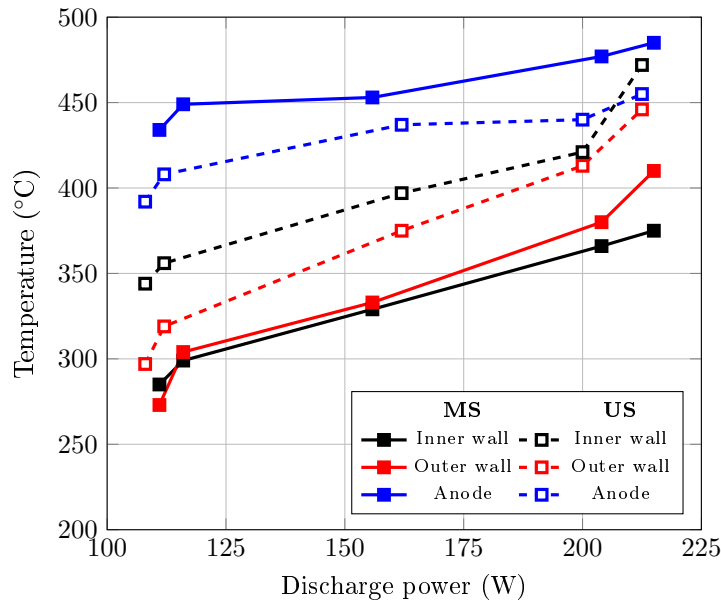


Figure 4.11: Temperature versus discharge power for the ISCT200-MS and ISCT200-US as measured by IR camera. Temperatures are averaged over the whole surface visible for each region of interest.

## 4.5 Ion behavior

### 4.5.1 Main acceleration region

The ion velocity distributions were first measured at different positions along the center of the discharge channel. Figure 4.12 shows the location of the probed points as well as the orientation of the laser with respect to the magnetic topology.

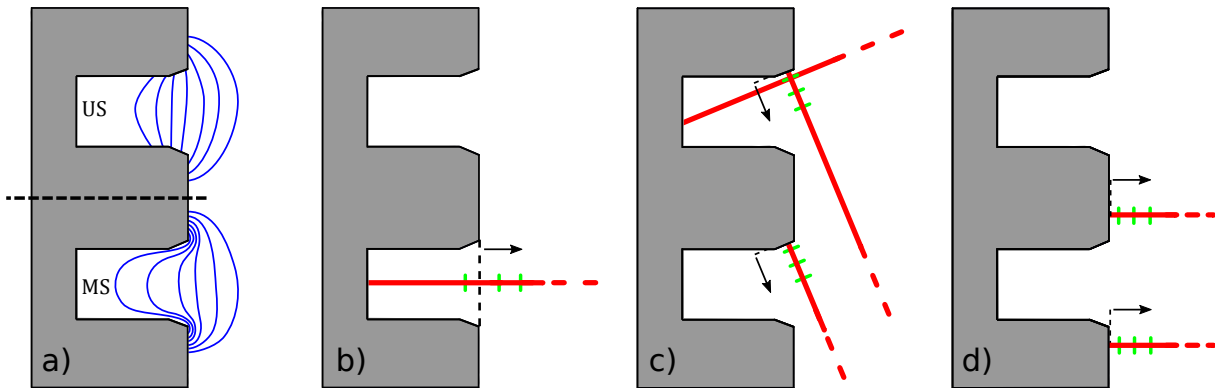


Figure 4.12: a) Magnetic field lines in an unshielded (top) and magnetic shielded thruster (bottom). Laser beam orientation for measurements b) along the center of the discharge channel, c) perpendicular to the inner and outer walls as well as parallel to the outer wall, d) perpendicular to the magnetic poles. The arrow represents the positive velocity direction

### Ion velocity distribution shape

Ion velocity distributions as well as ion mean and most probable velocities at the center of the discharge channel of classical unshielded thrusters have been extensively described in the literature [144,145]. A slow moving (few hundreds meter per seconds), thermalized ion group created several millimeters upstream of the exit plane is seen diffusing through the thruster. As it approaches the area of maximum magnetic

field the Maxwell distribution changes shape when part of the ions are accelerated and some more are created by the high energy electrons. After the high electric field region the majority of the ions is part of a main thermalized group which has a mean energy corresponding to the discharge potential drop. A trail of slower ions is also visible. The origin of those slower ions is not entirely clear but is suspected to be the result of ion/neutral collisions [146].

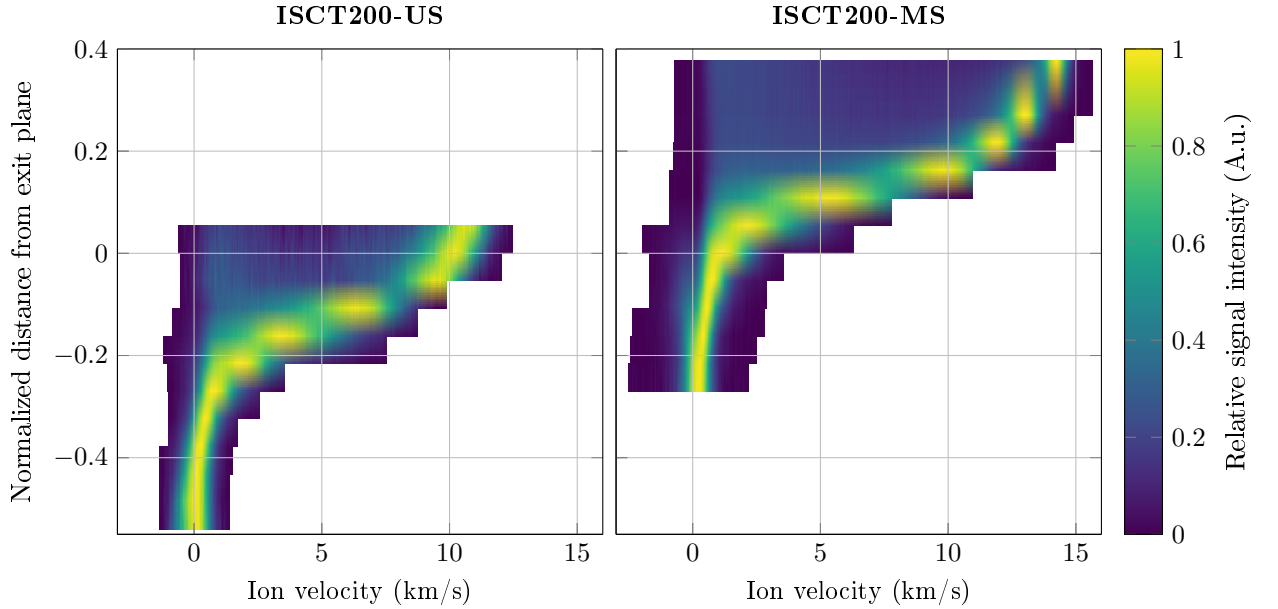


Figure 4.13: Normalized axial IVDFs along the center of the discharge channel

As illustrated in figure 4.13, the same three phases are observed for both US and MS thrusters. The positions are simply shifted downstream for the ISCT200-MS.

#### Axial electric field

The resulting plasma potential profiles and electric fields are plotted in figure 4.14. In the case of the magnetically shielded thruster the acceleration region is pushed outside the discharge channel. The maximum value of the electric field is higher but the final most probable velocity of the ions is very similar in the far plume of both thrusters (not displayed in figure 4.13). We measured 14.5 km/s for the US-HT and 14.7 km/s for the MS-HT at 200 V. The acceleration region is narrower in the ISCT200-MS.

As with US-HT the position of the maximum of the electric field in the MS-HT is located at the maximum of the magnetic field.

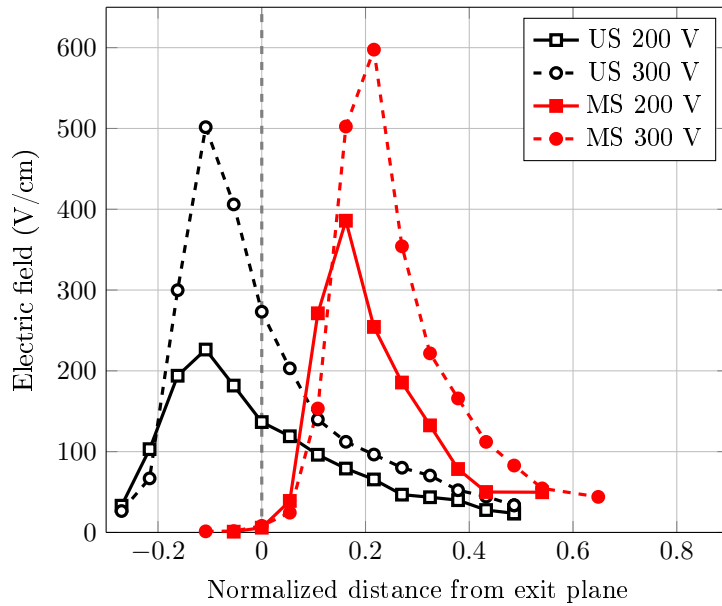


Figure 4.14: Electric field along the center of the discharge channel

### Ion density

It is possible to extract the relative ion density from the IVDF. If the laser wavelength is swept over a large enough range, the integral of the IVDF should capture all the velocity groups and be proportional to the density of the metastable ions. Getting the ground state ion density from this data require assuming that the proportion of metastable ions to ground state ions is constant. Then the integral of the IVDF over the can be considered proportional to the ion density. Note that this assumption is far reaching as the proportion of metastable to ground state ions is highly dependent on the pressure, electron density and electron temperature. Absolute values of the ion density would require very careful calibration against a known source and was not done in this work. It is however possible to get an idea of the relative density at different points for a given test run.

Figure 4.15 compares the normalized metastable density profiles in both thrusters. While the absolute density is not known it is not unreasonable to assume that the maximum ion density measured in the MS-HT is either equivalent or even lower (due to being outside the confines of the channel) than in the US-HT. This assumption is supported by how close the discharge characteristics are for those settings. With this assumption the ion density in the discharge channel of the shielded thruster is at least an order of magnitude lower than in a classical one. This alone should contribute to greatly reducing the wall sputtering.

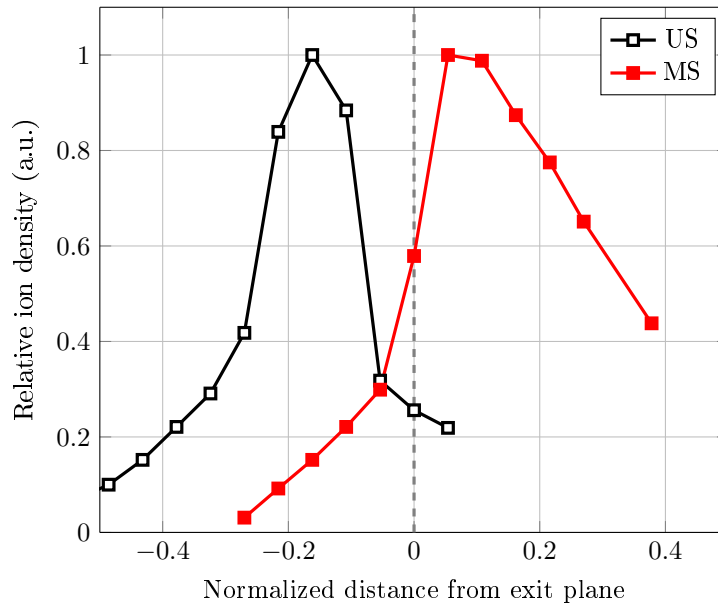


Figure 4.15: Comparison of relative metastable ion density profiles in US and MS Hall thrusters along the center of the discharge channel at 200 V discharge voltage. The profiles are normalized by their respective maximum value.

### Consequences on erosion

The downstream shift in the position of the ionization and acceleration contributes to the low observed erosion of the magnetically shielded thrusters. While a lot of attention has been dedicated to the behavior of the ions near the walls and to the influence of the “grazing line”, the bulk behavior should not be ignored. Not only the ion density is lower in the MS-HT but their bulk axial velocity at the exit plane is also considerably lower as they are mostly accelerated outside of the discharge channel. This reduces both the flux and mean energy of the ions density inside the thruster.

## 4.5.2 Near wall behavior

### Visual evidences of magnetic shielding

Direct measurements of the erosion rates require expensive and lengthy endurance testing followed by profilometry measurements which were not available to us. However several visual clues can provide good evidences of the low erosion behavior of the ISCT200-MS.

The most obvious evidence is presented in figure 4.16. During firing, sputtering of the vacuum vessel walls occurs. In order to protect sensitive equipment such as cryo-pumps heads, graphite baffles are placed in front of the thruster. The sputtered graphite particles coat the inside of the chamber and the thruster itself with a thin black layer. In an unshielded thruster, this layer is eroded away in the high erosion area near the exit plane. This produces a characteristic white erosion band on the ceramic wall. In the case of the ISCT200-MS the ceramics walls appear uniformly black, which means that the erosion rate has been reduced to below the deposition rate. Data from other vacuum chamber show that the deposition rate is at least a couple orders of magnitude lower than the erosion rate in classical thrusters. This points toward a greatly reduced erosion rate in the ISCT200-MS [147, 148].

Additionally, in kilowatt class MS-HT a clear separation appears between the plasma and walls [34, 133]. This effect was not as obvious when operating the ISCT200-MS but a small gap in the plasma allowed us a view all the way to the anode area (see figure 4.17). This gap was more pronounced near the inner pole [3].



Figure 4.16: Ceramic walls of the ISCT200-US (left) and ISCT200-MS (right) highlighting, for the MS case, the absence of the characteristic erosion pattern in the black deposit formed on the walls.

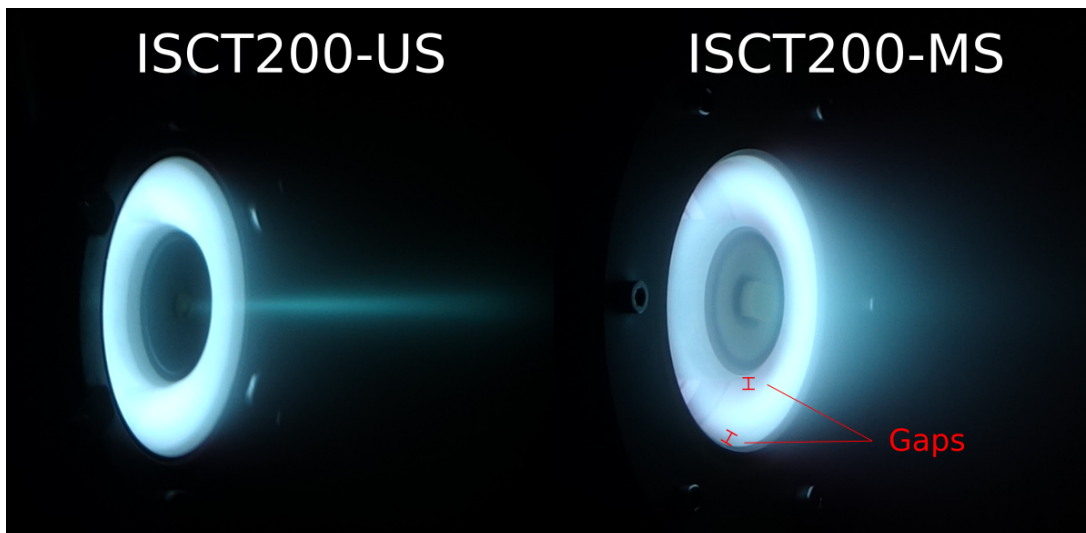


Figure 4.17: Picture highlighting the gap between the plasma and the walls in the magnetically shielded thruster.

### Ion velocity distributions

To measure the ion behavior near the inner and outer walls we took advantage of the beveled edge at the exit of the discharge channel. This bevel is present on both thruster and was initially designed for the ISCT200-US without consideration for the MS configuration. As it can be seen on figure 4.12 c) the bevel allows direct measurement of the IVDF normal to the walls. This area shows clear marks of erosion in the unshielded thruster but none in the shielded one (see figure 4.16).

The IVDF along the axis perpendicular to both the inner (figure 4.18) and outer (figure 4.19) walls are measured. For better visibility each plot has been normalized by the maximum value of the IVDFs for each measurement case. The relative amplitude of the IVDFs can not be compared between shielded and unshielded with those plots. The IVDFs show a clear difference in the bulk ion velocity. The majority of the ions in the US-HT have negative velocity near the walls (i.e. go toward the walls), while they have mostly positive velocities in the MS-HT. The LIF intensity signal, which can be assumed to be proportional to the ion density, is also seen to be sharply decreasing as we approach the wall of the ISCT200-MS while it remains fairly constant in the ISCT200-US. Finally the IVDFs in the unshielded thruster are a lot wider than in the shielded one.

The distribution functions for the ISCT200-MS are roughly gaussians, pointing toward a single population of ions originating from the same place in the thruster. Some of the IVDF in the unshielded thruster, particularly on the external wall and further from the walls, show a double peak structure. Such structure can appear when plasma density is so high that the laser is attenuated. Tests consisting in changing the plasma density (by varying the xenon mass flow) and laser intensity rule out the possibility of total laser absorption attenuating the most intense part of the IVDF.

This means that two populations of ions are observed there. The fainter, higher velocity group is difficult to explain. A possibility is that they are actually fast ions accelerated by the main axial electric field, with their IVDF projected on the slightly oblique laser axis. To be normal to the bevel the laser axis is at a 27 degree angle relative to the radial direction. At the center of the discharge channel ions reach an axial velocity of 10 km/s. On our oblique measurement axis this would translate to a observed velocity of about 4.5 km/s which is very close to what is measured at 2 mm from the bevel. The slower population must thus be created locally. Similar IVDFs have been observed near the walls of the H6 thruster [144].

In order to gather more information about the real two dimensional shape of the IVDFs, the same points as in figure 4.19 were investigated with the laser parallel to the surface. This method only provides us a second projection of the real two dimensional (ie 2V) velocity distribution. A complete picture of the 2D structure would require optical tomography [149]. Results for the velocity parallel to the external wall bevel are presented in figure 4.20. Geometric constraints made the same measurements on the internal wall impossible with our setup. Once again two ions groups are apparent in the ISCT200-US. A trail of high velocity ions is visible for both thrusters.

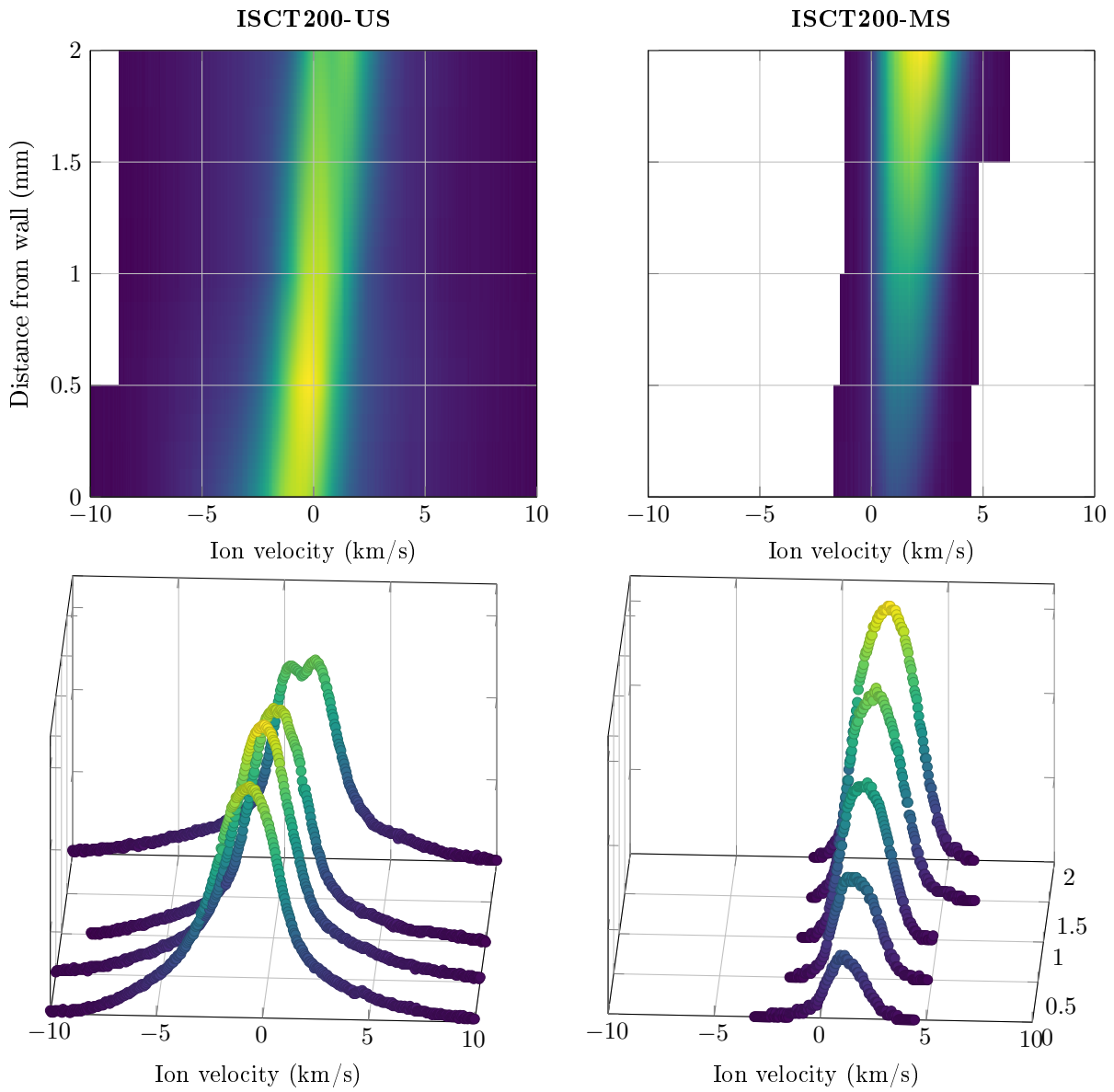


Figure 4.18: IVDF perpendicular to the internal wall. Negative velocities indicate ions moving toward the wall.

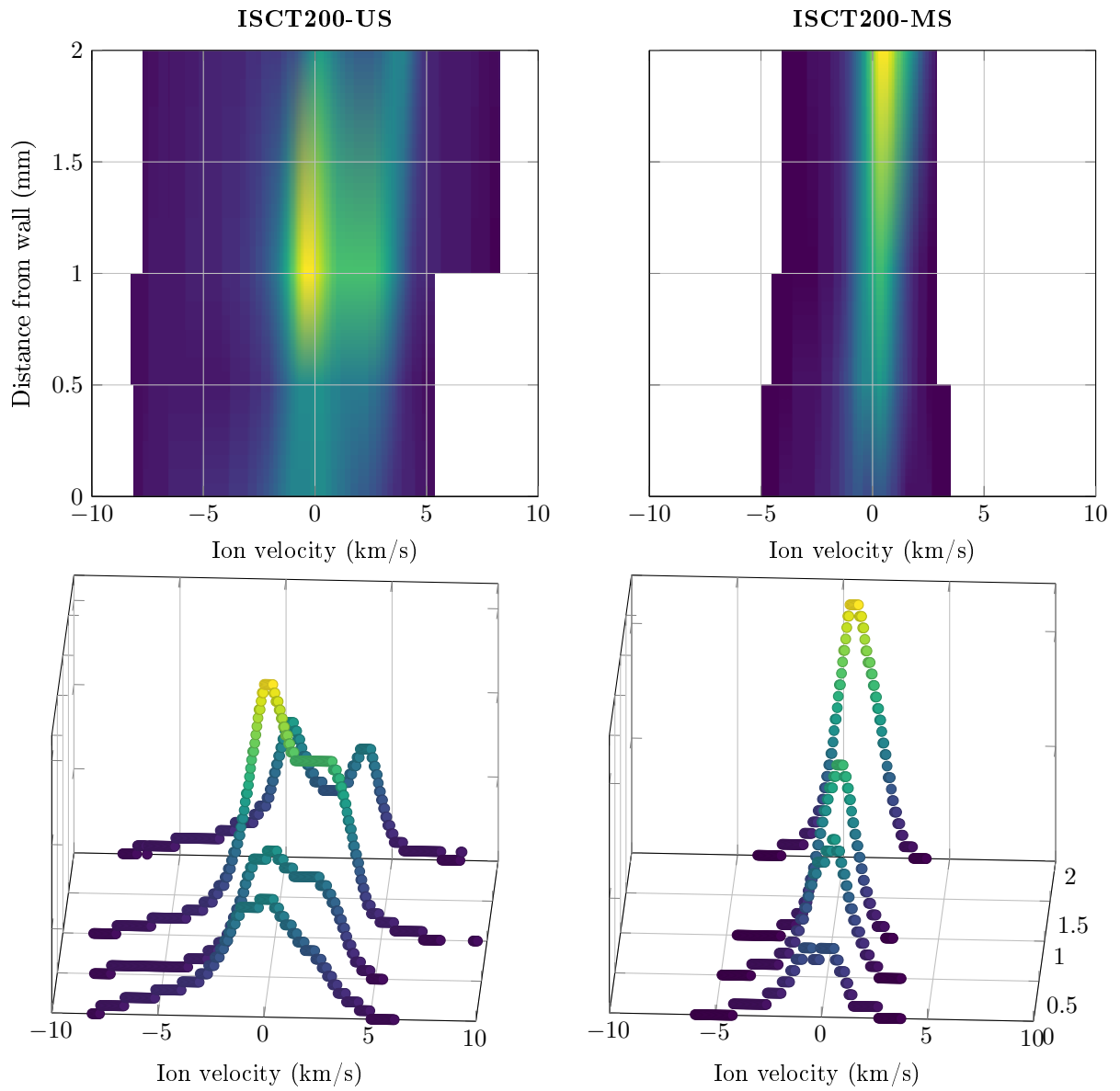


Figure 4.19: IVDF perpendicular to the external wall. Negative velocities indicate ions moving toward the wall.

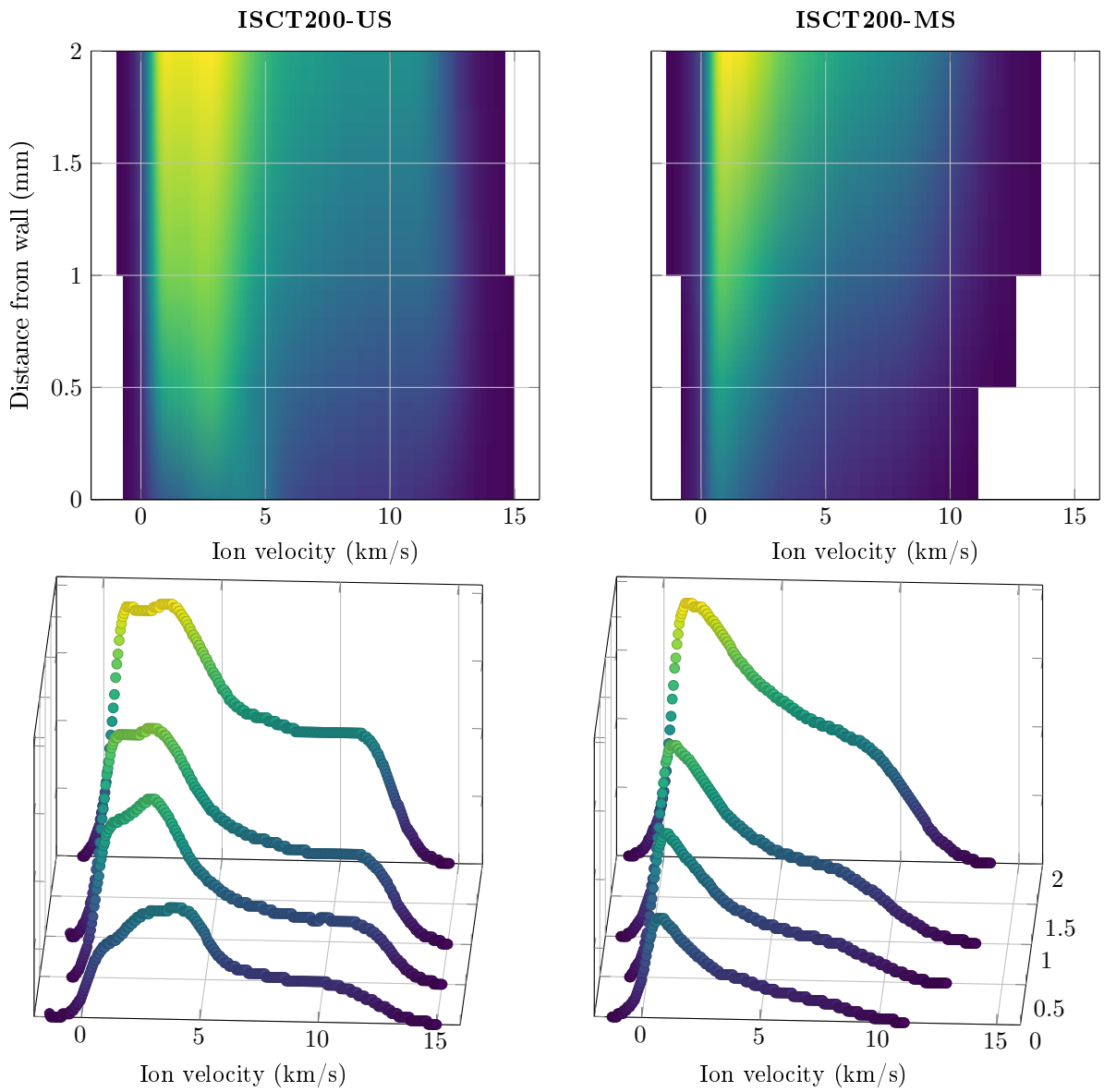


Figure 4.20: IVDF parallel to the external wall. Negative velocities indicate ions moving toward the anode.

### Ion flux at the walls

From the parallel and perpendicular measurement it is possible to compute both the normal incident velocity and relative ion density. However the two projection axis are not enough to extract the incidence angle of the different populations of ions.

The density is computed by assuming that the ratio of the probed metastable ions to ground state ions is constant and the same for both thrusters. Integrating the density functions then give a relative idea of the number of ions present in the probed volume. Great care was taken to ensure that the optical system remains the same when the thrusters are switched. However both collection and laser branch were moved between acquisitions on the internal and external wall. As a result the relative density values can not be compared between those two positions.

Table 4.1 shows a direct comparison between the results obtained for both thrusters with the IVDF at the wall surface and perpendicular to it.

Table 4.1: Ion density and flux at the walls

Case	$n_i$ (a. u.)	$\eta_{v-}$	$\eta_{<-30eV}$
ISCT200-US (inner wall)	723	0.63	0.022
ISCT200-MS (inner wall)	38	0.11	0
ISCT200-US (outer wall)	77	0.54	0.015
ISCT200-MS (outer wall)	19	0.62	0

The relative ion density at the wall ( $n_i$ ) is a lot lower in the MS-HT than in the US-HT (5% of the maximum measures for the inner wall, 25% for the outer wall). This matches visual observations as the plasma in shielded thrusters appears separated from the walls (see figure 4.17). More particularly in the ISCT200-MS the separation is more obvious for the inner wall than for the outer one.

In table 4.1 we also define two other important numbers. The first is  $\eta_{v-}$ , the proportion of ion observed going toward the wall. Those ions are the one that should impact the wall and can contribute to the erosion. The second figure is  $\eta_{<-30eV}$ , the fraction of ion with an energy superior to 30 eV (around 6.6 km/s for  $Xe^+$ ) going toward the walls. The 30 eV threshold is chosen because it is the minimum energy ions need to have any significant erosion effect. It is worth noting that this number doesn't capture all the ions with a total energy higher than 30 eV. For example an ion with an incidence angle of 70 degrees and a kinetic energy of 40 eV would only appear on figure 4.18 and 4.19 to have a velocity perpendicular to the walls corresponding to 13.7 eV. Considering the long tails of high velocity ions seen on figure 4.20, such population of ion must be non-negligible.

Nonetheless, there is only 11% of the ions near inner wall of the MS-HT that have negative velocity (i.e. are going toward the wall). In all other cases the proportion is closer to 60%. There was no ion detected with an energy greater than 30 eV for the magnetic shielding case. However we detected a clear fluorescence signal of a small portion of ion with high incoming velocity in the US-HT.

In summary there is both less ions near the walls, and fewer ones with high incoming energy, in the magnetically shielded thruster compared to an equivalent unshielded one.

### 4.5.3 Pole behavior

#### Visual evidences of pole erosion

Magnetic pole erosion has been identified as one of the possible failure points in MS-HT. While no erosion is visible in the discharge channel of the H6-MS some marking was observed on top of the magnetic poles after 150 hours of firing [150,151]. The eroded areas correspond to the top of the magnetic coils where the magnetic field lines are terminated. Measurements of the erosion rate on the poles have shown that some erosion is present (in the order of 0.1  $\mu\text{m/hr}$ ) but this erosion rate is two orders of magnitude smaller than the one seen on the walls of US-HT.

In order to observe this pole erosion, alumina "caps" were fitted over the top of the magnetic poles of the ISCT200-MS. Those caps are 1 mm thick. Figure 4.21 shows the erosion bands seen on the caps after 20 hours of firing. Those erosion bands correspond to the top of the magnetic circuit. They are about the same width as the top pole piece.

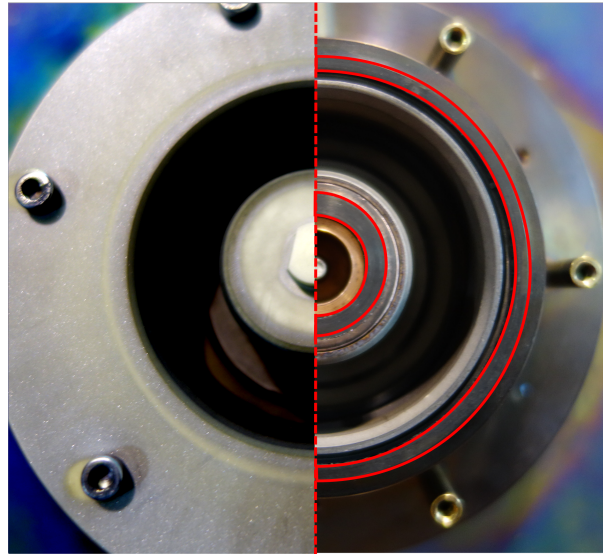


Figure 4.21: Evidence of erosion above the ceramic caps (left). On the right is a front view of the ISCT200-MS without the caps. The top of the magnetic circuit is highlighted in red [3].

It is worth noting that erosion on the magnetic poles especially on the internal one, is regularly observed in US-HT too. In most Hall thruster the metal parts covering the internal pole exhibits a characteristic surface finish associated with sputtered metal. However, poles erosion is not a failure mode encountered in US-HT as wall erosion is dominating.

#### Ion and neutral velocity distribution near the poles

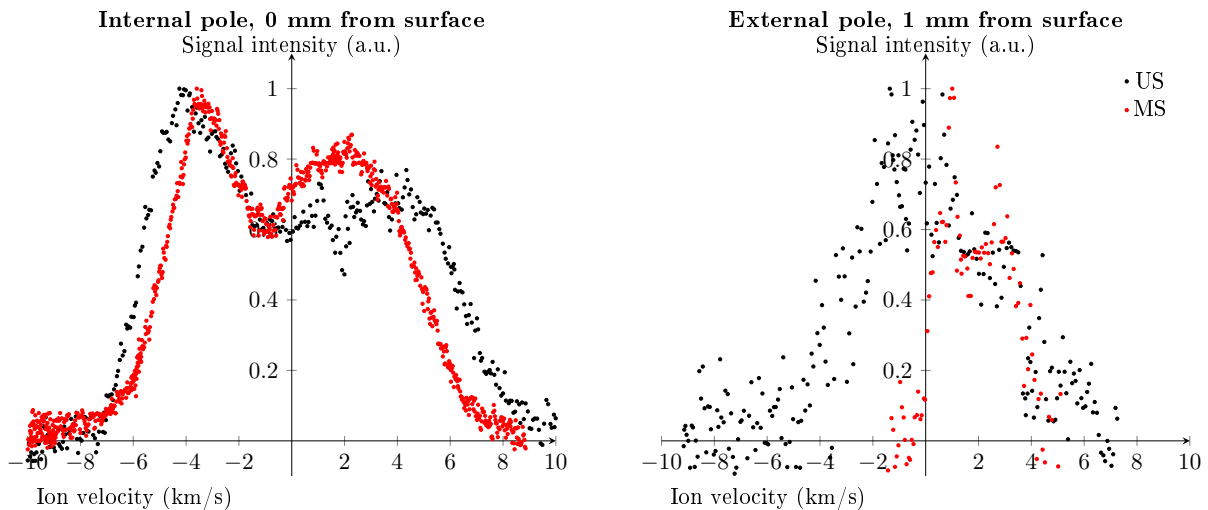


Figure 4.22: Worst signal to noise ratio for normalized IVDFs above the internal and external magnetic poles

To investigate this erosion zones we performed IVDF measurements at the radius corresponding to the center of the internal and external erosion bands (figure 4.12 d). The plasma density in these area is low. This translates to a lower signal to noise ratio that can make data interpretation complicated [40]. With our small thruster and a 51 mm diameter collection lens we were able to get close to the point of interest and collect fluorescence light over a large solid angle. Figure 4.22 shows the signal quality obtained at the most noisy positions on both the external and internal walls. While excellent signal to noise ratio is achieved all the way to the surface of the internal pole, it was impossible to find any significant signal

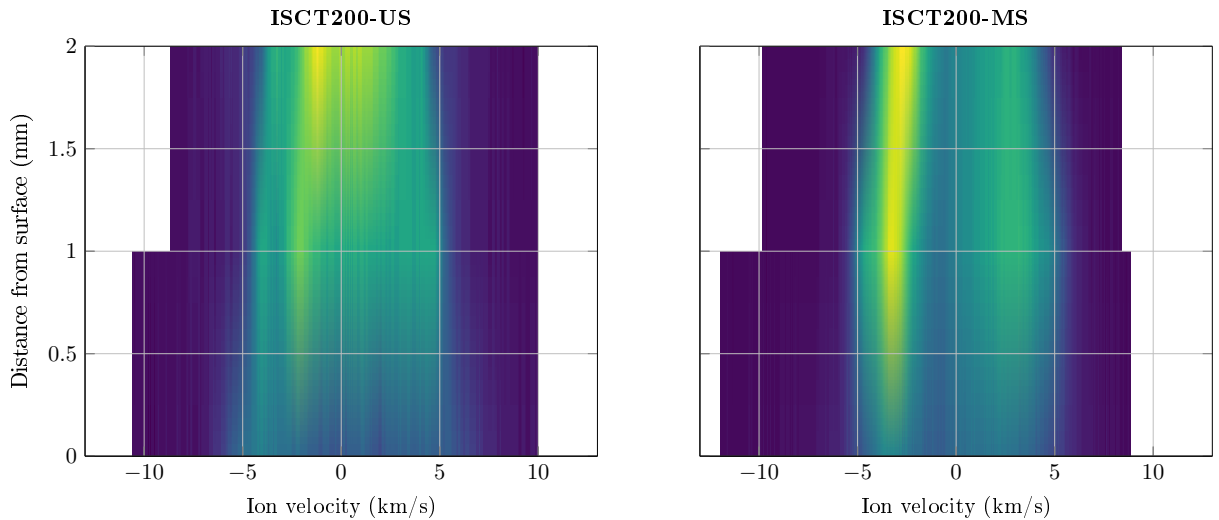


Figure 4.23: IVDF perpendicular to the inner magnetic pole

less than a millimeter away from the external pole. Due to the poor signal to noise ratio near the outer pole, only the results of the inner pole will be presented here.

Figure 4.23 shows the IVDFs above the inner magnetic pole of the US and MS thrusters. At first glance the IVDFs are shaped similarly. A main ion group is observed coming toward the walls with a normal velocity around 4 to 5 km/s. Another lower density group with the opposite velocity is also seen. Those two groups seem to slow down the further they are from the surface. This might explain the single thermalized group observed at JPL by Jorns [40]. A faint fast group of ions coming toward the wall is also seen in the unshielded ISCT200-US.

The existence of a group of ions with velocities away from the pole surface this close to it made us suspicious of spurious effects caused by measuring close to the surface. We checked if the symmetry in the IVDF was due to a ghost image caused by reflection of the laser on the pole surface. Figure 4.24 presents the IVDF 2 mm above the internal pole of the shielded thruster with a laser normal to the surface and one canted 20 degrees off axis. With this angle the specular reflection of the laser does not intercept the measurement volume. We found that the positive velocity group is still present and has the same amplitude. While effort were made to limit these effects it could still be the result of a diffuse reflection. Other ways to be able to probe that area without any reflections would require extensive modification of the thrusters. One solution is to have a hole going straight through the inner pole such that the laser could be injected from the back.

Another possibility we considered is that this population is actually ions that have had an elastic collision with the pole. However most ions colliding with the wall should be neutralized. The fast ions would then need to have been produced (and excited into a metastable state) from these neutrals on a distance less than a millimeter long. To investigate this possibility we looked for fast neutrals resulting from ions bouncing on the surface and being neutralized. The metastable state was probed at the 823 nm. Figure 4.25 shows the neutral velocity density function (NVDF) 1 mm above the inner pole of the MS-HT. There is no evidence of any group of neutrals in the +3 to +4 km/s range.

Neither laser reflection nor ion elastic collisions can satisfyingly explain this symmetric double peak structure. The magnetic field isn't strong enough to have any magnetic mirroring effect on the ions. One possible explanation could come from an inverted sheath caused by strong secondary electron emission. Such inverted sheath has been observed in simulation in the high electron temperature areas inside Hall thrusters [112]. This inverted sheath could reflect some ions back downstream. However inverted sheaths are associated with high electron temperatures ( $> 30$  eV). Such high energy electrons could be present above the poles in MS-HT but not in US-HT (see figure 4.7). This structure was present both on the stainless steel pole piece and the alumina one.

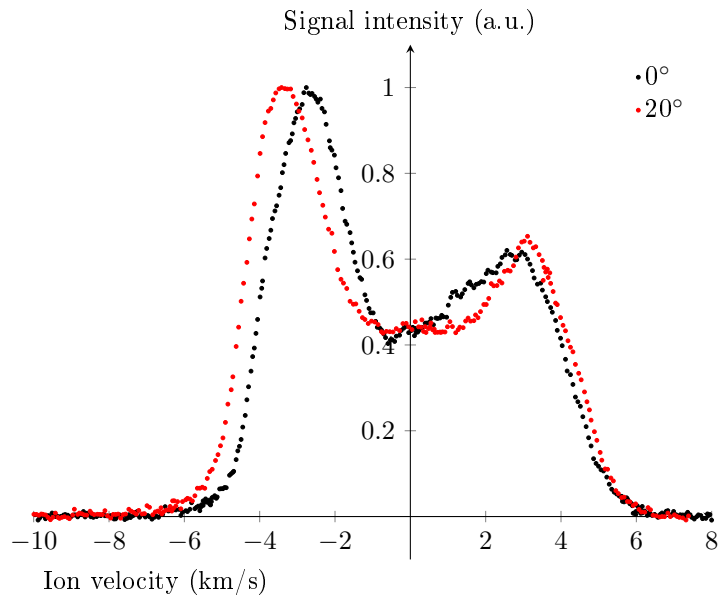


Figure 4.24: IVDF 2 mm above the internal pole of the ISCT200-MS with the laser firing along the thruster axis ( $0^\circ$ ) and off-axis ( $20^\circ$ )

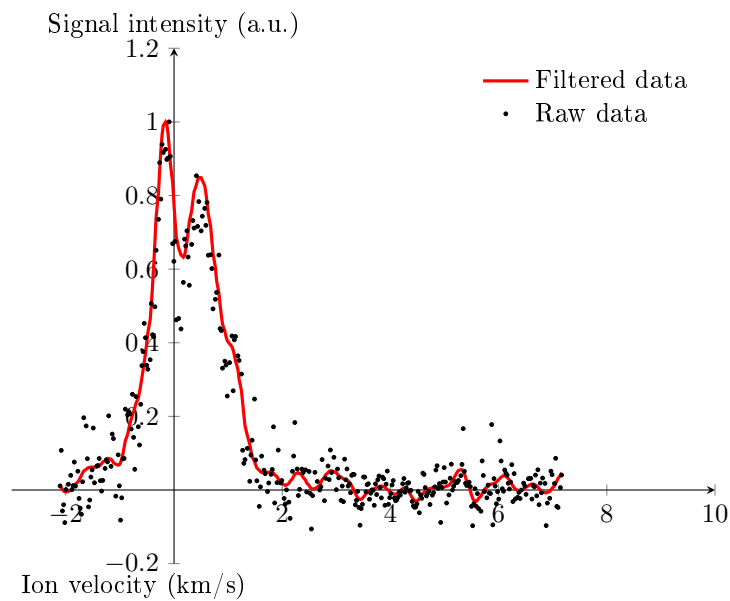


Figure 4.25: NVDF 1 mm above the internal pole of the ISCT200-MS

## 4.6 Conclusion

The data presented here shows that efficient shielding has been achieved in the ISCT200-MS thruster. This shielding has been achieved without dramatically altering its discharge characteristics or its stability.

Our results show multiple effects of the magnetic shielding configuration on the ion behavior that helps us to understand the reduction in erosion observed. The non-intrusive LIF spectroscopy measurements have confirmed that, in a magnetically shielded Hall thruster, the electric field is located outside the discharge channel. As a consequence, the plasma potential inside the channel is nearly constant and most of the ionization happens outside the thruster itself. This contributes to both a lower ion density and lower ion energy inside the thruster.

A small population of ions with a high velocity normal to the walls is observed in the unshielded thruster. This population could be the cause of the channel walls erosion. In the shielded thruster, this population is not detected. The bulk ion velocity is also pointing away from the walls. Furthermore, the ion density sharply decreases as it gets closer to the walls.

Finally, measurements above the magnetic poles yield IVDF normal to the surface with a symmetric “double peak” structure for both US and MS thrusters. This peculiar structure does not seem to be explainable by laser reflection nor elastic collision effects with the thruster surface. Both thrusters have a similarly shaped IVDF in this area. There is no evidence of any phenomenon that would increase pole erosion in a magnetically shielded thruster compared to a standard thruster.

## 4.6. CONCLUSION

---

# Chapter 5

## Performance of a magnetically shielded Hall thruster with graphite and ceramic walls<sup>1</sup>

### Contents

---

<b>5.1</b>	<b>Alternative wall material for Hall thrusters . . . . .</b>	<b>77</b>
5.1.1	Previous work on alternative material for Hall thrusters . . . . .	77
5.1.2	Implementation on the ISCT200-MS and ISCT200-US . . . . .	78
<b>5.2</b>	<b>Performance . . . . .</b>	<b>79</b>
5.2.1	Discharge current . . . . .	79
5.2.2	Electric field distribution . . . . .	83
5.2.3	Plume . . . . .	83
5.2.4	Thrust, specific impulse and efficiency . . . . .	85
<b>5.3</b>	<b>Discussion on the performance of the magnetically shielded thruster . . .</b>	<b>89</b>
5.3.1	Multiple ionization . . . . .	89
5.3.2	Effective ionization surface . . . . .	90
5.3.3	Magnetic topology . . . . .	91
5.3.4	Wall materials and Hall thruster physics . . . . .	92
5.3.5	Ground testing of magnetically shielded thrusters . . . . .	92
<b>5.4</b>	<b>Conclusion . . . . .</b>	<b>93</b>

---

## 5.1 Alternative wall material for Hall thrusters

### 5.1.1 Previous work on alternative material for Hall thrusters

Since the Hall thruster technology emerged from the Soviet Union the material of choice for the discharge channel has been boron nitride (BN) compounds. Most thrusters use either BN HP (95% BN with a calcium borate binder), BN M26 (40% BN, 60% SiO<sub>2</sub>) or the Russian Borosil (49% BN, 49% SiO<sub>2</sub>, 1% Y<sub>2</sub>O<sub>3</sub>). Those materials offer similar thruster performances [152, 153]. However additives such as silicon nitride and aluminum nitride can degrade performance by modifying the secondary electron emission behavior of the walls [154].

---

<sup>1</sup>Adapted from:

L. Grimaud and S. Mazouffre, "Performance comparison between standard and magnetically shielded 200 W Hall thrusters with BN-SiO<sub>2</sub> and graphite channel walls," *Vacuum*, vol. 155, pp. 514–523, Sep. 2018.

L. Grimaud and S. Mazouffre, "Conducting wall Hall thrusters in magnetic shielding and standard configurations," *J. Appl. Phys.*, vol. 122, no. 3, p. 033305, Jul. 2017.

Data on the performance of Hall thrusters with other materials is less common. Raitses and Ashkenazy performed some performance measurements with machinable glass ceramics [155, 156] which showed a considerable performance degradation. A large electron current is measured which lowers the efficiency of the thruster. Tests with alumina walls have shown a similar behavior as well as modification of the acceleration region [13, 157]. Raitses conducted a number of studies with thin conducting rings made of graphite and carbon velvet [102, 158–166]. Those highlight the importance of the secondary electron emissions (SEE) on the thruster performance. They also show how conducting materials can change the position of the electric field. Diamond was tested in Stanford’s linear Hall thruster [167]. This open drift geometry is not easily compared to classical Hall thrusters and the diamond walls induced very unstable operation under 200 V. A micro Hall thruster with alumina and diamond surfaces was also fired at Stanford but the setup was far from conventional HT [168]. Lastly, Gascon replaced the inner wall of a BHT-200 thruster with diamond [169]. The performances were only weakly modified by the change in wall material but only the inner wall was covered.

The most complete study up to date was carried out by Gascon in the early 2000’s [26, 99]. A full set of performance were measured on the SPT-100 thruster with BN-SiO<sub>2</sub>, Al<sub>2</sub>O<sub>3</sub>, SiC and graphite discharge channels. The boron nitride showed the best performance by far in terms of stability, operating range and thruster efficiency. Interestingly the thrust measured seemed only weakly affected by the wall material. The material effects were principally seen on the discharge current means value and oscillations. Those differences were explained by an increase in the electron current to the anode caused by the change in secondary electron emission properties of the walls.

More recently, Goebel et al, taking into account the reduced interaction between the walls and the plasma, as well as the constant plasma potential along the walls in magnetic shielded thrusters, tested graphite walls [139]. The magnetically shielded H6-MS showed only minor differences in performances, and operated at the same current and with the same dynamics with BN or graphite walls.

It is important to note that those experiments with conducting walls are not equivalent to thrusters with anode layers (TAL). The main characteristic of a TAL is that the whole discharge channel is conductive and is set at the anode potential. In most cases for the conducting wall SPTs discussed above the walls are left floating with respect to the anode and cathode. TAL also often feature a ring situated at the exit plane at the cathode potential [170].

### 5.1.2 Implementation on the ISCT200-MS and ISCT200-US



Figure 5.1: Discharge channel with the graphite inserts. The graphite inserts cover two thirds of the discharge channel length.

A special set of discharge channel walls was built to investigate the effects of conducting walls on the thruster performances. Figure 5.1 shows the BN-SiO<sub>2</sub> discharge channel with a small relief machined so that thin graphite inserts could be inserted. Those inserts are insulated from the anode and are left electrically floating with respect to the other components of the thrusters. The graphite is a fine grain isostatically pressed grade and has an electrical resistivity of 14  $\mu\Omega\text{m}$ .

The MS thruster was fired with both clean new BN-SiO<sub>2</sub> walls and graphite walls. The US-HT was fired with used BN-SiO<sub>2</sub> walls and graphite walls. Each thruster was left under vacuum for at least 12 hours and fired for one hour in order to outgase the new components. Before data acquisition started we waited 30 minutes for thermal stabilization.

The discharge current was recorded with a Tektronix current probe (TCP202, dc to 50 MHz bandwidth). The probe was connected to a Tektronix digital oscilloscope (TDS5104, 1 GHz, 5 GS/s) to monitor and record the electrical signals at a sampling rate of 2.5 MHz.

## 5.2 Performance

### 5.2.1 Discharge current

#### Envelope and discharge current

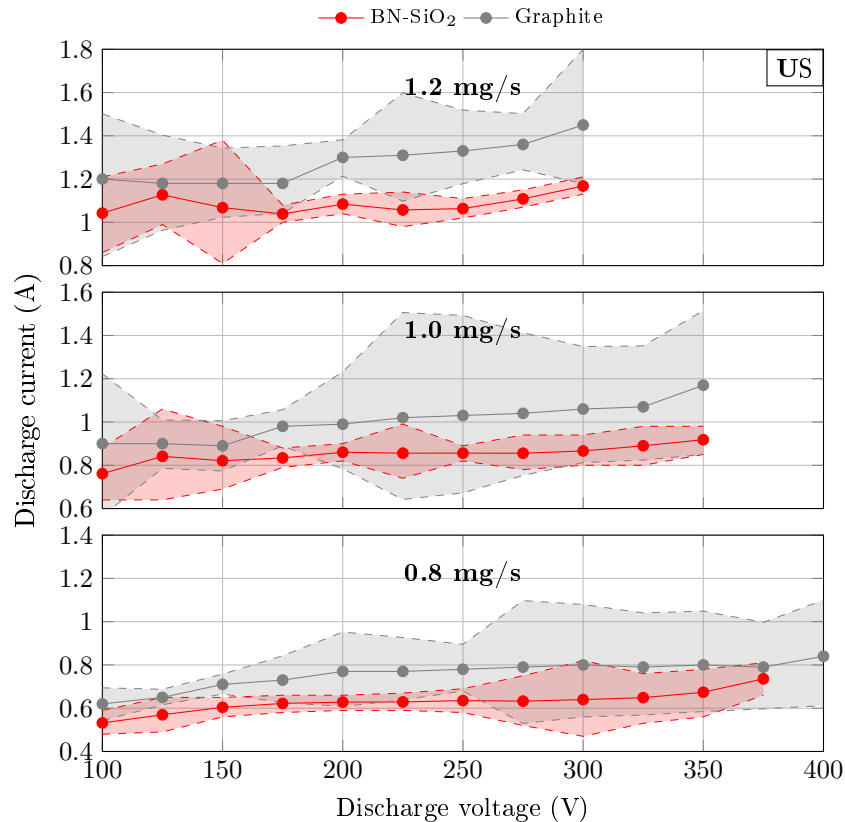


Figure 5.2: Discharge current for the US thruster with ceramic walls and graphite walls. The filled in areas delimit the top 10% and bottom 10% of the current oscillations are at this operating point.

The mean discharge current for different xenon mass flow and voltages is presented in figure 5.2 for the US-HT and in figure 5.3 for the MS-HT. The conducting walls increase the discharge current by 15 to 30% in the unshielded thruster when the discharge voltage is kept below 350 V. For the MS-HT the discharge characteristics between 150 and 300 V are very similar with the two materials. The graphite slightly reduces the discharge current but by no more than 10%.

At high discharge powers, operation is usually limited by the apparition of hot spots in the discharge channel. After those hot spots appear we usually observe a slow but steady increase in the discharge current even though the voltage and mass flow are maintained constant. With the graphite walls in the shielded thruster this behavior is not observed. The current remains stable and the thruster was operated for more than 15 minutes at nearly 400 W without any issue. Operation above 400 V was limited by the maximum range of the power supply.

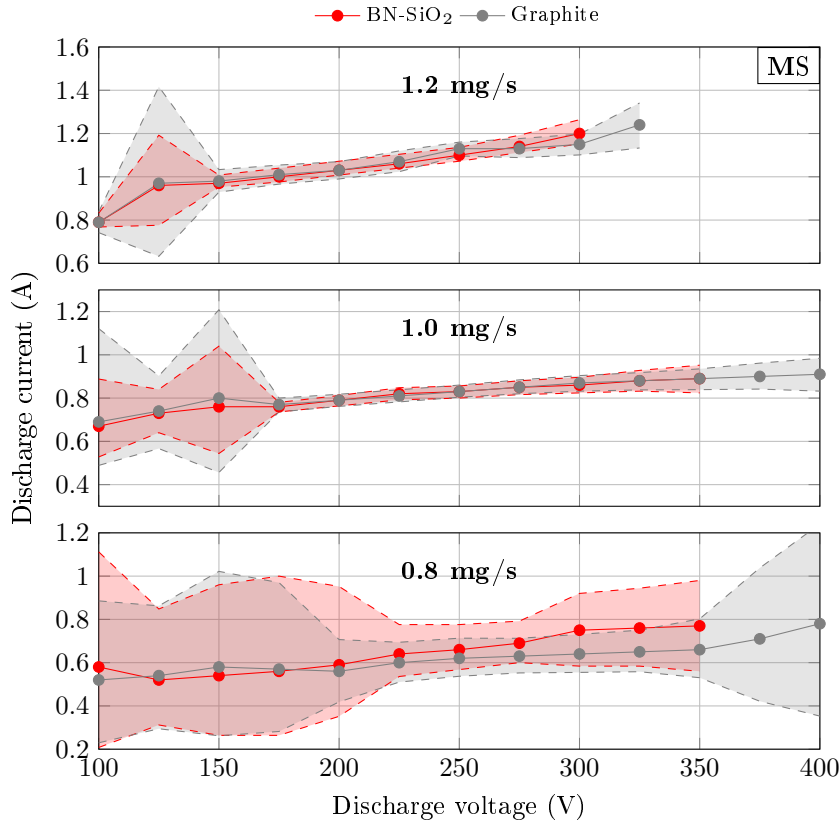


Figure 5.3: Discharge current for the MS thruster with ceramic walls and graphite walls. The filled in areas delimit the top 10% and bottom 10% of the current oscillations are at this operating point.

### Discharge stability

Figures 5.2 and 5.3 not only show the mean discharge current but also the amplitude of the current oscillations. The filled in area correspond to where the current is 90% of the time. The 90% threshold is taken in order to minimize the influence of potentially irregular current spikes or dips.

The unshielded and shielded thruster with BN-SiO<sub>2</sub> walls exhibit a typical stability range with oscillations at low voltages ( $\leq 150$  V) and a stable zone between 175 and 250 V before oscillations start to slowly increase at higher voltages.

With the graphite walls the US-HT is nearly always less stable than its ceramics counterpart. The current oscillations at high voltage appear sooner and are more pronounced. However in the magnetically shielded case the differences are minimal. The transitions follow the same pattern and have the same amplitude as with the ceramics for mass flow of 1.0 and 1.2 mg/s of xenon. For the lower 0.8 mg/s mass flow the graphite even reduces the oscillations.

Figure 5.4 and 5.5 represents the power spectra (Welch's method) of the current for different discharge voltages at 1 mg/s of xenon mass flow. Once again the differences the material makes in the US thruster are clearly visible. From 200 to 350 V a clear main frequency emerges between 10 and 20 kHz in the graphite case. A similar peak is visible around 40 kHz at 225 V in the ceramics US case but becomes more diffuse at higher voltages. This is consistent with the results of Gascon in the unshielded SPT-100-ML [26, 99].

Both shielded cases are similar. The low voltage oscillations are localized between 10 and 20 kHz but after reaching 175 V the spectrum flattens considerably. The increased oscillations at higher voltages engulf a wide range of frequencies between 5 and 50 kHz. The two characteristic frequencies at 8 and 70 kHz observed by JPL on the H6-MS at 300 V are not seen here [139].

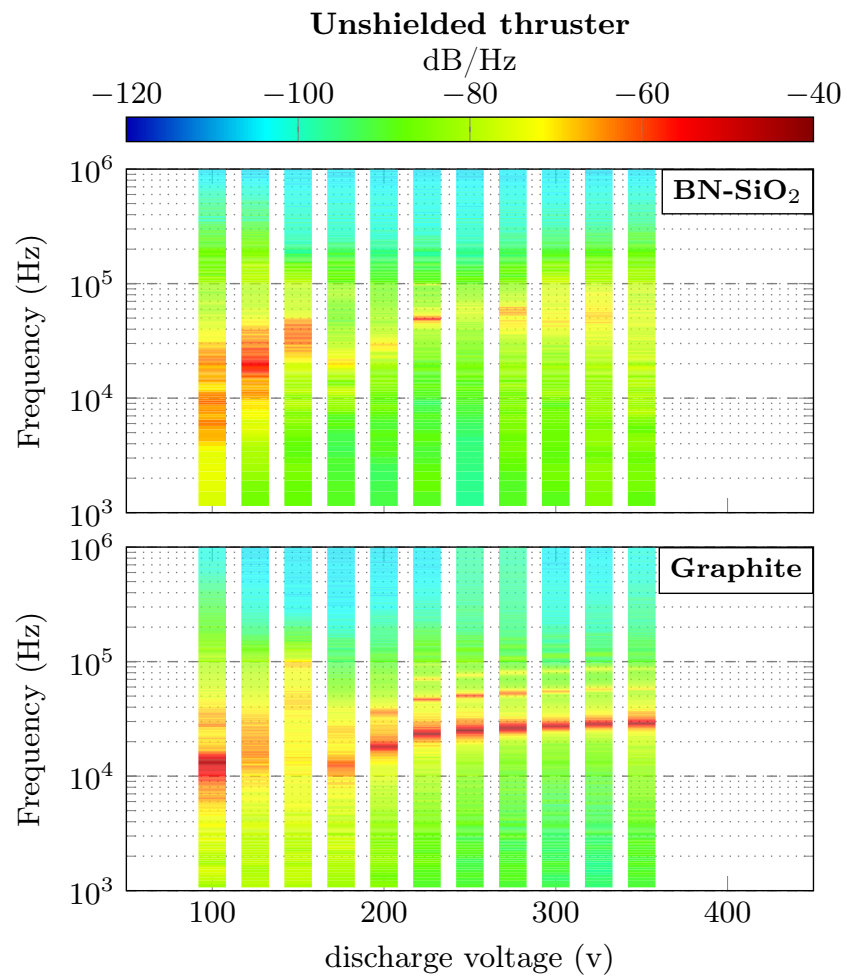


Figure 5.4: Spectra of the discharge current for the US-HT with BN-SiO<sub>2</sub> (top) and graphite (bottom) walls for a range of discharge voltages at 1 mg/s.

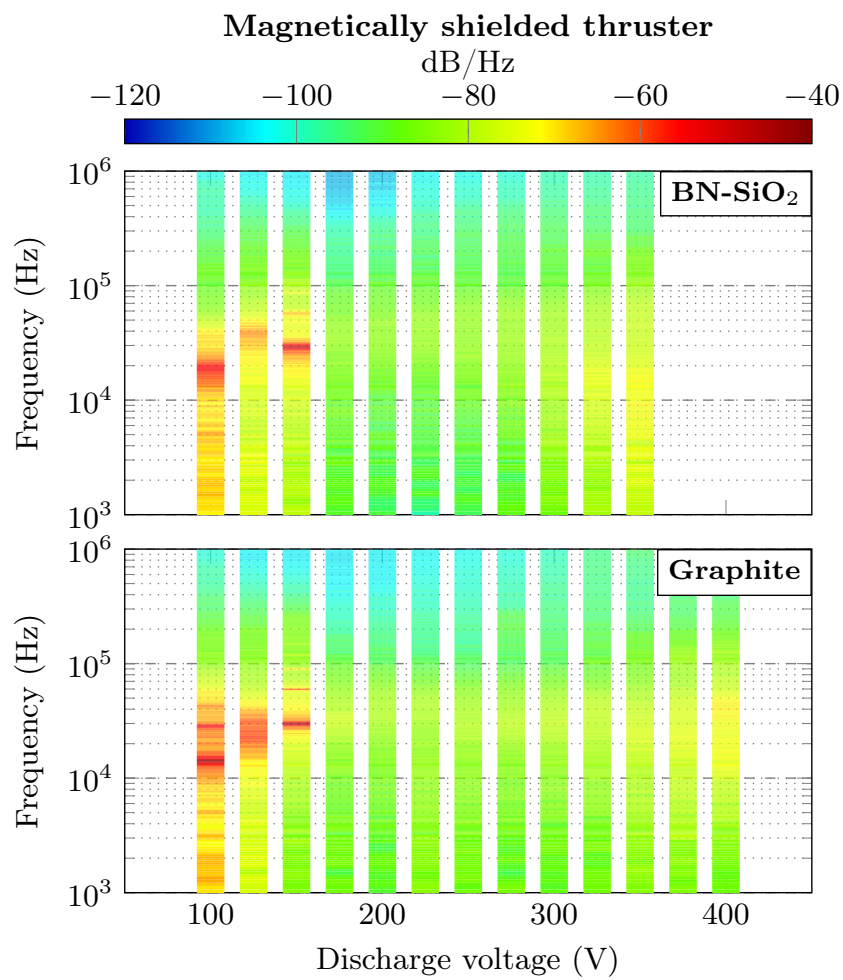


Figure 5.5: Spectra of the discharge current for the MS-HT with BN-SiO<sub>2</sub> (top) and graphite (bottom) walls for a range of discharge voltages at 1 mg/s.

### 5.2.2 Electric field distribution

LIF spectroscopy acquisitions were performed at 200 V and 1 mg/s. The most probable ion velocities measured by LIF as well as the resulting electric field computed from the IVDFs are presented in figure 5.6. Position is normalized by the discharge channel length.

Classically in the US and MS Hall thrusters the electric field is positioned near the maximum magnetic field. The measurements show a clear effect of the conducting walls on the unshielded thruster. While the field maximum intensity remains similar the electric field position is around 20% of the discharge channel length further downstream. It also doesn't correspond to the maximum magnetic field anymore.

In the MS-HT the wall material doesn't affect the acceleration region in any appreciable way. The slight shift upstream is within the absolute position error of the optical system.

As seen in figure 5.6 a), the final velocity of the ion is weakly affected by the change in material. In all cases it is about 75% of the total acceleration potential.

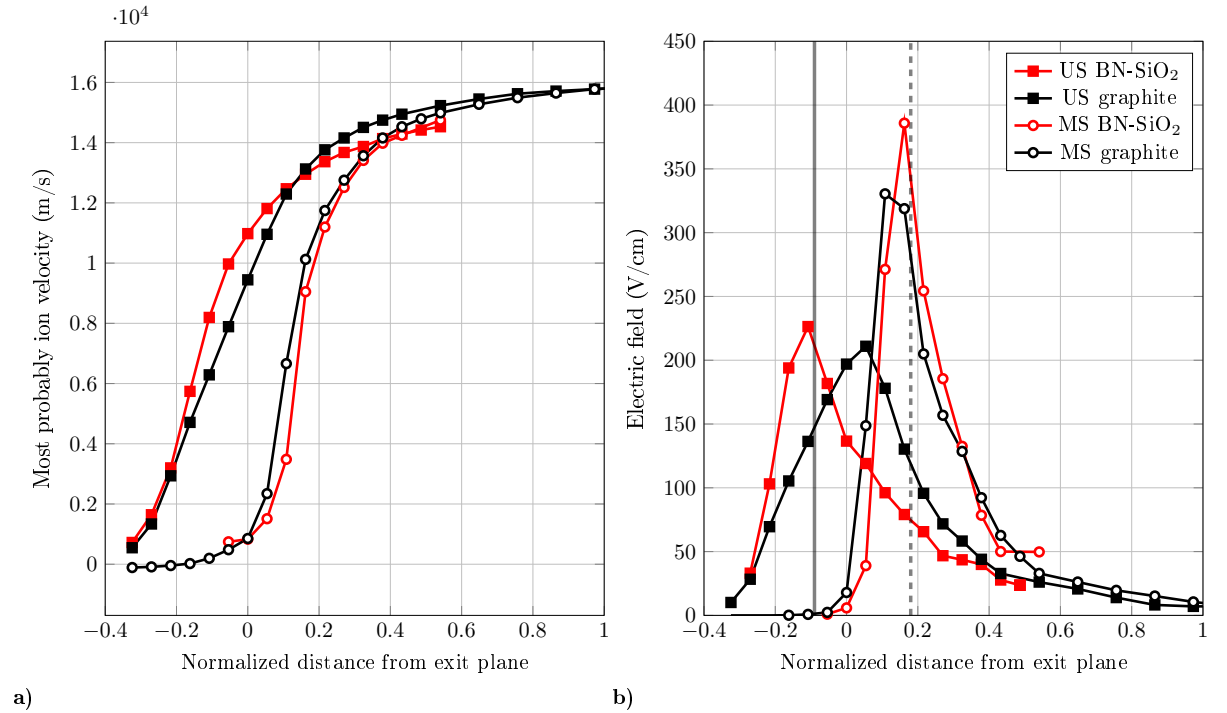


Figure 5.6: Most probable ion velocity (a) and electric field intensity (b) as a function of the distance from the exit plane. The vertical lines represent the position of the maximum of the magnetic field for the US-HT (continuous line) and MS-HT (dashed line).

The displacement of the electric field downstream is somewhat contrary to what was measured by Raites with graphite [165] and carbon-velvet [158] (a conducting material with no secondary electron emissions). It is worth noting that in those experiments the conducting segments spanned only about 10% of the discharge channel length compared to 60% in the ISCT200-MS and ISCT200-US. The measurements were also performed with emissive probes which are known to disturb the discharge [67, 68, 171].

### 5.2.3 Plume

#### Measurements in the NExET chamber

The current density profiles collected by the planar probe with guard ring is presented in figure 5.7. Those are not corrected for charge exchange or background plasma. Even just considering those profiles it can easily be seen how the shielded thruster plume isn't affected by the change of wall material while the unshielded thruster plume widens significantly when switching to the graphite walls.

Table 5.2 shows the calculated divergence angle, beam current efficiency and propellant utilization efficiency. As previously shown, with ceramics walls the US-HT and MS-HT have similar divergence angle

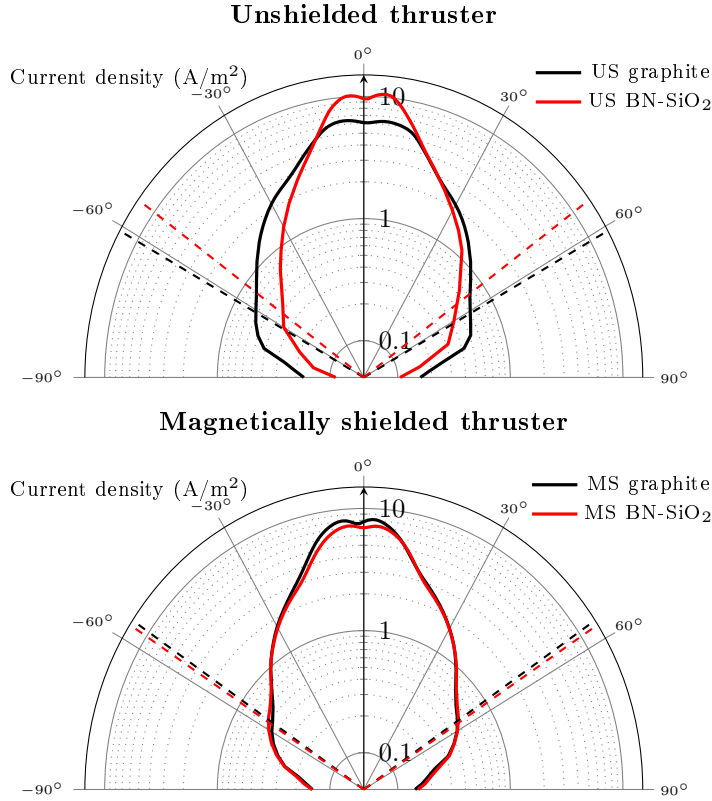


Figure 5.7: Current density profiles measured across the plume with planar probes with guard rings at 200 V and 1 mg/s of xenon for the US-HT (top) and MS-HT (bottom). The dashed lines represent the divergence angle for the BN-SiO<sub>2</sub> (red) and graphite cases (black).

and beam efficiency. The MS-HT is 6 to 7% less propellant efficient than the US-HT at similar discharge voltage and mass flow rate.

The switch to graphite walls does not change the MS-HT performances. The calculated efficiencies increase by only 2% or less and the divergence angle stays the same. In the US-HT however the conducting walls increase the divergence at 200 V and the computed propellant utilization at both voltages. Beam efficiency does not appear to be affected.

A propellant utilization efficiency of 100% as seen in the unshielded thruster with graphite walls is highly suspicious. This is a result of the rather simple data processing done here. Offsetting the discharge current by the background measured at high angle (as described in section 2.2.2) does not account for all charge exchange phenomena, multiply charged ions fractions or pressure effects. The data presented here is mostly useful as a qualitative comparison between measurements performed with the same system, in the same facility and with similar thrusters. In fact the results presented in section 5.2.3 in the PIVOINE-2g chamber show how much background pressure and probe design can influence the calculated values.

Table 5.1: Overview of the data derived from plume measurements in the NExET vacuum chamber. All the cases presented were obtained at a mass flow of 1 mg/s of xenon.

	$V_d$ (V)	BN-SiO <sub>2</sub>			Graphite		
		$\alpha_d$ (°)	$\eta_I$	$\eta_{prop}$	$\alpha_d$ (°)	$\eta_I$	$\eta_{prop}$
MS	200	57	66%	70%	56	68%	72%
	300	57	63%	75%	57	65%	77%
US	200	54	66%	77%	62	65%	91%
	300	58	64%	81%	60	66%	100%

### Measurements in the PIVOINE-2G chamber

Table 5.2: Overview of the data derived from plume measurements in the PIVOINE vacuum chamber. All the cases presented correspond to a 200 V discharge voltage and are not corrected for multiply charged ions.

	$\dot{m}_a$ (mg/s)	BN-SiO <sub>2</sub>			Graphite		
		$\alpha_d$ (°)	$\eta_I$	$\eta_{prop}$	$\alpha_d$ (°)	$\eta_I$	$\eta_{prop}$
MS	1.0	63	59%	60%	62	59%	63%
	1.2	62	60%	67%	61	60%	68%
US	1.0	60	68%	76%	66	63%	77%
	1.2	59	69%	76%	66	61%	82%

The divergence angles obtained in the PIVOINE-2G chamber show the same tendency as for the previous measurements in the much smaller NExET chamber [172]. With the ceramic walls, the divergence for the unshielded thruster is slightly smaller than the MS one. The divergence angle of the MS-HT is nearly identical with the graphite walls compared to the ceramic one while it increases dramatically in the US case.

Like in the previous study [172] the propellant utilization  $\eta_{prop}$  is higher in the US-HT than in the MS-HT. However the difference is more pronounced here (+10 to 15%) than in the other test chamber (+7%). This might be due to the difference in background pressure decreasing the smoothing effect of the background plasma [35]. The pressure in the PIVOINE-2g chamber was  $6 \times 10^{-6}$  mBar while in the NExET chamber is was around  $5 \times 10^{-5}$  mBar. Moreover the thrusters were identical and the data processing was done in the same way but the probe design was different. This could also explain the higher divergence angles calculated.

Compared to those earlier results a difference is seen here in the current fraction. The discharge current is the sum of the ion beam current and the electrons collected by the anode. The lower ion beam current over discharge current ratio for the MS-HT means that an important electron current is present in the shielded thruster. This results was not observed previously.

Comparing the ceramic and the graphite cases, very little variation is seen for the MS-HT. The US-HT on the other hand shows a decrease in the ion current fraction but an increase in the ionized propellant fraction for the 1.2 mg/s case.

#### 5.2.4 Thrust, specific impulse and efficiency

##### Unshielded thruster

The thrust versus voltage, and specific impulse versus voltage curves for the different anode mass flows and channel materials are shown in figures 5.8 b) and 5.8 c). The thrust ranges between 6 and 16 mN and the ISP between 600 and 1400 seconds at the points tested. The maximum anode efficiency is 39% ( $\pm 3\%$ ).

As described by Gascon et al. on the SPT-100 [26] the change in wall material does not significantly affect the thrust versus voltage behavior. The only differences for the ISCT200-US are observed at 200 V and below for a xenon mass flow of 1.2 mg/s. All the other points have similar results within the uncertainty of the measurement. However as seen in figure 5.8 a) the discharge current is significantly higher in the unshielded HT with graphite walls compared to the boron nitride case. This results in the behavior seen in figure 5.8 d) where the maximum efficiency is higher with ceramic than with graphite.

Like the thrust, the specific impulse dependence on voltage (figure 5.8 c) does not appear to be strongly affected by the change in material. Interestingly the points at a mass flow of 1 mg/s are nearly indistinguishable from the one at 1.2 mg/s while the specific impulse at 0.8 mg/s is significantly lower. This suggests that a higher proportion of the propellant is not ionized at low mass flow.

An overview of the anode efficiency achieved with low power Hall thrusters is available in the appendix A (figure A.2). The ISCT200-US has performances comparable to the CAM200-EM, PlaS-40, T-40 and SPT-30. It outperforms the HT100D by about 5% under 250 W. The BHT-200 and CAMILA-HT-55 are however in a class of their own with an efficiency of more than 45% at 200 W while most other HT only get 35%.

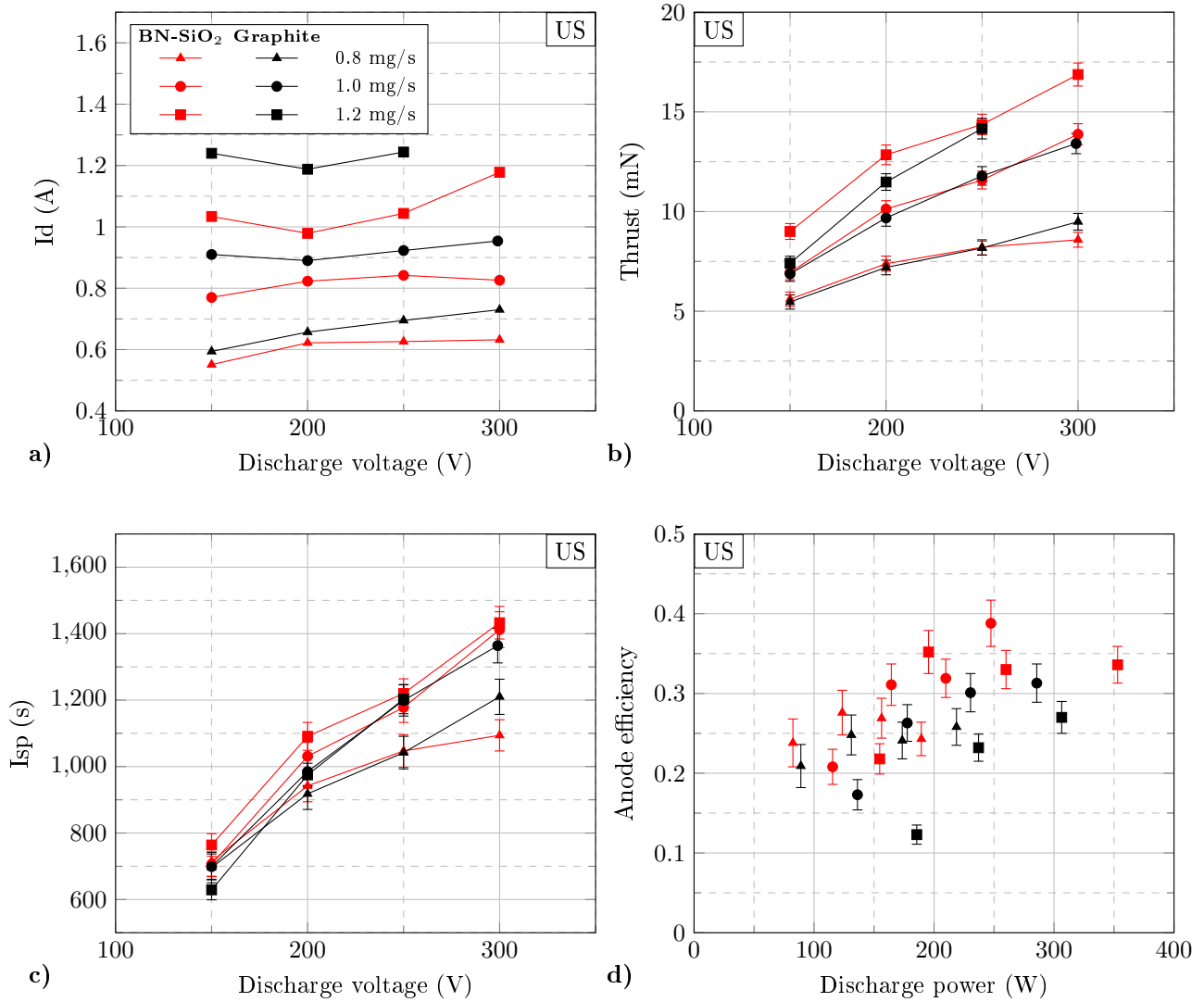


Figure 5.8: Discharge current (a), thrust (b), anode specific impulse (c) and anode efficiency (d) of the ISCT200-US.

Keeping in mind that the ISCT200-US is a laboratory thruster which has not been optimized for performances we think it adequately compares to commercial thrusters and constitutes a good benchmark to assess the performances of the magnetic shielding concept.

### Magnetically shielded thruster

As shown in figure 5.9 a), the change of wall material has nearly no effects on the discharge current. This is consistent with the previous results obtained in the small NExET test chamber [172].

The measured thrust of the magnetically shielded thruster ranges from 4 to 14 mN. As seen in figure 5.9 b) the thrust of the boron nitride and graphite versions are nearly identical at 250 V and below. A slightly higher thrust is measured with graphite walls but it is within the measurement uncertainty. At 300 V the graphite outperforms the ceramic by a more significant margin.

A similar trend is seen on the specific impulse (figure 5.9 c). The measured impulse ranges between 550 and 1250 s. The graphite and ceramic versions are fairly similar until the 300 V mark where the graphite has a measured ISP around 10 to 15% higher than the BN-SiO<sub>2</sub>. Contrary to the US-HT the specific impulse does not reach a plateau as the mass flow is increased at constant voltage. This is indicative of a poor propellant utilization and will be discussed in more details in sections 5.3.2.

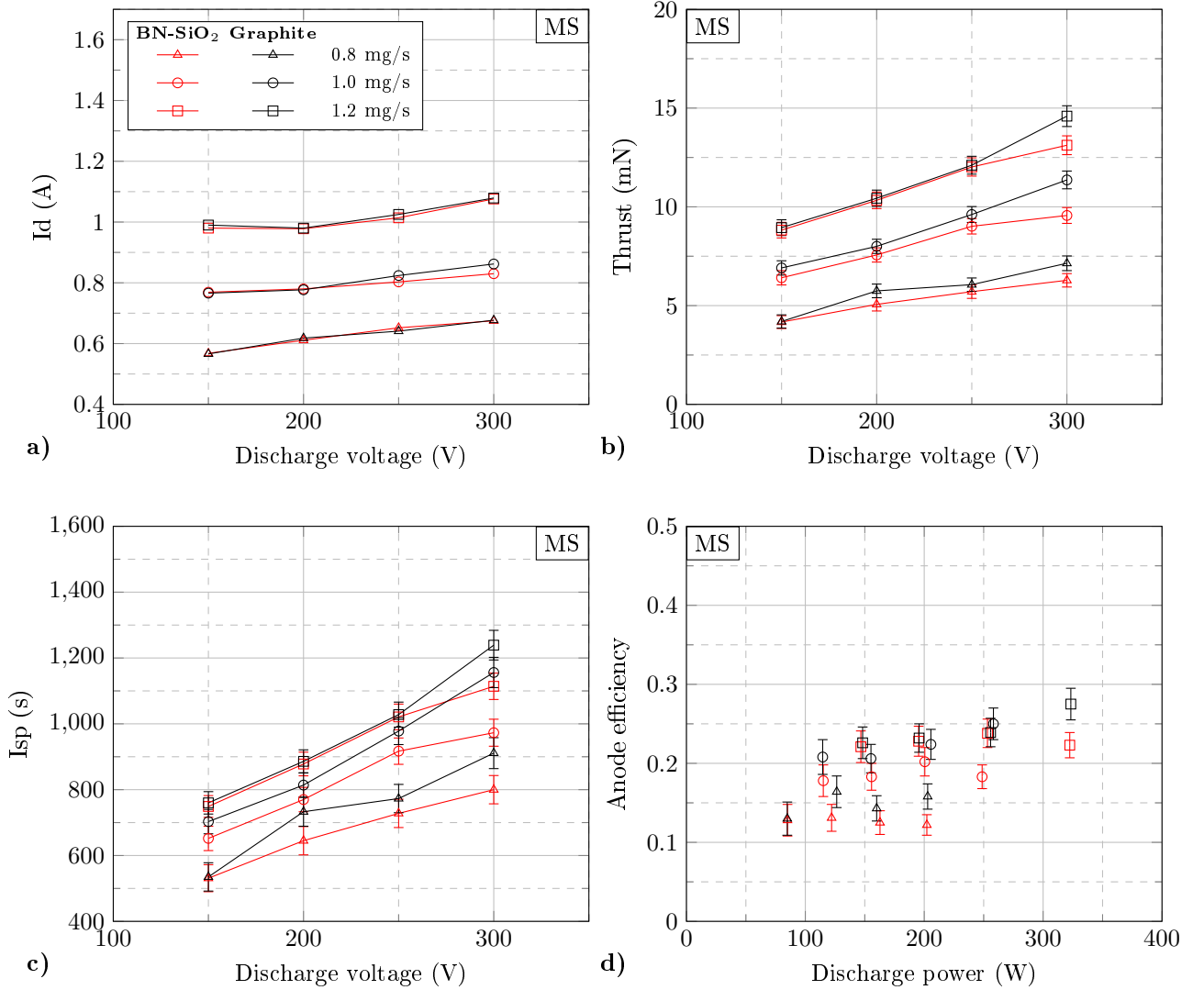


Figure 5.9: Discharge current (a), thrust (b), anode specific impulse (c) and anode efficiency (d) of the ISCT200-MS.

The magnetically shielded thruster only reaches 25% anode efficiency (figure 5.9 d). Once again the change of material has little effect on the performances of the MS-HT at lower discharge power. It's only above 300 W that we see a significant advantage for the graphite walls.

While this anode efficiency is rather low compared to classical unshielded Hall thrusters in the same power range (see figure A.2), it is comparable to the MaSMi-40 and MaSMi-60-LM1 magnetically shielded Hall thrusters built by Conversano [173]. This thruster design has also not been optimized for high performance in magnetic shielding. The difference in thrust at higher voltage between the two materials is not explained for now.

### Comparison between both thrusters

Figure 5.10 represents the point cloud of all the test cases performed with BN-SiO<sub>2</sub> during this campaign. It is readily apparent that the unshielded thruster has a higher thrust at equivalent discharge power. The difference is more pronounced at higher discharge powers.

This result is reflected in the anode efficiency (figure 5.11). The US-HT is about 10 points higher than the MS-HT over the whole power range covered in this study.

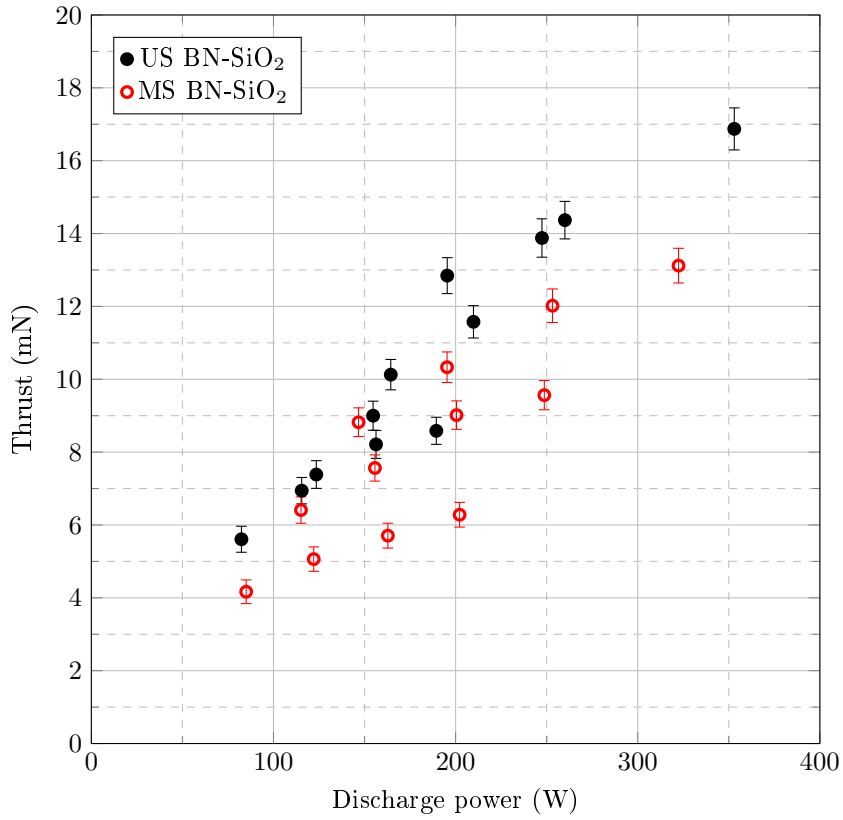


Figure 5.10: Comparison between the thrust of the US and MS thrusters with ceramic wall

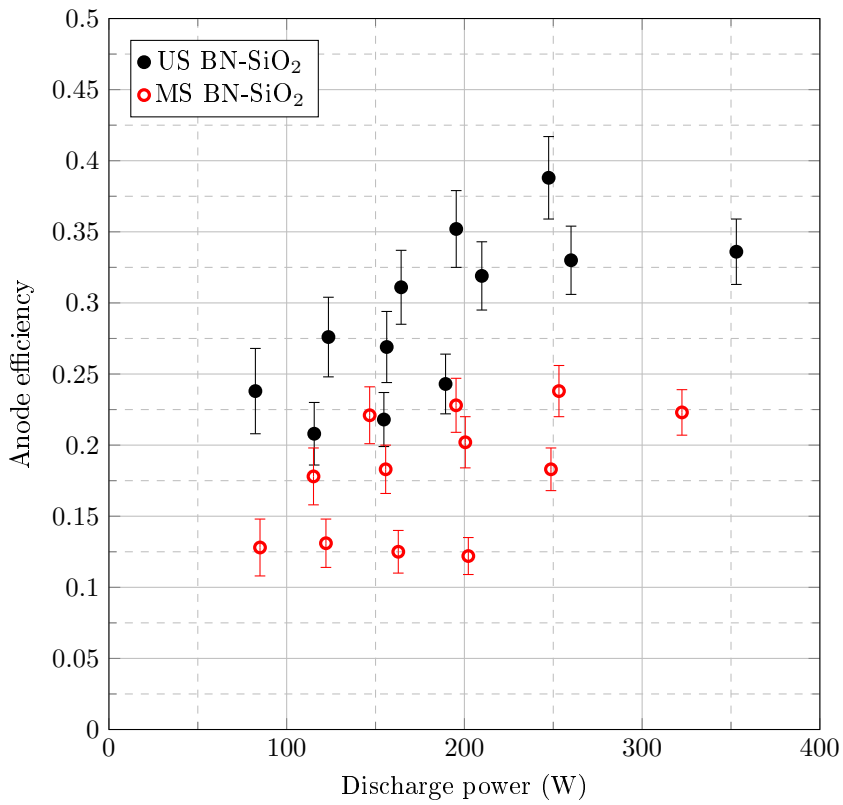


Figure 5.11: Comparison between the anode efficiency of the US and MS thrusters with ceramic wall

## 5.3 Discussion on the performance of the magnetically shielded thruster

### 5.3.1 Multiple ionization

As described in section 2.2, the results presented in section 5.2.3 assume that all ions are singly charged to compute the propellant utilization fraction. This approximation is not too far from the truth for traditional US-HT. The beam composition was measured to be 91% Xe<sup>+</sup>, 7% Xe<sup>2+</sup> and 2% Xe<sup>3+</sup> in the plume of the BHT-200 [174] which gives a mean ion charge of 1.11 *e*. In magnetically shielded thrusters such as the H6MS [121] and the MaSMi-60-LM1 [173] the proportion of doubly and triply charge ions is much higher. Conversano measured 61% Xe<sup>+</sup>, 25% Xe<sup>2+</sup> and 14% Xe<sup>3+</sup> in the plume of the MaSMi-60 operating at 250 W. This amounts to an average ion charge of 1.53 *e*. Replacing  $q_{mean}$  in equation (2.8) by those values we get a propellant efficiency of only 44% for the ISCT200-MS at 1.2 mg/s in BN-SiO<sub>2</sub> and 68% for the ISCT200-US in the same conditions (compared to 67% and 76% respectively without correcting for mean ion charge).

The high proportion of multiply charged ions in MS-HT is usually explained by the higher electron temperature in this type of thruster due to the reduced electron cooling at the walls [25].

It is tempting to explain the lower performance of the shielded thruster by this overabundance of multiply charged ions. Not only those take more energy per unit of charge to produce, but they only produce  $\sqrt{2}$  (and  $\sqrt{3}$ ) of the thrust for an equivalent acceleration voltage.

Assuming the ion population described above we can use the ionization energies required for the different ionization level to compute the power spent to produce them. This comes out at 13.3 watts per amperes of ion current in the US-HT and 16.3 for the MS-HT. Taking for example the case of the two thrusters at 200 V and 1.2 mg/s xenon mass flow, we can calculate the power spent ionizing the ion current observed. 8.9 W is spent on ionizing the propellant for the ISCT200-US and 9.6 W is used in the ISCT200-MS. The additional energy required to produce those doubly and triply charged ions is clearly not enough to explain the difference in efficiency. It should be noted however that in reality, since a non-negligible fraction of the ions are lost at the walls, the same atom can be ionized multiple times. Simulations (see section 6.1.2) shows that as much as 40% of the ions created can be neutralized at the walls. This means that the average ionization cost for extracted ions could be underestimated by as much as a factor two.

The thrust also depends on the ion charge. Neglecting the divergence and assuming the ions take advantage of 100% of the discharge voltage we can write equations (5.1) to (5.4). These equations assume all the ions are produced at the same location.

$$T = \dot{m}_I(\eta_{Xe^+} \cdot v_{Xe^+} + \eta_{Xe^{2+}} \cdot v_{Xe^{2+}} + \eta_{Xe^{3+}} \cdot v_{Xe^{3+}}) \quad (5.1)$$

$$T = \dot{m}_I \times \sqrt{\frac{2e \cdot V_d}{m_{Xe}}} \times (\eta_{Xe^+} + \sqrt{2} \cdot \eta_{Xe^{2+}} + \sqrt{3} \cdot \eta_{Xe^{3+}}) \quad (5.2)$$

$$T = \frac{I_{ion}}{q_{mean}} \sqrt{2e \cdot V_d \cdot m_{Xe}} \times (\eta_{Xe^+} + \sqrt{2} \cdot \eta_{Xe^{2+}} + \sqrt{3} \cdot \eta_{Xe^{3+}}) \quad (5.3)$$

$$T = I_{ion} \sqrt{\frac{2 \cdot V_d \cdot m_{Xe}}{e}} \times \frac{\eta_{Xe^+} + \sqrt{2} \cdot \eta_{Xe^{2+}} + \sqrt{3} \cdot \eta_{Xe^{3+}}}{\eta_{Xe^+} + 2 \cdot \eta_{Xe^{2+}} + 3 \cdot \eta_{Xe^{3+}}} \quad (5.4)$$

As a result for a given ion beam current ( $I_b$ ) a 200 W MS thruster with the ions population described above would produce only 84% of the thrust of an equivalent US thruster. All things being equal this reduces the anode efficiency by 30%. Accounting for the difference in ion beam current for the 200 V, 1.2 mg/s, BN-SiO<sub>2</sub> case the computed thrust for the MS-HT should only be 73% of the US-HT.

At this operating point we measure a thrust of 10.3 mN for the ISCT200-MS and 12.9 mN for the ISCT200-US in the same conditions. This results in a 80(± 4.5)% MS over US thrust ratio. This seems like a reasonable match with the calculation considering the uncertainty in the actual beam composition as well as the beam current.

One might then ask why the H6MS achieves an anode efficiency (0.672) so close to the unshielded H6 (0.682) [121]. First the 6 kW unshielded version of the thruster has a significantly higher fraction of multiply charged ions which adds to a mean charge of 1.27 *e* while the H6MS version is only at 1.45 *e*. This means that at equal ion beam current the thrust ratio is 92%. However the ion beam current is

actually higher in the MS version (87%) than in the US version (83%). This puts the thrust ratio, only accounting for multi-charged ions and beam current fraction, at 96% which is line with the measured thrust ratio of 95.8%. Of course one should be careful with this kind of approach as it neglects divergence and difference in ion energy.

This simple derivation shows that while the thrust of the ISCT200-MS, like other MS thrusters, is penalized by the multiply charged ions, this effect is worsened by the low ion beam current measured in the MS-HT.

### 5.3.2 Effective ionization surface

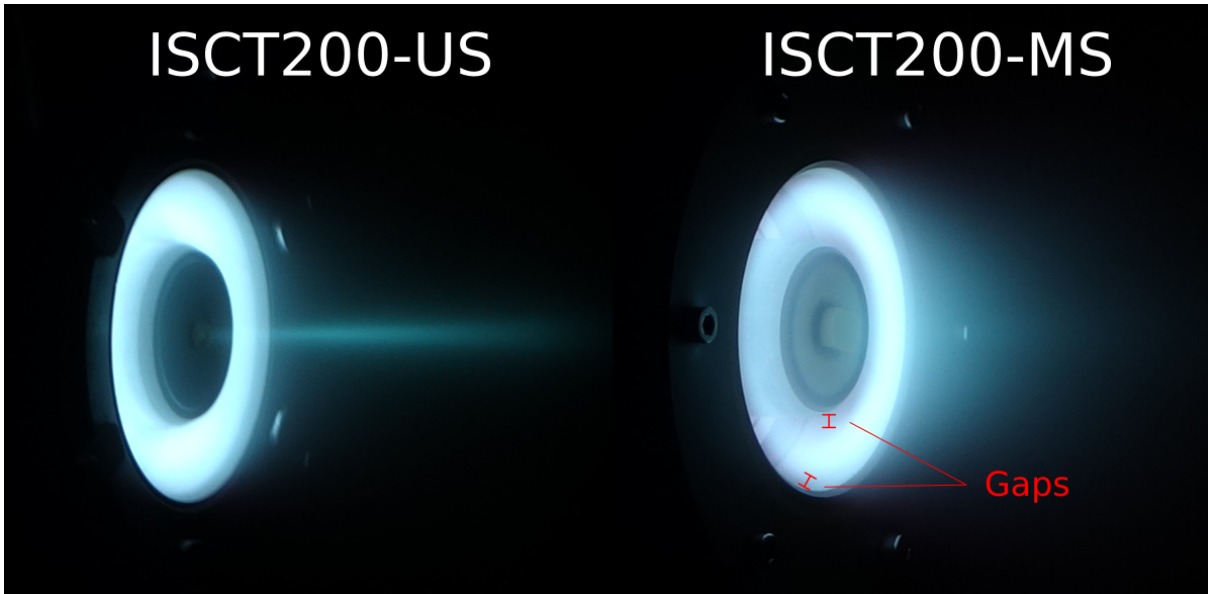


Figure 5.12: Comparison of the shape of the plasma between the unshielded and shielded thrusters.

A striking characteristic of magnetically shielded Hall thrusters is the gap visible between the bulk of the plasma and the walls [133]. Figure 5.12 highlights those gaps in the ISCT200-MS thruster. This less luminous area is a region of lower plasma density. This was seen with our LIF measurements near the walls [175] where we saw a sharp decrease of the ion density near the walls in the MS-HT. The US-HT on the other hand had a nearly constant ion density (see section 4.5.2). Similarly surface probe measurements in the H6US and H6MS near the exit plane show a decrease of the ions current density from 12 to 5 mA/cm<sup>2</sup> [121].

We propose that this gap is a path for the neutrals to leak outside the thruster without going through the ionization area. This would explain the poor propellant utilization in the 200 W MS thruster compared to the US one. It would also be consistent with the much smaller difference in propellant utilization between the H6MS and H6US. This leakage of neutral has been observed in simulations on the H6MS [25].

From the pictures of the ISCT200-MS firing we chose to assume a 1 mm gap between the plasma and the walls where no ionization take place. Under this assumption the effective ionization area would be reduced by 40% in the ISCT200 case but only by 4% in the H6.

The propellant utilization fraction shown in table 5.2 are not corrected for multiply charged ions as these fractions are not known for our thruster. However as explained in section 5.3.1 we can make use of the mean ion charge measured on other comparable thrusters. Once corrected for the mean charge the propellant utilization, in our previously used reference case of 200 V, 1.2 mg/s, is 36% lower in MS than in US. This 36% lower propellant utilization is fairly consistent with the 40% reduction in effective ionization area. This also fits the H6MS case [121]. The shielded version of the thruster has a 2% lower propellant utilization than its unshielded counterpart while the effective ionization area is reduced by 4%.

This assumption of a 1 mm gap with no ionization is very reductionist. It supposes a uniform ionization rate across the thruster and zero ionization in the gap. This is obviously not correct as some ions were measured in the area during in the ISCT200-MS [175] and in the H6MS [121]. However the spectroscopy

data seems to suggest the ion density is reduced by at least 4 at the wall in magnetic shielding. The width of the gap itself is also hard to define as it may be more or less apparent depending on the camera settings. This is especially true in the H6 where the dimensions of the thruster had to be inferred from photographic evidence.

Only two data points (ISCT200 and H6 thrusters) are available so far. However they seem consistent with a propellant loss proportional to the surface to volume ratio of the discharge channel. A smaller thruster with its large surface to volume ratio could be more sensitive to “leaks” near the channel walls than a larger one.

Conversano proposed that the poor ionization seen in the MaSMi-60-LM1 was due to non-optimal gas injection design as well as a too weak magnetic barrier [173,176]. This explanation is unsatisfactory in our case as the ISCT200-MS and ISCT200-US have been tested with the same gas injection system, same magnetic field intensity and same magnetic field gradients at the center of the discharge channel. A “leak” of the neutral atoms through the gap between the plasma and the walls has the advantage of providing the right ballpark figure for the dramatic reduction in propellant utilization as well as explaining why this is not seen in larger MS thrusters such as the H6MS, NASA-300MS [117] or HERMeS [125].

### 5.3.3 Magnetic topology

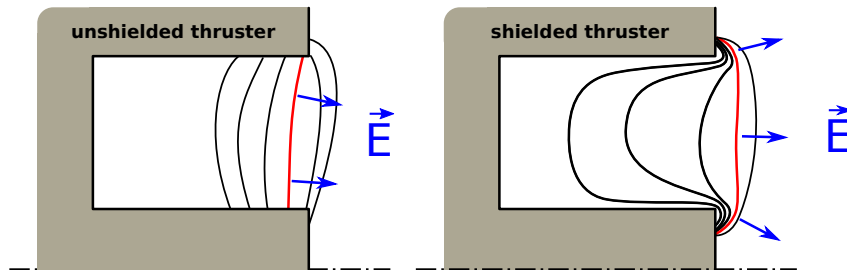


Figure 5.13: Magnetic field topology and US (left) and MS (right) thrusters. The red line represents the maximum magnetic field intensity as well as the area of maximum electric field. The blue arrows show the direction of the electric field.

The last major difference between the MS and US thrusters is the position of the acceleration region. Previous LIF spectroscopy measurements have shown that in the MS thruster the electric field is situated a few millimeters outside the discharge channel (section 4.5.1). This position coincides with the position of maximum magnetic field. As illustrated in figure 5.13, in a MS-HT in order to get the magnetic field lines going from the exit plane to the anode area (so called “grazing line”) this maximum needs to be pushed several millimeters downstream. The gap between the exit of the discharge channel and the acceleration region could cause the slow ions to diffuse toward the magnetic poles, thus not contributing to the thrust. The losses due to this phenomenon would also be proportional to the surface over volume ratio, or more accurately in this case perimeter over surface or the exit area, further disadvantaging small MS-HT. A 4 millimeter gap is less impacting in a large thruster than on a small one.

The external electric field can be, as a first approximation, considered to be normal to the magnetic field lines at this position. In a US-HT we take advantage of this effect by creating a “magnetic lens” that focuses the ion beam toward the center axis of the thruster and limits divergence. The shape of the magnetic field in a MS-HT imposes compromises between beam focusing and wall shielding. This is particularly acute in a small thruster where the magnetic field line curvature must be high in order to reach the anode area. This high curvature is also suspected to accelerate ions toward the magnetic pole causing some of the pole erosion seen on MS-HT [40,150,175,177].

This highly curved magnetic field with weak magnetic lensing is probably the cause of the higher divergence and hurts performances. This is presumably what Conversano calls “over-shielding” [173,176]. A compromise “low-erosion” topology, where the grazing lines do not reach as far back toward the anode would probably represent a good middle ground between wall shielding and performances. Such a configuration would also certainly reduce the gap between the bulk and the plasma and the walls as well as reduce the curvature of the magnetic field lines near the poles.

### 5.3.4 Wall materials and Hall thruster physics

As far as thruster characteristics are concerned the change from BN-SiO<sub>2</sub> to graphite as two main consequences.

First the discharge channel is switched from a dielectric to a conducting material. This means that any potential difference along the walls can be short-circuited through the wall material. As discussed in section 4.2 the grazing line along the walls limits the potential gradient along the walls in MS-HT. This makes it less likely to have significant currents going through them. In US-HT the electric field is usually located at the same axial position as where we set up the graphite inserts (see figure 5.6). This makes the electron likely to bypass the magnetic barrier by going through the walls. It seems that as a result the potential gradient relocates downstream. This push of the acceleration region downstream could explain the higher divergence.

The second difference between boron nitride compound and graphite is their secondary electron emissions properties. The secondary electron emission yield of BN-SiO<sub>2</sub> reaches unity near 40 eV [178–180] while it is always below 0.8 even at 100 eV for graphite [181,182]. This has a major influence on the plasma in the acceleration region of unshielded thrusters where the hot (around 30 eV) electron population is in contact with the walls. The secondary electron emission (SEE) is one of the key factor in the electron energy balance, and thus the thruster performances [96,98,183]. The mechanism by which they influence the transport across the magnetic barrier is not yet well understood [184–186]. However it appears that BN compounds have ideal SEE characteristics for Hall thruster discharge. Tests with higher SEE yield materials such as alumina do not show as good performances as boron nitride.

Study of SEE yield effects on Hall thrusters performances have traditionally been complicated. First, the actual SEE properties for dielectric material are not easily measurable and is often done at energies, current density and temperatures far from those encountered in Hall thrusters. While  $\sigma$  (the secondary electron emission coefficient) for BN-SiO<sub>2</sub> is often reported to be close to unity in typical Hall thruster conditions, it is less well known that this coefficient increases significantly when the temperature of the BN compound is increased. Belhaj et al reports a 40% decrease in the first cross-over energy at 400°C [187]. This temperature only represents the lower end of the typical operating temperature for Hall thruster ceramics [95]. The current density [180] and incidence angle of the electron beam [188] also have significant effects on the measured values. This illustrates how much uncertainty exists in the SEE and thus to its contribution to the bulk electron properties.

Attempts have been made to suppress SEE by replacing the boron nitride with other materials. Apart from diamond no other low SEE yield temperature resistant dielectric material is readily available. When using conducting materials such as graphite, or the very low SEE yield carbon-velvet, it is nearly impossible to decouple the effect of SEE from the effects of a conducting channel.

Interestingly the results presented here show that the wall material has very little effect on a MS-HT. This points toward a greatly reduced plasma/wall interaction. Why then, are shielded Hall thruster characteristics so close to unshielded thrusters with BN walls [3,151]? The near absence of interactions between the plasma and the wall should effectively emulate a classical unshielded thruster with zero secondary electron emissions. The SEE yield  $\sigma$  of BN in US-HT could be overestimated due to the measuring techniques employed and or not taking into account temperature and incidence angle effects. The similarities could also be explained by different energy loss mechanisms for the electrons. Instead of cooling down during their collisions with the walls, the high energy electrons contribute to the creation of Xe<sup>2+</sup> and Xe<sup>3+</sup> ions. High fractions of multi charged ions have been measured in MS-HT [121].

An interesting test to see if MS-HT are truly material agnostic would be to use a higher SEE yield material such as alumina [180].

### 5.3.5 Ground testing of magnetically shielded thrusters

MS-HT promise considerably increased lifespans for Hall thrusters while keeping similar performances to they unshielded counterparts. However they face specific challenges for ground testing and qualification. One of these issues is deposition of the material sputtered from the vacuum chamber walls. This material is mostly carbon from graphite protection screens (but also metals from various equipments) and creates a black conducting layer on the thruster surfaces not subjected to erosion. In unshielded thruster this deposit layer is eroded away at the exit of the discharge channel keeping the ceramic exposed (see figures 4.16).

In MS thrusters, where the erosion rate is lower than the deposition rate, the carbon layer tends to accumulate in the discharge channel. It changes channel material properties and is not representative of what is happening during operation in space. This is not compatible with the “test as you fly” philosophy of space hardware qualification. Showing that changing the wall material has little effect on the performances is a good indication that the deposition would have minimal impact on the thruster. Initially designing a MS thruster with graphite walls would also make this carbon deposition process less of a change in wall properties. Incidentally, tests in our facility have shown that the gradual build up of the carbon layer on the ISCT200-MS ceramic walls had no appreciable effects on the discharge.

Lastly BN is a brittle material and is hard to machine (hence the addition of silica for example). Furthermore it is fairly susceptible to cracking due to thermal shocks. If MS-HT are truly not affected by the wall material, tougher ceramics, or even metals could be used. Replacement materials would need to be heat resistant up to around 600°C and not disturb the magnetic field. Metals such as stainless steel or titanium [189] could be good candidates for such applications. The use of such readily available and easier to machine materials would reduce thruster cost.

## 5.4 Conclusion

In this chapter we have shown that the ISCT200-MS is not affected by a change of the discharge wall materials from BN-SiO<sub>2</sub> to graphite. The discharge current mean value and dynamics, the acceleration region position and amplitude and the thrust are similar between the two materials for the shielded thruster. The graphite even allowed for operation at higher discharge voltage and power. This is not the case for the ISCT200-US where the current increases by around 20%, the acceleration region is stretched and pushed downstream and the plume divergence increases. The thrust however is not significantly affected at similar discharge voltage and xenon mass flow. This is consistent with previous results available in the literature [26, 99, 123, 139, 142].

The ISCT200-US thruster has a peak anode efficiency of 39% and a specific impulse of 1400 s at 250 W with the ceramic discharge channel. However with graphite wall, the discharge current increases by 25% which reduces the efficiency down to 31% (1360 s specific impulse). The ISCT200-MS performances are significantly lower than the ISCT200-US at similar operating points. It only reaches 24% anode efficiency and 1020 s specific impulse at 250 W

The lower efficiency of the ISCT200-MS seems to be mostly due to a low propellant utilization and high electron mobility. We propose that this low propellant utilization is caused by lower ionization near the walls. This has a large impact on small thrusters due to their higher surface to volume ratio but is not as noticeable on larger thrusters.

## 5.4. CONCLUSION

---

## Chapter 6

# Improving performances of low power magnetically shielded Hall thruster

### Contents

---

<b>6.1</b>	<b>PIC hybrid simulation results of the ISCT200-MS</b>	<b>95</b>
6.1.1	Overview of the code	96
6.1.2	Results	97
6.1.3	Conclusions from the simulations	102
<b>6.2</b>	<b>Design of the ISCT200-MS V2</b>	<b>102</b>
6.2.1	Objectives	102
6.2.2	Magnetic topology	102
6.2.3	Magnetic circuit	103
6.2.4	Discharge channel	103
6.2.5	Insulation	104
6.2.6	Thermal design	104
6.2.7	Additively manufactured anode	104
<b>6.3</b>	<b>Conclusion</b>	<b>105</b>

---

## 6.1 PIC hybrid simulation results of the ISCT200-MS<sup>1</sup>

While the experimental data obtained in chapter 5 give us a good idea of the shortcomings of the ISCT200-MS, namely poor ionization and high electron current, they mostly consist of global performance figures. The diagnostics at hand did not give us access to much spatially resolved data on ionization process. Data such as local ionization frequency, plasma potential or electron temperature inside the discharge channel are difficult to obtain in a Hall thruster in general. Moreover, as explain in section 2.5, probing the inside of a small size Hall thruster induces significant perturbations that make any measurement unreliable.

The only solution to get an idea of what is happening inside the thruster and to obtain information on the plasma properties is to use numerical simulation tools. Since the electric propulsion team at ICARE has no simulation code this project was conducted by the LAPLACE laboratory in Toulouse, France [190].

---

<sup>1</sup>Adapted from:

L. Garrigues, S. Santhosh, L. Grimaud, and S. Mazouffre, "Operation of a Low-Power Hall Thruster: Comparison between Magnetically Unshielded and Shielded Configuration," *Plasma Sources Sci. Technol.*, 2018 - Submitted

### 6.1.1 Overview of the code

The LAPLACE laboratory uses a two dimensional hybrid particle in cell (PIC) approach. A thorough description of the code, its hypothesis, strength and limitations can be found in the literature [96,191–196]. Only a brief overview will be discussed here in order to highlight the aspects more relevant to this study. More details on the codes and the specific parameters used in this study are available in the companion article from Dr. Garrigues [190].

#### Ions and neutrals

The heavy species (ions and neutrals) are described as macro-particles. They are spread over a 2D grid in the axial and radial directions. Their velocity is defined in 3D. Since ions are not magnetized the only real force they experience is the electric field. A Monte Carlo scheme is used to compute ionization and neutralization thought collisions. Both single and doubly charged ions are considered.

At the walls a Bohm sheath criterion is applied in order to have realistic pre-sheath velocities since sheath phenomenon are not accurately captured. Ions colliding with the walls are neutralized and re-injected as randomly distributed neutrals at the wall temperature.

Neutrals are injected from a slot in the upstream surface with a Maxwellian distribution at a temperature of 500K. The model also includes the effects of back pressure to obtain results closer to the experiments.

Thrust is computed from the ion flux across the exit boundary of the computational domain. This boundary is defined as the magnetic field line that intercept the cathode position. Neutral crossing this line are removed.

#### Electrons

The code used is not a full PIC one because electrons are treated as a fluid. This allows for longer time steps and vastly shorter simulation times. However in order to accurately capture the physics of a Hall thruster discharge a careful treatment of the assumptions on the electron physics needs to be incorporated into the equations describing their behavior.

The plasma is assumed quasi-neutral, the electron density is obtained from the ion density. As described in section 4.2.1 the electron transport along the field lines is much higher than across them. This strong anisotropy makes the simulations prone to numerical error if not treated correctly. To decouple the two types of diffusions a solution is to work on a coordinate system aligned on the magnetic field lines. While the code developed at JPL uses a true magnetic field aligned 2D mesh [197, 198], it also shows that in most conditions a quasi-1D approximation produces very similar results [197]. In this simulation the magnetic field lines are assumed isothermal and the only free dimension is across them. The 1D cells are delimited by magnetic field lines.

The energy equation perpendicular to the magnetic field lines takes into account the electric field, collisions between heavy species and electrons and collisions between the electrons and the dielectric walls. The later is not trivial to estimate. The complex interactions between the walls and the electrons are covered in section 4.1.2. In our case a simplifying assumption is made where the energy deposited at the walls  $P^W$  is defined as

$$P^W = nW = n\alpha_e\epsilon_e e^{(-U/\epsilon_e)} \quad (6.1)$$

With  $n$  the electron density,  $\epsilon_e$  the electron energy and  $U = 20$  eV,  $\alpha_e = 0.5 \times 10^6$  as fitting parameters for both thrusters. More details on this wall interaction model can be found in reference [194]. The  $\alpha_e$  parameter is chosen to match the analytical relations described in reference [199].

Electrons are injected at the cathode line with an energy of 2 eV.

#### Anomalous transport

One of the fundamental issue with simulation of  $E \times B$  discharges is the so called “anomalous transport” observed experimentally. The classical diffusion of electrons through the magnetic field due to collision with heavy particles cannot explain the electron current measured in real devices. The ad hoc solution to solve this issue is to introduce an artificial diffusion term. In this case it takes the form of an anomalous electron collision frequency. Since none of the current models of anomalous transport can produce an

analytical equation of this additional transport we have to resort to manually set this parameter based on empiric data.

In order to manually set this profile along the main axis of the discharge channel the value of the anomalous collision frequency is adjusted until the ion velocity profile at the center of the discharge channel is equal to the one measure by LIF spectroscopy in section 4.5.1. This ensures a good match between experiments and simulations. This approach was previously used in references [192, 200]. The axial anomalous collision frequency profiles obtained with this method are relatively similar between the ISCT200-US and the ISCT200-MS. Their position is just shifted depending on the position of the maximum of the magnetic field.

### 6.1.2 Results

All the data presented here has been simulated for a 300 V discharge voltage and a mass flow of 1.0 mg/s of xenon.

#### Plasma properties

One of the most important result of the simulation work for our application is the data obtained on the plasma properties inside the thruster. Figure 6.1 and figure 6.2 present the time averaged results obtained on the ISCT200-US and ISCT200-MS.

As expected the subfigures (a) show that the acceleration is pushed downstream. The result is a nearly constant potential along the walls of the shielded thruster. Walls are maintained at the anode potential while in the unshielded case the difference between the anode and the exit plane at the wall is more than 200 V. It is however interesting to see that the electric potential lines are only loosely following the magnetic field lines. This is something that must be emphasized as it is often assumed that the magnetic field lines are true equipotential. As discussed in section 4.2.1 this is only the case if the plasma density is constant along that line.

Subfigures (b) show the electron temperature normalized to the maximum temperature. The maximum temperature for the ISCT200-US is 32 eV and 46 eV for the ISCT200-MS. This difference is somewhat expected and was measured with probes in the H6-MS [121] and the NASA-300MS [137]. While the uncertainty of electron temperature inside the discharge channel is high (see section 2.5) the difference seems less pronounced in those thrusters. This is however relatively close to the values calculated by Conversano on the MASMi-60-LM1 [25, 176]. It is worth noting that if the power lost at the wall is divided by 5 (by setting the electron collision frequency  $\alpha_e = 0.1 \times 10^6$  s instead of  $0.5 \times 10^6$  s in equation (6.1)) the electron temperature in the ISCT200-MS only increase by 15%. Variations of this parameter has more influence on unshielded thrusters [96]. This is consistent with the experimental results obtained with the graphite where no dependency on wall material was observed. The higher electron temperature is almost certainly responsible for the higher proportion of multicharged ions observed both numerically (see section 6.1.2) and experimentally [121, 173, 176].

In both thrusters the maximum electron temperature is localized near the maximum magnetic field region at the center of the channel. The area of hot electrons is well confined by the field lines and thus the walls of the MS-HT are well protected. The electron temperature at the wall in the MS-HT is calculated to be  $2 \pm 1$  eV, effectively strongly reducing the sheath energy.

Lastly the ionization frequency as well as the average ion velocity and direction are plotted on subfigures (c). The difference is striking, in the ISCT200-US the ionization nearly fills the channel. It reaches far upstream and goes from the inner to the outer wall. The region of intense ionization is located between 0.6 et 0.9 channel length. In the MS case the maximum ionization frequency is nearly the same ( $\tilde{10}^{24} \text{ m}^{-3} \text{ s}^{-1}$ ) but the ionization region is narrower. A clear gap exists close to the walls where very little to ionization occurs. Axially the ionization happens between 0.7 and 1.1 channel length. A significant portion of the ionization region is outside the discharge channel where neutral atoms can more easily diffuse out.

In both thrusters a lot of the ions created inside the discharge channel collide with the walls instead of exiting the thruster. This is indicated in subfigures (c) by the arrows representing the mean ion velocity. While they do not necessarily have the required energy to sputter the walls they are considered to be neutralized after the collision and the ionization energy spent to create them is lost.

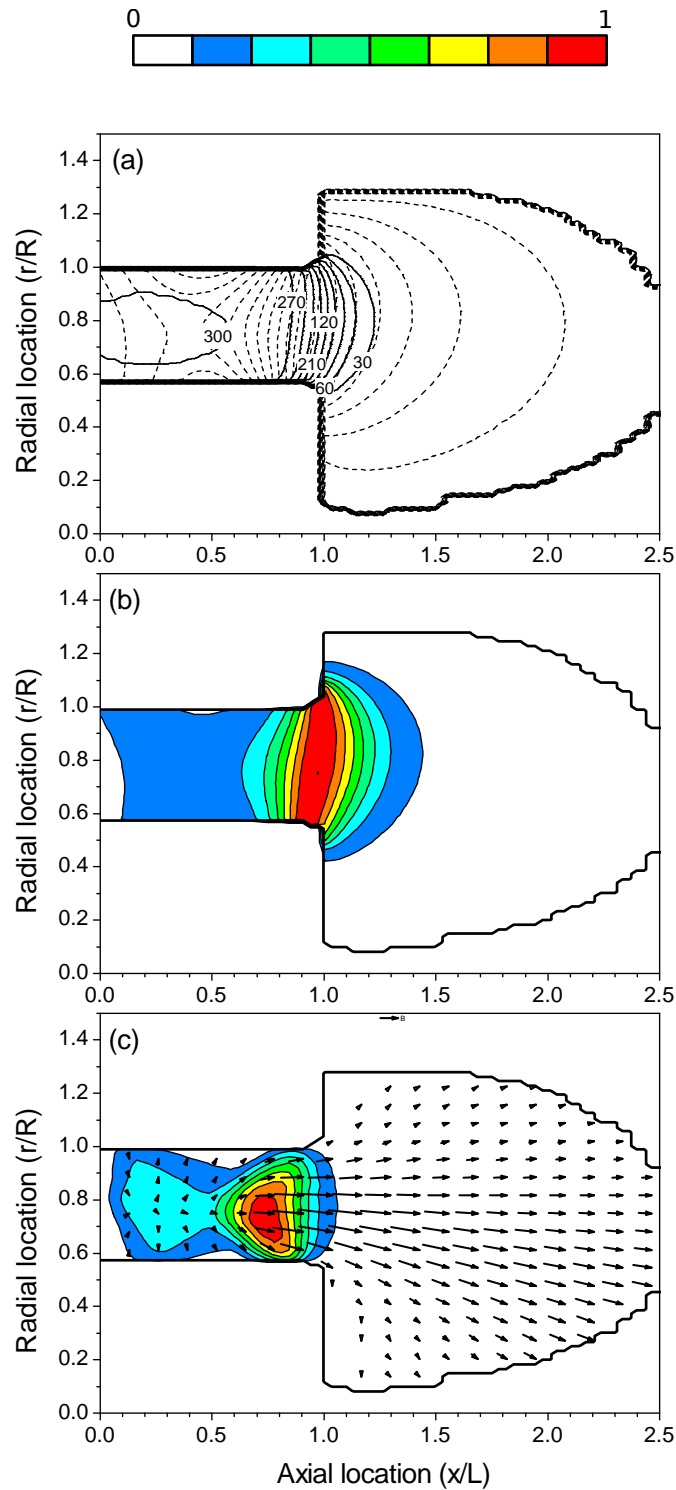


Figure 6.1: Simulation results for the ISCT200-US. **(a)** Electric potential (continuous lines) with respect to the magnetic field topology (dashed lines). **(b)** Electron temperature. **(c)** Ionization rate and mean ion velocity vectors

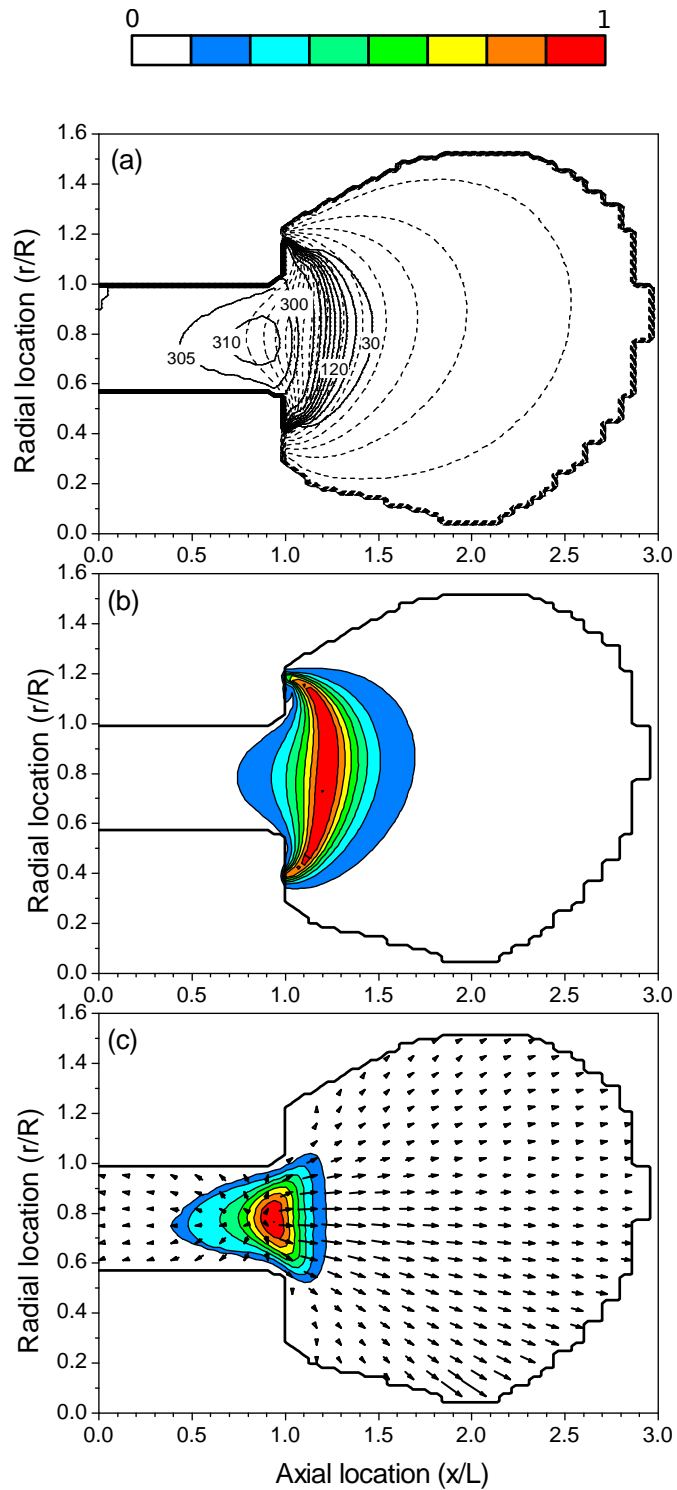


Figure 6.2: Simulation results for the ISCT200-MS. (a) Electric potential (continuous lines) with respect to the magnetic field topology (dashed lines). (b) Electron temperature. (c) Ionization rate and mean ion velocity vectors

### Performances

In order to judge the accuracy of the simulation one has to consider the macroscopic performance figures. Table 6.1 shows an overview of the simulation results as well as a comparison with experimental data.

The results obtained numerically are compared to experimental data presented earlier in this document. Sadly the experimental data is mixed between what was obtained in the NExET (plume data, IVDF) and in the PIVOINE-2g (discharge current, thrust) vacuum chamber. The pressure in NExET was around  $5 \times 10^{-5}$  mBar whereas in PIVOINE-2g a vacuum of  $6 \times 10^{-6}$  mBar was maintained during operation. That difference in pressure influences the average discharge current, but also the plume shape and content as well as the exact position of the acceleration region [35, 36, 201, 202]. Furthermore it is well known that background neutral are ingested by the thruster and tends to also artificially increase thrust. The simulation is done with a background pressure representative of the PIVOINE-2g chamber but the anomalous collision frequency is adjusted on velocity data obtained in the NExET chamber.

The discharge current mean value is captured within 4% and the thrusters are stable in both experiment and simulation. The main difference between simulation and experiment is on the thrust of the ISCT200-MS. It is overestimated by almost 30% on the simulation which has strong repercussion on the calculate anode efficiency. The relative difference between US-HT and MS-HT are respected for all the figures we have looked at. The anode efficiency, propellant efficiency, beam current efficiency and divergence efficiency are lower in the ISCT200-MS.

A few things are interesting to note on the simulation results. A large portion of the ions created are lost to collisions with the walls (referred to as “ion current losses” in table 6.1). This portion is much higher (nearly 3 times) than what is calculated in larger thrusters such as the SPT-100 [203]. This is not very surprising as the surface over volume ratio is 2.2 times larger in the ISCT200 thrusters than in the SPT-100. The ion current losses are reduced by more than 10% in the ISCT200-MS compared to the ISCT200-US. This means a reduction of the electron current at the walls which is responsible for most of the energy loss [95, 96]. Adding to this the reduction in electron energy observed in section 6.1.2 the energy losses to the walls should be greatly reduced in the MS-HT. This seems corroborated by the temperature measurements from section 4.4.2.

The propellant utilization efficiency calculated from the simulation is even lower than the one measured. However the measured ones are not compensated for multiple ionizations. Using the mean ion charge obtained in the model an “uncorrected” propellant utilization figure can be obtained which matches very well with the experimental results.

Lastly the simulation is able to capture the larger population of multicharged ions produced in magnetic shielding. While the model only accounts for  $\text{Xe}^+$  and  $\text{Xe}^{2+}$  ions, the proportion of doubly charged ions is 50% higher in the MS-HT. This is almost certainly due to the higher electron temperature observed in the ISCT200-MS.

Table 6.1: Comparison of simulated and experimental results for the shielded and unshielded thrusters. <sup>1</sup> from NExET test chamber, <sup>2</sup> from PIVOINE-2g test chamber.

Performances	ISCT200-US		ISCT200-MS	
	Sim.	Exp.	Sim.	Exp.
Discharge Voltage (V)	300	300	300	300
Anode mass flow (mg/s)	1	1	1	1
Discharge current (A)	0.82	0.82 <sup>2</sup>	0.86	0.83 <sup>2</sup>
Discharge current oscillations (A)	0.069	$\leq 0.1^2$	0.063	$\leq 0.1^2$
Ion current (A)	0.59	0.52 <sup>1</sup>	0.53	0.52 <sup>1</sup>
Ion current losses (A)	0.39	N/A	0.34	N/A
Thrust (mN)	14.4	13.8 $\pm$ 0.53 <sup>2</sup>	12.9	10.0 $\pm$ 0.4 <sup>2</sup>
Anode efficiency	0.41	0.39 $\pm$ 0.03 <sup>2</sup>	0.32	0.21 $\pm$ 0.015 <sup>2</sup>
Propellant utilization efficiency	0.71	N/A	0.67	N/A
Propellant utilization efficiency uncorrected for multiple charge	0.82	0.81 <sup>1</sup>	0.75	0.75 <sup>1</sup>
Beam current efficiency	0.72	0.64 <sup>1</sup>	0.62	0.63 <sup>1</sup>
Beam divergence efficiency	0.92	N/A	0.85	N/A
Xe <sup>+</sup> current fraction	0.92	N/A	0.87	N/A
Xe <sup>2+</sup> current fraction	0.08	N/A	0.13	N/A

### Erosion

Finally we can look at the erosion rate predicted by the simulation. The erosion law is taken from the model presented in section 4.1.1. This model is strongly dependent on an erosion threshold  $E_{th}$  (as defined in equation (4.2)). This threshold is usually defined between 20 and 60 eV for the boron nitride compounds used in Hall thruster. However very little experimental data exists at these low energy ranges and fitting the equation to experimental data yield very imprecise results [204].

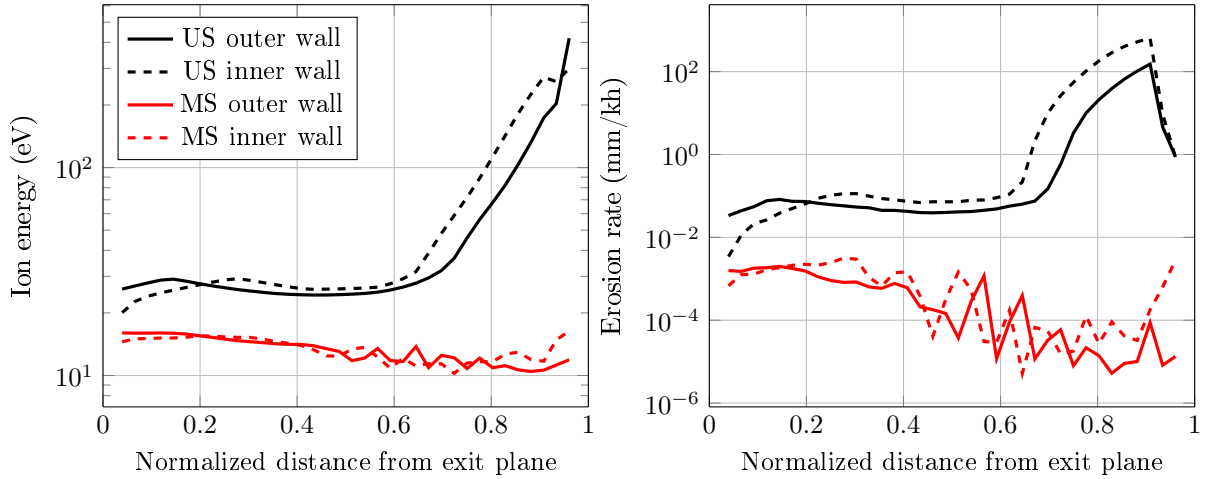


Figure 6.3: Ion energy at the wall surface (left) and erosion rate prediction (right).

Figure 6.3 shows the ion energy at the walls for both thrusters. In the ISCT200-US this energy reaches as much as 400 eV as the ions are accelerated both by the main electric field and the very energetic sheath near the exit plane. In the ISCT200-MS the ion velocity is much lower and the ion energy stays below 20 eV. Figure 6.3 also shows the erosion rate calculated for the two thruster at the inner and outer walls. For this calculation the  $E_{th}$  threshold is set to 30 eV. Everywhere in the thruster the erosion rate is at least two orders of magnitude lower for the MS-HT and nearly six orders of magnitude lower in the area of worst erosion. The maximum calculated erosion rate in the US-HT is 100 mm/kh which is high compared to the actual erosion measured on small and large Hall thrusters [205–208]. However one can assume that this overestimation would apply to both the ISCT200-US and ISCT200-MS thrusters.

### 6.1.3 Conclusions from the simulations

The simulation provides great insights on the physics of the ISCT200-MS. In particular the low propellant utilization identified in section 5.3 as one of the major cause of low thruster efficiency. It confirms that the ionization region in the MS-HT is smaller and leaves gaps near the walls where neutral atoms can escape.

It also shows that the walls of the thruster are extremely well shielded with no potential drop and a low electron temperature along them. As a result an erosion rate several orders of magnitude lower than in the ISCT200-US.

## 6.2 Design of the ISCT200-MS V2

### 6.2.1 Objectives

With the results obtained from the experimental campaigns on the ISCT200-MS as well as the knowledge gained from the simulations conducted by the LAPLACE laboratory it was decided to design and build a second version of the ISCT200-MS thruster. The goal of this new thruster is to use lessons learned on the first prototype to improve the performance of the thruster while maintaining the lifespan improvements. Some of the specific design problems caused by the implementation of magnetic shielding topology are also addressed.

Being a pure laboratory thruster it is not built to withstand the harsh mechanical constraints associated with rocket launch.

### 6.2.2 Magnetic topology

This thruster is built with a strong emphasis on magnetic flexibility. The idea is to be able to test both regular magnetic shielding topologies similar to what was done in the ISCT200-MS as well as modified ones and even standard topologies. Moreover, as described in chapter 3, low power thruster can benefit from more intense magnetic field, as such the thruster was designed to be able to accommodate more magnetic material and not saturate as much.

The thruster was designed to be able to produce a MS topology similar to the version 1. This “full” magnetic shielding, as described by the American research teams, has the grazing lines penetrating deep inside the discharge channel. However a consequence of these highly curved lines is that the maximum of the magnetic field has to be pushed several millimeters downstream of the exit plane. As it can be seen on the simulation results (figure 6.2) the shielding produced by those topologies is very efficient with electron temperatures along the walls around 20 times lower than the maximum and a constant plasma potential.

This kind of topology protects the walls very well but results in important parts of the discharge channel where no ionization takes place. Moreover while the magnetic field lines are often referred to as isopotential (see section 4.2.1) this is only true if the electron density is more or less constant (as per equation (4.10)). Simulation shows that the electron density is not constant and that the isopotential lines are reaching far deeper inside the thruster than magnetic field lines (see figure 6.2). We think that the grazing line does not have to reach quite as far inside the channel to produce the desired effect of erosion reduction.

A new shielding topology is devised as an alternative. In this one the grazing line penetrates less deep inside the thruster which allows us to bring the maximum magnetic field closer to the exit plane. The purpose of this intermediary topology is to bring the ionization region further upstream and closer to the walls to minimize neutral leaks and improve propellant efficiency. This should also minimize divergence as the electric potential lines can be made less convex.

To increase propellant utilization and obtain better electron confinement the maximum magnetic field attainable was also doubled. Since the magnetic field is generated by permanent magnets this does not require any additional energy and could reduce the electron current inside the thruster, increasing its efficiency.



Figure 6.4: The ISCT200-MS-V2 magnetically shielded, low power, permanent magnet Hall thruster

### 6.2.3 Magnetic circuit

In order to achieve the magnetic topologies discussed in section 6.2.2 the magnetic circuit had to be redesigned. As with the ISCT200-MS-V1 the topologies were simulated with FEMM [141] taking into account temperature effects on both the iron and the magnets.

In order to finely shape the magnetic field in the first version some of the pieces of the magnetic circuit had to be made extremely thin. This made them difficult to manufacture and easy to saturate magnetically. This new version is made with thicker parts, especially around the magnetic poles. One of the advantages of using permanent magnets is that they do not require as complicated a magnetic architecture to magnetically shielded configuration. This lets us only change the pole area to switch between the different configurations as well as make a lighter magnetic circuit.

The magnetic circuit is made of high purity iron. It was chosen over the more efficient iron-cobalt for cost and availability reasons. Great care was taken in choosing the magnets. They need to be able to generate sufficient flux at relatively high temperature (up to 400°C). Their properties also need to be known over the whole operating range in order to accurately predict the magnetic topology. The material of choice for magnets that can meet those requirements is samarium cobalt. Their Curie temperature is above 800°C and they have one of the highest flux densities of any common permanent magnets [209,210]. Depending on the grade they can reach very high flux and special treatments allow for good thermal stability over their operating range.

The magnets are designed as segmented rings which allow us to have fine control of the magnetic field strength without buying expensive bespoke magnets for each desired configurations. The homogeneity of the field is ensured by the magnetic circuit even when the rings are only partially filled with magnets.

Heat treating of the magnetic circuit is done to ensure homogeneity of the magnetic properties after machining.

### 6.2.4 Discharge channel

The discharge channel dimensions are kept identical to the previous ISCT200-US and ISCT200-MS thrusters. It is however built differently to be able to test different wall materials more easily. The inside and outside wall pieces are removable and fixed to the back of the channel. Since little to no erosion is

expected they can be kept very thin. The side walls are designed to be simple and inexpensive to replace. If they are made of conductive materials they can be set to different potentials.

The default material is once again BN-SiO<sub>2</sub> M26 from Saint-Gobain chosen for its cost, ease of manufacture and performance.

### 6.2.5 Insulation

One of the issue specific to the lack of erosion is electrical insulation of the different parts of the thruster. With no erosion of the walls, the sputtered material from the vacuum chamber accumulates on the visible surfaces of the thruster. This conductive coating is usually cleaned by erosion inside the thruster near the exit plane which ensure that the anode potential is not applied to the thruster body or the magnetic poles.

In a MS thruster this coating is not cleaned, as seen in figure 4.16. Since this coating is formed on any surface that has line of sight to the sputtered back stop of the chamber, we chose to implement gaps and obstruction to this line of sight to make sure that some of the ceramics remain free of any coating. This ensure that no conductive path exists between the anode and the thruster body even after several hundred hours of firing.

### 6.2.6 Thermal design

While it is not a flight thruster, more considerations were taken on this new and improved version for the thermal design. Previous thrusters of the ISCT family had a relatively simple approach to the thermal issues. They took advantage of the space gain the permanent magnets allowed to install big copper heat drains. The resulting thrusters operated at low temperatures ( $\leq 200^{\circ}\text{C}$ ) but were exceedingly heavy. The ISCT200-MS-V1 weight in around 2.5 kg with its copper radiator and 0.9 kg without. In the second version the mass is brought down to 0.85 kg total. With further thermal and mechanical optimization that total mass could easily be reduced by 20% at the cost of more complex machining.

In the new thruster a COMSOL model was realized and thermal simulations were conducted. The geometry of the thermal model is imported directly from the CAD model. It accounts for conduction and radiation. As with all thermal models for thrusters one of the hardest part for getting accurate results is the thermal conductivity of the interfaces between different parts. This was adjusted from previous thermal studies at ICARE (see section 4.4.2) and data obtained from other thruster [211–214]. The inputs to the model remained very simple with an estimated 50% of the discharge power lost at the walls inside the discharge channel and at the anode. No thermal conduction to the support structure is assumed to account for a worst case scenario.

With the insulation gaps between the channel walls and the rest of the thruster the model predicts that the magnets are kept below their maximum operating temperature even at the inner pole.

### 6.2.7 Additively manufactured anode

Previous ISCT thrusters had a separate gas injector and anode. The gas injection was done through a porous ceramic material at the back of the thruster. A cavity upstream of this porous ring ensures that the injection is homogeneous. While this system produces a very even stream of neutral it necessitates the propellant to go through various materials that have to be mated to each other without any leaks. This was done using various seals that proved to cause reliability problems.

The anode of the ISCT thrusters is a simple thin metal ring along the outside wall of the discharge channel. It is connected radially through the ceramic walls and the magnetic circuit which caused insulation issues.

In commercial thrusters the anode and gas injector are often combined in a monoblock piece with a tube protruding from the back of the thruster welded to a hollow ring inside the discharge channel. This ring contains various baffles to evenly spread the propellant azimuthally around the thruster. This construction with internal baffles make the anode complex and expensive to manufacture. The high temperatures reached by the anode as well as the accuracy requirements mean that specialty fabrication processes such as lasers or electron beam welding need to be used.

In order to copy this design while keeping a reasonable manufacturing cost the anode is manufactured using direct metal laser sintering (DMLS) additive manufacturing. The result is a one piece stainless

steel anode with complex internal shapes. The additive manufacturing process is inexpensive for the size and material chosen and manufacturing time is very short (less than a week). The injection ports and internal features can be finely tuned for the application.

With the increase in material availability and progress in additive manufacturing we can hope that greater flexibility and lower cost will soon be available for researcher developing new plasma thrusters.

### 6.3 Conclusion

The simulation results confirm that the poor performances of the ISCT200-MS thruster is due to zones of no-ionization near the walls which greatly penalize such a small thruster. It also shows that the erosion is negligible in this thruster compared to a traditional US-HT.

From those results a new and improved version of the ISCT200-MS is designed with a revised magnetic topology as well as numerous improvements in the thermal, material, gas handling and electrode design.

Sadly the ISCT200-MS-V2 couldn't be tested before this document was written. While it is not certain that magnetically shielded thrusters in the 100 to 300 W discharge power range can be made as efficient as unshielded thrusters, we hope that this new version can significantly improve the performances of the thruster. An efficiency in the neighborhood of 35% might be an acceptable compromise if the lifespan is significantly improved.

### 6.3. CONCLUSION

---

# Conclusion

## Summary of results

This dissertation has been focused on the performances and the physics of low power Hall thrusters and the application of magnetic shielding topologies to them.

Experimental work on two low power thrusters in the 100 and 200 W range have shown that the scaling of Hall thruster to low discharge powers has very strong effects on their performances. The width of the discharge channel was identified as one of the major factor influencing performance. Widening the channel leads to an increase in propellant ionization and a reduction in divergence for both 100 W and 200 W thrusters. The discharge stability was also improved and the discharge envelope extended. Those improvements are probably due a reduction of the losses at the walls thanks to a lower surface to volume ratio. The only drawback of increasing channel width that was observed is an increase in electron current in the widest configuration of the 200 W thruster. Wider discharge channel results in a higher propellant utilization. The increase in propellant utilization translates to an increase in specific impulse, thrust and anode efficiency in the 100 W thruster.

A change in magnetic intensity also influences the plasma discharge. While a larger magnetic field in a narrow channel might make it more difficult to start, it stabilizes the discharge and widens the discharge envelope. The electrons are better confined which reduces the total discharge current and increases the ion current fraction. This results in a higher anode efficiency. The optimal efficiency point with respect to the magnetic field intensity was not identified. We presume that efficiency and stability start to decrease above a certain value as in kilowatt class thrusters. However the optimal magnetic field intensity appears to scale inversely with power in a non-linear way. The use of permanent magnet allows the design of very compact small thrusters. This is especially apparent in the inner magnetic pole as it becomes too small to fit an electromagnet coil.

The magnetic shielding topology was applied to a 200 W permanent magnet Hall thruster. Two thrusters were built, a standard unshielded version called here the ISCT200-US and a magnetically shielded one called the ISCT200-MS. The two thrusters show similar current-voltage discharge characteristics. However non-intrusive LIF measurements highlight that the ion behavior inside the thrusters is radically different. The acceleration region is shifted downstream in the magnetically shielded case and most of the potential drop happens outside the discharge channel. There are also differences in the ion velocity distribution functions near the walls. For the magnetically shielded thruster the ions are mostly directed away from the walls and their density falls as we get closer to the surface. In the standard thruster the majority of the ions goes toward the walls. Their density does not change significantly either. Moreover the average velocity parallel to the external wall is lower in the MS-HT than in the US-HT. This explains the lower erosion observed on the MS thruster. Above the magnetic poles some erosion was observed in the ISCT200-MS. LIF measurements have detected a “double peak” distribution of ions with one population going toward the surface while another goes away from it at around the same absolute velocity. This structure in the IVDF is not understood. While we do not have information on the ion flux, the velocity toward the pole is similar in both thrusters and is low compared to the erosion threshold. This fails to explain the slight pole erosion seen in the ISCT200-MS.

The two 200 W thrusters were also fired with conducting graphite walls instead of dielectric BN-SiO<sub>2</sub>. The ISCT200-MS is not affected by the change in wall material. Mean discharge current as well as discharge stability are undisturbed. The axial electric field is identical. Plume measurements show the same ion content and divergence of the exhaust plume. Thrust, specific impulse and anode efficiency are similar with both materials. In the ISCT200-US the mean discharge current increases with graphite and the discharge is less stable. The electric field is more spread out and is pushed downstream. The

divergence of the plume increases and the propellant utilization is slightly higher while the ion beam current fraction is lower. The thrust and specific impulse are not affected much by the change in wall material but increase in discharge current means that the efficiency is lower with graphite than with BN-SiO<sub>2</sub>. The good performances of the ISCT200-MS Hall thruster with graphite wall alleviate some of the concerns associated with ground qualification of magnetically shielded thrusters. The black conductive coating formed during testing in a vacuum chamber should not have any significant effect on the thruster characteristics.

When comparing the two thrusters with BN-SiO<sub>2</sub> walls, The ISCT200-US has better propellant utilization and higher ion beam current fraction while maintaining a slightly lower divergence. At the same discharge power the thrust of the unshielded thruster is one or two millinewtons higher than its shielded counterpart. This results in a higher anode efficiency for the ISCT200-US with a maximum around 38% at 250 W while the ISCT200-MS only reached a maximum of 24% at the same power level.

The difference in performance is mostly due to the ionization process. A higher fraction on multi-charged ions in the MS-HT explains part of the performance deficit as it increases the specific impulse at the cost of less thrust. However this is not enough to explain the large performance difference between the two thrusters. We proposed an explication based on the leak of neutrals near the walls of the thrusters. The low electron temperature near the walls of the shielded thruster mean that little to no ionization takes place there. This creates a path for the neutral injected near the anode to leak from the thruster without being ionized. This is all the more noticeable in small thrusters where the wall area to plasma volume ratio is much higher than in larger Hall thrusters. If this is the case, it could mean that the classical magnetic shielding topology will not be able to achieve high performance in small Hall thrusters. This topology could be even more sensitive to the surface to volume ratio.

Numerical simulations of both the ISCT200-US and ISCT200-MS confirm the issues observed during the experimental campaigns. The low propellant ionization is caused by an ionization zone not covering the whole discharge channel and allowing a large portion of neutrals to escape the thruster. Simulations also confirm that the wall erosion rate in the ISCT200-MS is orders of magnitude lower than in the ISCT200-US.

This experimental and numerical insight into the physics of a small magnetically shielded Hall thruster is used to design a new version of the ISCT200-MS. This second version is designed to have a more flexible magnetic field topology to allow for more magnetic flux and a topology that should promote better ionization while limiting wall erosion.

## Perspectives

This work has shown that small Hall thrusters can achieve up to 40% efficiency between 150 and 250 W. These performances are achieved with wider discharge channel and larger magnetic field intensity than in higher power thrusters. We found that the more intense magnetic field can make the thruster harder to start. This is particularly an issue when the magnetic field is generated by permanent magnets and cannot be turned off. While permanent magnets present numerous advantages for smaller thruster they could present some challenges when ignition is concerned. Novel ignition methods should be investigated if the discharge power is scaled below 100 W.

The performances were lowered considerably in the magnetic shielding configuration. If the design goal is a long lifespan low power Hall thruster, while magnetic shielding is an option, it might be simpler to substitute the usual boron nitride wall compounds by more sputter resistant materials such as alumina. The performance hit from using a non-optimal material in term of efficiency could be an acceptable compromise if the resulting performances are comparable to the ones obtained in magnetic shielding.

Alternatives to the canonical magnetic shielding topology might be more adapted to small thrusters. Efficient shielding of the walls might be achievable without implementing a true grazing line reaching all the way to the anode area. This way the ionization region could come closer to the walls and increase the propellant ionization efficiency. This would also allow to pull the maximum magnetic field peak closer to the exit plane and further reduce propellant losses.

The magnetic shielding configuration has virtually zero erosion and very little sensitivity to wall material. It therefore opens new design possibilities in Hall thruster. Thrusters with extremely thin walls, maybe even just coatings on a structural part should be feasible. This would potentially help with thermal management as well as mechanical strength. The walls could also be made of magnetic materials

and take an active part in generating the magnetic topology. Even without such radical design change it minimizes any risks associated with chamber material contaminating the discharge channel and changing the thruster characteristics. Moreover the graphite wall seems to expand the envelope of the MS-HT at higher discharge voltage.

On the magnetic shielding side a few questions remain open. The exact origin of pole erosion is not very well understood yet. While some 2D LIF spectroscopy fields have been taken near the inner pole of a 6 kW thrust [40, 150, 177], the size of the thruster didn't allow for good resolution close to the surface of the pole. Similar experiment in a small MS thruster where the collection optics can be brought closer to the probed point should be able to yield more accurate data all the way up to the surface.

The exact mechanism of the shielding can also be debated. While American study emphasis the importance of the grazing line, Perez-Grande [215] suggest that most of the erosion reduction comes from the translation of the discharge downstream. As far as we could see, in order to get magnetic field lines tangent to the walls, the maximum of the magnetic field has to be pushed downstream of the exit plane. This means that the acceleration region shifts to this position (as measured in section 4.5.1) and the ionization region is also translated by the same amount (see section 4.5.1). Perez-Grande argues that this reduces the density of ions as well as their mean energy and is the main reason for the erosion reduction. With this model careful shaping of the grazing line wouldn't be as important.

### 6.3. CONCLUSION

---

# Appendix A

## Overview of low power thrusters

Table A.1: Source of the data presented in figure A.2

Thruster	Source
ISCT100 V1	Mazouffre 2018 [216]
ISCT100 V2	Unpublished
T-40	Frieman 2015 [217]
HT100D	Ducci 2013 [218]
PlaS-40	Potapenko 2015 [219]
BHT-100	Szabo 2017 [86]
BHT-200	Szabo 2012 [220]
CAM200-EM	Lev 2016 [221]
CAMILA-HT-55	Kapulkin 2011 [222]
KM-20M	Bugrova 2001 [223]
SPT-20	Loyan 2007 [83]
SPT-30	Jacobson 1998 [84]
SPT-50	Manzella 1996 [205]
PSAC 100	Lim 2018 [224]
MaSMi-40	Conversano 2014 [127]
MaSMi-60-LM1	Conversano 2017 [173]
MaSMi-60-LM2	Conversano 2017 [129]
MaSMi-DM	Conversano 2017 [130]

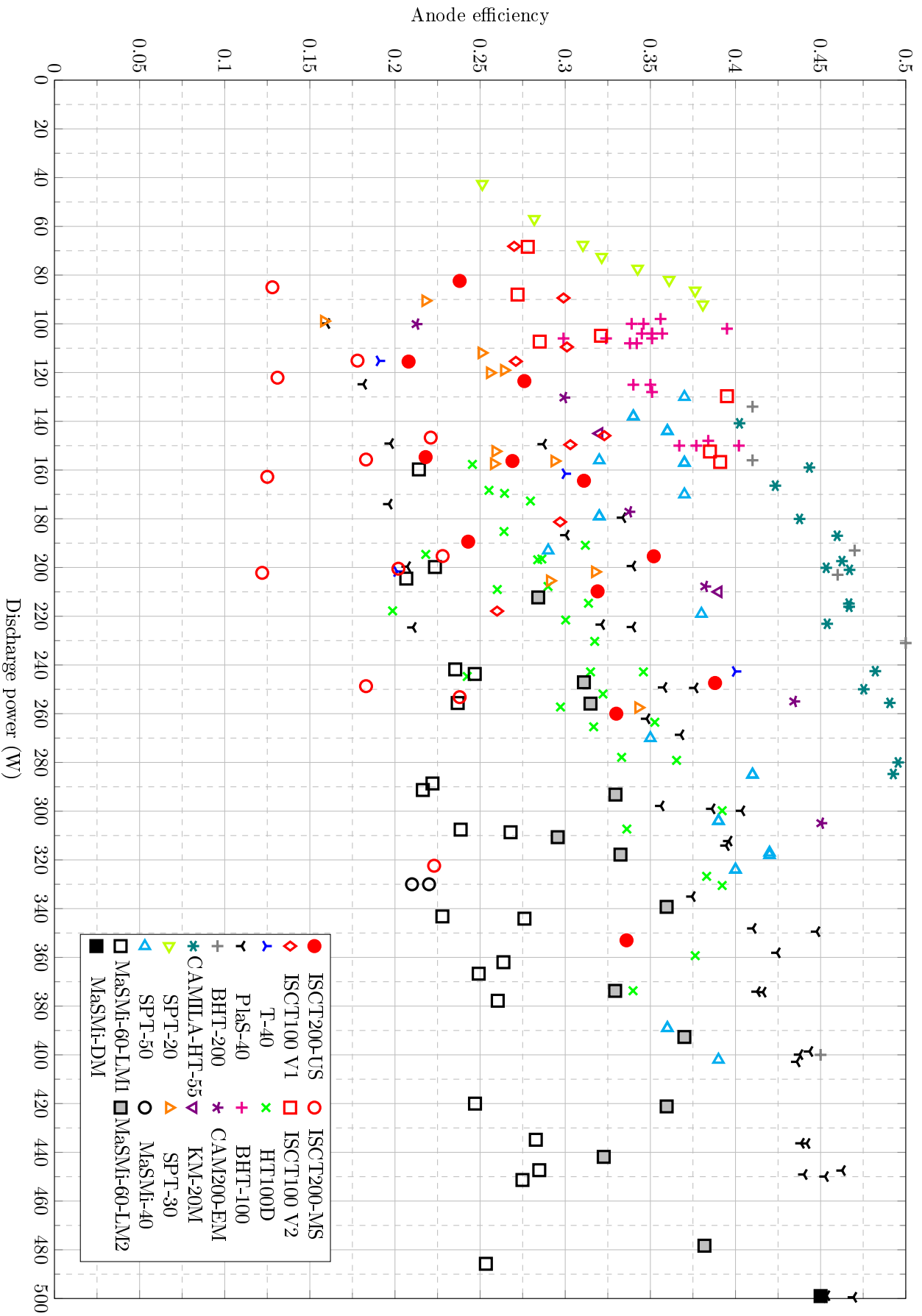


Figure A.1: Anode efficiency for low power thrusters

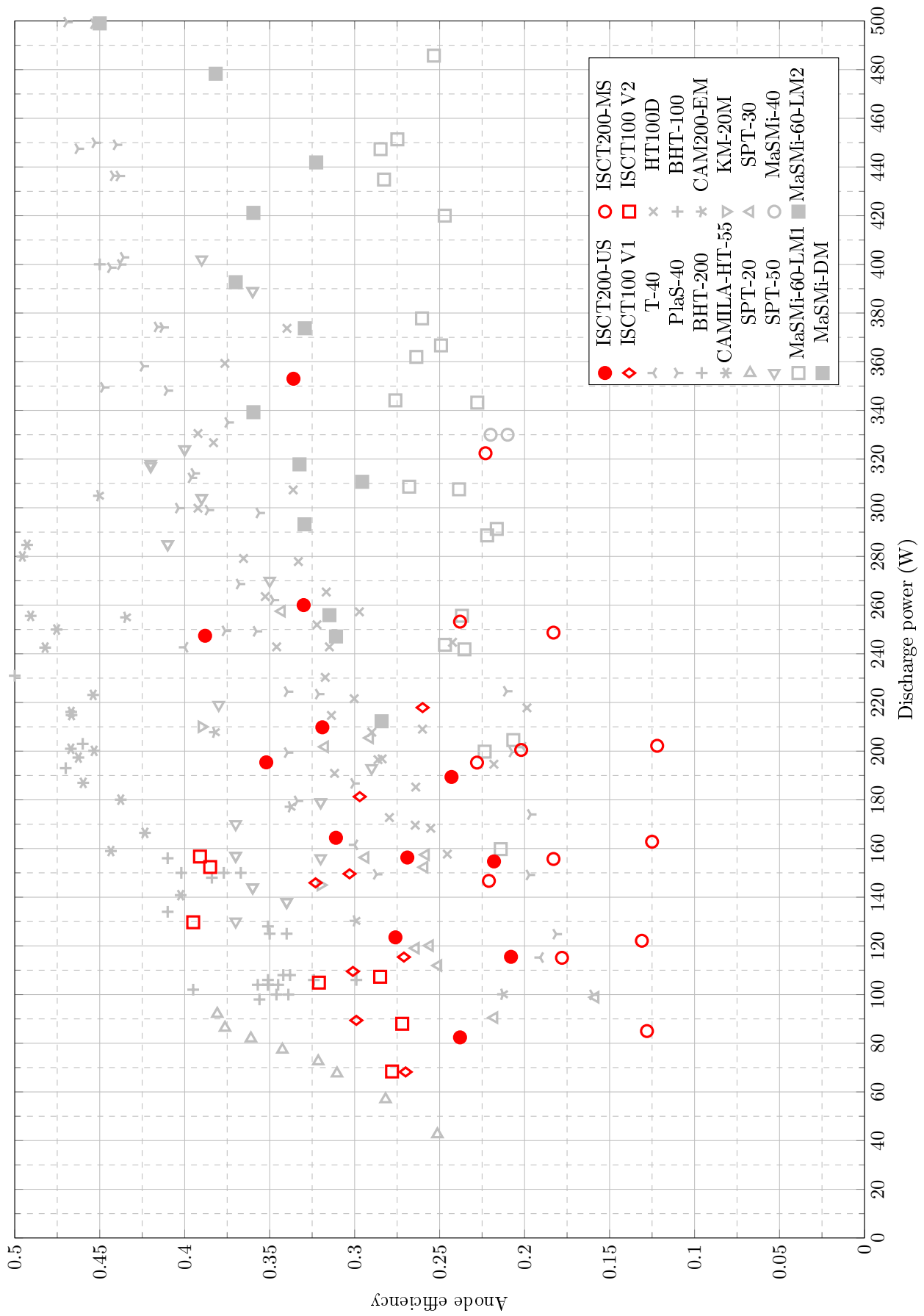


Figure A.2: Anode efficiency for low power thrusters, with ICARE's thruster highlighted

---

# Appendix B

## List of publications

### Journal articles (published)

- L. Grimaud, A. Pétin, J. Vaudolon, and S. Mazouffre, “*Perturbations induced by electrostatic probe in the discharge of Hall thrusters,*” **Rev. Sci. Instrum.**, vol. 87, no. 4, p. 043506, Apr. 2016.
- R. Jousot, L. Grimaud, and S. Mazouffre, “*Examination of a 5 A-class cathode with a LaB 6 flat disk emitter in the 2 A–20 A current range,*” **Vacuum**, vol. 146, pp. 52–62, Dec. 2017.
- L. Grimaud and S. Mazouffre, “*Ion behavior in low-power magnetically shielded and unshielded Hall thrusters,*” **Plasma Sources Sci. Technol.**, vol. 26, no. 5, p. 055020, Apr. 2017.
- L. Grimaud and S. Mazouffre, “*Conducting wall Hall thrusters in magnetic shielding and standard configurations,*” **J. Appl. Phys.**, vol. 122, no. 3, p. 033305, Jul. 2017.
- S. Mazouffre and L. Grimaud, “*Characteristics and Performances of a 100-W Hall Thruster for Microspacecraft,*” **IEEE Trans. Plasma Sci.**, vol. 46, no. 2, pp. 330–337, Feb. 2018.
- L. Grimaud and S. Mazouffre, “*Performance comparison between standard and magnetically shielded 200 W Hall thrusters with BN-SiO<sub>2</sub> and graphite channel walls,*” **Vacuum**, vol. 155, pp. 514–523, Sep. 2018.

### Journal articles (submitted)

- L. Garrigues, S. Santhosh, L. Grimaud, and S. Mazouffre, “*Operation of a Low-Power Hall Thruster: Comparison between Magnetically Unshielded and Shielded Configuration,*” **Plasma Sources Sci. Technol.**, 2018.
- S. Mazouffre, L. Grimaud, S. Tsikata, K. Matyash, and R. Schneider, “*Rotating spoke instabilities in a wall-less Hall thruster. Part I: Experiments.,*” **Plasma Sources Sci. Technol.**, 2018.
- K. Matyash, R. Schneider, S. Mazouffre, S. Tsikata, and L. Grimaud, “*Rotating spoke instabilities in a wall-less Hall thruster. Part II: Simulation.,*” **Plasma Sources Sci. Technol.**, 2018.

### Conference proceedings

- J. Vaudolon, L. Grimaud, and S. Mazouffre, “*Investigation of the ion transit time instability in a hall thruster combining time-resolved LIF spectroscopy and analytical calculations,*” in 51st AIAA/SAE/ASEE Joint Propulsion Conference, 2015.
- L. Grimaud, J. Vaudolon, S. Mazouffre, and C. Boniface, “*Design and characterization of a 200W Hall thruster in magnetic shielding configuration,*” in 52nd AIAA/SAE/ASEE Joint Propulsion Conference, 2016, pp. 1–17.

- 
- L. Grimaud, J. Vaudolon, and S. Mazouffre, “*Design and characterization of a 200 W low power Hall thruster in ‘magnetic shielding’ configuration,*” in Space Propulsion Conference 2016, 2016, no. May.
  - S. Mazouffre, L. Grimaud, S. Tsikata, and K. Matyash, “*Rotating plasma structures in the cross-field discharge of Hall thrusters,*” in Bulletin of the American Physical Society, 2016, vol. Volume 61, Number 9.
  - S. Mazouffre, L. Grimaud, S. Tsikata, K. Matyash, and R. Schneider, “*Investigation of rotating spoke instabilities in a wall-less Hall thruster. Part I: Experiments,*” in 35th International Electric Propulsion Conference, 2017, no. October, pp. 1–29.
  - K. Matyash, R. Schneider, S. Mazouffre, S. Tsikata, and L. Grimaud, “*Investigation of rotating spoke instabilities in a wall-less Hall thruster. Part II: Simulation.,*” in 35th International Electric Propulsion Conference, 2017, no. October, pp. 1–29.
  - A. Spethmann, T. Trottenberg, H. Kersten, F. Hey, L. Grimaud, and S. Mazouffre, “*Application of Force Measuring Probes for the Investigation of Sputtering and as Diagnostic for HEMP and Hall Thrusters,*” in 35th International Electric Propulsion Conference, 2017, p. IEPC-2017-245.
  - R. Jousset, G. Sary, L. Grimaud, L. Garrigues, S. Mazouffre, B. Laurent, C. Boniface, S. Oriol, F. Masson, S. A. Engines, S. Propulsion, and D. Lanceurs, “*Experimental and numerical investigations of a 5 A-class cathode with a LaB 6 flat disk emitter in the 2 A-20 A current range,*” in 35th International Electric Propulsion Conference, 2017, p. IEPC-2017-486.
  - L. Grimaud, S. Mazouffre, and C. Boniface, “*Performance comparison between standard and magnetically shielded 200 W Hall thrusters with BN-SiO<sub>2</sub> and graphite channel walls,*” in 35th International Electric Propulsion Conference, 2017, p. IEPC-2017-172.
  - L. Grimaud, S. Santhosh, L. Garrigues, S. Mazouffre, and C. Boniface, “*Performance and discharge characteristics of a 200 w magnetically shielded hall thruster: experimental results, numerical simulations and perspectives,*” in Space Propulsion 2018, 2018, no. May, p. SP2018\_00374.

# Appendix C

## Version française

### C.1 Propulsion électrique: principes de base, applications et nouveaux défis

Tout système de propulsion spatiale par réaction doit éjecter de la masse à une certaine vitesse pour pouvoir produire de la poussée. La poussée produite est proportionnelle au débit massique d'ergol éjecté et à sa vitesse. La célèbre équation de Tsiolkovski permet de calculer le gain de vitesse pour un véhicule en fonction de sa masse propre, de la masse d'ergol embarquée et la vitesse d'éjection des ergols. Elle montre que plus la vitesse d'éjection est grande plus le rapport masse d'ergol sur masse propre peut être petit. Cependant plus la vitesse d'éjection est grande plus il faut d'énergie à poussée équivalente. Cela signifie donc que tout système de propulsion à haute vitesse d'éjection est par nature très énergivore.

Les moteurs fusés chimiques fournissent l'énergie aux ergols via une réaction chimique exothermique. La quantité d'énergie par masse d'ergol est donc limitée par la chimie de la réaction. Cela limite les moteurs chimiques à une vitesse d'éjection maximale d'environ 5km/s. La propulsion électrique contourne cette limitation en découplant source d'énergie et masse de réaction. La puissance électrique sert directement à accélérer l'ergol. Ce dernier est la plupart du temps sous forme de plasma pour pouvoir utiliser directement les forces électromagnétiques. Plusieurs types de propulseurs électriques existent. Cette thèse porte sur le propulseur de Hall (PH) qui est l'un des plus utilisés actuellement. Leur relative simplicité ainsi que leur haut rapport poussé sur puissance en font un moteur particulièrement adapté aux applications commerciales telles que le maintien à post ou le transfert d'orbite.

Une des limitations principales des propulseurs de Hall est leur durée de vie. Dans la gamme traditionnelle des moteurs de 1 à 5 kW la durée de vie atteinte est aux alentours de 10 000 heures de tire. Mais pour les propulseurs de plus faible puissance celle-ci peut chuter à moins de 3000 heures. Cette limitation est due à l'érosion des parois du propulseur par le jet d'ions rapides. Pour remédier à ce problème une nouvelle technique dite « d'écrantage magnétique » a été testée aux États-Unis. Cette thèse se focalise sur l'utilisation de cette technique appliquée aux propulseurs de Hall de faible puissance.

### C.2 Diagnostiques plasmas et mesures de performances pour les propulseurs de Hall

Ce chapitre traite des différents moyens d'essais utilisés lors de cette thèse ainsi que de leurs limitations.

Les propulseurs testés dans ces études ont été tirés dans deux chambres différentes. La première est le banc d'essais NExET. Cette petite chambre de 1.8 par 0.7 m de diamètre permet le test de propulseurs de faible puissance jusqu'à 400 W. Le deuxième banc d'essais utilisé est PIVOINE-2g. Sa chambre sous vide est considérablement plus grande avec un diamètre de 2.2 m et 4 m de longueur. Ce banc d'essais est dimensionné pour accepter des propulseurs jusqu'à 20 kW de puissance électrique. Il possède également une balance de poussée.

Parmi les diagnostics utilisés l'un des plus fondamentaux sont les sondes planes et sondes de Faraday. Ces sondes balayent le panache des propulseurs afin de mesurer les propriétés du plasma. En particulier elles sont utilisées pour mesurer le courant ionique ce qui permet (après intégration) d'estimer la quantité

totale d'ions produite par le moteur ainsi que la proportion d'atomes ionisés.

Une balance de force est utilisée pour les mesures de poussée dans le banc d'essais PIVOINE-2g. La balance initiale est un pendule simple conçue pour des propulseurs de 1 à 20kW. Pour améliorer la précision de cette balance dans le cas de nos propulseurs de 100 et 200 W une version allégée a été testée. Malheureusement l'absence de systèmes d'amortissement a rendu la nouvelle balance trop instable pour une mesure précise et a dû être abandonnée. A sa place un traitement statistique des données collectées est utilisé pour améliorer la précision des mesures.

Un des moyens de mesure utilisé tout au long de cette thèse et la spectroscopie par fluorescence induite par laser (FIL). Cette technique repose sur l'excitation d'atomes ou d'ions métastables par un laser à une longueur d'onde bien définie. La longueur d'onde du laser est balayée afin de correspondre à celle d'excitation de l'espèce visée en tenant compte de l'effet Doppler. Lors de la désexcitation la lumière émise est collectée et son intensité peut être corrélée à la densité de particules voyageant à une certaine vitesse. Cela permet d'obtenir les profils de densité en vitesse des espèces ciblées.

Cette technique est comparée aux sondes de Langmuir et sondes émissives pour la mesure du potentiel plasma dans les propulseurs de Hall. Nos résultats obtenues sur des propulseurs de 200 et 1500 W démontrent des fortes perturbations de la décharge lorsque les sondes sont insérées dans le canal de décharge. La valeur moyenne du courant de décharge ainsi que ses dynamiques sont changées. Les perturbations sur les ions sont à la fois globales et locales.

### C.3 Propulseurs de Hall basse puissance: lois d'échelle et performances

Avec la miniaturisation des satellites des besoins émergent pour de petits systèmes de propulsion opérant à faible puissance ( $\leq 500$  W). Les lois d'échelles pour la conception de propulseurs de Hall sont mal définies. Par conséquent les petits PH ont des performances très variées.

Les deux paramètres étudiés dans ce chapitre sont l'intensité du champ magnétique ainsi que la largeur du canal de décharge. Ces paramètres sont variés sur deux propulseurs de faible puissances (100 et 200 W nominal). Des mesures de poussée, de divergence ainsi que de champ électrique sont réalisées avec ces propulseurs.

Les résultats obtenus montrent qu'un canal plus étroit résulte en un propulseur moins stable et plus difficile à démarrer. L'ionisation est également moins efficace avec le canal étroit ce qui diminue les performances du PH. Cette mauvaise ionisation peut être attribuée au rapport surface sur volume plus important quand le canal est étroit, ce qui rend les collisions entre les ions et les parois plus probables. Cela affecte particulièrement les petits propulseurs car leur rapport surface sur volume est bien plus élevé que pour les propulseurs de taille standard. La largeur du canal influence également la position du champ électrique d'accélération. Le champ se déplace en amont quand la largeur du canal augmente. Cela réduit la divergence du panache.

L'intensité du champ magnétique permet principalement de contrôler la plage de décharge du propulseur ainsi que le courant électronique vers l'anode. La décharge est plus stable et le propulseur peut opérer sur une plage de tensions et débit plus large lorsque le champ magnétique est plus élevé. La stabilité du courant de décharge est également améliorée. La valeur moyenne du courant de décharge est plus faible due au fait que le courant électronique diminue. Cela a pour effet d'augmenter le rendement du propulseur.

### C.4 La physique d'un petit propulseur de Hall à écrantage magnétique

L'une des principales limitations des propulseurs de Hall basse puissance est leur faible durée de vie. Du fait du rapport surface sur volume plus important dans ces propulseurs de petites tailles, le jet d'ions interfère plus avec les parois et cause une érosion plus importante. L'érosion est due à l'impact des ions avec les parois. Divers mécanismes sont responsables de l'accélération des ions vers les parois des propulseurs. Les deux effets les plus importants que l'on peut identifier sont le champ électrique principal qui accélère les ions à très haute énergie avec une direction presque tangente à la paroi ainsi que les

phénomènes de gaine le long des parois diélectriques. Ces derniers sont principalement dépendants de la nature des matériaux utilisés et de la température des électrons.

Une technique inventée au Jet Propulsion Laboratory permet de d'éliminer l'érosion. Elle repose sur une configuration dite d'écrantage magnétique qui protège les parois en diminuant la température électronique et en éloignant le champ électrique principal. Cette technique a démontré des résultats très prometteurs quand elle est appliquée à des propulseurs puissants (5 kW et au-delà). La poussée et l'impulsion spécifique ne sont pas modifiés alors que l'érosion est réduite au minimum de 3 ordres de grandeur.

Cette technique n'avait pour le moment pas été appliquée à des propulseurs de Hall de faible puissance. Pour étudier ce cas, l'ISCT200-US un propulseur de Hall standard a servi de base à la construction de l'ISCT200-MS, qui en est une copie qui implémente l'écrantage magnétique. Ces deux propulseurs de taille et construction identique servent de base de comparaison entre un propulseur standard et un propulseur écranté.

Les deux propulseurs ont des enveloppes de décharge similaires mais la version écrantée ne montre pas de signes d'érosion. Elle est également plus froide à puissance de décharge similaire.

La technique de diagnostic de fluorescence induite par laser est utilisée pour mesurer le comportement des ions à l'intérieur du canal de décharge. La mesure de leur vitesse au centre du canal montre que le champ électrique accélérateur est similaire en termes d'intensité mais est poussé en aval du plan de sorti. Cela réduit l'énergie moyenne des ions dans le canal.

De plus le comportement le long des parois est différent. Que ce soit sur la paroi interne ou externe la vitesse et densité des ions est plus faible en configuration écrantée. Cette mesure est une preuve directe de la réduction de l'érosion des parois.

Certaines études ayant montré que la surface supérieure des pôles magnétiques pouvait subir une érosion légère en écrantage magnétique, le comportement des ions a également été mesuré dans cette zone. Pour les deux propulseurs la spectroscopie FIL semble détecter des ions rapides allant à contre sens vers la surface des pôles. Ces ions ne sont pas expliqués. Malgré les précautions prises pour limiter les sources d'erreurs lors des mesures dans cette zone ils pourraient être la conséquence d'une aberration de mesure.

## C.5 Performances d'un propulseur de Hall à écrantage magnétique avec des parois en graphite et céramique

Dans ce chapitre les performances des deux propulseurs sont comparées.

En plus de leurs configurations normales avec des parois de canal en nitrure de bore, un jeu de parois en graphite est également utilisé. Il est connu que le matériau des parois des propulseurs de Hall a une grande influence sur la physique de la décharge et les performances.

Traditionnellement des composés à base de nitrure de bore sont utilisés avec différents additives. Ils présentent les meilleures performances en terme de rendement total du système de propulsion tout en ayant une résistance à l'érosion acceptable. Cependant de nombreux matériaux plus résistants à l'érosion existent. Dans les propulseurs standards ces matériaux résultent en un courant de décharge plus important pour une même poussée. Les performances sont donc significativement dégradées. L'une des propriétés physiques fondamentales qui influence la physique de la décharge est le comportement sous bombardement électronique. En fonction du matériau les électrons sont absorbés, réfléchis ou réémis de façon différentes ce qui change le comportement général des électrons dans le moteur.

Dans un propulseur à écrantage magnétique les électrons et le plasma en général interagissent moins avec les parois ce qui doit réduire leur influence sur la décharge. Pour tester cette hypothèse des parois en graphite sont testées. Non seulement le graphite est conducteur au lieu des isolants habituels mais ses propriétés d'émission électroniques secondaires sont très différentes des composés de nitrure de bore.

L'ISCT200-MS ne présente aucune différence dans ses caractéristiques de décharges entre les deux matériaux. Courant de décharge, divergence et contenu du jet plasma sont similaires. Pour le propulseur standard ISCT200-US le courant de décharge augmente de 20% pour le même débit et tensions de décharge. La zone d'accélération est décalée vers l'aval et la divergence du jet augmente.

L'ISCT200-US a un rendement total maximal mesuré de 39% et une impulsion spécifique de 1400 s à 250 W avec les parois en nitrure de bore. Avec le graphite ces performances sont réduites à 31% pour

1360s au maximum. Le propulseur écranté quant à lui n'atteint que 24% et 1020 s à 250 W quelque soit le matériau.

Ce rendement plus faible semble être principalement causé par une mauvaise ionisation du xénon. Cette mauvaise ionisation est attribuée aux pertes importantes près des parois dans le moteur écranté. Dans ces régions la densité électronique est faible et les atomes neutres ont plus de chance de s'échapper du canal sans être ionisés. Ce phénomène est d'autant plus sévère que le moteur est petit car le ratio de la taille de cette zone sur la taille totale du moteur est proportionnelle au diamètre du propulseur.

## C.6 Améliorations des performances de propulseurs de Hall à écrantage magnétique de faible puissance

Afin de vérifier les résultats et les conclusions obtenues lors des essais une série de simulations a été effectuée en collaboration avec Dr Laurent Garrigues du laboratoire LAPLACE. Le code utilisé utilise un modèle hybride particulaire et milieu continu. Les électrons sont considérés comme un fluide alors que les particules massives comme les atomes et les ions simplement ou doublement chargés sont représentés par des macro-particules. Cette technique représente un bon compromis entre la vitesse de calcul des modèles fluides et la précision potentiellement plus grande des modèles particuliers.

Une des limitations du modèle fluide pour les électrons est le phénomène de conductivité anormale observé dans les décharges en champs croisés. Pour prendre en compte cette mobilité non capturée par le modèle une fréquence de collision anormale est ajoutée. Cette fréquence de collision manuellement ajustée afin de pouvoir reproduire le profil de vitesse ionique mesuré par spectroscopie.

La simulation est en bon accord qualitatif avec les résultats expérimentaux. Le faible rendement de l'ISCT200-MS est reproduit et le problème d'ionisation est également identifié comme sa source. Le faible taux d'érosion du propulseur écranté est également obtenu numériquement.

La simulation permet également de mettre en évidence la proportion d'ions multichargés plus importante dans le propulseur écranté. Ce phénomène a été observé dans des propulseurs à haute puissance mais n'a pas pu être mesuré expérimentalement dans nos petits propulseurs.

Ayant confirmé l'analyse des problèmes réduisant les performances de l'ISCT200-MS une seconde version de ce propulseur est conçue. Afin d'augmenter le taux d'ionisation et de réduire les fuites près des parois l'intensité du champ magnétique est augmentée et la topologie magnétique est modifiée. Malheureusement ce propulseur n'a pas pu être testé avant la rédaction de ce manuscrit.

## C.7 Conclusion

# Bibliography

- [1] S. Mazouffre, L. Grimaud, S. Tsikata, K. Matyash, and R. Schneider, "Investigation of rotating spoke instabilities in a wall-less Hall thruster. Part I: Experiments," in *35th International Electric Propulsion Conference*, no. October, (Atlanta, Georgia), pp. 1–29, 2017. xii, 53
- [2] M. Lyszyk, E. Klinger, O. Secheresse, J. Bugeat, D. Valentian, A. Cadiou, T. Beltan, and C. Gelas, "Qualification status of the PPS 1350 plasma thruster," in *35th Joint Propulsion Conference and Exhibit*, no. June, (Reston, Virginia), American Institute of Aeronautics and Astronautics, jun 1999. xii, 54
- [3] L. Grimaud, J. Vaudolon, S. Mazouffre, and C. Boniface, "Design and characterization of a 200W Hall thruster in "magnetic shielding" configuration," in *52nd AIAA/SAE/ASEE Joint Propulsion Conference*, (Salt Lake City, UT), pp. 1–17, American Institute of Aeronautics and Astronautics, jul 2016. xiii, 16, 65, 72, 92
- [4] R. H. Frisbee, "Advanced Space Propulsion for the 21st Century," *Journal of Propulsion and Power*, vol. 19, pp. 1129–1154, nov 2003. 3
- [5] S. Mazouffre, "Electric propulsion for satellites and spacecraft: established technologies and novel approaches," *Plasma Sources Science and Technology*, vol. 25, p. 033002, jun 2016. 3, 4
- [6] S. N. BATHGATE, M. M. M. BILEK, and D. R. MCKENZIE, "Electrodeless plasma thrusters for spacecraft: a review," *Plasma Science and Technology*, vol. 19, p. 083001, aug 2017. 3, 4
- [7] E. Ahedo, "Plasmas for space propulsion," *Plasma Physics and Controlled Fusion*, vol. 53, no. 12, p. 124037, 2011. 3, 4
- [8] D. Krejci and P. Lozano, "Space Propulsion Technology for Small Spacecraft," *Proceedings of the IEEE*, vol. 106, pp. 362–378, mar 2018. 3, 4
- [9] M. Martinez-Sanchez and J. E. Pollard, "Spacecraft Electric Propulsion-An Overview," *Journal of Propulsion and Power*, vol. 14, no. 5, pp. 688–699, 1998. 3, 4
- [10] A. Khrabrov, "Development and Flight Tests of the First Electric Propulsion System in Space," in *30th International Electric Propulsion Conference*, (Florence, Italy), pp. IEPC–2007–109, 2007. 4
- [11] D. Y. Oh, J. S. Snyder, D. M. Goebel, R. R. Hofer, and T. M. Randolph, "Solar Electric Propulsion for Discovery-Class Missions," *Journal of Spacecraft and Rockets*, vol. 51, pp. 1822–1835, nov 2014. 5
- [12] J. R. Wertz, D. F. Everett, and J. J. Puschell, *Space mission engineering : the new SMAD*. Microcosm Press, 2011. 5
- [13] J. Vaudolon, *Electric field determination and magnetic topology optimization in Hall thrusters*. PhD thesis, Université d'Orléans, 2015. 6, 16, 38, 59, 78
- [14] V. V. Zhurin, H. R. Kaufman, and R. S. Robinson, "Physics of closed drift thrusters," *Plasma Sources Science and Technology*, vol. 8, pp. R1–R20, feb 1999. 7, 60
- [15] D. M. Goebel and I. Katz, *Fundamentals of Electric Propulsion*. Hoboken, NJ, USA: John Wiley & Sons, Inc., oct 2008. 7, 51, 52, 56

- [16] J.-P. Boeuf, "Tutorial: Physics and modeling of Hall thrusters," *Journal of Applied Physics*, vol. 121, p. 011101, jan 2017. 7
- [17] H. C. Cole, "A high-current hall accelerator," *Nuclear Fusion*, vol. 10, no. 3, pp. 271–275, 1970. 7
- [18] E. Y. Choueiri, "Fundamental difference between the two Hall thruster variants," *Physics of Plasmas*, vol. 8, pp. 5025–5033, nov 2001. 8
- [19] V. Kim, K. Kozubsky, V. M. Murashko, and A. Semenko, "History of the Hall Thrusters Development in USSR," *30th International Electric Propulsion Conference*, pp. 17–20, 2007. 9, 36, 53
- [20] L. H. Caveny, F. M. Curran, and J. R. Brophy, "Overview of the Ballistic Missile Defense Organization's Electric Propulsion Program," in *23rd International Electric Propulsion Conference*, pp. IEPC-90-002, 1993. 9
- [21] C. O. BROWN and E. A. PINSLEY, "Further experimental investigations of a cesium hall-current accelerator," *AIAA Journal*, vol. 3, pp. 853–859, may 1965. 9
- [22] C. M. BANAS, C. O. BROWN, and E. A. PINSLEY, "Hall-current accelerator utilizing surface contact ionization," *Journal of Spacecraft and Rockets*, vol. 1, pp. 525–531, sep 1964. 9
- [23] G. L. CANN and G. L. MARLOTTE, "Hall current plasma accelerator," *AIAA Journal*, vol. 2, pp. 1234–1241, jul 1964. 9
- [24] H. R. Kaufman and R. S. Robinson, "ELECTRIC THRUSTER RESEARCH," tech. rep., LEWIS RESEARCH CENTER NATIONAL AERONAUTICS AND SPACE ADMINISTRATION, 1982. 9
- [25] R. Conversano, *Low-Power Magnetically Shielded Hall Thrusters*. PhD thesis, Univeristy of California, Los Angeles, 2015. 11, 58, 89, 90, 97
- [26] N. Gascon, M. Dudeck, and S. Barral, "Wall material effects in stationary plasma thrusters. I. Parametric studies of an SPT-100," *Physics of Plasmas*, vol. 10, pp. 4123–4136, oct 2003. 11, 40, 44, 78, 80, 85, 93
- [27] A. M. Kapulkin, A. D. Grishkevich, and V. F. Prisnyakov, "Outside electric field thruster," *Space Technology*, vol. 15, no. 6, pp. 391–394, 1995. 11
- [28] V. Viktorov, A. Kapulkin, and V. Prisnyakov, "High-frequency oscillations in one-stage accelerator with external electric field," in *All-union conference on plasma accelerators and ion injectors*, 1989. 11
- [29] A. Antipov, A. Grishkevich, V. Ignatenko, and A. Kapulkin, "Energy characteristics of two-stage accelerator with external electric field," in *All-union conference on plasma accelerators and ion injectors*, 1989. 11
- [30] A. M. Kapulkin, V. F. Prisnyakov, and S. P. Vackhnyuk, "Outside electric field accelerators. Physics of processes and technical applications," tech. rep., Dniepropetrovsk State University 72, Dniepropetrovsk, Ukraine, 1993. 11
- [31] S. Mazouffre, S. Tsikata, and J. Vaudolon, "Development and experimental characterization of a wall-less Hall thruster," *Journal of Applied Physics*, vol. 116, no. 24, p. 243302, 2014. 11
- [32] J. Vaudolon, S. Mazouffre, C. Hénaux, D. Harribey, and A. Rossi, "Optimization of a wall-less Hall thruster," *Applied Physics Letters*, vol. 107, p. 174103, oct 2015. 11
- [33] L. Garrigues, S. Mazouffre, J. Vaudolon, and S. Tsikata, "Azimuthal micro-instability inside a wall-less hall thruster," in *2015 IEEE International Conference on Plasma Sciences (ICOPS)*, pp. 1–1, IEEE, may 2015. 11
- [34] I. G. Mikellides, I. Katz, R. R. Hofer, D. M. Goebel, K. de Grys, and A. Mathers, "Magnetic shielding of the channel walls in a Hall plasma accelerator," *Physics of Plasmas*, vol. 18, no. 3, p. 033501, 2011. 11, 65

- [35] S. Mazouffre, G. Largeau, L. Garrigues, C. Boniface, and K. Dannenmayer, "Evaluation of various probe designs for measuring the ion current density in a Hall thruster plume," in *Proceedings of the 35th International Electric Propulsion Conference*, (Atlanta, Georgia), pp. IEPC2017–336, 2017. 14, 16, 42, 85, 100
- [36] R. R. Hofer and J. R. Anderson, "Finite Pressure Effects in Magnetically Shielded Hall Thrusters," in *50th AIAA/ASME/SAE/ASEE Joint Propulsion Conference*, (Reston, Virginia), American Institute of Aeronautics and Astronautics, jul 2014. 14, 100
- [37] D. Brown and A. Gallimore, "Evaluation of Plume Divergence and Facility Effects on Far-Field Faraday Probe Current Density Profiles," *Proceedings of the 31st International Electric Propulsion Conference*, vol. 298, no. IEPC Paper 2009-030, 2009. 14
- [38] S. Mazouffre, "Laser-induced fluorescence diagnostics of the cross-field discharge of Hall thrusters," *Plasma Sources Science and Technology*, vol. 22, p. 013001, feb 2013. 21
- [39] S. Mazouffre, "Laser-induced fluorescence spectroscopy applied to electric thrusters," in *Electric Propulsion Systems: from recent research developments to industrial space applications - STO-AVT-263*, pp. 10–1, Von Karman Institute for fluid dynamics, vki lectur ed., 2016. 21
- [40] B. Jorns, C. A. Dodson, J. R. Anderson, D. M. Goebel, R. R. Hofer, M. J. Sekerak, A. Lopez Ortega, and I. G. Mikellides, "Mechanisms for Pole Piece Erosion in a 6-kW Magnetically-Shielded Hall Thruster," in *52nd AIAA/SAE/ASEE Joint Propulsion Conference*, no. July, (Salt Lake City, UT), pp. 1–21, American Institute of Aeronautics and Astronautics, jul 2016. 22, 72, 73, 91, 109
- [41] J. Vaudolon and S. Mazouffre, "Indirect determination of the electric field in plasma discharges using laser-induced fluorescence spectroscopy," *Physics of Plasmas*, vol. 21, p. 093505, sep 2014. 23
- [42] K. Dannenmayer, P. Kudrna, M. Tichý, and S. Mazouffre, "Measurement of plasma parameters in the far-field plume of a Hall effect thruster," *Plasma Sources Science and Technology*, vol. 20, p. 065012, dec 2011. 23
- [43] K. Dannenmayer and S. Mazouffre, "Compact high-speed reciprocating probe system for measurements in a Hall thruster discharge and plume," *Review of Scientific Instruments*, vol. 83, no. 12, p. 123503, 2012. 23, 24
- [44] A. W. Smith and M. A. Cappelli, "Time and space-correlated plasma potential measurements in the near field of a coaxial Hall plasma discharge," *Physics of Plasmas (1994-present)*, vol. 16, no. 7, p. 73504, 2009. 23
- [45] L. Albarede, S. Mazouffre, A. Bouchoule, and M. Dudeck, "Low-frequency electron dynamics in the near field of a Hall effect thruster," *Physics of Plasmas (1994-present)*, vol. 13, no. 6, p. 63505, 2006. 23
- [46] B. E. Beal, A. D. Gallimore, J. M. Haas, and W. A. Hargus, "Plasma Properties in the Plume of a Hall Thruster Cluster," *Journal of Propulsion and Power*, vol. 20, pp. 985–991, nov 2004. 23
- [47] B. E. Beal, A. D. Gallimore, and W. A. Hargus Jr, "Plasma properties downstream of a low-power Hall thruster," *Physics of Plasmas (1994-present)*, vol. 12, no. 12, p. 123503, 2005. 23
- [48] R. B. Lobbia and B. E. Beal, "Recommended Practice for Use of Langmuir Probes in Electric Propulsion Testing," *Journal of Propulsion and Power*, vol. 33, no. 3, pp. 566–581, 2017. 23
- [49] W. A. Hargus and M. A. Cappelli, "Interior and exterior laser-induced fluorescence and plasma measurements within a Hall thruster," *Journal of Propulsion and Power*, vol. 18, no. 1, pp. 159–168, 2002. 23, 30
- [50] J. M. Haas and A. D. Gallimore, "Internal plasma potential profiles in a laboratory-model Hall thruster," *Physics of Plasmas*, vol. 8, no. 2, p. 652, 2001. 23
- [51] J. Haas, *Low-perturbation interrogation of the internal and near-field plasma structure of a Hall thruster using a high-speed probe positioning system*. PhD thesis, University of Michigan, 2001. 23

- [52] J. A. Linnell and A. D. Gallimore, "Internal plasma potential measurements of a Hall thruster using xenon and krypton propellant," *Physics of Plasmas*, vol. 13, no. 9, p. 093502, 2006. 23
- [53] Y. Raitses, D. Staack, M. Keidar, and N. J. Fisch, "Electron-wall interaction in Hall thrusters," *Physics of Plasmas*, vol. 12, no. 5, p. 057104, 2005. 23
- [54] S. Mazouffre, G. Bourgeois, K. Dannenmayer, and A. Lejeune, "Ionization and acceleration processes in a small, variable channel width, permanent-magnet Hall thruster," *Journal of Physics D: Applied Physics*, vol. 45, p. 185203, may 2012. 23, 42, 47
- [55] M. Touzeau, M. Prioul, S. Roche, N. Gascon, C. Pérot, F. Darnon, S. Béchu, C. Philippe-Kadlec, L. Magne, and P. Lasgorceix, "Plasma diagnostic systems for Hall-effect plasma thrusters," *Plasma Physics and Controlled Fusion*, vol. 42, no. 12B, p. B323, 2000. 24
- [56] A. I. Morozov, "Stationary plasma thruster (SPT) development steps and future perspectives," in *23rd International Electric Propulsion Conference*, (Seattle, WA), p. 945, Electric Rocket Propulsion Society, 1993. 24
- [57] D. Gawron, S. Mazouffre, N. Sadeghi, and A. Héron, "Influence of magnetic field and discharge voltage on the acceleration layer features in a Hall effect thruster," *Plasma Sources Science and Technology*, vol. 17, p. 025001, may 2008. 24
- [58] A. Pétin, S. Mazouffre, Dannenmayer Kathe, P. Kudrna, and M. Tichy, "Time-averaged and time-varying plasma potential in the near-field plume of a Hall thruster," in *33rd International Electric Propulsion Conference*, (Washington, DC), pp. 1–14, Electric Rocket Propulsion Society, 2013. 24
- [59] S. Mazouffre, A. Petin, P. Kudrna, and M. Tichy, "Development of a High-Frequency Emissive Probe System for Plasma Potential Measurements in a Hall Thruster," *IEEE Transactions on Plasma Science*, vol. 43, pp. 29–34, jan 2015. 24
- [60] J. P. Sheehan, Y. Raitses, N. Hershkowitz, and M. McDonald, "Recommended Practice for Use of Emissive Probes in Electric Propulsion Testing," *Journal of Propulsion and Power*, pp. 1–24, nov 2016. 24
- [61] J. P. Sheehan and N. Hershkowitz, "Emissive probes," *Plasma Sources Science and Technology*, vol. 20, no. 6, p. 63001, 2011. 24
- [62] J. P. Sheehan, Y. Raitses, N. Hershkowitz, I. Kaganovich, and N. J. Fisch, "A comparison of emissive probe techniques for electric potential measurements in a complex plasma," *Physics of Plasmas*, vol. 18, no. 7, p. 073501, 2011. 24
- [63] J. P. Sheehan, Y. Raitses, and N. Hershkowitz, "Accurately Determining the Plasma Potential Using Emissive Probes," in *33rd International Electric Propulsion Conference*, (Washington, D.C), 2013. 24
- [64] G. D. Hobbs and J. A. Wesson, "Heat flow through a Langmuir sheath in the presence of electron emission," *Plasma Physics*, vol. 9, pp. 85–87, jan 1967. 24, 51
- [65] J. Vaudolon, B. Khiar, and S. Mazouffre, "Time evolution of the electric field in a Hall thruster," *Plasma Sources Science and Technology*, vol. 23, p. 022002, apr 2014. 26, 30
- [66] J. M. Haas, A. D. Gallimore, K. McFall, and G. Spanjers, "Development of a high-speed, reciprocating electrostatic probe system for Hall thruster interrogation," *Review of Scientific Instruments*, vol. 71, no. 11, p. 4131, 2000. 26
- [67] D. Staack, Y. Raitses, and N. Fisch, "Investigations of Probe Induced Perturbations in a Hall Thruster," in *38th AIAA/ASME/SAE/ASEE Joint Propulsion Conference & Exhibit*, (Reston, Virginia), American Institute of Aeronautics and Astronautics, jul 2002. 27, 83
- [68] B. Jorns, D. M. Goebel, and R. R. Hofer, "Plasma Perturbations in High-Speed Probing of Hall Thruster Discharge Chambers: Quantification and Mitigation," in *51st AIAA/SAE/ASEE Joint Propulsion Conference*, (Pasadena, CA), American Institute of Aeronautics and Astronautics, jul 2015. 27, 83

- [69] M. Bauccio, *ASM engineered materials reference book*. CRC, 1994. 33
- [70] D. Staack, Y. Raitses, and N. J. Fisch, “Shielded electrostatic probe for nonperturbing plasma measurements in Hall thrusters,” *Review of Scientific Instruments*, vol. 75, no. 2, p. 393, 2004. 33
- [71] B. Reid and A. Gallimore, “Plasma Potential Measurements in the Discharge Channel of a 6-kW Hall Thruster,” in *44th AIAA/ASME/SAE/ASEE Joint Propulsion Conference & Exhibit*, (Reston, Virginia), American Institute of Aeronautics and Astronautics, jul 2008. 33
- [72] I. Romadanov, Y. Raitses, A. Diallo, K. Hara, I. D. Kaganovich, and A. Smolyakov, “On limitations of laser-induced fluorescence diagnostics for xenon ion velocity distribution function measurements in Hall thrusters,” *Physics of Plasmas*, vol. 25, p. 033501, mar 2018. 33
- [73] ОКБ Факел, “КОСМИЧЕСКИЕ АППАРАТЫ С ОБОРУДОВАНИЕМ ОКБ «ФАКЕЛ»,” last accessed 2018-12-06. [http://www.fakel-russia.com/images/content/o\\_kompanii/letnaya\\_istoriya/KA\\_s\\_oborudovaniem.pdf](http://www.fakel-russia.com/images/content/o_kompanii/letnaya_istoriya/KA_s_oborudovaniem.pdf). 35
- [74] V. I. Garkusha, S. Grishin, and S. Mironov, “Electric propulsion activity in TsNIIMASH,” in *24th International Electric Propulsion Conference*, pp. IEPC-95-09, 1995. 36
- [75] G. C. Soulas, T. W. Haag, D. a. Herman, W. Huang, H. Kamhawi, and R. Shastry, “Performance Test Results of the NASA-457M v2 Hall Thruster,” *48th AIAA/ASME/SAE/ASEE Joint Propulsion Conference & Exhibit*, 2012. 36
- [76] H. Kamhawi, T. Haag, D. Jacobson, and D. Manzella, “Performance Evaluation of the NASA-300M 20 kW Hall Thruster,” in *47th AIAA/ASME/SAE/ASEE Joint Propulsion Conference & Exhibit*, (Reston, Virginia), American Institute of Aeronautics and Astronautics, jul 2011. 36
- [77] D. L. Brown, B. E. Beal, and J. M. Haas, “Air Force Research Laboratory High power Electric Propulsion Technology Development,” in *IEEE Aerospace Conference*, vol. 0188, pp. 1-9, 2010. 36
- [78] R. Florenz, P. Y. Peterson, and A. D. Gallimore, “Developmental Status of a 100-kW Class Laboratory Nested channel Hall Thruster,” in *33rd International Electric Propulsion Conference*, pp. 1-9, 2011. 36
- [79] J. Szabo, B. Pote, V. Hruba, L. Byrne, R. Tadrake, G. Kolencik, H. Kamhawi, and T. Haag, “A Commercial One Newton Hall Effect Thruster for High Power In-Space Missions,” in *47th AIAA/ASME/SAE/ASEE Joint Propulsion Conference & Exhibit*, (Reston, Virginia), American Institute of Aeronautics and Astronautics, jul 2011. 36
- [80] S. Zurbach, N. Cornu, P. Lasgorceix, Snecma, and Orleans, “Performance Evaluation of a 20 kW Hall Effect Thruster,” in *32nd International Electric Propulsion Conference*, pp. 1-10, 2011. 36
- [81] A. Piragino, A. Leporini, V. Giannetti, D. Pedrini, A. Rossodivita, T. Andreussi, M. Andrenucci, and D. Estublier, “Characterization of a 20 kW-class Hall Effect Thruster,” in *35th International Electric Propulsion Conference*, (Atlanta, Georgia), pp. IEPC-2017-381, 2017. 36
- [82] D. Yongjie, L. Hong, W. Liqiu, H. Yanlin, S. Yan, L. Hui, N. Zhongxi, M. Wei, and Y. Daren, “Overview of Hall Electric Propulsion in China,” *IEEE Transactions on Plasma Science*, pp. 1-20, 2017. 36, 58
- [83] A. Loyan and T. Maksymenko, “Performance Investigation of Spt-20M Low Power Hall Effect Thruster,” in *30th International Electric Propulsion Conference*, (Florence, Italy), pp. IEPC-2007-100, 2007. 36, 38, 111
- [84] D. T. Jacobson and R. S. Jankovsky, “Test results of a 200W class Hall thruster,” *AIAA/ASME/SAE/ASEE Joint Propulsion Conference and Exhibit*, *34th, Cleveland, OH, July 13-15, 1998*, no. December, pp. AIAA-1998-3792, 1998. 36, 111
- [85] D. Jacobson and R. Jankovsky, “Test results of a 200W class Hall thruster,” in *34th AIAA/ASME/SAE/ASEE Joint Propulsion Conference and Exhibit*, (Reston, Virginia), American Institute of Aeronautics and Astronautics, jul 1998. 36

- [86] J. J. Szabo, R. Tedrake, E. Metivier, S. Paintal, and Z. Taillefer, "Characterization of a One Hundred Watt, Long Lifetime Hall Effect Thruster for Small Spacecraft," in *53rd AIAA/SAE/ASEE Joint Propulsion Conference*, (Reston, Virginia), American Institute of Aeronautics and Astronautics, jul 2017. 36, 44, 58, 111
- [87] Y. Raitses and N. J. Fisch, "Parametric investigations of a nonconventional Hall thruster," *Physics of Plasmas*, vol. 8, no. 5, p. 2579, 2001. 36
- [88] T. Ikeda, K. Togawa, H. Tahara, and Y. Watanabe, "Performance characteristics of very low power cylindrical Hall thrusters for the nano-satellite "PROITERES-3"," *Vacuum*, vol. 88, pp. 63–69, feb 2013. 36
- [89] A. Smirnov, Y. Raitses, and N. Fisch, "Performance Studies of Miniaturized Cylindrical and Annular Hall Thrusters," in *38th AIAA/ASME/SAE/ASEE Joint Propulsion Conference & Exhibit*, no. July, (Reston, Virginia), pp. 1–8, American Institute of Aeronautics and Astronautics, jul 2002. 37
- [90] V. Khayms, *Advanced Propulsion for Microsatellites*. PhD thesis, MIT, 2000. 37
- [91] T. Ito, N. Gascon, S. Crawford, M. Cappelli, and Stanford, "Ultra-Low Power Stationary Plasma Thruster," in *29th International Electric Propulsion Conference*, pp. 1–7, 2005. 37
- [92] J.-D. de La Harpe, R. Branam, R. Huffman, S. Paintal, and R. Tedrake, " $\mu$ -Hall Effect Thruster Characterization," in *49th AIAA Aerospace Sciences Meeting including the New Horizons Forum and Aerospace Exposition*, no. January, (Reston, Virginia), pp. 1–15, American Institute of Aeronautics and Astronautics, jan 2011. 37
- [93] M. Warren, R. Branam, and C. Hartsfield, "Examination of Halbach Permanent Magnet Arrays in Miniature Hall-Effect Thrusters," *53rd AIAA/SAE/ASEE Joint Propulsion Conference*, no. July, pp. 1–10, 2017. 37
- [94] Dannenmayer Kathe, *Scaling laws and electron properties in Hall effect thrusters*. PhD thesis, Université d'Orléans, 2012. 37, 45
- [95] S. Mazouffre, P. Echegut, and M. Dudeck, "A calibrated infrared imaging study on the steady state thermal behaviour of Hall effect thrusters," *Plasma Sources Science and Technology*, vol. 16, pp. 13–22, feb 2007. 37, 50, 60, 92, 100
- [96] L. Garrigues, G. J. M. Hagelaar, C. Boniface, and J. P. Boeuf, "Anomalous conductivity and secondary electron emission in Hall effect thrusters," *Journal of Applied Physics*, vol. 100, p. 123301, dec 2006. 37, 50, 92, 96, 97, 100
- [97] G. Bourgeois, *Influence de la topologie magnétique , de la cathode et de la section du canal sur l'accélération des ions dans un propulseur à effet Hall*. PhD thesis, Université d'Orléans, 2012. 39, 53
- [98] S. Barral, K. Makowski, Z. Peradzynski, N. Gascon, and M. Dudeck, "Wall material effects in stationary plasma thrusters. II. Near-wall and in-wall conductivity," *Physics of Plasmas*, vol. 10, no. 10, p. 4137, 2003. 44, 92
- [99] N. Gascon, *Etude de propulseurs plasmiques à effet Hall pour systèmes spatiaux : performances, propriétés des décharges et modélisation hydrodynamique*. PhD thesis, Aix-Marseille 1, 2000. 44, 78, 80, 93
- [100] A. Lejeune, K. Dannenmayer, G. Bourgeois, S. Mazouffre, M. Guyot, and S. Denise, "Impact of the channel width on Hall thruster discharge properties and performances," in *Proceedings of the 32nd International Electric Propulsion Conference*, pp. IEPC–2011–019, 2011. 45
- [101] Y. Raitses, L. Dorf, A. Litvak, and N. Fisch, "Plume Reduction in Segmented Electrode Hall Thruster," *Journal of Applied Physics*, vol. 88, no. 2000, pp. 1263–1270, 2000. 47

- [102] Y. Raitses, Y. Raitses, D. Staack, D. Staack, L. a. Dorf, L. a. Dorf, N. J. Fisch, and N. J. Fisch, "Controlling Ion Acceleration Region in Hall thrusters," *Proceedings of the International Electric Propulsion Conference 2005 (IEPC05)*, no. May 2016, pp. 29–32, 2005. 47, 78
- [103] Y. Raitses, D. Staack, M. Keidar, and N. J. Fisch, "Electron-wall interaction in Hall thrusters," *Physics of Plasmas*, vol. 12, p. 057104, may 2005. 48
- [104] Y. Garnier, V. Viel, J.-F. Roussel, and J. Bernard, "Low-energy xenon ion sputtering of ceramics investigated for stationary plasma thrusters," *Journal of Vacuum Science & Technology A: Vacuum, Surfaces, and Films*, vol. 17, no. 6, p. 3246, 1999. 50
- [105] V. Kim, V. Kozlov, A. Semenov, and I. Shkarban, "Investigation of the Boron Nitride based Ceramics Sputtering Yield Under its Bombardment by Xe and Kr ions," *27th International Electric Propulsion Conference*, pp. 15–19, 2001. 50
- [106] Y. Yamamura and H. Tawara, "Energy dependence of ion-induced sputtering yields from monatomic solids at normal incidence," *Atomic Data and Nuclear Data Tables*, vol. 62, pp. 149–253, mar 1996. 50
- [107] I. G. Mikellides, I. Katz, R. R. Hofer, and D. M. Goebel, "Magnetic shielding of a laboratory Hall thruster. I. Theory and validation," *Journal of Applied Physics*, vol. 115, p. 043303, jan 2014. 50
- [108] S. Cheng and M. Martinez-Sanchez, "Hybrid Particle-in-Cell Erosion Modeling of Two Hall Thrusters," *Journal of Propulsion and Power*, vol. 24, pp. 987–998, sep 2008. 50
- [109] P. Sarrailh, M. Belhaj, V. Inguibert, and C. Boniface, "Synergic erosion of ceramic by electron and ion simultaneous irradiation of the Hall thruster channel walls," in *35th International Electric Propulsion Conference*, no. October, (Atlanta, GA), pp. IEPC–2017–314, 2017. 50
- [110] A. I. Morozov and V. V. Savelyev, "Fundamentals of Stationary Plasma Thruster Theory," in *Reviews of Plasma Physics 21*, pp. 203–391, Springer US, 2000. 51, 53, 56
- [111] M. Villemant, P. Sarrailh, M. Belhaj, L. Garrigues, C. Boniface, M. Villemant, P. Sarrailh, M. Belhaj, L. Garrigues, and C. B. Measurement, "Measurement of energetic efficiency of electron emission under low energy electron beam irradiation : application to Hall thruster dielectric walls," in *Spacecraft Charging Technology Conference*, (NOORDWIJK, Netherlands), 2016. 52
- [112] F. Taccogna, "Non-classical plasma sheaths: space-charge-limited and inverse regimes under strong emission from surfaces," *The European Physical Journal D*, vol. 68, p. 199, jul 2014. 53, 73
- [113] M. D. Campanell and M. V. Umansky, "Strongly Emitting Surfaces Unable to Float below Plasma Potential," *Physical Review Letters*, vol. 116, no. 8, pp. 1–5, 2016. 53
- [114] M. D. Campanell, A. V. Khrabrov, and I. D. Kaganovich, "Instability, collapse, and oscillation of sheaths caused by secondary electron emission," *Physics of Plasmas*, vol. 19, no. 12, 2012. 53
- [115] K. Matyash, R. Schneider, S. Mazouffre, S. Tsikata, and L. Grimaud, "Investigation of rotating spoke instabilities in a wall-less Hall thruster. Part II: Simulation.," in *35th International Electric Propulsion Conference*, no. October, (Atlanta, GA), pp. 1–29, 2017. 53
- [116] R. W. Conversano, D. M. Goebel, and R. E. Wirz, "Magnetically shielded miniature hall thruster," 2014. 56, 59
- [117] H. Kamhawi, W. Huang, T. W. Haag, R. Shastry, G. C. Soulas, T. Smith, I. G. Mikellides, and R. R. Hofer, "Performance and Thermal Characterization of the NASA-300MS 20 kW Hall Effect Thruster," in *33rd International Electric Propulsion Conference*, no. IEPC-2013-444, (Washington DC), pp. 1–23, 2013. 57, 58, 91
- [118] K. de Grys, A. Mathers, B. Welander, and V. Khayms, "Demonstration of 10,400 Hours of Operation on 4.5 kW Qualification Model Hall Thruster," in *46th AIAA/ASME/SAE/ASEE Joint Propulsion Conference & Exhibit*, (Reston, Virginia), American Institute of Aeronautics and Astronautics, jul 2010. 57

- [119] I. Mikellides, I. Katz, R. Hofer, D. Goebel, K. de Grys, and A. Mathers, “Magnetic Shielding of the Acceleration Channel Walls in a Long-Life Hall Thruster,” in *46th AIAA/ASME/SAE/ASEE Joint Propulsion Conference & Exhibit*, no. July, (Nashville, TN, ), pp. AIAA 2010–6942, American Institute of Aeronautics and Astronautics, jul 2010. 57
- [120] I. Mikellides, I. Katz, and R. Hofer, “Design of a Laboratory Hall Thruster with Magnetically Shielded Channel Walls, Phase I: Numerical Simulations,” in *47th AIAA/ASME/SAE/ASEE Joint Propulsion Conference & Exhibit*, no. August, (Reston, Virginia), pp. 1–18, American Institute of Aeronautics and Astronautics, jul 2011. 57
- [121] R. Hofer, D. Goebel, I. Mikellides, and I. Katz, “Design of a Laboratory Hall Thruster with Magnetically Shielded Channel Walls, Phase II: Experiments,” in *48th AIAA/ASME/SAE/ASEE Joint Propulsion Conference & Exhibit*, (Reston, Virginia), American Institute of Aeronautics and Astronautics, jul 2012. 57, 58, 89, 90, 92, 97
- [122] I. Mikellides, I. Katz, R. Hofer, and D. Goebel, “Design of a Laboratory Hall Thruster with Magnetically Shielded Channel Walls, Phase III: Comparison of Theory with Experiment,” in *48th AIAA/ASME/SAE/ASEE Joint Propulsion Conference & Exhibit*, (Atlanta, Georgia), American Institute of Aeronautics and Astronautics, jul 2012. 57
- [123] D. M. Goebel, R. R. Hofer, I. G. Mikellides, and I. Katz, “Conducting Wall Hall Thrusters,” in *49th AIAA/ASME/SAE/ASEE Joint Propulsion Conference*, (San Jose, CA), American Institute of Aeronautics and Astronautics, jul 2013. 57, 93
- [124] H. Kamhawi, W. Huang, T. Haag, J. Yim, L. Chang, L. Clayman, D. A. Herman, R. Shastry, R. Thomas, C. Griffith, J. Myers, G. Williams, I. G. Mikellides, R. R. Hofer, J. E. Polk, and D. Goebel, “Overview of the Development of the Solar Electric Propulsion Technology Demonstration Mission 12.5-kW Hall Thruster,” in *50th AIAA/ASME/SAE/ASEE Joint Propulsion Conference*, no. 353, (Cleveland, OH), pp. 2014–3898, American Institute of Aeronautics and Astronautics, jul 2014. 57
- [125] R. R. Hofer, H. Kamhawi, D. Herman, J. E. Polk, J. S. Snyder, I. Mikellides, W. Huang, J. Myers, J. Yim, G. Williams, A. L. Ortega, B. Jorns, M. Sekerak, C. Griffiths, R. Shastry, T. Haag, T. Verhey, B. Gilliam, I. Katz, D. M. Goebel, J. R. Anderson, J. Gilland, and L. Clayman, “Development Approach and Status of the 12.5 kW HERMeS Hall Thruster for the Solar Electric Propulsion Technology Demonstration Mission,” in *34th International Electric Propulsion Conference*, (Kobe, Japan), pp. IEPC–2015–186, 2015. 57, 91
- [126] R. W. Conversano, D. M. Goebel, and R. R. Hofer, “Magnetically Shielded Miniature Hall Thruster : Development and Initial Testing,” in *IEPC-2013-201 Presented*, pp. 1–21, 2013. 58
- [127] R. W. Conversano, D. M. Goebel, I. G. Mikellides, R. R. Hofer, T. S. Matlock, R. E. Wirz, and I. G. Mikellides, “Magnetically Shielded Miniature Hall Thruster: Performance Assessment and Status Update,” in *50th AIAA/ASME/SAE/ASEE Joint Propulsion Conference*, (Reston, Virginia), American Institute of Aeronautics and Astronautics, jul 2014. 58, 111
- [128] R. W. Conversano, L. Angeles, D. M. Goebel, R. R. Hofer, I. G. Mikellides, I. Katz, and R. E. Wirz, “Magnetically Shielded Miniature Hall Thruster: Design Improvement and Performance Analysis,” in *34th International Electric Propulsion Conference*, pp. IEPC–2015–100, 2015. 58
- [129] R. W. Conversano, D. M. Goebel, R. R. Hofer, and N. Arora, “Performance enhancement of a long-life, low-power hall thruster for deep-space smallsats,” in *2017 IEEE Aerospace Conference*, pp. 1–12, IEEE, mar 2017. 58, 111
- [130] R. W. Conversano, R. B. Lobbia, K. C. Tilley, D. M. Goebel, S. W. Reilly, I. G. Mikellides, and R. R. Hofer, “Development and Initial Performance Testing of a Low-Power Magnetically Shielded Hall Thruster with an Internally-Mounted Hollow Cathode,” in *35th International Electric Propulsion Conference*, (Atlanta, GA), pp. IEPC–2017–64, 2017. 58, 111
- [131] R. A. Martinez, J. D. Williams, J. Moritz, and j. C. Farnell, “Hall current plasma source having a center-mounted or a surface-mounted cathode,” 2018. 58

- [132] R. R. Hofer, S. E. Cusson, R. B. Lobbia, and A. D. Gallimore, “The H9 Magnetically Shielded Hall Thruster,” in *35th International Electric Propulsion Conference*, (Atlanta, GA), pp. 1–18, 2017. 58
- [133] S. Mazouffre, J. Vaudolon, G. Largeau, C. Henaux, A. Rossi, and D. Harribey, “Visual Evidence of Magnetic Shielding With the PPS-Flex Hall Thruster,” *IEEE Transactions on Plasma Science*, vol. 42, pp. 2668–2669, oct 2014. 58, 65, 90
- [134] T. Andreussi, V. Giannetti, A. Leporini, M. Saravia, and M. Andrenucci, “Influence of the magnetic field configuration on the plasma flow in Hall thrusters,” *Plasma Physics and Controlled Fusion*, pp. 0–22, sep 2017. 58
- [135] V. Giannetti, A. Piragino, F. Faraji, M. Reza, A. Leporini, M. M. Saravia, T. Andreussi, A. Rosso-divita, M. Andrenucci, and D. Estublier, “Development of a 5kW Low-erosion Hall Effect Thruster,” in *35th International Electric Propulsion Conference*, 2017. 58
- [136] C. Ducci, T. Misuri, S. Gregucci, D. Pedrini, and Kathe Dannenmayer, “Magnetically Shielded HT100 Experimental Campaign,” in *35th International Electric Propulsion Conference*, pp. IEPC–2017–372, 2017. 58
- [137] R. Shastry, W. Huang, T. W. Haag, and H. Kamhawi, “Langmuir Probe Measurements Within the Discharge Channel of the 20-kW NASA-300M and NASA-300MS Hall Thrusters,” in *33rd International Electric Propulsion Conference*, no. IEPC-2013-122, pp. 1–15, 2013. 58, 97
- [138] W. Huang, R. Shastry, G. C. Soulas, and H. Kamhawi, “Farfield Plume Measurement and Analysis on the NASA-300M and NASA-300MS,” in *33rd International Electric Propulsion Conference*, pp. IEPC–2013–057, 2013. 58
- [139] D. M. Goebel, R. R. Hofer, I. G. Mikellides, I. Katz, J. E. Polk, and B. N. Dotson, “Conducting Wall Hall Thrusters,” *IEEE Transactions on Plasma Science*, vol. 43, pp. 118–126, jan 2015. 58, 78, 80, 93
- [140] A. Leufroy, T. Gibert, and A. Bouchoule, “Characteristics of a permanent magnet low power Hall thruster (PPI),” in *31st International Electric Propulsion Conference*, pp. 1–11, 2009. 59
- [141] D. Meeker, “Finite Element Method Magnetics Version 4.2 User Manual,” 2010. 59, 103
- [142] D. M. Goebel, R. R. Hofer, I. G. Mikellides, I. Katz, J. E. Polk, and B. N. Dotson, “Conducting Wall Hall Thrusters,” in *33rd International Electric Propulsion Conference*, vol. IEPC-2013-, (Washington, D.C), IEEE, jan 2013. 61, 93
- [143] S. A. Khartov, A. B. Nadiradze, I. I. Shkarban, and Y. V. Zikeeva, “SPT’s high lifetime – some problems of solution,” in *29th International Electric Propulsion Conference*, (Princeton University), pp. IEPC–2005–62, 2005. 61
- [144] W. Huang, A. D. Gallimore, and T. B. Smith, “Interior and Near-Wall Ion Velocity Distribution Functions in the H6 Hall Thruster,” *Journal of Propulsion and Power*, vol. 29, pp. 1146–1154, sep 2013. 62, 67
- [145] S. Mazouffre, V. Kulaev, and J. P. Luna, “Ion diagnostics of a discharge in crossed electric and magnetic fields for electric propulsion,” *Plasma Sources Science and Technology*, vol. 18, p. 034022, aug 2009. 62
- [146] A. Lejeune, G. Bourgeois, and S. Mazouffre, “Kr II and Xe II axial velocity distribution functions in a cross-field ion source,” *Phys. Plasmas Phys. Plasmas Additional information on Phys. Plasmas Journal Homepage*, vol. 19, no. 19, pp. 73501–63507, 2012. 63
- [147] R. R. Hofer, D. M. Goebel, I. G. Mikellides, and I. Katz, “Magnetic shielding of a laboratory Hall thruster. II. Experiments,” *Journal of Applied Physics*, vol. 115, p. 043304, jan 2014. 65
- [148] I. G. Mikellides, I. Katz, R. R. Hofer, and D. M. Goebel, “Magnetic shielding of walls from the unmagnetized ion beam in a Hall thruster,” *Applied Physics Letters*, vol. 102, no. 2, pp. 13–18, 2013. 65

- [149] R. Koslover and R. McWilliams, "Measurement of multidimensional ion velocity distributions by optical tomography," *Review of Scientific Instruments*, vol. 57, pp. 2441–2448, oct 1986. 67
- [150] I. G. Mikellides, A. Lopez Ortega, and B. Jorns, "Assessment of Pole Erosion in a Magnetically Shielded Hall Thruster," in *50th AIAA/ASME/SAE/ASEE Joint Propulsion Conference*, (Pasadena, CA), American Institute of Aeronautics and Astronautics, jul 2014. 71, 91, 109
- [151] M. J. Sekerak, R. R. Hofer, J. E. Polk, B. a. Jorns, and I. G. Mikellides, "Wear Testing of a Magnetically Shielded Hall Thruster at 2000 s Specific Impulse," in *34th International Electric Propulsion Conference*, (Kobe, Japan), pp. IEPC–2015–155, 2015. 71, 92
- [152] P. Peterson, D. Manzella, and D. Jacobson, "Investigation of the Erosion Characteristics of a Laboratory Hall Thruster," in *39th AIAA/ASME/SAE/ASEE Joint Propulsion Conference and Exhibit*, (Huntsville, Alabama), American Institute of Aeronautics and Astronautics, jul 2003. 77
- [153] R. Eytan, D. Lev, G. Alon, A. Warshavsky, A. Kapulkin, and M. Rubanovitz, "Wall Material Selection Process for CAM200 Low Power Hall Thruster," in *Joint Conference of 30th International Symposium on Space Technology and Science 34th International Electric Propulsion Conference and 6th Nano-satellite Symposium*, (Hyogo-Kobe, Japan), 2015. 77
- [154] H. Tahara, K. Imanaka, and S. Yuge, "Effects of channel wall material on thrust performance and plasma characteristics of Hall-effect thrusters," *Vacuum*, vol. 80, pp. 1216–1222, sep 2006. 77
- [155] Y. Raiteses, J. Ashkenazy, G. Appelbaum, and M. Guelman, "Experimental Investigation of the Effect of Channel Material on Hall Thruster Characteristics," in *25th Int. Electric Propulsion Conf.*, (Cleveland, OH), 1997. 78
- [156] J. Ashkenazy, Y. Raiteses, and G. Appelbaum, "Parametric Studies of the Hall Thruster at Soreq," tech. rep., IEAC, 1997. 78
- [157] N. Gascon and M. A. Cappelli, "Wall effects on the excitation and propagation of instabilities in Hall thrusters," in *28th Internation Electric Propulsion Conference*, vol. 3032, pp. 1–10, 2003. 78
- [158] Y. Raiteses, I. D. Kaganovich, A. Khrabrov, D. Sydorenko, N. J. Fisch, and A. Smolyakov, "Effect of Secondary Electron Emission on Electron Cross-Field Current in E X B Discharges," *IEEE Transactions on Plasma Science*, vol. 39, pp. 995–1006, apr 2011. 78, 83
- [159] Y. Raiteses, D. Staack, and N. Fisch, "Controlling the Plasma Potential Distribution in Segmented-Electrode Hall Thruster," *IEEE Transactions on Plasma Science*, vol. 36, pp. 1202–1203, aug 2008. 78
- [160] Y. Raiteses, D. Staack, A. Dunaevsky, and N. J. Fisch, "Operation of a segmented Hall thruster with low-sputtering carbon-velvet electrodes," *Journal of Applied Physics*, vol. 99, p. 036103, feb 2006. 78
- [161] K. D. Diamant, J. E. Pollard, R. B. Cohen, Y. Raiteses, and N. J. Fisch, "Segmented Electrode Hall Thruster," *Journal of Propulsion and Power*, vol. 22, pp. 1396–1401, nov 2006. 78
- [162] Y. Raiteses, A. Smirnov, D. Staack, and N. J. Fisch, "Measurements of secondary electron emission effects in the Hall thruster discharge," *Physics of Plasmas*, vol. 13, p. 014502, jan 2006. 78
- [163] Y. Raiteses, D. Staack, A. Dunaevsky, and N. J. Fisch, "Operation of a segmented Hall thruster with low-sputtering carbon-velvet electrodes," *Journal of Applied Physics*, vol. 99, p. 036103, feb 2006. 78
- [164] Y. Raiteses, A. Smirnov, N. Fisch, and D. Staack, "Segmented Electrodes in Annular and Cylindrical Hall Thrusters," in *42nd AIAA/ASME/SAE/ASEE Joint Propulsion Conference & Exhibit*, (Reston, Virginia), American Institute of Aeronautics and Astronautics, jul 2006. 78
- [165] Y. Raiteses, M. Keidar, D. Staack, and N. J. Fisch, "Effects of segmented electrode in Hall current plasma thrusters," *Journal of Applied Physics*, vol. 92, pp. 4906–4911, nov 2002. 78, 83

- [166] Y. Raitses, L. A. Dorf, A. A. Litvak, and N. J. Fisch, “Plume reduction in segmented electrode Hall thruster,” *Journal of Applied Physics*, vol. 88, pp. 1263–1270, aug 2000. 78
- [167] N. B. Meezan, N. Gascon, and M. A. Cappelli, “Linear Geometry Hall Thruster with Boron Nitride and Diamond Walls,” in *27th International Electric Propulsion Conference*, (Pasadena, CA), pp. 15–19, 2001. 78
- [168] T. Ito, N. Gascon, W. S. Crawford, and M. A. Cappelli, “Experimental Characterization of a Micro-Hall Thruster,” *Journal of Propulsion and Power*, vol. 23, pp. 1068–1074, sep 2007. 78
- [169] N. Gascon, S. Crawford, R. Corey, and M. Cappelli, “Coaxial Hall Thruster with Diamond Inner Channel Wall,” in *42nd AIAA/ASME/SAE/ASEE Joint Propulsion Conference & Exhibit*, no. July, (Sacramento, California), pp. AIAA–2006–4995, American Institute of Aeronautics and Astronautics, jul 2006. 78
- [170] E. Y. Choueiri, “Fundamental difference between the two Hall thruster variants,” *Physics of Plasmas*, vol. 8, no. 11, p. 5025, 2001. 78
- [171] L. Grimaud, A. Pétin, J. Vaudolon, and S. Mazouffre, “Perturbations induced by electrostatic probe in the discharge of Hall thrusters,” *Review of Scientific Instruments*, vol. 87, p. 043506, apr 2016. 83
- [172] L. Grimaud and S. Mazouffre, “Conducting wall Hall thrusters in magnetic shielding and standard configurations,” *Journal of Applied Physics*, vol. 122, p. 033305, jul 2017. 85, 86
- [173] R. W. Conversano, D. M. Goebel, R. R. Hofer, I. G. Mikellides, and R. E. Wirz, “Performance Analysis of a Low-Power Magnetically Shielded Hall Thruster: Experiments,” *Journal of Propulsion and Power*, vol. Accepted, pp. 1–9, apr 2017. 87, 89, 91, 97, 111
- [174] J. Ekholm and W. Hargus, “E x B Measurements of a 200 W Xenon Hall Thruster,” in *41st AIAA/ASME/SAE/ASEE Joint Propulsion Conference & Exhibit*, (Tucson, Arizona), American Institute of Aeronautics and Astronautics, jul 2005. 89
- [175] L. Grimaud and S. Mazouffre, “Ion behavior in low-power magnetically shielded and unshielded Hall thrusters,” *Plasma Sources Science and Technology*, vol. 26, p. 055020, apr 2017. 90, 91
- [176] R. W. Conversano, D. M. Goebel, I. G. Mikellides, R. R. Hofer, and R. E. Wirz, “Performance Analysis of a Low-Power Magnetically Shielded Hall Thruster: Computational Modeling,” *Journal of Propulsion and Power*, vol. Accepted, pp. 1–10, apr 2017. 91, 97
- [177] D. M. Goebel, B. Jorns, R. R. Hofer, I. G. Mikellides, and I. Katz, “Pole-piece Interactions with the Plasma in a Magnetically Shielded Hall Thruster,” in *50th AIAA/ASME/SAE/ASEE Joint Propulsion Conference*, (Pasadena, CA), pp. 1–7, American Institute of Aeronautics and Astronautics, jul 2014. 91, 109
- [178] V. Viel-Inguibert, “Secondary electron emission of ceramics used in the channel of SPT,” in *28th International Electric Propulsion Conference*, (Toulouse, France), pp. IEPC–2003–258, 2003. 92
- [179] A. Dunaevsky, Y. Raitses, and N. J. Fisch, “Secondary electron emission from dielectric materials of a Hall thruster with segmented electrodes,” *Physics of Plasmas*, vol. 10, no. 6, pp. 2574–2577, 2003. 92
- [180] T. Tondu, M. Belhaj, and V. Inguibert, “Electron-emission yield under electron impact of ceramics used as channel materials in Hall-effect thrusters,” *Journal of Applied Physics*, vol. 110, no. 9, pp. 1–5, 2011. 92
- [181] J. M. Pedgley and G. M. McCracken, “Plasma sheath properties calculated using measured secondary electron emission coefficients,” *Plasma Physics and Controlled Fusion*, vol. 35, pp. 397–409, mar 1993. 92

- [182] M. Belhaj, J. Roupie, O. Jbara, J. Puech, N. Balcon, and D. Payan, "Electron emission at very low electron impact energy: experimental and Monte-Carlo results," in *Proceedings of ECLOUD'12*, vol. CERN-2013, p. 137, aug 2013. 92
- [183] E. Ahedo, J. M. Gallardo, and M. Martínez-Sánchez, "Effects of the radial plasma-wall interaction on the Hall thruster discharge," *Physics of Plasmas*, vol. 10, pp. 3397–3409, aug 2003. 92
- [184] A. Héron and J. C. Adam, "Anomalous conductivity in Hall thrusters: Effects of the non-linear coupling of the electron-cyclotron drift instability with secondary electron emission of the walls," *Physics of Plasmas*, vol. 20, no. 8, p. 082313, 2013. 92
- [185] D. Sydorenko, A. Smolyakov, I. Kaganovich, and Y. Raitses, "Kinetic simulation of secondary electron emission effects in Hall thrusters," *Physics of Plasmas*, vol. 13, p. 014501, jan 2006. 92
- [186] F. Taccogna, P. Minelli, M. Capitelli, and S. Longo, "Physics of Hall-effect thruster by particle model," in *28TH INTERNATIONAL SYMPOSIUM ON RAREFIED GAS DYNAMICS 2012*, vol. 1501, pp. 1390–1399, AIP Publishing, nov 2012. 92
- [187] M. Belhaj, N. Guibert, K. Guerch, P. Sarrailh, and N. Arcis, "Temperature effect on the electron emission yield of BN-SiO<sub>2</sub> under electron irradiation," in *Spacecraft Charging Technology Conference 2014 (13th SCTC)*, (Pasadena, United States), jun 2014. 92
- [188] N. Bundaleski, M. Belhaj, T. Gineste, and O. M. N. D. Teodoro, "Calculation of the angular dependence of the total electron yield," *Vacuum*, vol. 122, no. April, pp. 255–259, 2015. 92
- [189] Y. Ding, H. Sun, W. Peng, Y. Xu, L. Wei, H. Li, P. Li, H. Su, and D. Yu, "Experimental test of 200 W Hall thruster with titanium wall," *Japanese Journal of Applied Physics*, vol. 56, no. 5, p. 050312, 2017. 93
- [190] L. Garrigues, S. Santhosh, L. Grimaud, and S. Mazouffre, "Operation of a Low-Power Hall Thruster: Comparison between Magnetically Unshielded and Shielded Configuration," *Plasma Sources Science and Technology*, 2018. 95, 96
- [191] L. Garrigues, G. Fubiani, and J. P. Boeuf, "Appropriate use of the particle-in-cell method in low temperature plasmas: Application to the simulation of negative ion extraction," *Journal of Applied Physics*, vol. 120, p. 213303, dec 2016. 96
- [192] L. Garrigues, S. Mazouffre, and G. Bourgeois, "Computed versus measured ion velocity distribution functions in a Hall effect thruster," *Journal of Applied Physics*, vol. 111, p. 113301, jun 2012. 96, 97
- [193] L. Garrigues, G. J. M. Hagelaar, J. Bareilles, C. Boniface, and J. P. Boeuf, "Model study of the influence of the magnetic field configuration on the performance and lifetime of a Hall thruster," *Physics of Plasmas*, vol. 10, pp. 4886–4892, dec 2003. 96
- [194] G. J. M. Hagelaar, J. Bareilles, L. Garrigues, and J. P. Boeuf, "Two-dimensional model of a stationary plasma thruster," *Journal of Applied Physics*, vol. 91, pp. 5592–5598, may 2002. 96
- [195] V. Latocha, L. Garrigues, P. Degond, and J. P. Boeuf, "Numerical simulation of electron transport in the channel region of a stationary plasma thruster," *Plasma Sources Science and Technology*, vol. 11, pp. 104–114, feb 2002. 96
- [196] J. P. Boeuf and L. Garrigues, "Low frequency oscillations in a stationary plasma thruster," *Journal of Applied Physics*, vol. 84, no. 7, p. 3541, 1998. 96
- [197] I. G. Mikellides and I. Katz, "Numerical simulations of Hall-effect plasma accelerators on a magnetic-field-aligned mesh," *Physical Review E - Statistical, Nonlinear, and Soft Matter Physics*, vol. 86, no. 4, 2012. 96
- [198] I. G. Mikellides, I. Katz, H. Kamhawi, J. L. Vannoord, and N. Aeronautics, "Numerical Simulations of a 20-kW Class Hall Thruster Using the Magnetic-Field-Aligned-Mesh Code Hall2De," in *32nd International Electric Propulsion Conference*, (Wiesbaden, Germany), pp. IEPC–2011–244, 2011. 96

- [199] K. Dannenmayer and S. Mazouffre, "Elementary Scaling Relations for Hall Effect Thrusters," *Journal of Propulsion and Power*, vol. 27, pp. 236–245, jan 2011. 96
- [200] L. Garrigues, "Ion properties in a Hall current thruster operating at high voltage," *Journal of Applied Physics*, vol. 119, p. 163305, apr 2016. 97
- [201] S. E. Cusson, B. Jorns, and A. Gallimore, "Simple Model for Cathode Coupling Voltage Versus Background Pressure in a Hall Thruster," *53rd AIAA/SAE/ASEE Joint Propulsion Conference*, no. July, 2017. 100
- [202] R. Spektor and W. G. Tighe, "Laser Induced Fluorescence Measurements in a Hall Thruster as a Function of Background Pressure," in *52nd AIAA/SAE/ASEE Joint Propulsion Conference*, (Reston, Virginia), pp. 1–7, American Institute of Aeronautics and Astronautics, jul 2016. 100
- [203] J. Galy, *Modélisation 2D hybride d'un propulseur à effet Hall pour satellites*. PhD thesis, Université Paul Sabatier, 2002. 100
- [204] J. T. Yim, "A survey of xenon ion sputter yield data and fits relevant to electric propulsion spacecraft integration," in *35th International Electric Propulsion Conference*, pp. IEPC–2017–060, 2017. 101
- [205] D. Manzella, S. Oleson, J. Sankovic, T. Haag, A. Semenko, and V. Kim, "Evaluation of low power Hall thruster propulsion," in *32nd Joint Propulsion Conference and Exhibit*, no. July, (Reston, Virginia), American Institute of Aeronautics and Astronautics, jul 1996. 101, 111
- [206] O. B. Duchemin, S. Zurbach, F. Marchandise, and N. Cornu, "Qualification of the PPS-1350 Hall plasma thruster at 2.5 kW," in *49th AIAA/ASME/SAE/ASEE Joint Propulsion Conference*, (Reston, Virginia), American Institute of Aeronautics and Astronautics, jul 2013. 101
- [207] F. Marchandise, N. Cornu, F. Darnon, and Denis E, "PPS®1350-G Qualification status 10500 h," *30th International Electric Propulsion Conference*, pp. IEPC–2007–164, 2007. 101
- [208] P. Dumazert, S. Lagardere-Verdier, F. Marchandise, C. R. Koppel, P. Garnerio, and F. Balme, "PPS® -1350-G Qualification Status March 2003," Tech. Rep. March, 2003. 101
- [209] L. Lorello, I. Levchenko, K. Bazaka, M. Keidar, L. Xu, S. Huang, J. W. M. Lim, and S. Xu, "Hall Thrusters With Permanent Magnets: Current Solutions and Perspectives," *IEEE Transactions on Plasma Science*, pp. 1–13, 2017. 103
- [210] J. M. D. Coey, "Hard Magnetic Materials: A Perspective," *IEEE Transactions on Magnetics*, vol. 47, pp. 4671–4681, dec 2011. 103
- [211] S. Reilly and R. Hofer, "Thermal Analysis of the 100-kW class X3 Hall Thruster," in *47th International Conference on Environmental Systems*, 47th International Conference on Environmental Systems, jul 2017. 104
- [212] J. L. Myers, H. Kamhawi, J. Yim, and L. Clayman, "Hall Thruster Thermal Modeling and Test Data Correlation," *52nd AIAA/SAE/ASEE Joint Propulsion Conference*, pp. 1–23, 2016. 104
- [213] S. W. Reilly, M. J. Sekerak, and R. R. Hofer, "Transient Thermal Analysis of the 12.5 kW HERMeS Hall Thruster," *52nd AIAA/SAE/ASEE Joint Propulsion Conference*, pp. 1–11, 2016. 104
- [214] W. Huang, H. Kamhawi, J. L. Myers, J. Yim, and G. Neff, "Non-Contact Thermal Characterization of NASA's 12.5-kW Hall Thruster," in *51st AIAA/SAE/ASEE Joint Propulsion Conference*, Propulsion and Energy Forum, (Reston, Virginia), American Institute of Aeronautics and Astronautics, jul 2015. 104
- [215] D. Pérez-Grande, P. Fajardo, and E. Ahedo, "Evaluation of Erosion Reduction Mechanisms in Hall Effect Thrusters," in *Joint Conference of 30th International Symposium on Space Technology and Science, 34th International Electric Propulsion Conference*, (Hyogo-Kobe), 2015. 109
- [216] S. Mazouffre and L. Grimaud, "Characteristics and Performances of a 100-W Hall Thruster for Microspacecraft," *IEEE Transactions on Plasma Science*, vol. 46, pp. 330–337, feb 2018. 111

- [217] J. D. Frieman, T. M. Liu, M. L. R. Walker, J. M. Makela, A. Mathers, and P. Y. Peterson, "Performance Evaluation of the T-40 Low-Power Hall Current Thruster," *30th International Electric Propulsion Conference*, no. IEPC-2015-305, pp. 1–13, 2015. 111
- [218] C. Ducci, S. Oslyak, R. Albertoni, D. Dignani, M. Andrenucci, and Alta, "HT100D performance evaluation and endurance test results," *33rd International Electric Propulsion Conference*, pp. 1–9, 2013. 111
- [219] M. Potapenko, V. Gopanchuk, and S. Olotin, "PlaS-40 Development Status: New Results," in *Joint Conference of 30th International Symposium on Space Technology and Science 34th International Electric Propulsion Conference and 6th Nano-satellite Symposium*, (Hyogo-Kobe, Japan), 2015. 111
- [220] J. Szabo, B. Pote, S. Paintal, M. Robin, A. Hillier, R. D. Branam, and R. E. Huffmann, "Performance Evaluation of an Iodine-Vapor Hall Thruster," *Journal of Propulsion and Power*, vol. 28, pp. 848–857, jul 2012. 111
- [221] D. Lev, D. Lev, R. Eytan, G. Alon, A. Warshavsky, L. Appel, R. Advanced, and D. Systems, "CAM200 Hall Thruster - Development Overview," *66th International Astronautical Congress*, no. October 2015, pp. IAC-15-C4.4.4, 2016. 111
- [222] A. Kapulkin, V. Balabanov, M. Rubanovich, E. Behar, L. Rabinovich, A. Warshavsky, Technion, and Rafael, "CAMILA Hall Thruster: New Results," *32nd International Electric Propulsion Conference*, pp. 1–14, 2011. 111
- [223] a. I. Bugrova, a. D. Desiatskov, and H. R. Kaufman, "Design and Experimental Investigation of a Small Closed Drift Thruster," in *27th International Electric Propulsion Conference*, no. 1, 2001. 111
- [224] J. W. M. Lim, S. Y. Huang, L. Xu, J. S. Yee, R. Z. Sim, Z. L. Zhang, I. Levchenko, and S. Xu, "Automated Integrated Robotic Systems for Diagnostics and Test of Electric and Micropropulsion Thrusters," *IEEE Transactions on Plasma Science*, vol. 46, pp. 345–353, feb 2018. 111



Lou GRIMAUD

# Topologie d'écrantage magnétique appliquée aux moteurs de Hall faible puissance

Les propulseurs de Hall sont l'une des techniques de propulsion fusée par plasma les plus utilisés. Ils possèdent une impulsion spécifique moyenne et un haut rapport poussé sur puissance qui les rend idéal pour une grande partie des applications commerciales et scientifiques. Une de leurs limitations principales est l'érosion des parois du propulseur par le plasma qui réduit leur durée de vie. La topologie dite "d'écrantage magnétique" est une solution proposée pour prolonger cette durée de vie. Elle est ici appliquée à un petit propulseur de Hall de 200 W. Dans cette thèse les règles de mise à l'échelle pour les propulseurs de Hall de la gamme de 100 à 200W sont testées expérimentalement. Un propulseur écranté de 200 W est comparé avec un propulseur standard similaire. Le comportement des ions dans ces deux moteurs est extrêmement différent. Des mesures de performance ont été réalisées avec des parois en BN-SiO<sub>2</sub> et graphite. Le courant de décharge augmente de 25% avec le graphite dans le propulseur non-écranté. Le résultat est un rendement maximum de 38% avec le nitrure de bore mais de seulement 31% pour le graphite. Le propulseur écranté quant à lui n'atteint que 25% de rendement quel que soit le matériau.

Cette baisse de performance dans les petits moteurs écrantés peut être attribuée à un mauvais rendement d'utilisation de l'ergol. Analyses des résultats expérimentaux ainsi que la conduite de simulations suggèrent que cela est dû au fait que la zone d'ionisation ne couvre pas l'ensemble du canal de décharge. Un nouveau design pour un petit propulseur de Hall écranté est proposé.

Mots clés : Propulsion spatiale électrique, propulsion par plasma, propulseur de Hall, Écrantage magnétique

## Magnetic shielding topology applied to low power Hall thrusters

Hall thrusters are one of the most used rocket electric propulsion technology. They combine moderate specific impulse with high thrust to power ratio which makes them ideal for a wide range of practical commercial and scientific applications. One of their limitations is the erosion of the thruster walls which reduces their lifespan. The magnetic shielding topology is a proposed solution to prolong the lifespan. It is implemented on a small 200 W Hall thruster.

In this thesis the scaling of classical unshielded Hall thrusters down to 200 and 100 W is discussed. A 200 W low power magnetically shielded Hall thruster is compared with an identically sized unshielded one. The ion behavior inside the thruster is measured and significant differences are found across the discharge channel. Both thrusters are tested with classical BN-SiO<sub>2</sub> and graphite walls. The magnetically shielded thruster is not sensitive to the material change while the discharge current increase by 25% in the unshielded one. The result is a maximum efficiency of 38% for boron nitride in the unshielded thruster but only 31% with graphite. The shielded thruster achieves a significantly lower efficiency with only 25% efficiency with both materials.

Analysis of the experimental results as well as simulations of the thrusters reveal that the performance difference is mostly caused by low propellant utilization. This low propellant utilization comes from the fact that the ionization region doesn't cover all of the discharge channel. A new magnetically shielded thruster is designed to solve this issue.

Keywords : Electric space propulsion, Plasma propulsion, Hall thruster, magnetic shielding, laser induced fluorescence, alternative materials, low power.



ICARE - CNRS  
1C avenue de la Recherche Scientifique  
45071 Orléans Cedex 2, France

